RARE EARTH IONS (La^{3+} AND Eu^{3+}) DOPED NICKEL ZINC FERRITE NANOMATERIALS AND THEIR COMPOSITES WITH REDUCED GRAPHENE OXIDE FOR PHOTOCATALYTIC AND ELECTROCHEMICAL SENSOR APPLICATIONS

BY:

Workneh Mechal Shume

A Dissertation Submitted to

The Department of Applied Chemistry

Applied Natural Sciences

Postgraduate Studies

Adama Science and Technology University

June, 2024

Adama, Ethiopia

RARE EARTH IONS (La^{3+} AND Eu^{3+}) DOPED NICKEL ZINC FERRITE NANOMATERIALS AND THEIR COMPOSITES WITH REDUCED GRAPHENE OXIDE FOR PHOTOCATALYTIC AND ELECTROCHEMICAL SENSOR APPLICATIONS

BY:

Workneh Mechal Shume

Supervisors: Major-Supervisor: Enyew Amare (Assoc. Prof., Ph.D.)

Co-Supervisor: Fedlu Kedir (Assoc. Prof., Ph.D.)

Co-Supervisor: H C Ananda Murthy (Prof.)

A Dissertation Submitted to

The Department of Applied Chemistry

Applied Natural Sciences

Presented in Fulfillment of the Requirement for the Degree of Doctor of Philosophy Materials Chemistry

Postgraduate Studies

Adama Science and Technology University

June, 2024

Adama, Ethiopia

APPROVAL SHEET

We hereby certify that the recommendations and suggestions made by the board of examiners are appropriately incorporated into the final version of the dissertation entitled "**Rare Earth Ions (La^{3+} And Eu^{3+}) Doped Nickel Zinc Ferrite Nanomaterials and Their Composites with Reduced Graphene Oxide for Photocatalytic and Electrochemical Sensor Applications"** by **Workneh Mechal Shume**.

Enyew Amare (Assoc. Prof., Ph.D.)	_____	_____
Major Supervisor	Signature	Date
Fedlu Kedir (Assoc. Prof., Ph.D.)	_____	_____
Co-supervisor	Signature	Date
H C Ananda Murthy (Prof.)	_____	_____
Co-supervisor	Signature	Date

We, the undersigned, members of the Board of Examiners of the dissertation open defense by **Workneh Mechal Shume,** have read and evaluated the dissertation entitled "**Rare Earth Ions (La^{3+} And Eu^{3+}) Doped Nickel Zinc Ferrite Nanomaterials and Their Composites with Reduced Graphene Oxide for Photocatalytic and Electrochemical Sensor Applications"** and examined the candidate during open defense. This is, therefore, to certify that the dissertation is accepted for partial fulfillment of the requirement of the degree of Doctor of Philosophy in "**Materials Chemistry**".

Dr. Defaru Negera	_____	_____
Chairperson	Signature	Date
Gemechu Deressa (Assoc. Prof., Ph.D.)	_____	_____
Internal Examiner	Signature	Date
Bedasa Abdisa (Assoc. Prof., Ph.D.)	_____	_____
Internal Examiner	Signature	Date
Prof. Tesfaye Rafera	_____	_____
External Examiner 1	Signature	Date
Alemayehu Paulose (Assoc. Prof., Ph.D.)	_____	_____
External Examiner 2	Signature	Date

Finally, approval and acceptance of the dissertation is contingent upon submission of its final copy to the Office of Postgraduate Studies (OPGS) through the candidate's Department Graduate Council (DGC) and Graduate Committee (GC).

_____	_____	_____
Department Head	Signature	Date
_____	_____	_____
School Dean	Signature	Date
_____	_____	_____
Office of Postgraduate Studies, Dean	Signature	Date

DECLARATION

I hereby declare that this Dissertation entitled **"RARE EARTH IONS (La^{3+} AND Eu^{3+}) DOPED NICKEL ZINC FERRITE NANOMATERIALS AND THEIR COMPOSITES WITH REDUCED GRAPHENE OXIDE FOR PHOTOCATALYTIC AND ELECTROHEMICAL SENSOR APPLICATIONS"** is my original work. That is, it has not been submitted for the award of any academic degree, diploma, or certificate in any other university. All sources of materials used for this thesis have been duly acknowledged through appropriate citations.

Workneh Mechal	_____	_____
Name of student	Signature	Date

This Ph.D. Dissertation has been submitted to the department for further examination and defense, with our approval as the dissertation supervisor.

1. **Enyew Amare (Assoc. Prof., Ph.D.)** _____ _____
   Major Supervisor — Signature — Date
2. **Fedlu Kedir (Assoc. Prof., Ph.D.)** _____ _____
   Co-supervisor — Signature — Date
3. **H C Ananda Murthy (Prof.)** _____ _____
   Co-supervisor — Signature — Date

ACKNOWLEDGEMENT

GOD is my ultimate strength and power who brings the best out of me!

I want to express my heartfelt gratitude and sincere appreciation to my advisor, Dr. Enyew Amare, Associate Professor of Inorganic Chemistry, Department of Chemistry, Adama Science and Technology University, Ethiopia, for his kind supervision, indispensable guidance, illuminating suggestions, and constant inspiration throughout the whole research period.

I am also greatly obliged to Dr. Fedlu Kedir, Physical Chemistry, Department of Applied Chemistry, Adama Science and Technology University, Ethiopia, for his kind supervision. I thank Dr. Gemechu Deressa for his valuable help in providing europium oxide. I am also thankful to Dr. Amare Aregahegn, Addis Abeba University, for his kind facilitation of SEM/EDX, HR-TEM/SAED, XPS, and BET characterization.

I want to acknowledge Professor Neeraj K. Gupta, who helped on the gramatical edition of the dissertation.

I want to thank every Department of Applied Chemistry staff member at ASTU for their direct and indirect assistance throughout my work.

I am also thankful to the Department of Applied Chemistry, Department of Applied Biology, Department of Applied Physics, and Department of Materials Science and Engineering at Adama Science and Technology University for providing laboratory space and experimental facilities during measurements.

I thank Dilla University for funding this dissertation work.

Finally, I would like to express my warmest thanks to my family members for their continuous inspiration, moral support, and immeasurable sacrifices during this dissertation work.

TABLE OF CONTENTS

CHAPTER **PAGE**

LIST OF TABLES

TABLE **PAGE**

LIST OF FIGURES

FIGURE **PAGE**

LIST OF ACRONYMS

A.R	Analytical grade reagents
BET	Brunauer-Emmett-Teller
CB	Conduction band
CMCPEs	Chemically modified carbon paste electrodes
CV	Cyclic Voltammetry
CWES	Coated wire electrodes
DPV	Differential pus voltammetry
DTA	Differential thermal analysis
EFSA	European Food Safety Authority
Eg	Band gap energy
FCC	Face center cubic
FTIR	Fourier transforms infrared spectra
GCE	Glass carbon electrode
GO	Graphene oxide
ISFET	Ion-selective field effect transistors
ISE	Ion selected electrode
IFFT	Inverse fast Fourier transmission
LOD	Limit of detection
MB	Methylene blue
MCPE	Modification of carbon paste electrode
MNPs	Magnetic nanoparticles
MO	Methyl orange
NCs	Nanocomposite
NPs	Nanoparticles
NZF	Nickel-zinc iron
NZSFNPs	Nickel-zinc spinel ferrite nanoparticles
NZREF	Nickel-zinc rare earth metal doped ferrite
PL	Photoluminescence spectroscopy
REE	Rare earth elements
rGO	Reduced graphene oxide
SEM/EDX	Scanning electron microscope /energy dispersive X-ray
SPNF	Spinel nano ferrites
SWV	Square wave voltammetry
TGA	Thermo gravimetric analysis
TEM	Transmitted electron microscopy
XRD	X-ray diffraction
XPS	X-ray photon electron spectroscopy

ABSTRACT

The regulation of colorants used in food products and industrial wastes is crucial, as they negatively affect human health and the environment. In this study magnetically separable rare earth metal ions (RE=La^{3+} and Eu^{3+}) doped nickel-zinc (NZF) spinel ferrite ($Ni_{0.75}Zn_{0.25}RE_xFe_{2-x}O_4$) nanoparticles and their composite with reduced graphene oxide ($Ni_{0.75}Zn_{0.25}RE_{0.06}Fe_{1.94}O_4$@rGO) were successfully synthesized by sol-gel auto-combustion and ultra-sonication methods respectively. The synthesized nanomaterials and nanocomposites were characterized by using different advanced instruments. The X-ray diffraction (XRD) analysis confirmed the formation of Face-centered cubic (FCC) ferrites with a crystal size range of 21.41 and 44.94 nm. The formation of the desired nanocomposite, with uniformly distributed spherical-shaped polycrystalline nanoparticles on nanosheets of reduced graphene oxide, was verified by scanning electron microscopy (SEM) equipped with energy dispersive x-ray (EDAX) and high resolution –transmitted electron microscope equipped with small angle electron diffraction (HR-TEM/SAED). The elements' surface composition and valance states in $Ni_{0.75}Zn_{0.25}RE_{0.06}Fe_{1.94}O_4$@rGO nanocomposite were identified using X-ray photon electron spectroscopy (XPS). The specific surface area and pore size distribution of $La^{3+}$and Eu^{3+} doped $Ni_{0.75}Zn_{0.25}Fe_2O_4$ nanomaterials and their composite with rGO were obtained by Brunauer-Emmett-Teller *(BET) analysis. From UV-diffractive spectroscopy (UV-DRS) analysis, the band gap energies were found to be 1.691 eV, 1.797 eV, and 1.624 eV for NZLF@rGO, NZEF@rGO, and NZL-EF@rGO nanocomposite respectively. The synthesized nanocomposite materils (NZLF@rGO, NZEF@rGO, and NZL-EF@rGO) were applied for the photocatalytic decolorization of selected binary dyes (methylene blue (MB) and methyl orange (MO)) under irradiation of visible light and modification of carbon paste electrode for selective detection of common food colorants (sunset yellow (SY) and tartrazine (TZ)). Results showed that as compared to $La^{3+}$and Eu^{3+} doped NZF ferrite nanoparticles, $Ni_{0.75}Zn_{0.25}RE_{0.06}Fe_{1.94}O_4$@rGO nanocomposite had exhibited potential photocatalytic efficiency for simultaneous degradation of MB and MO and electrochemical detection of SY and TZ. Their degradation efficiency was exhibited up to 92-97 % for MB and 96-99 % for MO within 40 min under the optimized conditions of pH = 9, initial concentration of dyes (5mg/L), and catalyst dosage of (50 mg), irradiation time (40 min). Compared to other reactive species, hydroxyl radical (•OH) plays a vital role in the simultaneous degradation of binary dyes. The synergetic effect of $Ni_{0.75}Zn_{0.25}Fe_2O_4$, RE ion, and rGO in Ni0.75Zn0.25RE0.06Fe1.94O4@rGO nanocomposite also efficiently improved the electrochemical response of carbon paste electrode on the simultaneous detection of SY and TZ. The detection limits were in the range of 0.0043-0.0067 μM for SY and 0.0034-0.0048 μM for TZ under the optimized pH=6, analyte concentration 10 mg, and scan rate (50 mV/s). The high sensitivity, selectivity, reproducibility, straightforward fabrication process, good electrode stability, and capacity to regenerate the electrode surface under the optimized conditions make the fabricated electrode ideal for the simultaneous detection of SY and TZ in real samples.*

Keywords: Nickel-zinc spinel ferrite, rare earth ions, nanomaterials, nanocomposite, dyes, photocatalyst, electrochemical sensor & rGO

CHAPTER ONE

1 INTRODUCTION

1.1 Background of The Study

Nanomaterials are the most captive class of materials due to their small size and their variety of applications in different fields of life. All the nanomaterials show different chemical and physical properties from the bulk material from which they are formed, i.e., charge storage capacity, color, melting point, and magnetic properties. Nanocrystalline ferrites show substantial magnetic properties at room temperature (Anwar *et al.*, 2018). The spinel ferrites group contains many materials with a wide range of magnetic, electrical, and chemical properties. Ferrites have contained two main sites, tetrahedral (A) sites and octahedral (B) sites with the general formula of $(M_{1-x}Fe_x)_A[M_x\ Fe_{2-x}]_BO_4$, where M represents the divalent metal ion such as Ca^{+2}, Mg^{+2}, Cd^{+2}, $Ni^{+2,}$ etc (Anwar *et al*., 2020; Bhargava *et al*., 2020; Narang *et al*., 2021).

Due to their tunability, the physicochemical properties and applications of spinel ferrites change with the change of method of their synthesis, chemical composition, and cationic distribution (Philosophy, 2018). Cationic distribution in the spinel ferrite system is also affected by the preparation method, particle size, and substitution. Therefore, we can change the physicochemical properties and applications of ferrites by changing the type and amount of substituting elements (Somvanshi *et al*., 2020). The impact of rare earth cation substitution on the properties of different ferrites has been investigated and reported in the literature. Substitution of rare earth metals in spinel ferrites distorts the structure of spinel ferrites and produces strain. It also changes spinel ferrites' magnetic and electrical properties, which benefits many desired applications. When rare earth ions replace Fe from the octahedral site in nickel-spinel ferrites $NiZnFe_2O_4$, it become ferroelectric (Srivastava *et al*., 2012).

Graphene-based spinel ferrite composites have been intensively investigated (Ain *et al.*, 2016). Graphene, a two-dimensional structure consisting of a single layer of carbon atoms arranged in a hexagonal pattern, has received significant attention during the last few years due to its versatile electronic, thermal, fastest electron mobility, high surface area, and mechanical properties. Graphene also shows potential applications in several fields, i.e., electronics, composite, sensor,

catalysis energy storage, and biomedical applications (biosensor, bio-devices, drug and gene delivery, cancer therapy, etc.) (Iftikhar *et al*., 2020).

Due to their unique properties, spinel ferrites are used in a variety of applications such as in transformers, indicators, magnetic recorders, hyperthermia, drug delivery, electrochemical sensors, biosensors, photocatalysis, and magneto-optical devices (Kefeni *et al*., 2020). However, this study focuses on spinel ferries' photocatalytic and electrochemical applications.

Photocatalysis is used to clean contaminated water based on the principles of oxidizing and reducing contaminated species on the surface of the photocatalyst. There are three main types of wastewater contaminants: (i) organic-based compounds, (ii) pathogens, (i) organic-based compounds, (ii) pathogens, and (iii) dissolved metal ions. Organic-based groups present in water are commonly removed using photocatalyst materials (Lacombe *et al*., 2012). The primary contamination in water is due to organic-based groups, which negatively impact human health and the environment. Thus, various studies have been reported about the degradation of organic pollutants through photocatalytical means. TiO_2 was the first discovered photocatalyst with numerous advantages and disadvantages. The main drawback of TiO_2 is that it is only active in UV light due to a large band gap (~3.2eV). However, solar energy contains 3-4% UV and ~40% visible light (Shahid *et al*., 2020). In recent times, different semiconductor materials, including metal oxides such as Ag_2O (Jiang *et al*., 2015), CuO (Nazim *et al*., 2021), ZnO-CeO_2 (Saravanan *et al.* 2022), CuO/NiO (Mary *et al*. 2022.), sulfides (Baig *et al.*, 2020), etc., were used as a photocatalyst for degrading organic pollutants under suitable light irradiation. However, most of these materials still suffer from various drawbacks, including the rapid recombination of photo-induced carriers, low photostability, difficulty isolating from treated samples, and poor light utilization. All these drawbacks lead to limited their drawbacks lead to limited photocatalytic efficiency and practicability (Labchir *et al.*, 2020; Tanwar *et al.*, 2019).

Today, there is a need to develop photocatalysts that show maximum efficiency in visible light and can be recycled and recovered easily, which have emerged as an active research subject for environmental problems (Baig *et al.*, 2020). The nano-ferrites are expected to have more prominent photocatalytic activity than in the bulk. Spinel ferrites are a type of hetero-structured nanoferrite that attracted significant attention in the design of visible light active photocatalysts (Gupta *et al*., 2020; O, 2019). This is due to their ability to catalyze the photodegradation of organic

pollutants in visible light and their magnetic properties, which make it easy to separate them from the purified water after application by applying an external magnetic field (Gupta *et al.*, 2020; O, 2019). Nickel-zinc (NZF) spinel ferrite is also classified as a part of semiconductor-based spinel ferrite material, with unique properties including large volume, narrow band gap ($h\nu \sim 1.57$ eV) (Rashmi, Naik, et al., 2017), long life span, high stability, easy preparation, reusability, easy to separate from solution and their utility in various applications (Ciocarlan *et al.*, 2018; Rashmi *et al.*, 2017). In this respect, NZF spinel ferrite is the base material for a wide range of applications, particularly for photocatalytic applications (Ciocarlan *et al.*, 2018; Jadhav *et al.*, 2020; O, 2019; Rashmi *et al.*, 2017). However, the pure NZF spinel ferrite alone cannot act as an efficient photocatalyst because they have less tendency to absorb the maximum amount of solar light and recombination of electron-hole pair as compared to their composites (Ciocarlan *et al.*, 2018; Jadhav *et al.*, 2020; O, 2019; Rashmi *et al.*, 2017). Thus, to improve the photocatalytic activity of nickel-zinc ferrite, it needs to couple with other metal-semiconductors (Anwar *et al.*, 2018; Baig *et al.*, 2020; Dhiman *et al.*, 2019; O, 2019; Patil *et al.*, 2017; Peymani *et al.*, 2019; Rashmi *et al.*, 2017; Somvanshi *et al.*, 2020; Tanwar *et al.*, 2019).

Among the conventional modifications, the doping of rear earth (RE) ions in ferrite can provide additional excited states under the conduction band of ferrite and reduce the recombination rate of photo-induced holes and photo-generated electrons in the material system (Baig *et al.*, 2020). According to reports from various studies, this new exited state made in the system after doping rare-earth ions gives rise to radical changes in the photocatalytic performance of spinel ferrites. Peymani *et al*. (2019) reported the synthesis of RE ions (Gd^{3+}, Pr^{3+}, or Sm^{3+}) doped cobalt zinc ferrite for photocatalytic degradation of methylene orange (MO) and shows the effect of RE ions. The report of Baig *et al.* (2020) shows that lanthanum ion-substituted manganese ferrites ($La_xMnFe_{2-x}O_4$) have performed an excellent photocatalytic activity than the pure manganese ferrite. The study reported by Rashmi et al. (2017) concluded that RE ion (Eu(III) and Tb(III)) doped samples have a faster and better catalytic efficiency than the pure $NiFe_2O_4$ and $Zn_{0.5}Ni_{0.5}Fe_2O_4$ spinel ferrite samples. Nd^{3+} ion substituted $NiFe_2O_4$ and Sm^{3+} ion substituted $ZnFe_2O_4$ was also employed as an efficient photocatalyst for photocatalytic degradation of organic pollutants (Harish *et al*., 2013 ; Keerthana *et al*., 2021). As compared to other RE, lanthanum, and europium have a distinct position among rare earths due to their large size, simple spectra (electronic), paramagnetic behavior, reactive (Baig *et al*., 2020)

Although the doping of rare earth elements has a positive effect on the photocatalytic degradation efficiency of spinel ferrites, they still have complaints about incomplete degradations of organic pollutants, which may attributed to a high recombination rate of charge carriers (Peymani *et al.*, 2019; Rashmi *et al*., 2017). Considering all the mentioned facts, researchers are still looking for a better RE ions-modified spinel ferrite photocatalyst. Due to its ultrafast electron transport, higher specific surface area, higher rate of adsorption, high mechanical strength, and chemical and thermal stability, graphene (2D nanomaterial) has been employed as a support for nanoparticles (Rahman *et al*., 2020). Its π-conjugated electronic structure and zero-band gap energy make it an ultimate electron acceptor and very quickly transfers the accepted electrons, which resist the recombination of photo-generated charge carriers (Shahid *et al*., 2020). These unique properties of graphene may resolve the fast electron-hole recombination problems of RE ions-modified spinel ferrite, which improves their photocatalytic efficiency. Moreover, the 2D structure of graphene with more trapping sites holds the semiconductors very firmly and prevents them from leaching from the composite (Mishra et al., 2020). Reduced graphene oxides (rGO) are a welcomed derivative with structural similarity with graphene. Today, several studies have reported the reduced graphene oxide-based modification of spinel ferrites for photocatalytic applications (Ain *et al.*, 2016; Javed *et al*., 2019 ; Shahid *et al*., 2020). The conclusion of all these reports shows that the introduction of rGO has remarkably improved the photocatalytic efficiency of spinel ferrites in the degradation of organic dyes. Even though effluents of industrial wastes may contain two or more two harmful organic pollutants, most of the studies reported the fabrication of modified catalysts for the degradation of only one organic dye at a time. Thus, no detailed studies have been reported about the simultaneous decolorization of multiple organic pollutants. As a result, besides improving the degradation efficiency of photocatalysts, the synthesis of photocatalysts capable of harvesting visible light and degrading various types of organic dyes in their mixture needs to emerge as an active research area to remediate the environment.

Besides the photocatalytic application, spinel ferrites are suitable electrode modifiers and attract much attention from researchers due to their chemical stability, electronic conductivity, and expansive electrochemical windows (Ghoreishi *et al*., 2012; Masoumeh *et al*., 2020) . As one of the very common spinel ferrites, NZF ferrite is also one of the promising materials used for the fabrication of sensitive and selective electrochemical sensors due to its high electrical conductivity, low band gap and stability, tenability, and low toxicity (Ciocarlan *et al*., 2018; Jadhav *et al*., 2020;

O, 2019; Rashmi *et al*., 2017). As per the reports of various studies, the changes in grain size, conductivity, and surface area are linearly improving the sensor's sensitivity, selectivity, and speed of analysis. Considering such alteration, the substitutions of rare earth ions in spinel ferrites and their composite with rGO has quite promising potentiality for the improvement in sensitivity, selectivity, and conductivity of the designed sensor for efficient and selective identification of toxic food dyes (Taei, 2020; Hanafi *et al*., 2019; Moarefdoust *et al.*, 2021). The results of these studies affirmed that the doping of RE ions possesses the remarkable potential for simultaneous detection of food colorants in cloured food products. Even though RE ions are suitable modifiers for the fabrication of sensitive electrodes, the reported studies to apply these rare earth ion modifications of electrochemical sensors for detecting food colorants at a lower detection limit with higher efficiency are not enough yet. The regulation of the concentration of colorants used in food products is critical to designing specific, selective, and sensitive analytical devices to track the level of synthetic dyes in typical colored food products. Thus, studies about the fabrication of more sensitive, selective, healthy, easy-to-scale-up electrochemical sensors using RE ions still need to be employed as an active research area for the selective quantification of food colorants at the low detection limit.

In this study, $Ni_{0.75}Zn_{0.25}RE_xFe_{2-x}O_4$ nanoparticles and $Ni_{0.75}Zn_{0.25}RE_xFe_{2-}xO_4$@rGO nanocomposite (RE = La & Eu; x=0.00, 0.02, 0.06 and 0.1) were effectively synthesized by using sol-gel auto combustion and ultra-sonication routes respectively. These synthesized samples were efficiently applied for photocatalytic degradations of mixed organic pollutants (MB and MO) under Visible light irradiations and fabrication of an electrochemical sensor ($Ni_{0.75}Zn_{0.25}RE_xFe_{2-x}O_4$@rGO/CPE) for simultaneous determination of sunset yellow (SY) and tartrazine (TZ) in their mixture.

1.2 Statement of the problem

Even though NZF spinel ferrites have attracted significant attention in the design of various applications, particularly for photocatalytic applications, the pure NZF spinel ferrite has low photocatalytic efficiency due to incomplete degradations of organic pollutants, attributed to a fast recombination rate of the photo-generated electron-hole pairs (Ciocarlan *et al.*, 2018). Thus, the NZF spinel ferrite needs to be modified as an active research area to decolorize organic pollutants efficiently. On the other hand, industrial waste effluents may contain two or more harmful organic

pollutants. However, most studies reported on the fabrication of modified catalysts for the degradation of only one organic dye at a time. Thus, no detailed studies have been reported yet about the simultaneous degradation of multiple organic pollutants using modified catalysts. As a result, besides improving the degradation efficiency of the photocatalysts, the synthesis of visible-light-driven photocatalysts capable of simultaneously degrading various types of organic dyes in their mixture needs to emerge as an active research area to remediate the environment.

Besides environmental issues, NZF spinel ferrites are also applicable to detecting coloring agents (dyes) in colored food products. However, the reported studies show that the electrochemical sensor efficiency of NZF spinel ferrites is not enough yet. Hence, considering the risks posed by food colorants, designing reliable, sensitive, selective, and robust analytical tools to determine ADI and monitor the level of synthetic dyes at a trace level becomes an essential health protection issue. Thus, studies about the improvements in its sensitivity, selective, and limited detection with higher efficiency still need to be employed as an active research area for the selective quantification of food colorants at low detection limits.

1.3 Objectives of the Study

1.3.1 General objective

The general objective of this study is to investigate the effect of RE ions (RE = La^{3+}, Eu^{3+}, and La^{3+}-Eu^{3+}) and rGO on the properties (band gap, conductivity, crystal size, crystal structure, and morphology) and applications (photocatalytic and electrochemical sensor) of synthesized NZF spinel ferrites.

1.3.2 Specific objectives

- To synthesize reduced graphene oxide.
- To synthesize RE ion (La^{3+} and Eu^{3+}) doped NZF spinel ferrite nanomaterial and their reduced graphene oxide composite.
- To synthesize La^{3+}- Eu^{3+}co- doped NZF spinel ferrite nanomaterial and its reduced graphene oxide composite.
- To characterize the synthesized rare earth ions doped NZF ferrite nanomaterials and their composite of reduced graphene oxide using advanced techniques: UV-DRS, PL, TGA/DTA, FTIR, XRD, SEM/EDX, TEM/HRTEM/SAED, XPS and BET.

- To investigate the photocatalytic activities of the synthesized spinel ferrite-based nanomaterials for MB & MO dyes.
- To study the electrochemical sensor applications of synthesized spinel ferrite-based nanomaterials to detect synthetic food colorants (SY & TZ).

1.4 Significance of the study

Environmental pollutants must be converted to an acceptable level to develop a healthier and greener environment. The current investigation provided scalable, environmentally friendly capability to harvest sustainable solar energy and recyclable photocatalysts for efficient decolorization of organic pollutants under irradiation of visible lights. This applied to society's benefit for environmental remediation, to provide the possibility of water refining, solve health problems caused by polluted water, and provide a safe environment for aquatic animals.

Furthermore, current research provides an electrochemical sensor for selectively and quantitatively identifying food colorants with a lower detection limit. This sensor can also inform the stakeholders of food safety laboratories and hint about the safe use of colored food products.

1.5 Scope of the study

This study is focused on the synthesis and detail characterizations of La^{3+} and Eu^{3+} doped nickel - zinc spinel ferrite nanomaterials and their nanocomposites with rGO ($Ni_{0.75}Zn_{0.25}RE_xFe_{2-x}O_4$@rGO (x=0.00, 0.02, 0.06 & 0.1)) by using sol-gel auto combustion and ultra-sonication routs respectively. The scope of the study is limited to the application for photocatalytic degradation of organic pollutants (MB & MO) under irradiation of visible light and electrochemically identification of synthetic food colorants (SY & TZ) using $Ni_{0.75}Zn_{0.25}RE_xFe_{2-x}O_4$@rGO NCs modified CPE electrode.

CHAPTER TWO

2 LITERATURE REVIEW

2.1 Nanomaterials

Nanomaterials with structural features at the nanoscale can be found in clusters, thin films, multilayer, and nanocrystalline materials, often expressed by the dimensionality of 0, 1, 2, and 3 (Figure 2.2). These materials include metals, amorphous and crystalline alloys, semiconductors, oxides, nitride and carbide ceramics, etc. (Pattanayak *et al*. 2018).

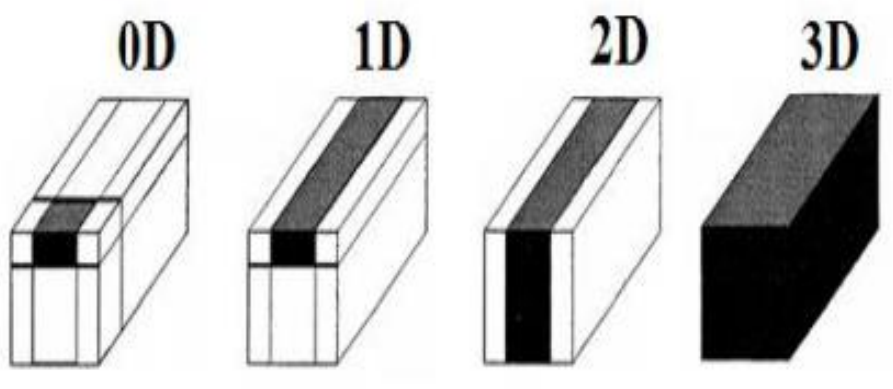

Figure 2. 1: Classification of nanomaterials according to the dimension

The behavior of materials at the nanoscale, as compared to the macroscale, is often found to be highly desirable properties created due to size confinement, the dominance of interfacial phenomena, and quantum effects (Pattanayak *et al.,* 2018). These new and unique properties of nanostructured materials lead to improved properties such as catalysts, tunable photo activity, increased strength, better conductivity towards heat and electricity, different magnetic properties, light reflection, and also change colors according to their size, and many other interesting characteristics (Sevilla, 2013). It plays a significant role in the development of innovative methods to produce new products, substitute existing production equipment, and reformulate new materials and chemicals with improved performance, resulting in less consumption of energy and materials and reduced harm to the environment as well as environmental remediation (Burda *et al*., 2005). Nanomaterials also have larger surface areas than similar volumes of larger-scale materials, which signifies that more surfaces are available for interactions with other materials around them (El-Sayed *et al.,* 2005).

2.2 Nanomaterials Synthesis and Processing

To synthesize nanomaterials allows us to think in both the 'bottom-up' and the 'top-down' approach, i.e., to assemble atoms or to disassemble (break or dissociate) bulk solids into finer pieces until they are constituted of only a few atoms. This domain is a pure example of interdisciplinary work encompassing physics, chemistry, and engineering up to medicine (Alagarasi *et al.,* 2017.).

2.3 Ferrites

The term ferrite is commonly used generically to describe a class of magnetic oxide compounds that contain iron oxide as a principal component. Magnetite (Fe_3O_4), also called loadstone, is a genuine ferrite and was the first magnetic material known to the ancient people are well versed by staunch philosopher Sankara (Srivastava *et al*., 2012). The unpaired electrons are responsible for the origin of magnetism. In ferrite lattice, cations are separated by oxygen anions (O^{2-}). The oxygen anions have zero magnetic moment as they have filled shells. The metal cations, e.g., Ni^{2+} (d8), Zn^{2+} (d10), and Fe^{3+} (d5) of ferrites have 2, 0, and 5 unpaired electrons in outermost shells, respectively. Hence, divalent nickel and trivalent iron have a magnetic moment because of partially filled shells. On the other hand, in divalent Zn^{2+} ions, the outermost shell is filled, giving a diamagnetic characteristic.

The history of magnetic minerals is quite old. This became possible due to a natural mineral called 'magnetite.' Magnetite is an iron oxide (Fe_3O_4). From the Greek word "Magnesia," the word 'Magnet' is derived. The direction-finding application named magnetite 'Lodestone,' meaning 'Waystone.' Much later, "De Magnete" was the first technical study of magnetism by William Gilbert (1540 - 1603). He recognized that the Earth is a giant magnet and the compass functions on this rationale.

The ferrites are ionic compounds with certain double oxides of iron and other metals. Several ferrites are naturally occurring minerals in rocks with impure states. Ferrites are dark grey or black, hard and brittle ceramic materials. These materials are synthesized by heat-treating the transition metal oxides (Vedrtnam *et al.,* 2020). Several laboratories have begun research to grow such materials worldwide, for example, Kato, Takei, and Kawai in Japan in the 1930s (Singh *et al*., 2010) and Snoek in the Netherlands from 1935 to 45 (Philosophy, 2018). Snoek has established

the fundamentals of practical ferrite materials. Neel's Theory of ferrimagnetism put forward the theoretical understanding of ferrites in 1948. Snoek has prepared the first functional modern ferrite. Snoek and Neel worked together and significantly impacted the research of ferrimagnetism. This has created the potential to develop new materials for several applications.

Ferrites are technologically necessary materials and have been an object of study for quite a long time (Singh *et al*., 2010). The discovery of ferrites at the beginning of the twentieth century and the later theoretical understanding of ferrites was put forward by Neel Theory of ferrimagnetism in 1948, an upsurge of research and developments. However, the Snoek has prepared the first functional modern ferrite (Philosophy, 2018). This has caused significant attention in the scientific community to develop new ferrite-based materials for several applications (Ali *et al*., 2018.). These applications are in radar, audio–video, digital recording, bubble devices, memory cores of computers, satellite communication, and microwave devices (Bharamagoudar *et al.*, 2019).

Ferrites are a unique class of compounds comprising lanthanides and active transition metals, in particular, iron, chromium, and manganese (El-sayed *et al*., 2005). Ferrites are hard and brittle, comparable to nearly all other ceramics. The general formula is $M'M''_2O_4$, where M′ is a transition metal ion (divalent metal ions such as Fe^{2+}, Mg^{2+}, Ni^{2+}, Co^{2+}, Zn^{2+}, Cu^{2+}) and M″ is trivalent metal ions that is, Fe^{3+}, Cr^{3+}, Al^{3+}, Mn^{3+}. A crystal lattice comprising of cubic close-packed (fcc) oxides (O^{2-}) with M′ cations involving $(1/8)^{th}$ of the tetrahedral locales and M″ cations possessing (1/2) of the octahedral sites represents spinel structure for ferrites. Further, if $(1/8)^{th}$ of the tetrahedral sites are filled by M″ cation, so afterward $(1/4)^{th}$ of the octahedral sites are filled by M′ cation and the other $(1/4)^{th}$ by M″ cation, and this type of structure is termed as inverse spinel structure. There are also the possibilities for mixed spinel structures in ferrites having the formula $[M^{2+}_{1-\delta}Fe^{3+}_{\delta}][M^{2+}_{\delta}Fe^{3+}_{2-\delta}]O_4$ is mixed ferrite, where δ is the degree of inversion (Srivastava *et al*., 2012). Ferrites are classified based on magnetic properties, structural arrangement, and compositional state.

2.3.1 Classification of ferrites

2.3.1.1 According to magnetic properties

The magnetic properties of ferrites depend on the ions they contain and their coercive strength. Hence, based on their coercive strength, ferrites are classified as soft ferrites (i.e., the low

coercivity of magnetism or coercive field strength < 10 Oe) and hard or permanent ferrites (i.e., the high coercivity of magnetism or coercive field strength > 125 Oe) (Anwar *et al*., 2018).

Soft ferrites have a low coercivity value and can be easily demagnetized. Because of this, magnetization can be effortlessly authorized in the opposite direction without disseminating much energy as hysteresis losses. Because of their low losses at high frequencies, soft ferrites are generally utilized in the centers of little transformers and inductors.

Soft ferrites are ferrimagnetic materials that do not hold their magnetism after being magnetized. These materials can be produced by heating and slow cooling and can easily be magnetized and demagnetized (Vedrtnam *et al.*, 2020). Soft ferrites are ceramic insulators with cubic crystal structure MFe_2O_4, where M is transition metal ions, such as Ni, Mn, Zn, etc. They also have high values of susceptibility and permeability (for example, nickel-zinc ferrite has 1.26×10^{-5}–2.89×10^{-3} H/m), low eddy current losses, and low resistivity and coercivity (Anwar *et al*., 2018). Manganese-zinc ferrites and nickel-zinc ferrites are some usual soft ferrites. The estimations of saturation magnetization and permeability of Mn-Zn ferrite are higher than those of Ni-Zn ferrite. Ni-Zn ferrites are more suited for frequencies over 1 MHz because the resistivity of Ni-Zn ferrites is higher than the Mn-Zn ferrite. Soft ferrites are used in electromagnets, computer data storage, cores of transformers, telephone signal transmitters, receiver transformers, telephone signal transmitters, and receivers, etc. (Vedrtnam *et al*., 2020).

Hard ferrites are also known as permanent magnetic materials because they can hold their magnetism after being magnetized. They can be produced by heating and sudden cooling and cannot be easily magnetized and demagnetized (Anwar *et al.*, 2018). Hard ferrites are compounds of iron and barium or strontium oxides. They have high saturation flux density, low susceptibility and permeability, high eddy current losses, and high receptivity and coercivity (Vedrtnam *et al*., 2020).

Hard ferrites are hard to demagnetize, and after the magnetization process, hard ferrites have a high estimate of coercivity and remanence. Hard ferrites are utilized to make lasting ferrite magnets. Hard ferrites are likewise used to make permanent magnets for gadgets, such as magnets for refrigerators, electric motors, loudspeakers, DC magnets, and loudspeakers. Permanent magnets have an essential characteristic of high coercivity. This means the materials have a high

resistance to becoming demagnetized. The permeability of a permanent magnet is very high. They are additionally named ceramic magnets. These are inexpensive and generally utilized in different household items. The common hard ferrites are strontium ferrite, barium ferrite, and iron-cobalt ferrite.

2.3.1.2 According to crystal structure

Based on their crystal structures, ferrites are classified as cubic, spinel ferrite, garnet ferrite, hexagonal ferrite, and ortho-ferrites (Bharamagoudar *et al*., 2019).

2.3.1.2.1 Cubic Ferrites

The general formula of cubic ferrites is $MO.Fe_2O_3$, where M is a divalent metal ion like Mn, Ni, Fe, Co, Zn, Mg, Cd, Cu, etc. All other cubic ferrites except cobalt ferrite ($CoO.Fe_2O_3$) are magnetically soft. Usually, ferrites have spinel structures, often called ferro-spinel, because their crystal structure is closely related to mineral spinel $MgO.Al_2O_3$ (Anwar *et al*., 2018). In the case of these ferrites, the divalent ions replace Mg, and trivalent ions replace Al. In all cases, the ionic radii of the substitution ion should be between about 0.5 to 1Å

2.3.1.2.2 Garnet ferrites

Garnet ferrite is a class of ferrites with "hard magnetic" characteristics and general chemical composition $R_3(Fe_5O_{12})$, where R is the rare-earth trivalent cation. Yttrium (Y) garnet is a typical example of garnet ferrite (Narang *et al*., 2021). Their fundamental crystal structure is derived from the garnet mineral, $Mn_3Al_2Si_3O_{12}$, in which Y and AlY can substitute Si and Mn, and Al can substitute Si and Mn to form $Y_3Al_5O_{12}$. For magnetic garnets, Al is further substituted by Fe (Shinde, 2016). A unit cell of garnet, therefore, consists of eight formula units, where the oxygen sub-lattice has a polyhedral combination with three types of interstitial sites: dodecahedral (eight-fold), octahedral (six-fold), and tetrahedral (four-fold) sites (Pubby *et al*., 2021). The entire polyhedral is distorted, where the cation distributions can be represented as follows:

$$\{R_3\}[Fe_2](Fe_3)O_{12}$$

where { }, [ ], and ( ) represent dodecahedral, octahedral, and tetrahedral sites, respectively (Shinde, 2016).

2.3.1.2.3 Ortho-ferrites

Ortho-ferrites have an ortho-rhombic crystal structure with the chemical formula of $REFeO_3$, where RE is the rare-earth element. Ortho-ferrites are commonly weak ferromagnetic materials. $LaFeO_3$ and $DyFeO_3$ are typical examples of ortho-ferrites (Pubby *et al*. 2021).

2.3.1.2.4 Hexagonal ferrites

Hexagonal ferrites have a chemical formula of $MFe_{12}O_{19}$, where M can be barium, strontium, calcium, or lead. There are two types of crystallographic sites in hexagonal ferrites: tetrahedral and octahedral. Hexa-ferrites have complex crystal structures with an easy axis of magnetization. These ferrites are magnetically hard (Narang *et al*., 2021). Their compositions combine three oxides, MO, Fe_2O_3, and BaO, where M is a divalent metal. In the crystal structure, all the related compounds can be understood as stacking of three basic block units, S, R, and T, where the S unit is formed by two formula units MFe_2O_4, R unit has the stoichiometry $(BaFe_6O_{11})_2$ and the T unit has four layers with formula $Ba_2Fe_8O_{14}$. Unlike spinel and garnet ferrites, hexagonal ferrite has more than one type of crystal structure (Shinde *et al*., 2016).

2.3.1.2.5 Spinel ferrites

The structure of spinel ferrites (SFs) as possessed for $MgAl_2O_4$ was first determined by Bragg and Nishikawa in 1915 (Soufi *et al*., 2021). The term 'spinel' is used for the face-centered cubic structure that has a formula of AB_2O_4, where A stands for the divalent metal ions like Fe, Co, Ni, Mn, Mg, Cu, and Zn, etc., or a combination of these ions and *B* represents trivalent cation (Anwar *et al*., 2020; Bhargava *et al*., 2020; Narang *et al*., 2021). A unit cell of spinel ferrite MFe_2O_4 contains eight formula units with 56 ions. There are 32 (8 formula units*4 ions) oxygen anions, 8 (8 formulas units*1 ion) M^{2+} cations, and 16 (8 formula units*2 ions) Fe^{3+} cations. As demonstrated by the ferrite researchers, a representative structure for spinel ferrite is depicted in Figure 2.3. Large-sized oxygen ions form a closely packed face-centered cubic (FCC) structure with smaller divalent metal cations occupying the interstitial positions with space group $Fd_{3m}O_{7k}$ (Pubby *et al*., 2021). In one unit ferrite cell, 96 interstices (64 tetrahedral and 32 octahedral) exist between the close packing of oxygen atoms (Soufi *et al*., 2021).

Since two different valence cations (+2 and +3) are available, two types of crystallographic nonequivalent sites (tetrahedral-A and octahedral-B) are present in the spinel structure, $(M^{2+}{}_{1-}$

$_xFe^{3+}{}_x)_{tetra}[Me^{2+}{}_x\ Fe^{3+}{}_{2-x}]_{octa}O^{2-}{}_4$. At which M represents any divalent metal cation (Anwar *et al*., 2020; Rewatkar *et al*., 2020; Norouzi *et al*., 2020; Bhargava *et al*., 2020; Kefeni *et al*., 2020). The tetrahedral "A" site is surrounded by four oxygen ions, and the other is the octahedral "B" site, surrounded by six oxygen ions. There are eight A-sites and 16 B-sites in a spinel unit cell. Ions located at the tetrahedral sites are known as 'network formers', while those located at the octahedral sites are known as 'network modifiers' (Narang *et al*, 2021). The distribution of each metal in respective sites depends on their affinity for both positions. This affinity depends on the stabilization energy, the ion rays of the specification, the size of the interstices, the synthesis method, and the conditions employed during the synthesis time (Soufi *et al*., 2021). The allocation of cations among two intrinsic lattice sites of spinel ferrite (SF) is subjected to the balancing of ions (Anwar *et al*., 2020; Kaur *et al.*, 2020). As a whole, the spinel unit cell remains electrically neutral. $Charge\ on\ unit\ cell = Q_{unit\ cell} = Q_{Oxygen\ anion} + Q_{Divalent\ cation} + Q_{Ferric\ ion} = 32 * (-2) + 8 * (+2) + 16 * (+3) = —64 + 16 + 48 = 0$ (Pubby et al., 2021). A diagram of the spinel crystal structure is illustrated as follows.

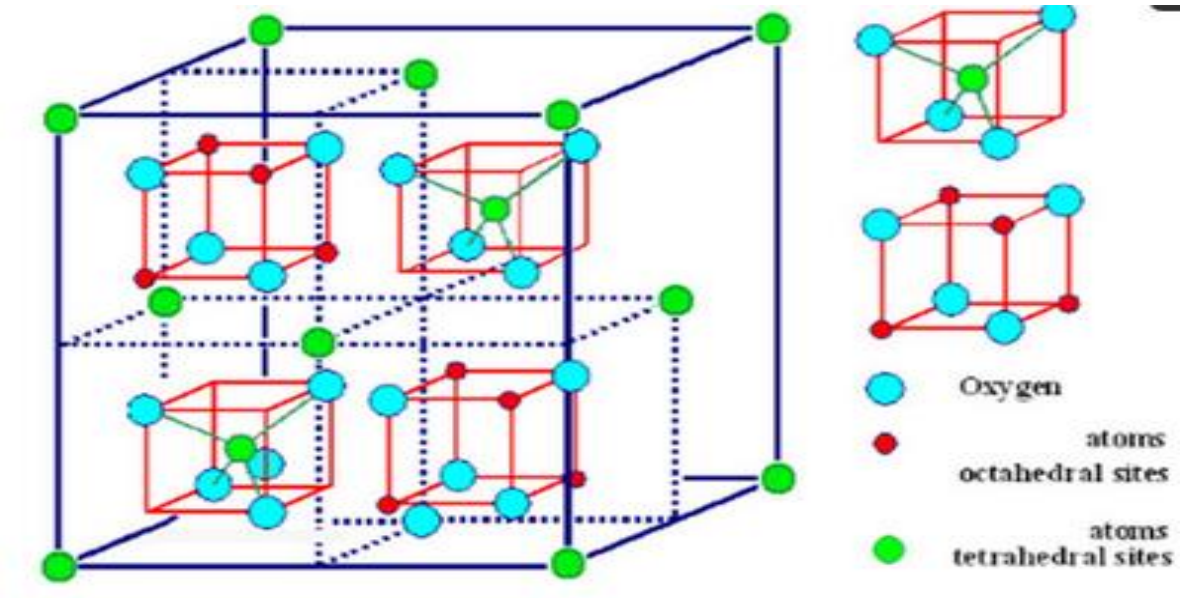

Figure 2.2: The crystal structure diagram for unit cell spinel ferrites (Kaur *et al.*, 2016).

Note: The spinel structure's oxygen anions are outside the fcc array's ideal positions. This is because of the presence of tetrahedral cations, where ionic sizes are always larger than the space of an ideal tetrahedral site, forcing oxygen anions to shift in that direction (Pubby *et al.*, 2021).

2.3.1.2.5.1 Classification of spinel ferrites

The distribution of cations at tetrahedral and octahedral sites has a significant implication on both the physical and chemical properties of ferrite nanoparticles (Shinde, 2016). Hence, based on the degree of inversion, x, which can be defined as the fraction of cations, M^{2+}, occupying octahedral and tetrahedral sites, $[M^{2+}_{1-x}Fe^{3+}_{x}]_{(A)}[M^{2+}_{x}Fe^{3+}_{2-x}]_{(B)}O_4$, spinel ferrites can be classified as normal spinel, inverse spinel, and mixed spinel ferrite (Pubby *et al*, 2021).

i) Normal spinel ferrites, x=0, i.e., all divalent cations, M^{2+}, are located in tetrahedral (A) sites, while all trivalent cations Fe^{3+} are located in octahedral (B) sites (Anwar et al., 2020; Kaur *et al.*, 2020). The structural formula of such spinel ferrite is $[M^{2+}]_{(A)}[Fe^{3+}_{2}]_{(B)}O_4^{-2}$, examples: $ZnFe_2O_4$, $CdFe_2O_4$ (Narang *et al.*, 2021).

ii) Inverse spinel ferrites, x=1, i.e., the divalent cations M^{2+} are located in octahedral (B) sites, while trivalent cations Fe^{3+} are equally distributed in both tetrahedral (A) and octahedral (B) sites. The structural formula of this SF's is $[Fe^{3+}]_{(A)}[M^{2+}Fe^{3+}]_{(B)}O_4^{-2}$, examples: Fe_3O_4, $CoFe_2O_4$ and $NiFe_2O_4$, $CuFe_2O_4$, $MgFe_2O_4$ (Anwar *et al*., 2020; Kaur *et al*., 2020).

iii) Mixed spinel ferrite,$0<x<1$, i.e., the divalent cations M^{2+} and trivalent cations Fe^{3+} ions are distributed at both the tetrahedral (A) site and the octahedral (B) site. The structural formula for this spinal ferrite is $[M^{2+}Fe^{3+}_{x}]_{(A)}[M^{2+}Fe^{3+}_{2-x}]_{(B)}O_4^{-2}$ Example: $MnFe_2O_4$. It can also be obtained by mixing normal and inverse spinel ferrite. For example, the mixing of zinc spinel ferrite and nickel spinel ferrite, $NiZnFe_2O_4$ (Narang *et al*., 2021) and magnesium-zinc ferrites.

Several factors influence the distribution of an individual cation occupying a particular site, including elastic energy, electrostatic energy, crystal field stabilization energy, the electronic configuration of cations, the saturation magnetization of the lattice, and the processing parameters as well as the particle size of cations (Pubby *et al*., 2021; Soufi *et al*., 2021). electrostatic energy of the spinel lattice. Even though many possible combinations for ferrites occur, manganese-zinc, manganese-magnesium, and nickel-zinc ferrites are the three main commercial ferrite families. Mn- Mg ferrites are employed for microwave applications. Ni-Zn ferrites are employable at high frequencies as well as low frequencies. Ni-Zn ferrites are the best multipurpose ferrites and have been extensively studied due to their several applications. Several researchers have studied several ferrites, considering their broad applications.

2.3.1.2.5.2 Properties of spinel ferrite

The SFs are unique materials exhibiting ferrimagnetic and semiconductor properties. They can be considered magnetic semiconductors, which are used for a wide range of applications (Rewatkar *et al*., 2020). The specific properties of spinel ferrite, including structural, optical, high electrical resistance, high chemical/thermal stability, magnetic, high permeability, and mechanical properties, have attracted considerable interest among researchers (Rimus *et al*., 2023; Soufi *et al*., 2021). They also possess special physicochemical properties, including moderate saturation magnetization, high coercivity, high electrical resistivity, low eddy current losses, high Curie temperature, large magneto crystalline anisotropy, good thermal stability, and modest chemical composition. In addition, they have excellent, tunable size and shape, high specific surface area, surface active sites, high chemical stability, and also the ease with which they can be modified or functionalized (Ali *et al*., 2017; Sanida *et al*., 2019). These properties mainly depend on the nature of the divalent cation in the spinel structure (besides Fe^{3+}) and their distribution at tetrahedral and octahedral sites, the synthesis method, grain size, morphology, and annealing temperature (Ali *et al*., 2017).

2.3.1.2.5.3 Application of spinel ferrite

In the present technological world, spinel ferrites (SF) have vast applications ranging from biomedical to environmental and industrial applications (Anwar *et al*., 2020). Amongst the wide diversity of applications, the most frequent applications of spinel ferrites are presented in Figure 2.4 (Kefeni *et al*., 2020). The major applications of SFNPs, in the former case, are based on transducers, microwave absorption, computer technology, hyperthermia, magneto-optical devices, magnetic recording, spintronic, information storage devices, electronic chips and magnetic resonance imaging (Anwar *et al*., 2020), cancer diagnosis, cancer gene therapy, and magnetically guided drug delivery. Due to their low cost, good catalytic activity, interesting band gap, selectivity, low toxicity, the capability to recover and reuse in further cycles without remarkable loss of activity [28], recently they have been used in wide variety of investigations including water treatment, catalyst and pollutant removal via adsorption or photodegradation (Lakshmi *et al*. 208. ; Petrisor *et al*., 2015), sensor (Afkhami *et al*., 2016; Masoumeh *et al*., 2020), high-frequency device (Belaiche *et al*., 2022), water splitting, and membrane modification, antibacterial activity (Patil *et al*., 2019; Rehman *et al.*, 2019).

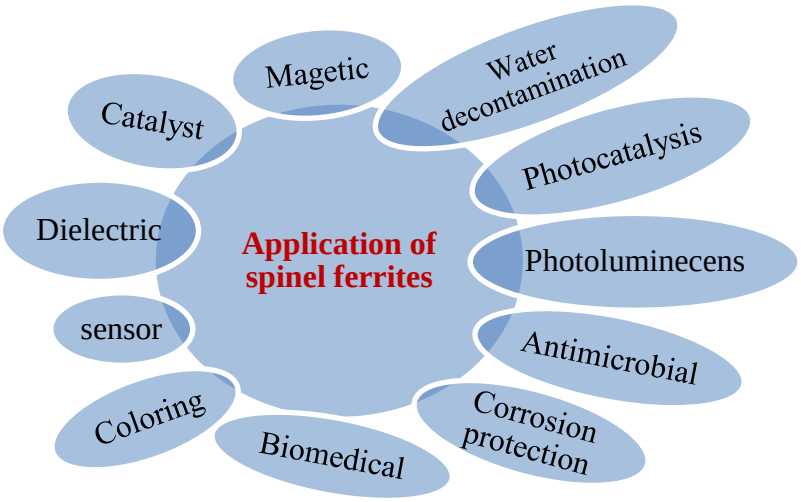

Figure 2. 3: Applications of Nano sized spinel ferrite.

As per Scopus database, depicted in Figure 2.5, it can be seen that the increasing numbers of published research papers pertaining to these ferrites with respect to the year which confirmed the interest in the spinel ferrites has grows significantly.

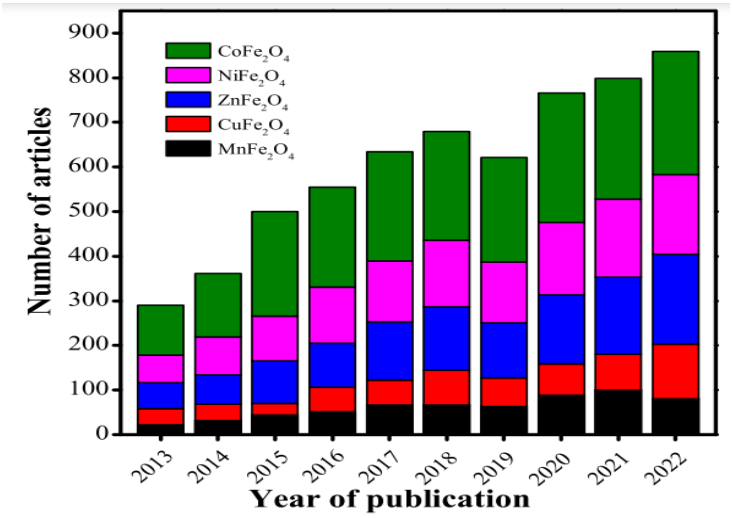

Figure 2. 4: Research trend in spinel ferrite that publishes in the Scopus database from 2013 to 2022 (Rimus *et al.*, 2023).

2.3.2 Nickel-Zinc spinel ferrite

This class of soft ferrites has been studied due to its high resistivity compared to other soft ferrites like Mg-Zn. Nickel-zinc spinel ferrites are among the most widely used soft magnetic materials.

It is a type of spinel ferrite and is composed of Ni ferrite and Zn ferrite (Chuan *et al*., 2017). Zinc ferrite is called a normal spinel structure of the form $ZnFe_2O_4$, while nickel ferrite is called an inverse spinel structure of the form $FeNiFeO_4$ due to a high degree affinity Ni^{2+} for the octahedral site. The sample having both cations is termed a "mixed/intermediate" spinel ferrite (Singh et al., 2010b). In which the unit cell for NZF ferrite is represented by $(Zn_xFe_{1-x})_{tetra}$ $[Ni_{1-x}Fe_{1+x}]_{octa}O_4$ (Dasan, Guan *et al*., 2017). This shows that in the spinel structure of NZF spinel ferrite, the tetrahedral sites are occupied by Zn^{2+} and Fe^{3+} ions, while the octahedral sites are occupied by Ni^{2+} and Fe^{3+} ions (Kesavamoorthi *et al*., 2017). This distribution of cations among the available tetrahedral A sites and octahedral B sites of NZF spinel ferrite are controlled by their physicochemical properties (Anwar *et al.*, 2018; Baig *et al.*, 2020; Dhiman *et al*., 2019; O, 2019; Patil *et al*., 2017; Peymani-Motlagh *et al*., 2019; Rashmi, Naik, *et al*., 2017; Singh *et al.*, 2010; Tanwar *et al*., 2019).

Nanosized NZF spinel ferrites are a class of magnetic nanoparticles (MNPs) with superior magnetic and electrical properties (Demir *et al*., 2020). Since the first publication of nickel zinc ferrite by Wilson *et al.* in 1954 using neutron diffraction (Pubby *et al*., 2021), several researchers have received a significant boost for the synthesis and characterization of this spinel ferrite with different morphology, particle size, and compositions by using various types of novel synthesis methods for a wide range of applications (Singh *et al*., 2010b, Ali *et al*., 2017; Dasan *et al*., 2017).

Among these applications, electronic devices (Belaiche et al., 2019), transformers, antennae, video magnetic heads, and magnetic heads of multiple-path communication are the most promising candidates. Furthermore, it also has potential applications in magnetic liquid absorbing materials (Lahiri et al., 2019), telecommunication (Belaiche *et al*., 2018.), magnetic recording media, drug delivery (Dasan *et al*., 2017), etc. Furthermore, the report of literature findings in recent times shows that NZF ferrites have been widely used in practicable activities, including electrochemical sensors, antibiotics, catalysts (Adamet al., 2020), removal of heavy metals (Afkhami *et al*., 2015), removal of organic pollutant via adsorption or photodegradation as a new nanosized material (Anwar *et al.*, 2018; Jadhav *et al*., 2020). Due to its tunability, the properties of NZF spinel ferrites are easily modified and applied for further miniaturizing applications.

Leng *et al*. (2013) studied Ni-Zn ferrite's structural and magnetic characteristics prepared using the reverse micelle technique at room temperature. XRD characterization confirmed the pure

spinel crystal structure of the prepared sample. Magnetism has been reported to decrease with the addition of diamagnetic zinc in Ni-Zn ferrite.

Verma *et al*. (2000) have analyzed the structural and magnetic properties of Ni-Zn ferrites prepared by the citrate precursor method. XRD characterization confirmed the pure spinel structure of prepared samples. Samples sintered at 1200°C have shown better characteristics like Curie temperature, coercivity, and saturation magnetization.

Desai *et al.* (2021) have examined the consequences of cobalt doping on the structural and magnetic characteristics of Ni-Zn ferrites processed by the citrate-nitrate combustion route. The pure spinel structure of all prepared samples was observed using XRD characterization. The grains have been reported to be agglomerated from SEM characterization. The magnetic behavior studied using VSM characterization shows increased saturation magnetization, coercivity, and retentivity on cobalt doping. The real and imaginary parts of initial permeability decrease, whereas the loss factor increases with the enhancement of cobalt doping in Ni–Zn ferrites. Sun et al. described the consequences of sintering temperature on Ni-Zn ferrites prepared by solid-state reaction technique. A pure spinel structure for all prepared samples was observed using XRD characterization. Using SEM characterization, an increase in the growth of grains was observed with the rise in sintering temperature.

2.3.2.1 Modification of Ni-Zn spinel ferrite

The tunable properties of spinel NZF ferrites lead to altered or modified physicochemical properties, applications, shape, and structure using different ways like mode of preparations (synthesis), stoichiometric proportions, the types, amounts, positions, and valence states of guest metal ions incorporated into the crystallographic structures of spinel NZF lattice (Anwar *et al*., 2018; Elayakumar *et al*., 2019; Somvanshi *et al*., 2020). Furthermore, incorporating guest ions, either magnetic/nonmagnetic or divalent/ trivalent, in a spinel lattice results in drastic changes in structural and other properties using cationic redistribution (Somvanshi *et al*., 2020). Hence, in ferrite manufacturing, composition and synthesis conditions are critical to achieving the required quality (Srivastava *et al*., 2012). In this light, besides synthesis methods, the appropriate selection of guest ions or dopants is a prerequisite to achieving the desired alteration or improvement in the pristine spinel ferrite.

As the conformation of numerous researchers reported in recent time (Anwar et al., 2018; Dhiman et al., 2019; Tsvetkov *et al*., 2019; Shahid et al., 2020; Somvanshi et al., 2020), from the conventional type of dopants, substituting Fe^{+3} ions with rare earth metal ions (REE) with nominal concentration leads to improved, different physicochemical parameters of NZF ferrite, which can attain radical changes in their applications. Such type of variation with substitution of REE is related to their large ionic radii in comparison to Fe^{3+}, Zn^{2+}, and Ni^{2+} (Dhiman *et al*., 2019 ; Somvanshi *et al*., 2020). Thus, due to the increasing trends in ferrite technology, the modifications of the properties of ferrites are interesting. All these assured a bright future for ferrite technology (Structural *et al*., 2018).

2.3.3 Rare Earth ferrite

Ferrites have been studied since 1936. A newer family of ferrite materials has been discovered, which are rare-earth types. The addition of a small amount of rare earth ions to ferrite samples produces a change in their magnetic and electrical as well as structural properties depending upon the types and the amount of rare earth elements used (Of *et al*., 2018). Hence, the influence of rare earth-substituted ferrites is becoming a promising material for different properties.

Rare-earth elements (from now on referred to as REE) are a group of seventeen chemical elements that range in atomic number from 57 (lanthanum) to 71 (lutetium) with an ionic radius of La^{3+} (1.06 Å) to Lu^{3+} (0.85 Å) on the periodic table of elements (Anandan *et al*., 2012; Elements, 1966). They are officially called "lanthanoids" (Anandan *et al*., 2012). Moreover, they are never found as free metals in the Earth's crust. Hence, pure minerals of individual rare earths do not exist. Therefore, they are found as oxides, which have proved challenging to separate. The early Greeks defined earths as materials that could not be changed further by heat sources, and these oxides seemed to fit that definition. Hence, the rare part of their name refers to the difficulty in obtaining the pure elements, not their relative abundances in the Earth's crust (Jha *et al.*, 2018).

However, most REEs are less rare than the group's name suggests. They have average crustal abundances that are similar to commonly used industrial metals such as chromium, nickel, zinc, molybdenum, tin, tungsten, and lead (Of *et al.*, 2018). Cerium is the most abundant REE and is more common in the Earth's crust than copper or lead. All REEs, except promethium, are more abundant on average in the Earth's crust than silver, gold, or platinum. However, concentrated and economically minable deposits of REEs are unusual (Elements *et al.*, 1966)The rare earth ions can

be divided into two categories: one with a radius close to Fe ions and the other with an ionic radius larger than Fe ions. (Of *et al.*, 2018).The difference in their ionic radii leads to micro strains, which may cause domain wall motion, resulting in deformation of the spinel structure. REEs ions commonly reside at the octahedral sites by replacing Fe^{3+} ions and have limited solubility in the spinel lattices due to their large ionic radii (Elements *et al.*, 1966).

Moreover, the 4f shell of rare earth ions is insulated by $5s^2$ $5p^6$ and is nearly wholly unaffected through the prospective domain of neighboring molecules (Ahmad *et al.,* 2023). The unpaired 4f electrons of rare earth ions lead to forming strong spin-orbit coupling of the angular momentum. Hence, by substituting rare earth ions into spinel-type ferrites, the occurrence of 4f-3d couplings, which determine the magneto-crystalline anisotropy in spinel ferrites, can also improve the various properties and applications of spinal ferrites (Of *et al.*, 2018).

Due to this, researchers have made an admirable interest in the influence of RE incorporation on spinel ferrite's structure, application, and properties (Somvanshi *et al*., 2020). Vasambekar et al. reported that the substitutions of rare earth are found to decrease the grain size, increase DC electrical resistivity, reduce dielectric loss, and increase the saturation magnetization in NZF and Mg-Cd ferrites (Vasambekar *et al.*, 2013). Samoila et al. reported that substituting rare earth ions (RE = La, Sm, Gd, and Dy) with a minimal amount remarkably increased nickel's catalytic performance (Petrisor *et al.*, 2017). Peymani-Motlagh et al. exhibited that the substitutions of Rare earth metal ions (Gd^{3+}, Pr^{3+}, or Sm3+) into cobalt zinc ferrite lead to outstanding photocatalytic effects in the degradation of MO under ultraviolet (UV) light (Peymani-Motlagh *et al.*, 2019). The report of previous work verified that the behavior of different rare earth ions varied in different spinel ferrites and yielded different structural properties (Dasan *et al.*, 2017; Petrisor *et al.*, 2017; Peymani-Motlagh *et al.*, 2019; Somvanshi *et al.*, 2020).

2.3.3.1 Applications of REE

Rare-earth metals have many outstanding properties, unique qualities, and pervasive applications. Development has been rapid since the 1950s, with the realization of industrialized production, and various nations have given their serious attention. The applications of rare-earth metals have a bright future in aviation (Division, 1984).

In the 21st century, REEs have gained visibility through many media outlets because Rare-earth elements (REEs) are used in the components of many devices used daily in our modern society, such as the screens of smartphones, computers, and flat-panel televisions; the motors of computer drives; batteries of hybrid computer monitors, and electric cars; digital cameras, computer hard disks, fluorescent and light-emitting-diode (LED) lights, and new generation light bulbs. Lanthanum-based catalysts are employed in petroleum refining. Large wind turbines use generators that contain strong permanent magnets composed of neodymium-iron-boron (Anandan et al., 2012 ; Elements, 1966). Large quantities of REEs are used in clean energy and defense technologies. Because of these many important uses of REEs, nations dependent on new technologies, such as Japan, the United States, and members of the European Union, reacted with great concern to China's intent to reduce its REE exports. Consequently, exploration activities intent on discovering economic deposits of REEs and bringing them into production have increased (Elements, 1966).

Moreover, specific REEs are used individually or in combination to make phosphor substances that emit luminescence for many types of ray tubes and flat panel displays in screens that range in size from smartphone displays to stadium scoreboards. Yttrium, europium, and terbium phosphors are the red-green-blue phosphors used in many light bulbs, panels, and televisions. The glass industry is the largest consumer of REE raw materials, using them for glass polishing and as additives that provide color and unique optical properties. Lanthanum makes up as much as 50 percent of digital camera lenses, including cell phone cameras. Lanthanum-based catalysts are also used to refine petroleum. Cerium-based catalysts are used in automotive catalytic converters. Rare-earth magnets are also used in computer hard disks and CD–ROM and DVD drives. The spindle of a disk drive attains high stability in its spinning motion when driven by a rare-earth magnet. These magnets are also used in various conventional automotive subsystems, such as power steering, electric windows, power seats, and audio speakers. Nickel-metal hydride batteries are built with lanthanum-based alloys as anodes. When used in hybrid electric cars, these battery types contain significant amounts of lanthanum, requiring as much as 10 to 15 kilograms per electric vehicle (Elements, 1966).

Figure 2. 5: Image for different technological applications of REE metal ions.

Besides the modern technological applications, the substitution of rare earth elements by other cheaper processes or other substances can play an essential role in future applications

2.3.4 Synthesis of spinel ferrite

The synthesis technique is essential in controlling spinel ferrite nanomaterials composition, size, and surface area (Srivastava *et al*., 2012). There are different types of popular methods used for the synthesis of ferrites, which include sol-gel (Chen *et al*., 2016; Petrisor *et al*., 2017; Tsvetkov *et al*., 2019), hydrothermal (Fu *et al*., 2019b; Rehman *et al*., 2019; Jun *et al*., 2020), co-precipitation (Afkhami *et al*., 2015; Phor *et al.*, 2019; Iftikhar *et al*., 2020; Bhargava *et al.*, 2020; Shahid *et al.*, 2020; Agboola *et al*., 2022), Sol-gel auto-combustion (Dubey *et al*., 2018; Dubey *et al*., 2019; Mullaiet *et al*., 2012; Grigoras *et al.*, 2015; Šoka, *et al*., 2018) and solid-state method (Ahmed *et al.*, 2005; Wu *et al.*, 2015). Other methods, such as the son chemical method (Demir et al., 2020), inert gas condensation, micro-emulsion, electrochemical method, thermal decomposition, electro-spinning method, etc., are also used for synthesizing ferrites.

2.3.4.1 Hydrothermal synthesis method

As the report of various researchers (Jun *et al.*, 2020; Li *et al.*, 2019b; Rehman *et al.*, 2019), the hydrothermal method is simple, low-cost, and one of the most common methods for the preparation of ferrites. This route provides an enhanced reaction rate to produce multi-metal oxide compounds. In hydrothermal synthesis, a solution of metal salts and a base are autoclaved under

pressure. This method synthesized crystalline structures (films, nanoparticles, single crystals, etc.) from aqueous solutions under high vapor pressure. For ferrites, iron nitrate and metal nitrate are generally dissolved in distilled water to prepare metal salts. Then, the suspension of precipitated precursors is put in a sealed autoclave and heated very slowly for different temperatures and times. The temperature inside the autoclave starts decreasing after some time due to the relatively large thermal capacity. Surfactants like oleic acid may be used to avoid agglomeration of nanoparticles during hydrothermal treatment. After this process, each product is thoroughly washed, as shown in Figure 2.6. The particle size depends on the hydrolysis rate and the solubility of oxide metal oxide in this process. The advantages of this non-conventional process are high purity, chemical homogeneity, small and uniform particle size, and controlled particle shape. The drawbacks of this synthesis method are prior knowledge of the solubility of starting materials, the expensive autoclave, hydrothermal slurries that are potentially corrosive, accidental explosion of the high-pressure vessel, etc. (Vedrtnam *et al*., 2020).

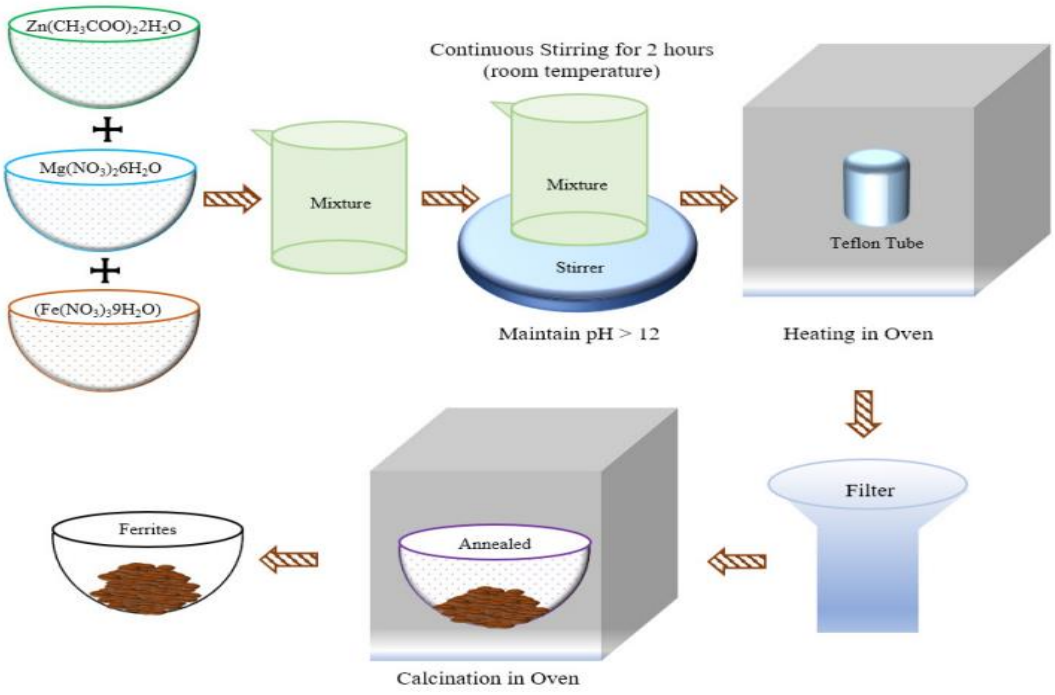

Figure 2. 6: The synthesis of ferrite via hydrothermal method (Vedrtnam *et al*., 2020).

2.3.4.2 Sol-gel auto combustion synthesis method

The sol-gel auto-combustion process is a chemical route for the low-temperature synthesis of single and multiple component materials in ultrafine powders (Vedrtnam *et al.*, 2020). A typical sol-gel process comprises four steps, including the formation of the solution, the formation of a wet gel, the ignition of the gel, and the calcination of the dried powder. The flowchart of ferrite synthesis through the sol-gel auto-combustion process is shown in Figure 2.7. In the sol-gel auto-combustion technique, materials are obtained from a stoichiometric combination of chemical solution with fuels via combustion. There are two types of routes, i.e., the metal-organic route with metal alkoxides in organic solvent and the inorganic route with metal salts in aqueous solution (chloride, oxychloride, and nitrate). The inorganic route is much cheaper and easier to handle than metal alkoxides, but their reactions are more difficult to control. This method allows more accurate control over the phase formation, desired stoichiometry, and uniformity in particle size (Wang *et al*., 2016; Petrisor *et al.*, 2017; Tsvetkov *et al.*, 2019). There is an even elemental distribution within the gel, thereby no chance of a potential source of contamination. There are also some disadvantages to the method, such as raw materials for this process are expensive, products containing high carbon content, several steps are involved; close monitoring of the process is needed, long period for processing, and difficulty related to phase separation (Vedrtnam *et al*., 2020).

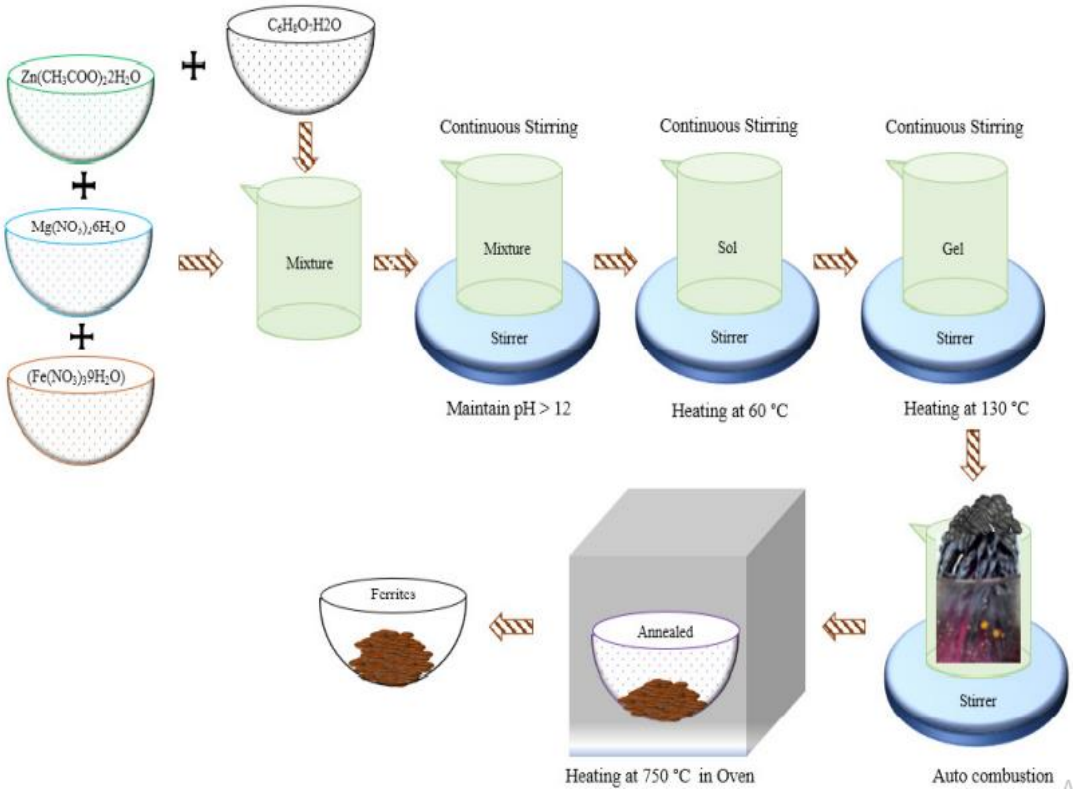

Figure 2. 7: The flowchart for the synthesis of ferrite via sol-gel method (Tsvetkov *et al.*, 2019).

2.3.4.3 Co-precipitation method

The chemical co-precipitation method is the most straightforward and most convenient method to synthesize magnetic particles (Afkhami et al., 2015; Iftikhar *et al.*, 2020; Bhargava *et al*., 2020; Phor *et al*., 2019; Shahid *et al.*, 2020; Agboola *et al.*, 2022). In this method, a uniform composition is obtained by precipitation reaction of two or more cations (Vedrtnam *et al.*, 2020). This method involves four steps, i.e., the simultaneous occurrence of nucleation, growth, coarsening, and agglomeration. In the co-precipitation method, precipitation is conducted by adding a mixture solution containing chloride of cations (Fe, Ni, etc.) dropwise into a $NaOH/Na_2CO_3$ solution. Carbonate or nitrate of cations can be used instead of chloride cations to synthesize NPs. However, in the latter case, cations of carbonate, such as NiCO3, are converted into cations of chloride by hydrochloric acid. The formed precipitates are filtered and washed with water a few times by washing with ethyl alcohol until no NaCl can be detected, and the pH value should be kept at a desired value. The washed powders are dried and then calcined, as shown in Figure 2.8. This method has certain advantages such as being simple, easy control of particle size, homogeneity of

nanomaterial with small size, bulk production of magnetic nanoparticles that are energy efficient, etc. Some of the disadvantages of this method are trace impurity, time consumption, and instability of nanoparticles (Vedrtnam *et al*., 2020).

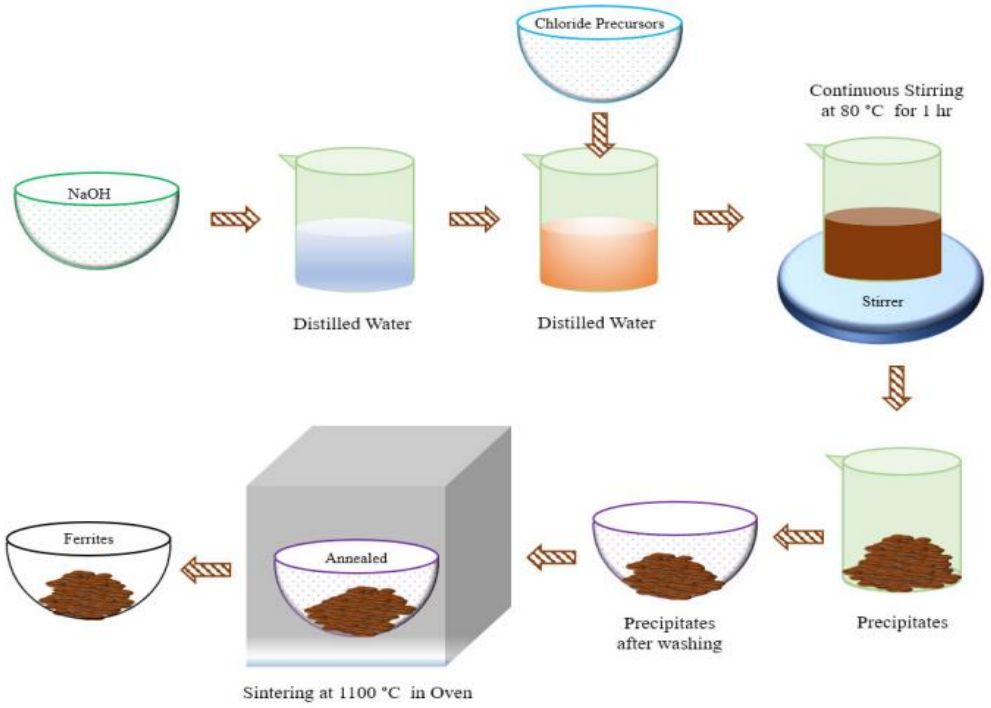

Figure 2.8: The synthesis of ferrite via the chemical coprecipitation method (Petrisor *et al.*, 2017).

2.3.4.4 Ceramic method

The conventional ceramic method synthesizes various materials, including nitrides, aluminosilicates, sulfides, ferrite, and mixed metal oxides. In this synthesis method, several stages are required, such as two or more solid compounds being mixed (homogenization), then grinding them in a wet medium (to regulate the particle size and to make the homogeneous mixture), compaction, and heating the mixture at an elevated temperature as shown in Figure 2.9 (Ahmed *et al.*, 2005; Wu *et al*., 2015; Vedrtnam *et al.*, 2020).

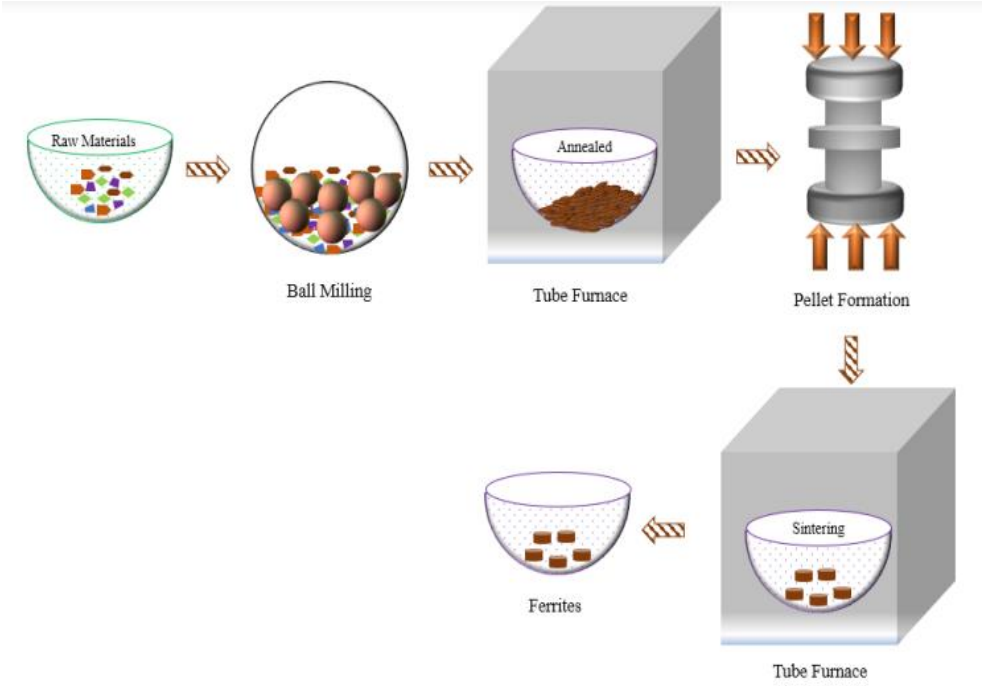

Figure 2.9: The flowchart for the synthesis of ferrite via the ceramic method (Wang *et al*., 2016).

2.3.5 Characterization of ferrites

The significant advances in nanosciences and nanotechnology would not have occurred without the ability to characterize the materials' nanoscale structural, chemical, and physical properties. Hence, this part presents the characterization techniques used in this thesis. These techniques allow the direct relationship with the crystallography, structural morphology, chemistry (identification of chemical constituents, chemical composition, and their distribution), thermal properties, magnetic properties, and electrical properties of the synthesized samples.

2.3.5.1 X-Ray Diffraction (XRD) analysis of ferrite

X-ray diffraction is one of the most fundamental techniques used to characterize the crystal structure of materials. The principle of XRD is that the incident X-rays with a fixed wavelength (λ) on a sample are scattered off at an equal angle, and the constructive interference occurs for a fixed set of interplanar spacing (d) and incidence angle (θ) as shown in Figure 2.10. Bragg‟ 's Law is one of the most important laws used for interpreting X-ray diffraction data and the relationship between the wavelength of incident X-rays, the distance between the layer, and the angle of diffraction, which has given a mathematical equation (Vedrtnam *et al.*, 2020).

$$n\lambda = 2dsin\theta$$ ----------(2.1)

where n = an integer (1, 2, 3, 4, …etc.) representing the diffracted beams' serial order.

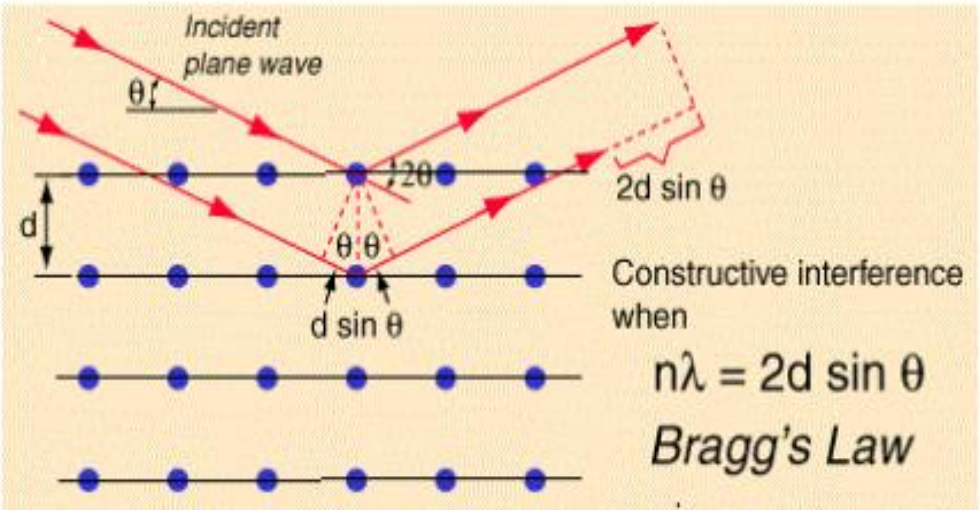

Figure 2.10: Bragg's law of X-ray diffraction (Submitted et al., 2013).

X-ray diffraction (XRD) analysis provided information about the crystal structure, crystallite size and strain, phase identification, long-range order, unit cell volume, porosity, etc. (Vedrtnam et al., 2020). Furthermore, the XRD results identified the effect of substitutions and their percentage of doping on the crystallite size, structure, and properties of ferrites (Stergiou *et al.*, 2014; Peymani-Motlagh *et al.*, 2019; Pawar *et al.*, 2020; Ahmad *et al*., 2023).

2.3.5.2 Fourier Transformed Infrared (FTIR) analysis of ferrite

FTIR spectroscopy is used to identify the possible functional groups of the active components on the surface of ferrite NPs responsible for reducing, capping, and stabilizing synthesized nanoparticles. Most of the time, the possible functional groups are identified in 4000-400 cm^{-1}(Duki *et al*., 2021). The FTIR peaks attributed to stretching and bending vibrations are identified and assigned to determine the type of functional groups, crystal structure, ion distribution, and the formation of the desired structure of the synthesized ferrite nanoparticles. Moreover, the FTIR results identified the effect of substitutions and their percentage of doping on the structure and properties (Baig *et al.*, 2020; Pawar *et al.*, 2020; Wu *et al.*, 2020). The spectrum obtained is compared with a standard reference chart to identify functional groups present in the sample (Wu *et al.*, 2020)

2.3.5.3 The Scanning Electron Microscope (SEM) analysis of ferrite

A scanning electron microscope (SEM) is used to create images of a sample by scanning through a high-energy beam of electrons. The images are obtained as raster scan pattern (Vedrtnam *et al*., 2020). Signals are produced due to the interaction between electrons and atoms. Information regarding the sample's surface topography, composition, shape, size and structure, and other properties like electrical conductivity can be obtained through these signals (Peymani-Motlagh *et al.,* 2019). Furthermore, the effect of the variation in doped concentration on the grain size of ferrites has also been analyzed *(*Almessiere *et al.,* 2019; Peymani-Motlagh *et al.,* 2019; *Baig et al.,* 2020).

2.3.5.4 Transmission Electron Microscopy (TEM)

TEM is a microscopic technique with a complex setup in which a beam of high-energy electrons passes through an ultrathin specimen to be subsequently analyzed. The transmitted portion of the electron beam is focused and magnified using electromagnetic lenses to form either a diffraction pattern or an image using an imaging device such as a fluorescent screen, on a layer of photographic film, or to be detected by a sensor such as a CCD camera (Wu *et al.,* 2020). From the image obtained information regarding the microstructures, particle morphology, chemical analysis, and particle size of the specimen (Almessiere *et al.,* 2019; Peymani-Motlagh *et al.,* 2019; Wu *et al.,* 2020). This enables the instrument's user to examine fine detail even as small as a single column of atoms, which is tens of thousands of times smaller than the smallest resolvable object in a light microscope (Wu *et al.,* 2020).

2.3.5.5 TGA/DTA analysis

The annealing temperature is an essential factor in forming the spinel structure of ferrite. TGA (Thermogravimetric analysis) is essential for estimating the appropriate annealing temperature (Baig *et al*., 2020). Thermal analysis is used to determine the traces of water content in nanoferrites with the help of Differential Thermal Analysis (DTA), Thermogravimetry (TGA), Differential Thermo gravimetry (DTG), and Differential Scanning Calorimetry (DCS). The TGA curve represents the change in weight as a function of temperature, while the DSC curve displays the change in energy as a function of temperature (Baig *et al.,* 2020; Vedrtnam et al., 2020).

2.3.5.6 Brunauer, Emmet, and Teller (BET) analysis

One of the most essential characteristics of a semiconductor photocatalyst is surface area and porosity, which affect the properties and efficiency of the photocatalyst in the degradation of pollutants (Nasirian, 2006). Brunauer, Emmet, and Teller (BET) method is the most preferred model utilized to determine the area of a solid. Surface area and porosity are two of the most essential characteristics of a semiconductor photocatalyst that affect the properties and efficiency of the photocatalyst applications. A photocatalyst with a specific surface area performs better in eradicating contaminants. In the BET method, samples are heated first, and at the same time, gas over samples is depleted to eliminate released contaminants. Then, by employing liquid nitrogen, the samples are cooled. Finally, the volume of gas (usually N_2 or Kr) that is adsorbed on the surface is measured (Nasirian, 2006).

2.4 Chemistry of Graphene and its Derivatives

Few and single-layer transferable graphene nanosheets were first obtained by mechanical exfoliation ("Scotch-tape" method) of bulk graphite and by epitaxial chemical vapor deposition (Liu *et al*., 2020). Carbon-based materials are used in different fields, from composites to electronic devices. In recent years, the most preferred carbonic materials are graphene and carbon nanotubes (CNTs). These carbon allotropes show favorable results, which can be seen as an excellent alternative to other materials with their outstanding features, such as easy functioning of the surfaces to provide various properties, high mechanical strength, and unusual electronic properties, especially their possible technological applications Duki, 2021).

2.4.1 Graphene

In recent years, graphene is a single layer of atoms in a two-dimensional hexagonal lattice with sp^2 hybridization. A one-atom-thick planar sheet of sp2-bonded carbon atoms densely packed in a honeycomb crystal lattice has grabbed appreciable attention to be used as a next-generation electronic material. This is due to its exceptional properties, including high current density, ballistic transport, chemical inertness, high thermal conductivity, optical transmittance, and super hydrophobicity at the nanometer scale, organized in a honeycomb lattice (Kosowska *et al*., 2019). This also enables the facile fabrication of many carbon-based materials (Hashim et al., 2016) including graphite, carbon nanotubes, diamond, and fullerenes (Figure 2.11) (Katsnelson *et al*., 2007). As compared to other carbon materials, graphene contains higher thermal conductivities

(4.84x103 to 5.30x10^3 W/mK), higher breaking strength approximately 200 times higher than steel, and high-speed of electron mobility (200000 $cm^2 V^{-1} s^{-1}$) at room temperature, high stiffness and strength with Young's modulus of around 1000 Gpa and break strength of 130 Gpa (Lü *et al.*, 2013). Furthermore, graphene is the thinnest material in the universe and has flexible properties; however, it is more complex than diamond and conducts electricity at room temperature better than copper (Lü *et al*., 2013).

The outstanding mechanical, electrical, and thermal properties of graphene have attracted significant attention in materials science applications, including storage energy, gas sensors, and bioelectronic sensor (Yenier *et al*., 2016). Functionalizing graphene with molecules that have water solubility and affinity toward target analytes improves the selectivity of adsorbents or detection devices and prevents aggregation. It has been used as an ideal support for nanoparticles due to its large specific surface area (2630 $m^2 \cdot g^{-1}$) and high electron mobility (2×10^5 $cm^2 V^{-1} \cdot s^{-1}$) (Liang *et al*., 2018). Graphene can also be modified based on covalent bonds' formation and non-covalent interactions. It has potential in nano-applications in many scientific and industrial fields, including the study of nano-electronics, molecular separation, composite additives, catalysis, nano-sensors, and transport (Duki, 2021).

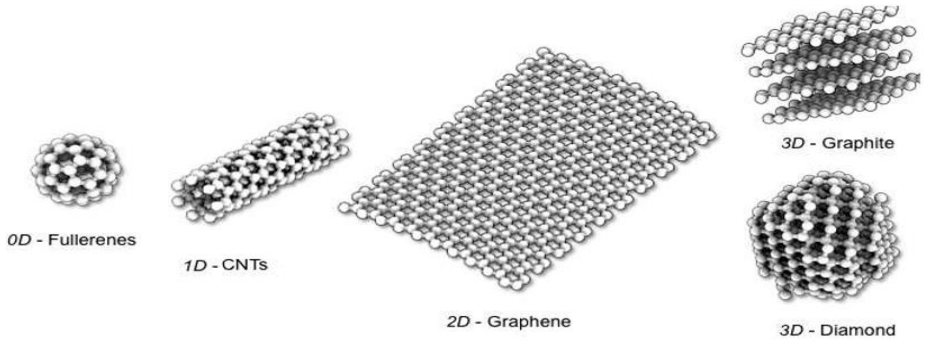

Figure 2. 11: Crystal structures of the different allotropes of carbon (Katsnelson *et al.*, 2007).

2.4.2 Graphene Oxide

Graphene oxide (GO) is a two-dimensional layered material derived from graphene by introducing covalent C-O bonding. The bulk form of GO, conventionally named graphite oxide, has attracted recurring interest since Brodie first synthesized it in 1855 (Nguyen *et al*., 2010). GO has been successfully tested in numerous applications in electronics, conductive films, electrode materials, and composites (Dimiev *et al*., 2014).

The structure of graphene oxide is similar to that of graphene; it carries several oxygenated functional groups attached to its basal planes and edges. These include hydroxyl (OH), epoxy (COC), and carboxyl (COOH) groups (Figure 2.12). They enable GO not only to have characteristics of graphene but also provide other physical and chemical properties, including attachment of various functional groups to its surface (Kosowska *et al*., 2019), easy to assemble into deferent morphologies and easily dispersed into a variety of solvents, such as water (Yan et al., 2011) and allowed to have a high affinity for positively charged molecules/ ions (Cortinez *et al.*, 2020). At the same time, due to the introduction of oxygen-containing functional groups, the large π conjugate structure of graphene is destroyed, so the ability to conduct electrons is lost, and the conductivity is reduced (Spyrou *et al.*, 2014).

2.4.3 Reduced Graphene Oxide (rGO)

Reduced graphene oxide (rGO) is a derivative of graphene obtained through chemical, electrochemical, and thermal reduction of graphene oxide containing oxygen functional groups. As compared to GO, reduced graphene oxide has few reduced sites and high conductivity (Ain *et al.*, 2016). On the other hand, rGO demonstrates properties of both pristine graphene (high surface area, conductivity, and strength) and GO (moderate dispensability in water). Therefore, graphene characteristics are partially restored through rGO generations, as shown in Figure 2.12.

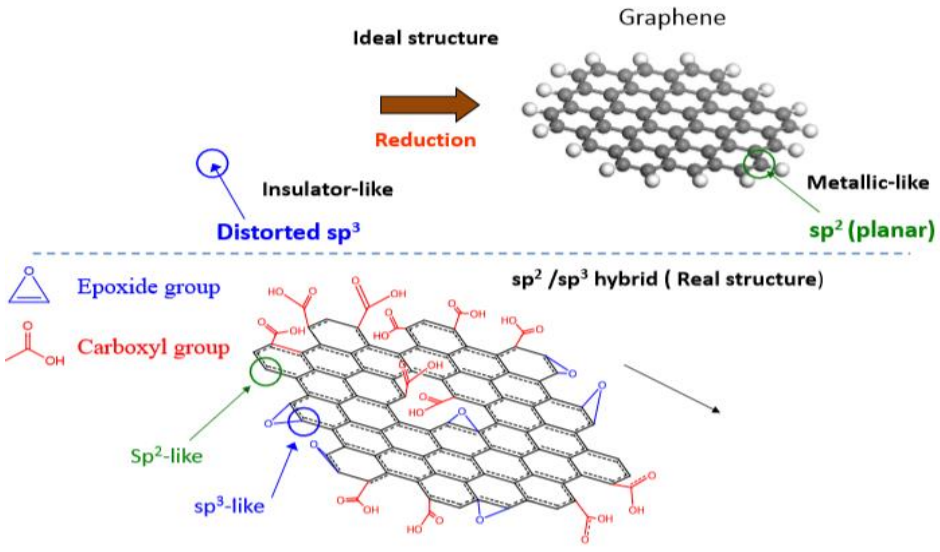

Figure 2. 12: Atomic and electronic structure of GO and Graphene (Mohammed *et al.*, 2020).

Since the surface of both GO and rGO are susceptible to modifications with different molecules, including biological ones, they allow composites with strictly controlled and desired properties to be synthesized. Due to their large active surface areas, GO and rGO can serve as a platform for biological molecules (both organic and inorganic) to be safely introduced into the organism without the risk of uncontrolled and undesirable spreading into the surrounding tissues (Jagiełło *et al.*, 2020). Furthermore, owing to the expanded structural diversity and modification of overall properties, the composites of reduced graphene oxide with RE ions substituted spinel ferrites hold great promise for versatile modern applications, including energy storage/conversion and environmental protection, hydrogen storage materials, photocatalyst (Iftikhar *et al.*, 2020), removal of air pollutants, and water purification (Anwar *et al.*, 2018), as well as electrode materials for various lithium batteries, sensor (Benvidi *et al.*, 2017) and supercapacitors and also drug carriers (Cortinez *et al.*, 2020).

2.5 Electrochemical sensors

Electrochemical sensors are a broad subject, spanning many aspects of physical and analytical chemistry, materials science, biochemistry, solid-state physics, device fabrication, electrical engineering, and statistical analysis (Power *et al*., 2013). The study of electrochemistry began in the 18^{th} century, bloomed until the early 20^{th} century, and then faded owing to excessive use of thermodynamic principles in analyzing the processes at points in the system where the various parts form interfaces.

Since about 1950, the interest in electrochemical sensors continues unabated today, stimulated by the wide range of potential applications. Their impact is most clearly illustrated in the widespread use of electrochemical sensors seen in daily life, where they continue to meet the expanding need for rapid, simple, and economical methods of determination of numerous analytes. Through the refinement of existing sensing technologies along with the development of innovative functional sensor materials, including nano- and biological materials, improved data analysis, and sensor fabrication and miniaturization, opportunities for the construction of new generation sensors with much-improved performances are emerging (Power *et al.*, 2013).

With this new emphasis, electrochemistry is becoming a core science. It promises to be an essential part of the foundation of the ecology-oriented society of the future because electricity is not a pollutant. Significant technological advances during the 1980s and early 1990s are certain to

facilitate the environmental applications of electrochemical devices (Wang *et al*., 2016). An overview of analytical chemistry development demonstrates that electrochemical sensors represent the most rapidly growing class of chemical sensors.

A chemical sensor can be defined as a device that provides continuous information about its environment. Practically, a chemical sensor provides a specific type of response (like oxidation or reduction) directly related to the quantity of a specific chemical species (Stradiotto *et al*., 2003). All chemical sensors consist of two separate parts, namely, (i) a chemically selective layer, which isolates the response of the analyte from its immediate environment to detect the parameter of interest, and (ii) a transducer, which transforms the response into a detectable signal on modern instrumentation. This signal can have different forms: it could be binary (yes/no) or a numeric value (for example, temperature, light, wind, humidity, precipitation, position, composition), and it provides us with the desired information (Patella *et al.*, 2018).

The interest in electrochemical sensors continues unabated, stimulated by the wide range of potential applications. Several journals specialize in electrochemical sensors, large professional societies have electrochemical sensor divisions, and several international conferences on electrochemical sensors take place regularly, testifying to their importance in chemistry and correlated areas. During the past 20 years, electrochemical sensors have become an accepted part of analytical chemistry. After all, they satisfy the expanding need for rapid, simple, and economical methods of determination of many analytes simultaneously (Stradiotto *et al*., 2003). However, despite their broad applications of electrochemical sensors for pollution control and environmental monitoring, they are still in their infancy (Joseph *et al*. 2019).

2.5.1 Modification of electrochemical sensors

An essential requirement for the electrochemical sensor is its change in electrical conductivity with exposure of chemical species to semiconducting materials, which depends on their band gaps, surface morphology, size, the diffusion rate of species, and specific surface area (Srivastava *et al.*, 2012; Vasambekar *et al.*, 2013). Hence, the design of a newly modified material can improve the sensor's sensitivity, selectivity, and stability and, or find a balance between these three criteria to detect a specific type of analyte. The detection speed is also a concern, especially when dealing with harmful pollutants. (Hanafi *et al*., 2019). Thus, the fabrication of highly selective chemical or biological recognition layers of molecular devices or sensor arrays and developments in the

areas of microfabrication, computerized instrumentation, and flow detectors satisfy many of the requirements of electrochemical analysis (Joseph *et al*. 2019).

Carbon paste electrode, i.e. a mixture of carbon (graphite) powder and a binder (pasting liquid), is one of the most popular electrode materials that has obtained increasing attention among the mercury-free solid electrodes and used for the laboratory preparation of various electrodes, sensors, and detectors over the past five decades that has the advantages of easy preparation, low cost, porous surface, wide potential range (from -1.40 to 1.30 V), low residual current and convenient surface renewal (Afkhami *et al.*, 2016). From this, special attention in recent decades has been given to electrochemically modified electrodes (Lipskikh *et al*., 2018). The modification of an electrode involves a deliberate immobilization of a modifier agent onto the electrode surface through chemical reactions, chemisorption, composite formation, or polymer coating that change the electrochemical characteristics of the bare surface (Patella *et al*. 2018 ; Joseph, 2018). Such manipulation of the molecular composition of the electrode thus allows one to tailor the response to meet specific sensing needs (Joseph, 2018). Thus, sensors based on chemically modified electrodes (CME) represent an upcoming trend in analytical chemistry (Sunseri *et al.*, 2018).

The properties of such chemically modified carbon paste electrodes (CMCPEs) depend on the properties of the modifier materials used to import selectivity and sensitivity toward the target species (Afkhami *et al.*, 2016). With the advancement of technology over the years, sensors based on nanotechnology modifiers have been expanded (Tavakkoli *et al.*, 2018). Hence, in the last decade, researchers have tried to provide selective, sensitive, and cost-wise chemically modified carbon paste electrodes that can selectively detect a wide range of organic and inorganic contaminants by using different nanoparticles. Amongst ferrites and their composites with rGO have received significant attention in the field of modifying the electrode surface of sensors, which is due to their greater specific surface area, excellent surface reactivity, porosity, and temperature-dependent surface morphology (Srivastava *et al.*, 2012).

Based on this fact, many researchers have recently focused on modifying carbon-based materials with ferrite nanoparticles.

Tavakkoli *et al.* (2018) reported simultaneous voltammetric sensing of acetaminophen, epinephrine, and melatonin using a carbon paste electrode modified with zinc ferrite nanoparticles.

The results show the synthesized nanocomposite as a promising transduction platform for simultaneous sensing of the targets.

Hongru *et al.* (2019) reported that the hydrothermal route synthesis of $ZnFe_2O_4$ for the applications of gas sensors for the detection of ethyl glycol.

Taei *et al*. (2020) worked on simultaneously determining sunset yellow and tartrazine in soft drinks samples using nanocrystallites of spinel ferrite ($ZnCrFeO_4$) modified carbon paste electrode. From this, they affirmed that the modified electrode ($ZnCrFeO_4$/CPE) possessed the remarkable potential to determine sunset yellow and tartrazine in soft drink samples simultaneously.

Afkhami *et al*. (2016) presented the electrochemical determination of molybdenum (VI) in plant foodstuff samples using a $Ni_{0.5}Zn_{0.5}Fe_2O_4$ nanocomposite-modified carbon paste electrode. According to the results of this study, $Ni_{0.5}Zn_{0.5}Fe_2O_4$ modified carbon paste electrodes have high electrical conductivity and high resistance to interferences, which selectively and efficiently determine molybdenum (VI) compared to unmodified carbon paste electrodes.

Afkhami *et al.* (2020) synthesized nickel–zinc nano ferrite by sol-gel route for the efficient simultaneous pre-concentration of arsenite and arsenate ions from aqueous solutions.

Afkhami *et al.* (2015) also constructed a new $Ni_{0.5}Zn_{0.5}Fe_2O_4$ modified carbon paste electrode ($Ni_{0.5}Zn_{0.5}Fe_2O_4$/CPE) for rapid, simple, accurate, highly sensitive, and selective determination of cadmium and mercury in wastewater and foodstuff samples using square wave anodic stripping voltammetry.

Vasambekar *et al.* (2013) reported on the gas (ethanol, LPG, and chlorine) sensing behavior of Nd^{3+} substituted zinc ferrites.

Nevertheless, all these results show that ferrite nanoparticles are applicable for modifying CPE due to their high electrical conductivity, ferromagnetic properties, and low toxicity when doped with rare earth ions and composited with rGO. Their positive working potential and large specific surface area make them an essential material for applying electrochemical sensors to identify toxic food dyes to identify toxic food dyes selectively.

One of the limitations of magnetostrictive materials is the production of eddy currents, which causes energy loss; however, since oxides have high electrical resistivity, this concern is

eliminated. This property and other properties have sparked interest in spinel ferrite magnetostriction materials. Ferrites are also very chemically and thermally stable, allowing for incorporation into higher temperature and pressure applications required for the automotive industry. Currently, most commercially viable materials are composed of rare-earth metals, making their product cost high. Ferrites have the fundamental properties to become the next generation of magnetostrictive materials for industrial applications.

2.6 Photocatalysis and Their Mechanisms

The term photocatalyst combines two words: photo related to photon and catalyst, a substance altering the reaction rate in its presence. Therefore, photocatalysis refers to a reaction when the catalyst is activated by light. The substrate that absorbs light and acts as a catalyst for chemical reactions is known as a photocatalyst (Lacombe *et al*., 2012).

Berzelius coined the catalysis process at the beginning of the nineteenth century; photocatalysis remains a recent discipline (Keller *et al.*, 2012). Photocatalysis differentiates from conventional catalysis by the activation of the chemical reactions through photon absorption rather than by thermal activation (Lacombe *et al*., 2012). In the last four decades, heterogeneous photocatalysis has expanded rapidly and undergone various developments, especially regarding energy and the environment. Besides that, the multidisciplinary nature of the field includes semiconductor physics, surface sciences, photo and physical chemistry, materials science, and chemical engineering, which has increased significantly (Ibhadon *et al*., 2013). This shows that photocatalysis represents a new way to meet the challenges of energy and environmental sustainability and has become a strategic field of science (Harish *et al*., 2013).

Semiconductors can conduct electricity even at room temperature in the presence of light and, hence, work as photocatalysts. As a result, all the photocatalysts are semiconductors. Therefore, researchers use semiconductor materials as photocatalysts for the removal of ambient concentrations of organic and inorganic species from aqueous or gas phase systems in environmental clean-up, drinking water treatment, industrial and health applications (Fitzpatrick *et al*., 2013).

When a photocatalyst is exposed to light of the desired wavelength, the energy of photons (equal to or higher than the band-gap energy (Ebg)) is absorbed by an electron (e−) of the valence band,

which is excited to the conduction band. This process induces electron (e^-) and hole (h^+) pairs in the conduction band (CB) and valence band (VB) of the semiconductor catalyst, respectively. (Shume *et al*., 2020). Such photo-generated e^-/h^+ pairs lead to induce the formation of aggressive species (OH^- ions, hydroxyl radicals ($OH^\bullet$) and superoxide radicals ($O_2^\bullet$), which are strong enough to oxidize and decompose or mineralize harmful organic pollutants (Harish *et al*., 2013).

The band gap energy (Eg) is the energy difference between the valence band (VB) and the conduction band (CB). Hence, based on band gap, the materials are classified into three basic categories (Figure 16):

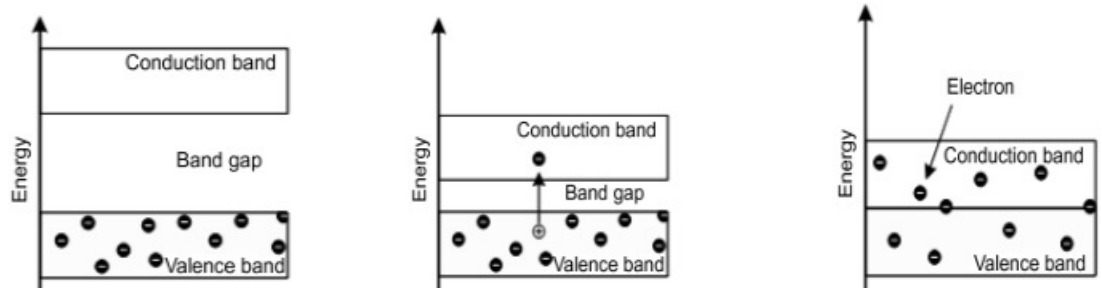

Figure 2. 13: The band gap structure of materials: (a), insulator: E_g >5.0 eV; (b), semiconductor: E_g <1.5–3.0 eV; (c), conductor: E_g <1.0 eV (Harish *et al*., 2013).

The relative positions of the conduction and valence bands of the semiconductor and the redox levels of the substrate decide the fate of the excited electron and hole. Depending upon the relative positions of the valence and conduction bands, the redox level of the semiconductor and the substrate can be classified into four ways, which are illustrated in Figure 2.17.

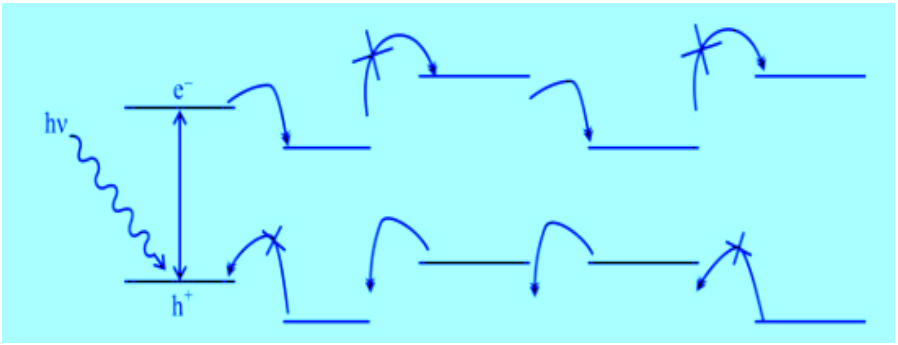

Figure 2. 14: Different possibilities of reactions. (A) Reduction. (B) Oxidation. (C) Redox reaction. (D) No reaction (Harish *et al*., 2013).

A. Substrate reduction occurs when the substrate's redox level is lower than the semiconductor's conduction band.
B. Substrate oxidation occurs when the substrate's redox level exceeds the semiconductor's valence band.
C. Both reduction and oxidation occur when the substrate's redox level is lower than the conduction band and higher than the valence band.
D. Neither oxidation nor reduction is possible when the redox level of the substrate is higher than the conduction band and lower than the semiconductor's valence band.

2.6.1 Modification of photocatalytic materials

However, most semiconductor materials suffer from their intrinsic limitations (band gap > 3.1 eV) that only ultraviolet radiation (UV) can be utilized and the rapid recombinations of the photo-induced e^-/h^+ pairs. It is well known that although the sun can provide an abundant source of photons, UV light accounts for only a tiny fraction (4%) of the solar energy (Rashmi *et al.*, 2017; Ciocarlan *et al.*, 2018; O, 2019; Jadhav *et al.*, 2020). However, visible light accounts for approximately half of solar light (45%), which indicates that low band gap catalysts are more desirable. In this respect, extending photocatalytic activity into the visible region and hindering electron-hole recombination has become a great challenge and one of the most active research topics in photocatalysis (Harish *et al.*, 2013). Besides the catalytical capability of the photocatalytic materials, recycling the suspended ultrafine photocatalysts after degradation is also very important. Hence, introducing magnetic nanoparticles to various photocatalysts allows for magnetic separation and substantially saves costs.

Spinel ferrites are magnetic semiconductor materials with band gap energy of ($h\nu \sim 1.57$ eV to 2.4 eV) (Ciocarlan *et al.*, 2018; Rashmi *et al.*, 2017). In this respect, many researchers have explored strategies to synthesize spinel ferrite photocatalysts (Ciocarlan *et al*., 2018; Jadhav *et al*., 2020; O, 2019; Rashmi *et al.*, 2017). However, in pure spinel ferrite photocatalysts, the generated electron-hole pairs recombine faster; due to this reason, their photocatalytic ability is hampered. To avoid this limitation, researchers have tried to modify spinel ferrite with various types of metal or non-metal dopants (Harish *et al*., 2013). Hence, because of their substantial modification in optical properties with impressive visible-light-driven photocatalysis process, the ferrites doped with inner transition metal have fascinatingly emerged as a more efficient and new form of

photocatalyst in heterogeneous catalysis (Naik *et al.*, 2017). Thus, nowadays, much research is being carried out in the direction of doping rare earth (RE) elements into spinel ferrite to improve their innovative applications (Harish *et al*., 2013; Kaiser, 2017; Naik, *et al.*, 2017; O, 2019; Peymani-Motlagh *et al*., 2019).

Nevertheless, most research findings show that the doping of rare earth elements has an appositive effect on the photocatalytic degradation efficiency of spinel ferrites; rapid recombination of photo-induced electron-hole pairs remains a limitation. Hence, in order to improve this drawback, researchers continued their efforts to modify rare earth elements substituted ferrite using carbon-based materials (Rashmi *et al*., 2017; Ciocarlan *et al.*, 2018; Jadhav *et al.*, 2020; O, 2019). Hence, the use of graphene as a support matrix has increased the photocatalytic activity of the pristine ferrite to a new level owing to several benefiting factors such as limited charge carrier recombination, increased surface adsorption sites, zero bandgap and π conjugated structure for better and faster charge migration (Mishra *et al.*, 2020). As the conformation of many researchers, as compared to REE substituted spinel ferrites, their composite with reduced graphene oxide (rGO) exhibited high photocatalytic activity under irradiation of visible light (Ain *et al*., 2016; Javed *et al.*, 2019; Shahid *et al.*, 2020). This enhanced photocatalytic activity can be attributed to the presence of graphene, which enhances the stability of nanocomposite and reduces the recombination of charge carriers.

CHAPTER THREE

3 MATERIALS AND METHODS

3.1 Chemicals and Reagents

Analytical grade reagents of zinc nitrate hexahydrate ($Zn(NO_3)_2.6H_2O$, 99%, Chemical Reagents), nickel nitrate hexahydrate ($Ni(NiO_3)_2.6H_2O$, 98%, Merck, Germany), iron (III) nitrate monohydrate ($Fe(NiO_3)_3.9H_2O$, 98.5%, Sigma Aldrich), lanthanum (III) nitrate hexahydrate ($La(NiO_3)_3.6H_2O$, 99%, Sigma Aldrich) and europium (III) oxide (Eu_2O_3 98%, AR, Merck, Germany), were used as precursors for the synthesis of rare earth ions (RE) substituted NZF spinel ferrite. This synthesis used citric acid ($C_6H_8O_7.H_2O$, 98.7%, Sigma Aldrich) and ammonia solution (NH_4OH, 25%, AR, Sigma Aldrich) as a fuel and pH adjustment, respectively.

Graphite flakes (99%, mesh size 100 mm), potassium permanganate ($KMnO_4$, 98.5%, AR, Alpha Chemika, India), hydrogen peroxide (H_2O_2, 30%, Fisher Scientific, India), L-Ascorbic acid (98%, Merck, Germany), concentrated sulfuric acid (H_2SO_4, 99.7%, AR, India), ortho-phosphoric acid (H_3PO_4, 85% AR, Merck, Germany), hydrochloric acid (HCl, 37%, Merck, Germany) and barium chloride ($BaCl_2$, 98.9%, Alpha Chemika, India) were used for the synthesis of reduced graphene oxide (rGO).

Potassium hexacyanoferrate (II) trihydrate ($K_4[Fe(CN)_6].3H_2O$, 98%, Sigma Aldrich), and potassium hexacyanoferrate (III) (K_3 $[Fe(CN)_6]$, 99%, Sigma Aldrich) were used as a redox probe for electrochemical characterization of the fabricated modified electrodes. Besides that, the mixture of di-sodium phosphate buffer (Na_2HPO_4, 98.5%, AR, Alpha Chemical, India) and mono-sodium phosphate buffers (NaH_2PO_4, 98.5%, AR, Alpha Chemical, India) was used to prepare phosphate-buffered saline (PBS) which was employed as the supporting electrolyte during electrochemical activities.

Organic dyes methylene blue (MB, $C_{16}H_{18}ClN_3S$, 90%) and methyl orange (MO, $C_{14}H_{14}N_3NaO_3S$, 95%, Shantou, Guangdong, China) were used as representative organic pollutants for photocatalytic activity studies and typical food colorants such as sunset yellow (SY, $C_{16}H_{10}N_2Na_2O_7S_2$, 92.1 %, Shantou, Guangdong, China)), and Tartirazin (TZ, $C_{16}H_9N_4Na_3O_9S_2$,

90.2 %, Shantou, Guangdong, China) were used for electrochemical activity studies. For the experiments, double-distilled water (DDW) was used as a solvent (Dubey *et al*., 2019; Patil *et al*., 2019). The experimental work used all the chemicals without further purification.

3.2 Instruments and Equipment

A thermo gravimetric-differential thermal analyzer (TG-DTA, DTG-60H, Shimadzu, Japan) with a ramp rate of 10 ºC/min in nitrogen (N_2) was used to elucidate the phase transformations during the calcination process. The crystallinity, crystal size, and phase structure of all the synthesized samples were analyzed by a powder X-ray diffractometer (model XRD-7000, Shimadzu, Japan] using Cu Kα radiation (λ = 1.5405 Å) as an X-ray source in the 2θ range from 10 to 80°. The vibrational modes, structural studies, and bond formation between metal and oxygen in the octahedral and tetrahedral sites of the spinel structure were confirmed by using a Fourier Transform Infrared (FTIR) (Perkin Elmer 65, Perkin Elmer, Inc., USA) in the range 4000-400 cm^{-1} with samples prepared using KBr pellets. The synthesized samples' compositional analysis, grain size, and surface morphological characterization were analyzed using a scanning electron microscope with an energy-dispersive X-ray (SEM-EDX) (model S-3400, Hitachi, Japan). The surface morphology, shape, particle size, and agglomeration state were analyzed by a high-resolution transmitted electron microscope (HR-TEM) [(EVO 18, ALTO 1000, Carl Zeiss, Germany]. The degree of crystallinity and purity of the synthesized spinel ferrites and their composite were estimated by the selected area of electron diffraction (SAED). Surface parameters such as surface area, volume, the radius of the pores, and distribution of the pore sizes and N_2 physisorption isotherms at 77.35 Kelvin. X-ray photoelectron spectroscopy (XPS) AXIS ULTRA from AXIS 165, integrated with Kratos patented magnetic immersion lens, was used for synthesized nanomaterials, nanocomposites' elemental analysis, and chemical states. The synthesized materials' optical response and energy band gaps were measured using a double-beam spectrophotometer equipped with diffuse reflectance (DRS-UV) [model JASCO, V-7V-770 Double Beam UV-Visible/NIR Spectrophotometer, JASCO, Japan] in the 200 and 800 nm range. Photoluminescence measurements were carried out using a fluorescence spectrometer (model Agilent Cary Eclipse, Agilent, USA). During photo-catalytic analysis, the decolorization of the organic dyes was measured by a double-beam UV-Vis spectrophotometer (model Sm-1600, 4nm Advanced UV-vis Spectrophotometer, AZZOTA Scientific, USA). A potentiostat (model SP-300

Potentiostat, BioLogic, USA) with a three-electrode conjugation system and electrochemical system software (EC-LAB V11.30) was used for electrochemical characterization of the samples and application tests.

3.3 Materials Synthesis

3.3.1 Preparation of rare-earth (RE = La^{3+} and Eu^{3+}) ions doped NZF ferrites Nanomaterials

The nanomaterials, $Ni_{0.75}Zn_{0.25}RE_xFe_{2-x}O_4$ (La^{3+}, Eu^{3+}, and La^{3+}-Eu^{3+}; x = 0.00, 0.02, 0.06 & 0.10) were synthesized by the sol-gel auto combustion method (Pawar *et al*., 2020). Citric acid was used as organic fuel, providing for the redox reaction between the reactants during combustion. For instance, to synthesize RE ions (La^{3+}, Eu^{3+} and La^{3+}-Eu^{3+}) doped NZF spinel ferrite ($Ni_{0.75}Zn_{0.25}RE_xFe_{2-x}O_4$); nickel nitrate ($Ni(NO_3)_2.6H_2O$), zinc nitrate ($Zn(NO_3)_2.6H_2O$), lanthanum nitrate ($La(NO_3)_3.6H_2O$), Eu^{3+} oxide (Eu_2O_3), ferric nitrate ($Fe(NO_3)_3.9H_2O$) and citric acid ($C_6H_8O_7H_2O$) were used as the starting materials. In this process, the aqueous solution of metal nitrates, iron nitrate, rare earth ions, and citric acid was prepared by dissolving in double distilled water using separate beakers with their stoichiometric proportion (1:2:2: respectively) as depicted in Table 3.1. Then after, the aqueous solutions of metal nitrates were mixed in a 500 mL beaker and stirred continuously for 30 min to form a homogenized solution. The aqueous citric acid (fuel) solution was poured into the homogenized metal nitrate solutions. The mixed solution was heated to 30 °C with continuous stirring using a magnetic stirrer with a hot plate. Ammonia solution (NH_4OH 25%) was added dropwise until the pH of the solution reached pH 7. After that, the temperature was increased to 70 °C and stirred continuously until the solution was converted into a sticky gel. Soon after the formation of the gel, the temperature was stopped by stirring and increased to 110 °C to start the combustion process, and it continued until the formation of loose fluffy powder.

For all the reactions, the final products were obtained through the calcination of the powders at 800 °C for three h in an electrical muffle furnace after being softly crushed into a fine powder using a mortar and pestle (Dubey *et al*., 2019; Hamdi *et al*., 2020; Kesavamoorthi *et al*., 2017; Patil *et al*., 2019). The as-prepared powders were coded and kept in sample holders at room temperature for further characterization and application studies (Table 3.2). The same procedures were adopted to synthesize $Ni_{0.75}Zn_{0.25}Fe_2O_4$, $Ni_{0.75}Zn_{0.25}La_xFe_{2-x}O_4$ (x = 0.02, 0.06 & 0.01), $Ni_{0.75}Zn_{0.25}Eu_xFe_{2-}$

$_xO_4$, (x = 0.02, 0.06 & 0.01), and $Ni_{0.75}Zn_{0.25}(La\text{-}Eu)_{0.06}Fe_{1.94}O_4$ (1:1 of La^{3+} and Eu^{3+} ions) nanomaterials. The details of the experimental setup for these procedures are illustrated in Figure 3.1.

Table 3.1: Stoichiometric mass (mg) of metal nitrates and citric acid taken to prepare various compositions of ferrite nanoparticles based on their oxygen balance.

Composition	Nickel nitrate (0.5 M)	Zinc nitrate (0.5 M)	Ferric nitrate (1 M)	Lanthan-um nitrate (1 M)	Europium oxide (0.5 M)	Citric acid (1 M)
	mg	mg	mg	mg	Mg	mg
$Ni_{0.75}Zn_{0.25}Fe_2O_4$ (undoped)	5.45	1.859	20.2	0.00	0.00	10.507
$Ni_{0.75}Zn_{0.25}RE_{0.02}Fe_{1.98}O_4$	5.45	1.859	19.998	0.193	0.088	10.507
$Ni_{0.75}Zn_{0.25}RE_{0.06}Fe_{1.94}O_4$	5.45	1.859	19.594	0.574	0.264	10.507
$Ni_{0.75}Zn_{0.25}RE_{0.10}Fe_{1.9}O_4$	5.45	1.859	19.190	0.956	0.477	10.507
$Ni_{0.75}Zn_{0.25}(La^{3+}\text{-}Eu^{3+})_{0.06}Fe_{1.9}O_4$	5.45	1.859	0.0485	0.287	0.143	10.507

Table 3.2: Sample code

No.	Nanomaterials	Sample code
1	*Nickel Zinc ferrite:- ($Ni_{0.75}Zn_{0.25}Fe_2O_4$)*	*NZF- x = 0.00*
2	*La^{3+} ion doped Nickel-Zinc ferrite: - ($Ni_{0.75}Zn_{0.25}Fe_{2-x}La_xO_4$)*	*NZL_2F -x = 0.02* *NZL_6F -x = 0.06* *$NZL_{10}F$ -x = 0.1*
3	*Eu^{3+} ion doped Nickel Zinc ferrite: - ($Ni_{0.75}Zn_{0.25}Eu_xFe_{2-x}O_4$)*	*NZE_2F -x = 0.02* *NZE_6F -x = 0.06* *$NZE_{10}F$ -x = 0.1*
4	*La^{3+}-Eu^{3+} (1:1) Co- doped Nickel Zinc ferrite:- ($Ni_{0.75}Zn_{0.25}La_{0.5x}Eu_{0.5x}Fe_{2-x}O_4$)*	*NZL-EF*

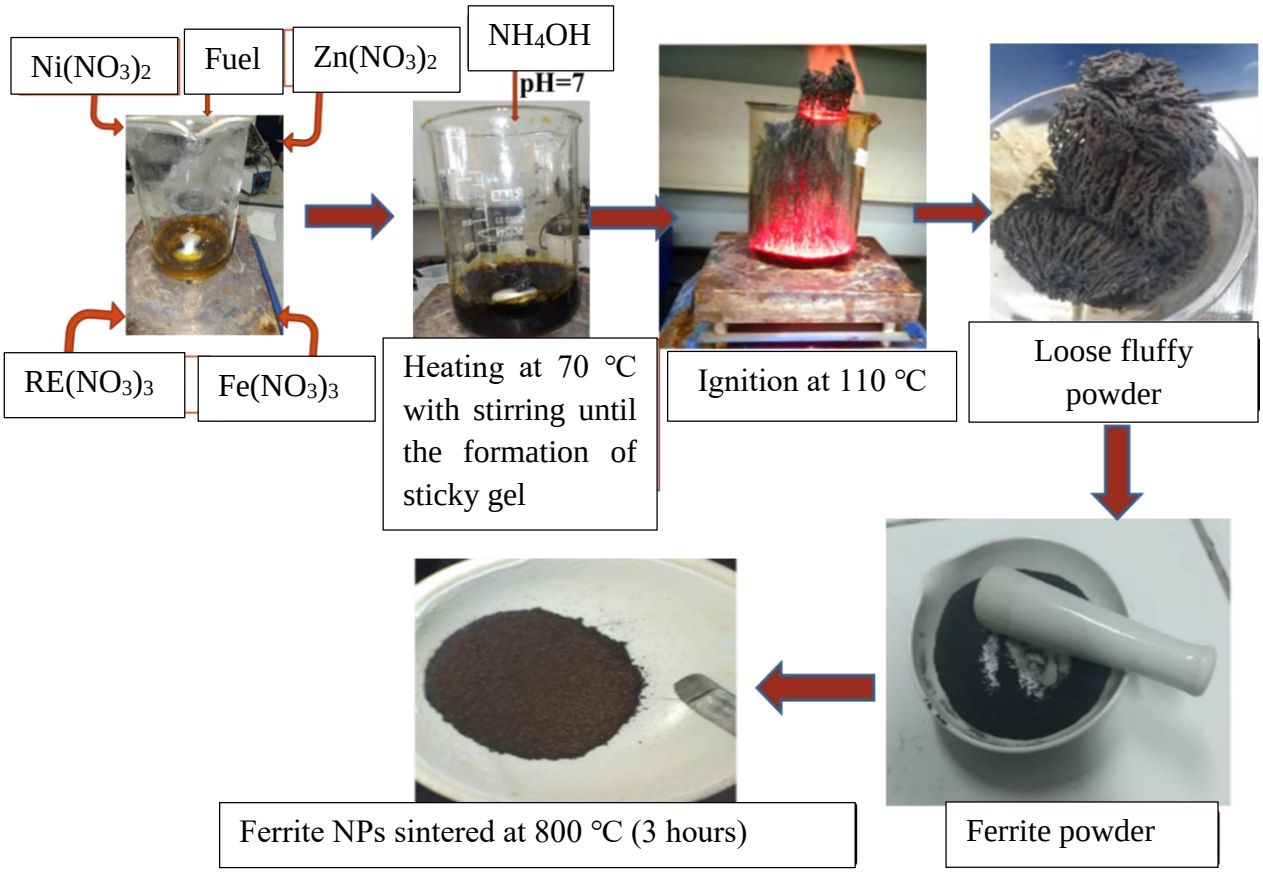

Figure 3.1: Experimental setup for the synthesis of the ferrite nanoparticles.

3.3.2 Fabrication of rGO

As illustrated in Figures 3.2 and 3.3, the fabrication of reduced graphene oxide (rGO) consists of three steps: intercalation (oxidation), exfoliation, and reduction. At first, graphene oxide (GO) was synthesized using Tour's method (Habte *et al*., 2019). Typically, a mixture of 10 mL of ortho-phosphoric acid (H_3PO_4) and 90 mL of concentrated sulfuric acid (H_2SO_4) was prepared and slowly poured into a round bottom conical flask placed in an ice bath which contained a mixture of 0.45 g of graphite powder and 2.7 g of potassium permanganate ($KMnO_4$). After that, the contents were stirred continuously for 30 min at four °C. Due to the formation of highly oxidizing manganese (VII) oxide, Mn_2O_7, the solution became deep green. After that, the solution was heated while constantly agitated using a magnetic stirrer with a hot plate for 12 hours in a water bath with a regulated temperature of 50 °C. After 12 hours, the hot and slightly brown color solution was taken off the water bath and cooled to room temperature. Then, H_2O_2 (30 % w/w) was added

dropwise until a yellowish-colored solution was formed, followed by 400 mL of double-distilled ice water to stop the reaction.

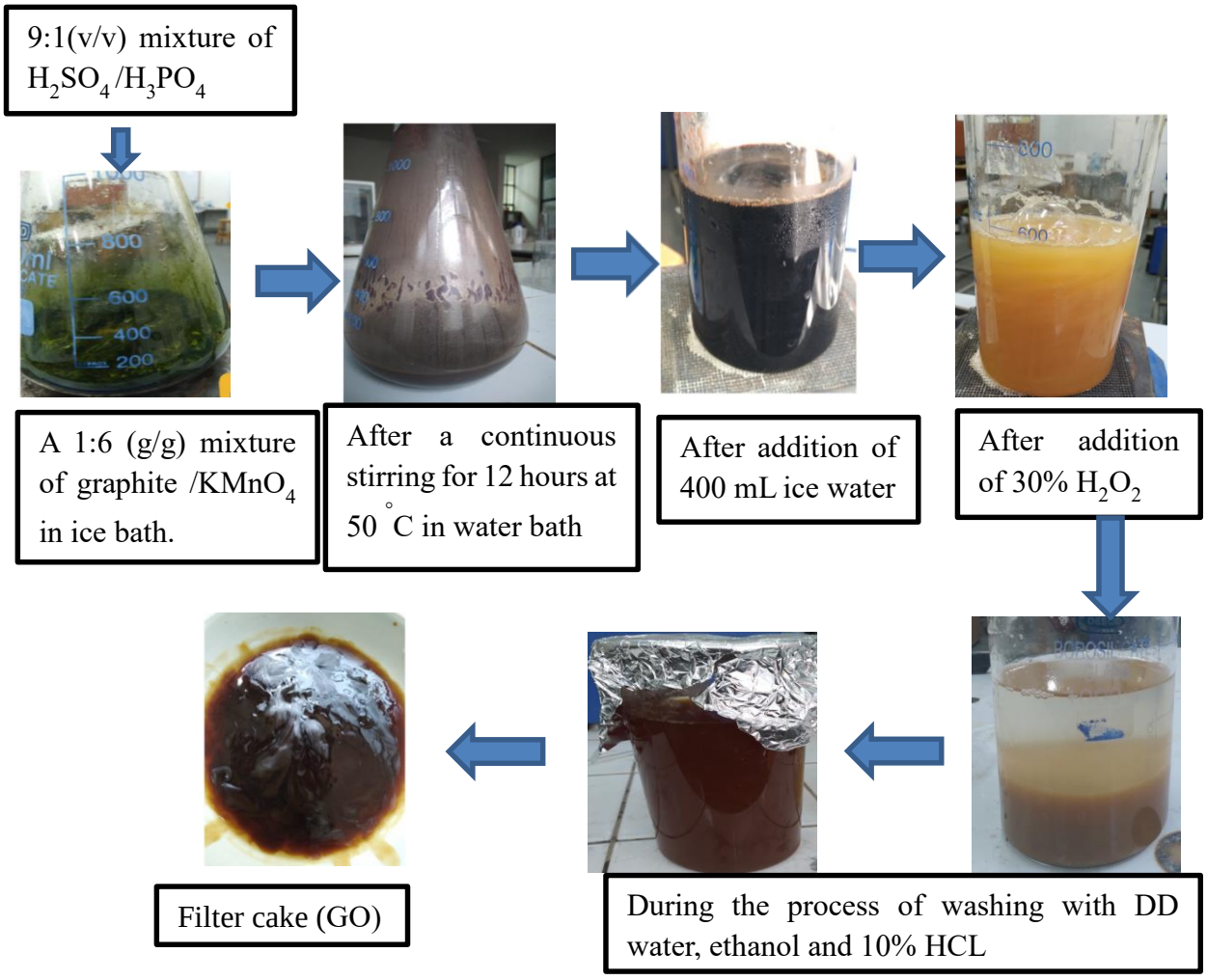

Figure 3.2: Experimental procedure for the synthesis of graphene oxide.

The resulting yellowish product was allowed to stand for 2 hours at room temperature. After that, a separate layer was obtained, and the supernatant part was washed. This washing process was repeated until a clear brown solution of GO was obtained. Finally, the brown suspension GO was centrifuged at 4000 rpm, and the filtered cake was collected using porous filter paper and washed with ethanol, double-distilled water, and 10% HCl solution. The washing of the filtered cake with 10% HCl aqueous solution was continued until the complete removal of sulfate ions (SO_4^{2-}), which was confirmed by the addition of barium chloride ($BaCl_2$) to the supernatant (i.e., the formation of

white precipitate with the addition of $BaCl_2$ indicate the presence of sulfate ions). Finally, the resulting brown cake was dried at 60 °C in an oven for 8 hours to produce graphene oxide (GO).

According to the protocol reported by (Habte *et al*., 2019), synthesized graphene oxide (GO) was chemically reduced to form reduced graphene oxide (rGO) using ascorbic acid as a reducing agent. 40 mg of the synthesized GO was dispersed in 400 mL of double distilled water (0.1 mg/mL) and stirred for 20 min using a magnetic stirrer. The suspension was ultrasonically treated for one hour to exfoliate the layer of graphene oxide sheets. After that, 4 g of ascorbic acid (AA) was poured into the suspension and agitated for 30 min at 70 °C using a hot plate with a magnetic stirrer. During this time, the brown color of the suspension was changed to black, confirming the formation of rGO (Habte *et al*., 2019). Excess H_2O_2 (30% w/w) was added to the black solution while stirring for 30 min at 60 °C to oxidize the leftover ascorbic acid. Then, the black product was allowed to stand for 24 h, and the obtained black paste was filtered using Whatman filter paper, followed by discarding the supernatant. The black paste was washed with ethanol and double distilled water three times before being dried overnight at 120 °C in an oven (Figure 3.3). Finally, the obtained powder was ground using mortar and pistil and stored for further characterization and application studies.

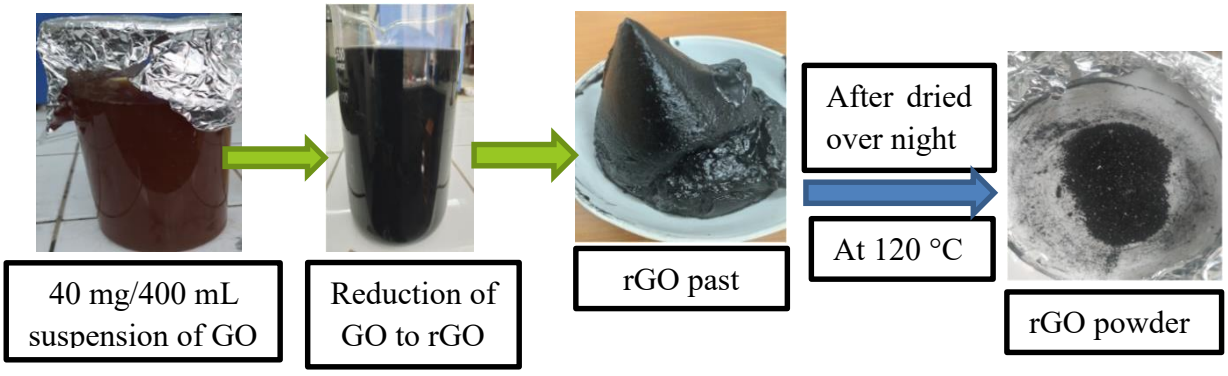

Figure 3.3: Experimental procedure for Tour's method synthesis of rGO.

3.3.3 Preparation of RE (La^{3+}, Eu^{3+} and La^{3+}-Eu^{3+}) ions doped NZF/rGO NCs

The $Ni_{0.75}Zn_{0.25}RE_xFe_{2-x}O_4$/rGO NC was prepared using an ultra-sonication route (Shahid *et al*., 2020). In a typical synthesis, 50 mg of rear earth ions (La^{3+}, Eu^{3+}, and La^{3+}-Eu^{3+}) doped NZF spinel ferrite was added into 100 mL of dispersion containing 5 mg of rGO. Then, the resultant suspension was ultrasonicated for 2 hours to produce a homogenized suspension. After that, the obtained suspension was heated at a temperature of 100 °C using a hot plate until the complete vaporization

of water and the formation of composite powder. The obtained powder was then dried overnight in an oven at 100 °C. The resultant composites in Table 3.3 were used for further characterization and application testing.

Table 3.3: Sample codes of the nanocomposites

No.	Nanocomposites	Sample codes
1	*Nickel zinc ferrite/rGO- $Ni_{0.75}Zn_{0.25}Fe_2O_4$/rGO*	*NZF/rGO*
2	*La^{3+} ion doped Nickel-Zinc ferrite/rGO – $Ni_{0.75}Zn_{0.25}La_{0.06}Fe_{1.94}O_4$/rGO*	*NZLF/rGO*
3	*Eu^{3+} doped Nickel Zinc ferrite/rGO - $Ni_{0.75}Zn_{0.25}E_{0.06}Fe_{2-x}O_4$/rGO*	*NZEF/rGO*
4	*La^{3+}-Eu^{3+}co- doped (1:1) Nickel Zinc ferrite/rGO- $Ni_{0.75}Zn_{0.25}La_{x/2}Eu_{x/2}Fe_{2-x}O_4$/rGO*	*NZL-EF/rGO*

3.4 Photocatalytic Experiments

The photocatalytic experiments were conducted adopting a procedure in the literature (Vinosha *et al.*, 2021). Photocatalytic activities of the synthesized samples, $Ni_{0.75}Zn_{0.25}RE_xFe_{2-x}O_4$, (x = 0.00, 0.02, 0.06 and 0.1) and the composite of the selected samples $Ni0_{.75}Zn_{0.25}RE_{0.06}Fe_{1.94}O_4$/rGO (RE = La^{3+}, $Eu^{3+,}$ and La^{3+}-Eu^{3+})) were evaluated by the degradation of mixed organic dyes (MB & MO) in aqueous solutions under visible light irradiation using a 150 W Tungsten halogen lamp as the light source in the wavelength range of 200 to 800 nm in a photo reactor. The inside of the photoreactor consisted of a reactor lamp used as the visible light source with a water circulator plastic tube and magnetic stirrer, surrounded by a reactor box, as illustrated in Figure 3.4. In these experiments, 50 mg of photocatalyst was dispersed into 100 mL of aqueous solution containing mixed dyes (50 mL of MB and 50 mL of MO) with optimized concentration (10 mg/L). The pH of the suspension was adjusted to pH nine by using HCl/NaOH (0.1 M) and kept in the dark for about 30 min with aeration to attain adsorption-desorption equilibrium. After that, three drops of 8 ppm H_2O_2 solution were added, which acted as an oxidizing agent, and the reaction mixture was irradiated by visible light and the supernatant suspension from the reaction at an interval of every 5 min. The catalyst was separated magnetically by applying an external magnetic field. The same degradation procedure was applied for mixed dyes without adding a photocatalyst and with only an H_2O_2 solution, which was used to test the degradation of dyes under different conditions.

Figure 3. 4: Setup for photocatalytic experiments.

Finally, the photocatalytic activities of the synthesized photocatalysts were monitored by comparing the change in the absorbance of mixed organic dyes with their corresponding λ_{max} using a UV-Vis absorption spectrophotometer.

The percentage of degradation was measured using the expression below.

$$\%\ of\ degradation = \left[\frac{C_o - C_t}{C_o}\right] x100 \qquad 3.1$$

C_o is the initial concentration of dyes; C_t is the concentration of dyes at every 5-minute intervals of degradation.

In these experiments, the effect of pH, the content of RE ions, irradiation time, the photocatalyst dosage, and the concentration of mixed dyes were optimized. Moreover, five activity cycles were conducted to confirm the reusability efficiency of the photocatalysts. After each cycle, the photocatalysts were isolated by applying an external magnetic field. Then, the isolated photocatalyst samples were washed with DDW and ethanol and dried at room temperature before reusing under the same optimized conditions.

3.5 Electrochemical Experiments

3.5.1 Preparation of modified electrodes

The working electrodes of $Ni_{0.75}Zn_{0.25}RE_xFe_{2-x}O_4$/CPE and $Ni_{0.75}Zn_{0.25}RE_xFe_{2-x}O_4$@rGO/CPE (RE = La and Eu, x = 0.00, 0.02, 0.06 & 0.10) were fabricated according to the literature (Darabi et al., 2021). A 0.45 g of graphite powder and 50 mg of the synthesized sample were mixed uniformly and milled well with 3 mL of paraffin oil several times to give a homogenous and uniformly wetted paste of $Ni_{0.75}Zn_{0.25}Fe_{2-x}RE_xO_4$/CPE and $Ni_{0.75}Zn_{0.25}Fe_{2-x}RE_xO_4$@rGO/CPE. The obtained pastes were inserted into 1.5 mm diameter and 5 cm long plastic syringes. The electrical connection was made by a copper wire, which was installed into another head of the syringe, as illustrated in Figure 3.5. The unmodified carbon paste electrode (CPE) was constructed similarly and used for comparison. Cyclic voltammetry (CV), Square wave voltammetry (SWV), and Differential pulse voltammetry (DPV) techniques were used for electrochemical investigations.

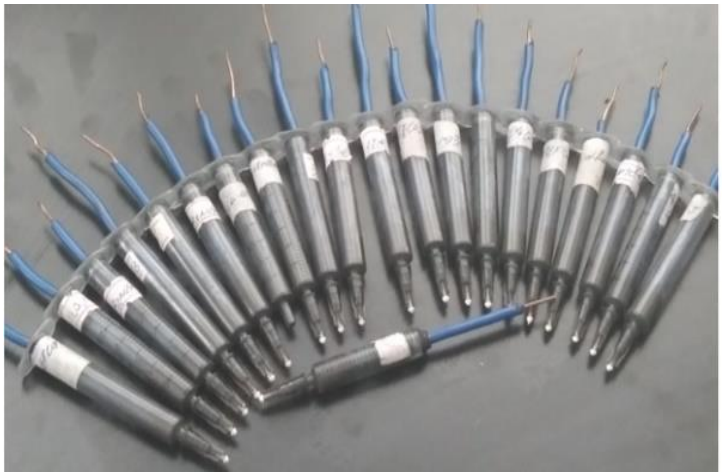

Figure 3.5: Fabricated working electrodes using $Ni_{0.75}Zn_{0.25}RE_xFe_{2-x}O_4$ and $Ni_{0.75}Zn_{0.25}RE_xFe_{2-x}O_4$@rGO.

3.5.2 General procedure for electrochemical application

Electrochemical characterization of RE ions doped NZF ferrite and its composites with rGO was performed by cyclic voltammetry (CV) and electrochemical impedance spectrometer (EIS) on a potentiostat (BioLogic, SP-300) electrochemical workstation. A conventional three-electrode system setup in 5 mM $K_3Fe(CN)_6/K_4Fe(CN)_6$ (1:1) containing 0.1 M KCl was used with a

modified carbon paste electrode (CPE) (1.5 mm in diameter) as the working electrode, a platinum wire as the counter electrode and a silver-silver chloride electrode (Ag/AgCl (3 M KCl)) as the reference electrode. After a 100 s accumulation at the potential of −0.1 V, cyclic voltammograms (CVs) were recorded in the potential range from -0.5 to 1.0 with a scan rate of 50 mV s^{-1}. The impedance spectra were recorded within the frequency range of 10 mHz to 10^5 Hz. The applied sinusoidal wave potential in each case was 14 mV.

All electrochemical measurements were recorded in a 20 mL electrochemical cell containing 5 mM of mixed synthetic food dyes (2.5 mL of SY and 2.5 mL of TZ) and a 10 mL of phosphate-buffered saline (PBS) (0.1 M) as supporting electrolyte and using a conventional system with three electrodes: platinum wire as auxiliary electrode, Ag/AgCl (3 M) as a reference electrode and CPE with and without modification as a working electrode. The setup for this activity is depicted in Figure 3.6. The reagents orthophosphoric acid, di-sodium phosphate buffer (Na_2HPO_4), and mono-sodium phosphate buffers (NaH_2PO_4) were used to adjust the pH of the electrolyte solution.

All electrochemical measurements were recorded using 20 mL electrochemical cells containing 5 mM of the selected dyes, SY, and TZ (1:1) and 10 mL of phosphate-buffered saline (PBS 0.1 M) as supporting electrolytes under pH 6. Cyclic voltammograms (CV) were obtained in the potential range of 0 V to 1.2 V at a scan rate of 50 mV/s. Differential pulse voltammograms (DPV) analysis of these dyes were recorded under optimal conditions of potential range 0 V to 1.2 V, pulse height 50.0 mV, pulse width 5 ms, step potential 5.0 mV, and step time 100 ms. The square wave voltammograms were also recorded under a pulse amplitude of 50.0 mV, voltage step height of 10 mV, and pulse width of 50 ms. Under these conditions, EIS, CV, DPV, and SWV were recorded in the positive potential direction. When it was necessary to have a fresh electrode surface, the new surface was generated by rapidly extruding a small paste plug with a glass rod and smoothing the resulting surface on the white paper. The renewed and activated electrode surface permitted the elimination of the irreversible surface contamination. It was also used to minimize the minor effects, especially in real sample analysis. All experiments were conducted at room temperature for four times of replication.

All the above experimental procedures were optimized by varying parameters such as scan rate (10 mV/s-100 mV/s), pH of the supporting electrolyte (2 to 11), and the number of RE ions (0.00, 0.02, 0.06, and 0.10) per mole.

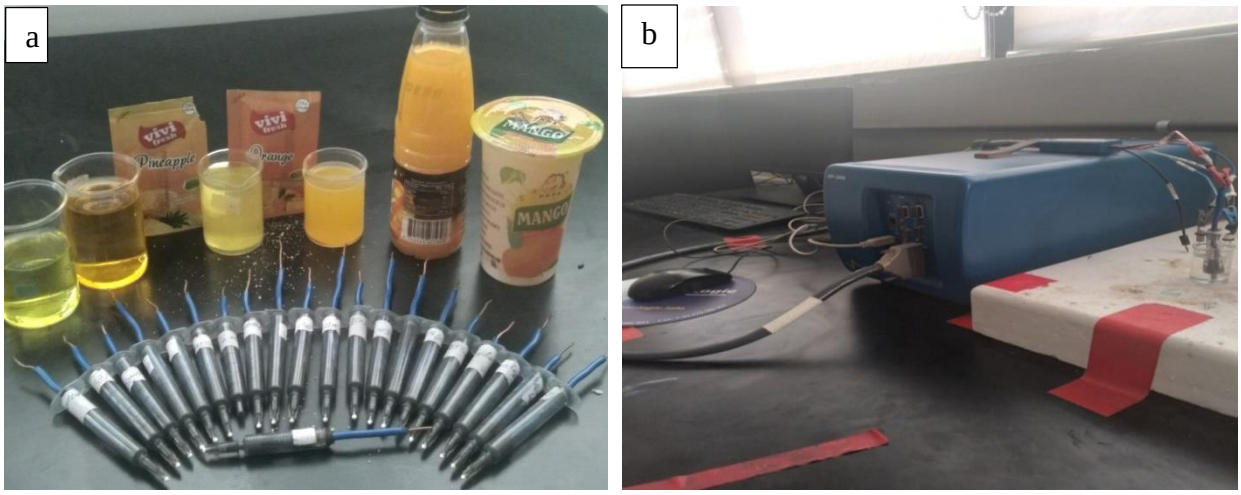

Figure 3.6: (a) The fabricated modified electrode with the selected real samples, (b) the experimental setup for electrochemical activity.

3.5.3 Real samples analysis

The real samples were obtained from the local market for the investigation of food colorants based on the method reported in the literature (Darabi *et al*., 2021; Moarefdoust, *et al*., 2021). This included pineapple powder, orange powder, and mango juice samples. For mango juice, no pretreatment was done. At the same time, for powder products, five g of powder was taken and dissolved separately in double distilled water and diluted to a final volume of 100 mL. After that, the samples were analyzed per the analytical protocol of the above-optimized conditions by adding five mL of the selected real samples to 10 mL of PBS (0.1 M). To obtain reliable results, co-detection of Tartrazine and Sunset yellow in each sample were done in sample was done in the quartet using the standard addition method.

CHAPTER FOUR

4 RESULTS AND DISCUSSION

In this section, the rare earth ions (La^{3+} and Eu^{3+}) doped NZF ferrite nanomaterials and composites with reduced graphene oxide (rGO) their characterization, photocatalytic degradation of the organic pollutants (MB and MO) under irradiation by visible light with the optimal photocatalyst and, electrochemical sensor simultaneous detection of synthetic food colorants (Sunset yellow (SY) & Tartirazine (TZ)) are presented and discussed. Furthermore, the characterization and application of co-doping (NZL-EF@rGO) nanocomposite are also presented.

4.1 Characterization of GO and rGO

4.1.1 XRD analysis

Figure 4.1 illustrates the XRD patterns of GO and rGO. As seen in the Figure, the XRD patterns of the samples verified the formation of GO and rGO and exhibited their crystalline structure. The XRD pattern of GO shows a diffraction peak (001) at 2θ value of 10.5° with d-spacing of 0.73 nm. This XRD pattern indicates the formation of excess hydroxyl, carbonyl, and epoxy groups at the interlayer of the graphite, which confirms the successful oxidation of graphite to form GO (Meka *et al*., 2021). Moreover, shifting the XRD peak to a lower value of 2θ (10.5°) also indicates the deformation of graphite structure and separation of its layers with trapped water molecules and oxygen-containing functional groups. The peak for rGO was found at 22.5° (0.38 nm) with a diffraction plane of (002) (Javed *et al*., 2019). The shifting of the 2θ value from 10° to 22.5° and the decreasing of the interplanar distance from 0.73 nm to 0.38 nm verified that the re-gaining of graphite structure and the successful synthesis of rGO through a chemical reduction of GO (Javed et al., 2019; Meka Chufa *et al*., 2021). FTIR and UV-Vis spectroscopy also provided proof of the successful synthesis of GO and rGO.

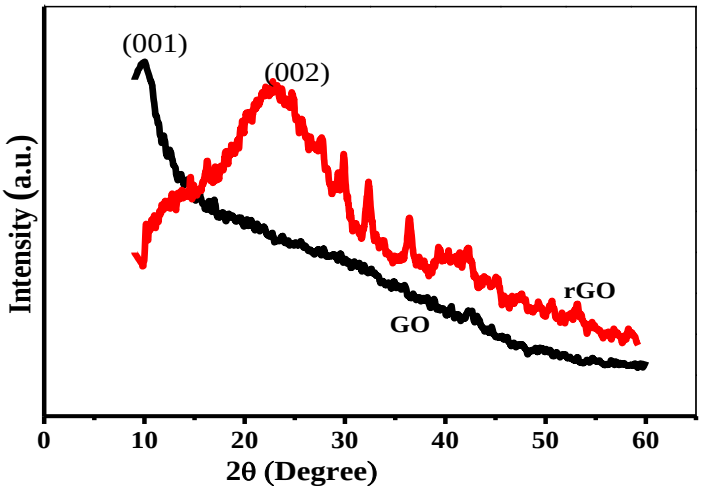

Figure 4.1: XRD patterns of GO and rGO.

4.1.2 FTIR analysis

The FTIR is one of the helpful techniques for revealing structural parameters, the type of molecular bonds, and the presence of functional groups in the synthesized materials (Baig *et al*., 2020). The FTIR spectra of GO and rGO illustrated in Figure 4.2 confirmed the formation of several oxygen-containing functional groups and their corresponding reduction to rGO (Abdisa *et al*., 2021). The FTIR spectra of GO displayed a broad and intense stretching vibration band at 3425 cm^{-1}, which was assigned to –OH of the intercalated residual water molecules, which were almost removed, but the remaining small band was shifted to 3443 cm^{-1} in rGO due to reduction (Abdisa *et al*., 2021). Furthermore, the bands at 1754 cm^{-1}, 1626 cm^{-1}, 1395 cm^{-1}, and 1125 cm^{-1} correspond to C=C stretching, C=O stretching modes, epoxy, stretching mode, and C-O (alkoxy) stretching mode, respectively (Habte *et al*., 2019; Meka *et al*., 2021). The two intense absorption bands centered at 2856 and 2925 cm^{-1} in the GO spectrum also remain prominently in rGO and were assigned to symmetrical and anti-symmetrical stretching vibrations of $–CH_2$ (Habte *et al.*, 2019). As the reducing agent removed the oxygen-containing functional groups, the characteristic absorption bands of oxide groups decreased significantly, the C=O band at around 1754 cm^{-1} vanished, and the small shift of bands to the shorter wave number indicates the successful reduction of GO. The broadband formed at 1626 cm^{-1} was attributed to the (C=C) stretching of the aromatic ring of the rGO attributed to the regaining of sp^2-hybridization (structural order) (Meka *et al*., 2021). The intensity of bands related to C-O (1395 cm^{-1}) also increased, showing some epoxide

groups in rGO (Dhanda *et al*., 2016). All these results clearly confirmed the successful formation of rGO.

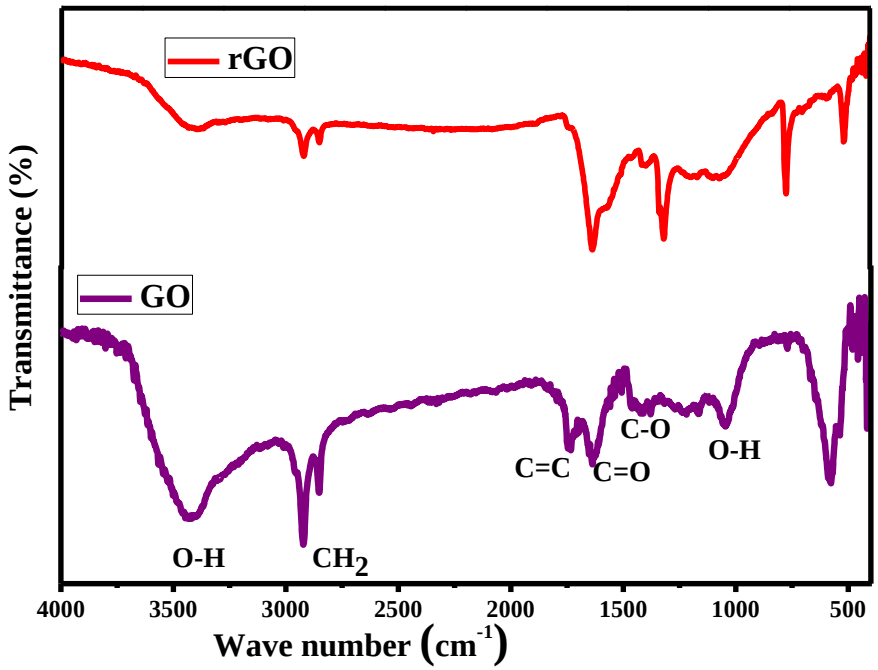

Figure 4.2: FTIR spectra of GO and rGO.

4.1.3 UV-Visible analysis

The UV-Vis absorption spectra of GO and rGO are illustrated in Figure 4.3. As can be seen in the UV-Vis spectrum, GO has a strong absorption peak at 228 nm, which is possibly due to π-π* excitation of aromatic C-C bonding in the ring, and also the absorption peak at 302 nm was observed due to n-π* excitations of the carbonyl group (C=O) (Habte *et al*., 2019; Riaz *et al*., 2020). L-Ascorbic acid was used as a reducing agent for the chemical reduction of oxygen-containing functional groups in GO. Hence, after the reduction process, the red shifting of the absorption spectrum at a wavelength from 228 nm to 262 nm was observed. This reveals the successful reduction of GO and the formation of rGO through the chemical reduction process (Meka *et al*., 2021). Furthermore, the disappearance of the peak at 302 nm confirmed the reduction of oxygen functionalities (like C=O groups and epoxide) (Javed *et al*., 2019). The shifting peaks from 228 nm to 262 nm and disappearance peaks at 302 nm of the UV-Vis band in the rGO spectrum confirmed the regaining of sp^2-hybridization and structural order of graphene in rGO. The XRD, FTIR, and UV-Vis absorption spectra of both GO and rGO have confirmed the

successful oxidation of graphite into graphene oxide and its reduction into reduced graphene oxide. This result agrees with the results reported by researchers in the recent past (Habte *et al*., 2019; Meka *et al.*, 2021).

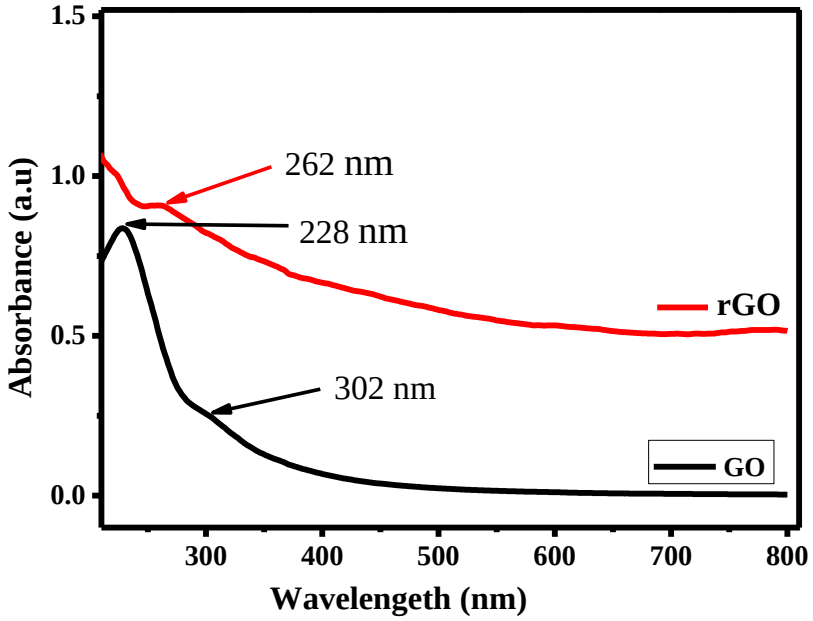

Figure 4.3: UV-Vis absorbance spectra of GO and rGO

4.2 Characterization of La^{3+} Ions Doped NZF Spinel Ferrite NPs and NZLF@rGO NCs

4.2.1 TGA/DTA analysis

The thermal analysis study helps determine the optimal temperature to synthesize the nanomaterials with their desired structure. Hence, TGA-DTA analysis was undertaken to determine the proper annealing temperature for the synthesis of spinel ferrite (Baig *et al*., 2020). Figure 4.4 illustrates the TGA and DTA plots with the increase in temperature from room temperature to 950 ℃.

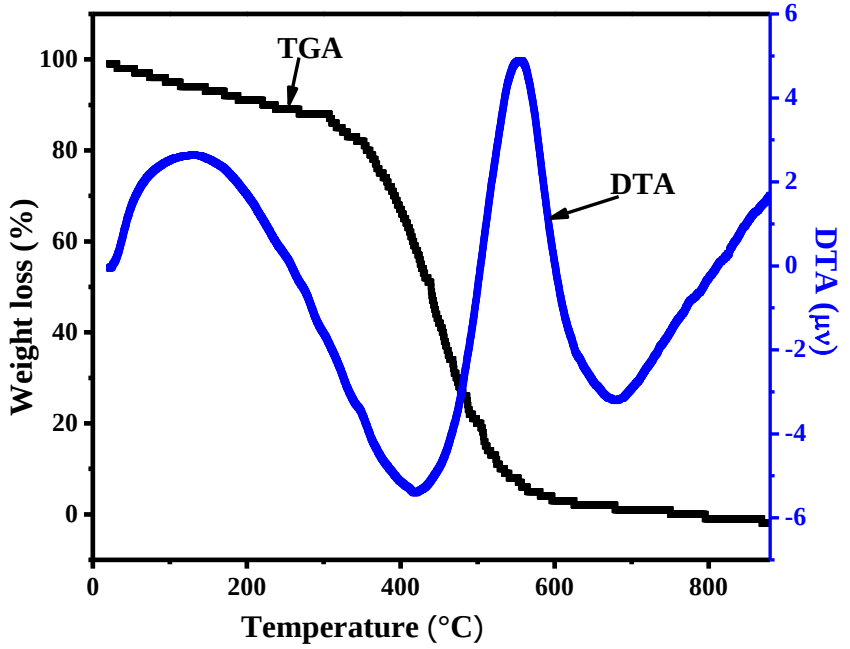

Figure 4.4: TGA/DTA thermograms of $Ni_{0.75}Zn_{0.25}Fe_2O_4$.

As can be seen from Figure 4.4, two exothermic peaks at 124 and 557 °C and one endothermic peak at 420 °C were observed in the DTA thermogram. The exothermic peak at 124 ℃ is linked to self-combustion, at which nitrate ions and citric acids act as an oxidizing agent and fuel, respectively (Singh *et al*., 2010a). The transformation step observed between 350 and 450 °C, corresponding to a broad endothermic peak at 420 °C in the DTA thermogram, is due to the dehydration of the OH group in the spinel structure and the formation of semi-organic carbon material/metal oxide (Baig *et al*., 2020). A maximum exothermic peak at 557 °C in DTA could be observed, closely followed by a significant weight loss between 450 to 600 °C, demonstrating the occurrence of decomposition of the nitrate-citrate powder. During this process, 8.04% of the mass was lost. This could be related to the removal of H_2O, O_2, NO_2 and CO_2 from the precursor salts (Mullai *et al.*, 2012; Samikannu, 2013). Moreover, the endothermic peak observed between 600 and 750 ºC indicates the gradual crystallizing process of ferrite precursor. Above the temperature of 800 °C almost no significant weight loss was detected, which indicated that the complete removal of organics and other impurities and formation of stable $Ni_{0.75}Zn_{0.25}Fe_2O_4$ spinel phase (Baig *et al*., 2020; Samikannu, 2013; Wu *et al*., 2015). Therefore, 800 °C was used as an optimal calcination temperature for the synthesis of entire NZF spinel ferrite-based samples in this work.

4.2.2 FTIR analysis

The FTIR spectra of the synthesized $Ni_{0.75}Zn_{0.25}La_xFe_{2-x}O_4$ (x=0.00, 0.02 0.06, and 0.10) nanocrystalline powder analyzed in the wavelength range of 400-4000 cm^{-1} at room temperature are illustrated in Figure 4.5a. As can be seen in the figure, the two prominent absorption bands observed in the range of 600 and 400 cm^{-1} are characteristics of spinel ferrite structures (Dasan *et al*., 2017). The intensity of these absorption bands depends on the nature of cation distribution and their occupancy in the spinel-type sublattices (Iftikhar *et al*., 2020; Aslam *et al*., 2021). For NZF spinel ferrite, the higher-frequency absorption band (ν_1), which appears in the range of 500-600 cm^{-1}, is due to the intrinsic vibration of the metal-oxygen bond at tetrahedral sit, while the lower absorption band (ν_2) appeared in the range of 400-480 cm^{-1} is assigned to metal-oxygen bond at the octahedral site (Dasan *et al*., 2017; Dubey, 2018; Jacob *et al*., 2018; Baig *et al*., 2020; Shahid *et al*., 2020). These two bands are considered to confirm the formation of spinel ferrite (Iftikhar *et al*., 2020; Shahid *et al*., 2020; Dubey, *et al*. 2021).

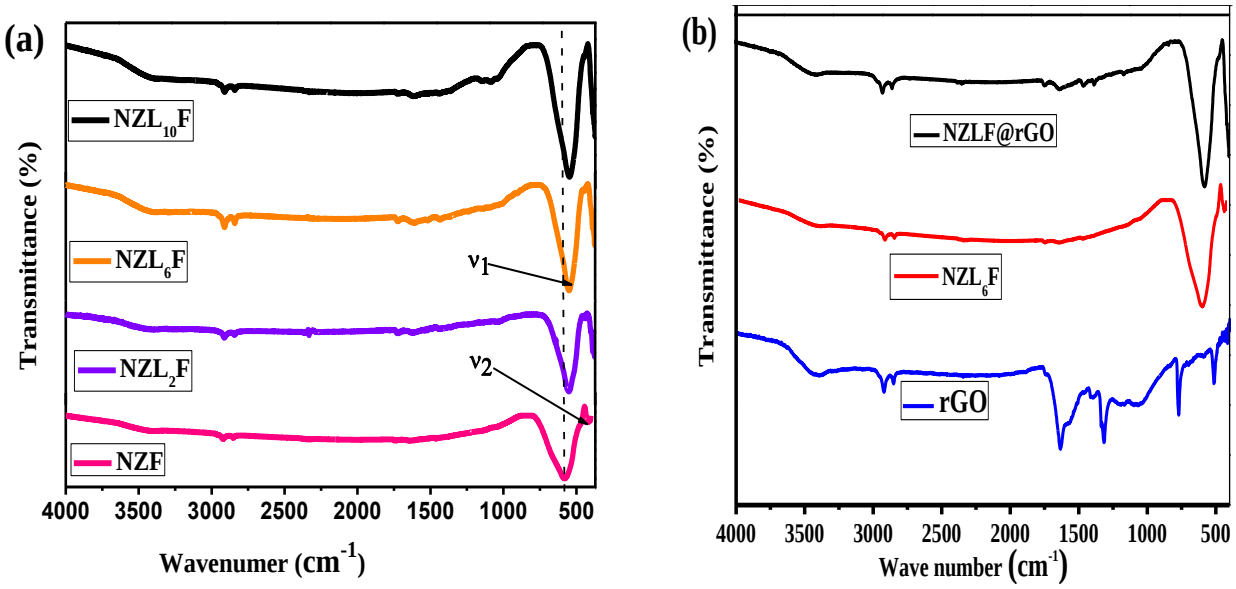

Figure 4.5: FTIR spectra of (a) $Ni_{0.75}Zn_{0.25}La_xFe_{2-x}O_4$ (x=0.00, 0.02, 0.06 and 0.1); (b) rGO, $Ni_{0.75}Zn_{0.25}La_{0.06}Fe_{1.94}O_4$, $Ni_{0.75}Zn_{0.25}La_{0.06}Fe_{1.94}O_4$@rGO.

Moreover, with an increase in the content of La^{3+} ions doping in NZF lattice, the formation of additional shoulder peaks, increasing the intensity, broadness, and shifting of the absorption band at the B-sit (octahedral) towards lower frequency from their original positions was observed. These variations in intensity and position bands are directly attributed to the nature of the La^{3+} ion, which

prefers to occupy the octahedral (B-site) (Dasan *et al.,* 2017). This is due to their high octahedral crystal field stabilization energy in the B-site of the spinel ferrite structure (Shaikh, 2021). Thus, the increasing La^{3+} ion content causes the migration of Fe^{3+} ions from the octahedral site to the tetrahedral site of the NZF ferrite structure. This migration of ions also caused the variation in bond length Fe^{3+}-O^{2-} and expansion in the radius of A-site and B-site ferrite structure (Dasan *et al*., 2017; Šoka *et al*., 2018).

Moreover, besides these two prominent bands, other absorption bands also appeared in the FTIR spectra. the adsorption band around 3400 cm^{-1} is attributed to stretchable vibration of the H–O–H group due to the presence of small amount of adsorbed moisture (Dasan *et al.,* 2017; Aslam *et al.*, 2021). The pair of two weak bands at around 2850 and 2950 cm^{-1} are assigned to the C–H stretching vibrational mode (Dasan *et al*., 2017). A shoulder band at 1000 cm^{-1} is related to the incomplete decomposition of the products. The FTIR results agree with the literature (Dasan *et al.,* 2017; Dubey, 2019; Jacob *et al*., 2018).

Figure 4.6b illustrates the FTIR spectra of rGO, $Ni_{0.75}Zn_{0.25}La_{0.06}Fe_{1.94}O_4$, and $Ni_{0.75}Zn_{0.25}La_{0.06}Fe_{1.94}O_4$@rGO NCs. The weak bands observed at 2856 and 2925 cm^{-1} in the $Ni_{0.75}Zn_{0.25}La_{0.06}Fe_{1.94}O_4$ ferrite NPs spectrum are assigned to $–CH_2$ stretching vibrations, which became intense, broad, and more visualized in $Ni_{0.75}Zn_{0.25}La_{0.06}Fe_{1.94}O_4$@rGO NCs with the introduction of rGO sheets (Rahman *et al*., 2020). Besides that, the small stretching band vibration of the O–H group at 3425 cm^{-1} in the spectrum of $Ni_{0.75}Zn_{0.25}La_{0.06}Fe_{1.94}O_4$ ferrite NPs due to the adsorption of environmental moisture became broad and intense with the introduction of rGO to form $Ni_{0.75}Zn_{0.25}La_{0.06}Fe_{1.94}O_4$@rGO NCs. Moreover, the two prominent bands in the spectrum of NZL_6F ferrites in the range of 400-600 cm^{-1}, assigned to metal-oxygen bonds, also appeared in NZLF@rGO nanocomposite (Shen, 2021). These results corroborate the successful formation of nanocomposite.

4.2.3 XRD analysis

XRD is a well-known tool for the identification of the crystal structure of materials (Baig *et al.,* 2020; Agboola *et al*., 2022). Figure 4.7 illustrates the XRD patterns of calcinated $Ni_{0.75}Zn_{0.25}La_xFe_{2-x}O_4$ (x=0.00, 0.02, 0.06, 0.1). Prominent peaks appeared at 2θ values of 18.5°, 30.3°, 35.6 °, 37.17 °, 43.3°, 53.8°, 57.4°, and 63°, corresponding to diffraction planes (111), (220), (311), (222), (400), (422), (511), and (440), respectively, in good agreement with JCPDS data card

No. 00-052-0278. These planes are associated with the crystal planes of pure spinel ferrite NPs (Dasan *et al*., 2017; Rahman *et al*., 2020; Shahid *et al*., 2020), which confirmed the formation of the face-centered cubic (FCC) structure of spinel ferrite (Agboola *et al*., 2022). The XRD patterns of all samples contained the main spinel phase along with a secondary phase (♠) designated as lanthanum orthoferrite ($LaFeO_3$), which appeared after doping with La^{3+} ions (Dasan e*t al*., 2017).

The degree of substituting of Fe^{3+} by La^{3+} is mainly dependent on their ionic radii (Martin *et al.*, 2018). As a result, the significant variation between the ionic radii of La^{3+} ions (1.06 Å) and Fe^{3+} ions (0.67 Å) limits the replacement of Fe^{3+} ions by La^{3+} ions at B sites in the crystal lattice structure. Moreover, since the bond energy of La^{3+}-O^{2-} is more significant than Fe^{3+}-O^{2-}, La^{3+} ions need more energy to enter the lattice (Phor *et al*., 2020). Hence, after the replacement of a small amount of $La^{3+,}$ the solubility limits are reached, and an excess of La^{3+} ions accumulated on the grain boundaries to form $LaFeO_3$ aggregation, in agreement with the literature (Dasan *et al*., 2017; Šoka *et al*., 2018; Agboola *et al*., 2022) That is why the intensity of peaks (♠) related to the secondary phases increases with increased concentration of La^{3+} ions (Dasan *et al*., 2017). The secondary phase formed in this process prevents the growth of grain size during the sintering process (Rezlescu *et al*., 1997). Since the photocatalytic activities are inversely related to the grain size, the suppression of the grain size is one of the essential parameters for improving the photocatalytic efficiency of the synthesized materials. All these results agree with the results reported in recent literature (Dasan *et al*., 2017 ; Šoka *et al*., 2018 ; Phor *et al.*, 2020 ; Agboola *et al.*, 2022).

As the concentration of La^{3+} ions increased, a higher ionic radius of ion hindered entering into the crystal lattice structure, producing distortion and strain (Agboola *et al.*, 2022). Thus, the broadening and shifting of diffraction peaks with increasing the concentration of La^{3+} ion are related to inducing the lattice strains, distortion of the lattice structure, and the formation of strong crystal field effects, as illustrated in Figure 4.7(b) (Agboola *et al*., 2022).

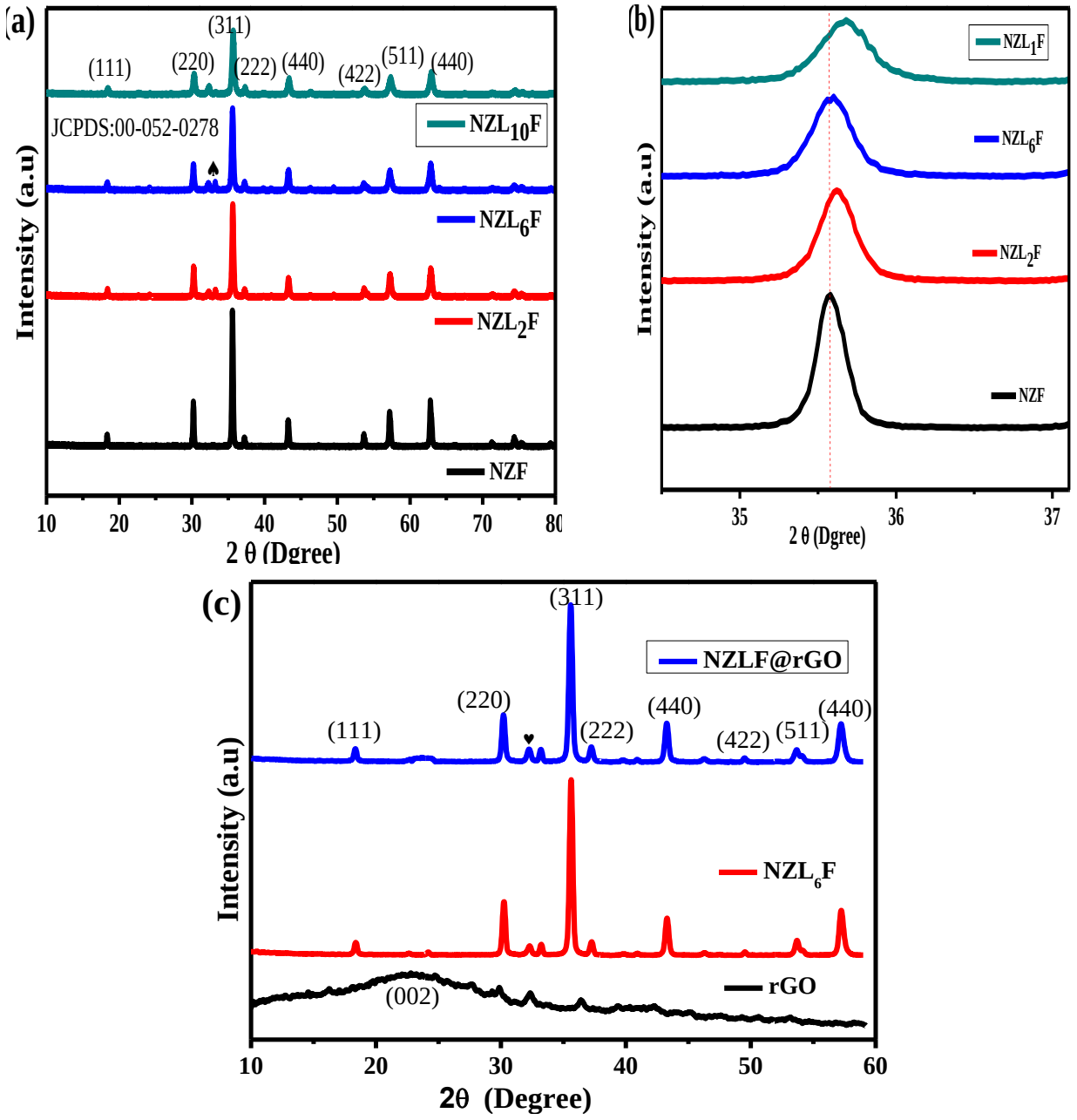

Figure 4.6: (a) XRD pattern of La^{3+} ion doped NZF spinel ferrite ($Ni_{0.75}Zn_{0.25}La_xFe_{2-x}O_4$ (x=0.00, 0.02, 0.06, and 0.1); (b) shifting of the corresponding peaks; (c) XRD pattern of rGO, $Ni_{0.75}Zn_{0.25}La_{0.06}Fe_{1.94}O_4$ and $Ni_{0.75}Zn_{0.25}La_{0.06}Fe_{1.94}O_4$@rGO.

Various crystallographic parameters, such as average crystallite size (D), lattice constant (α), x-ray density (ρ_x), cell volume (V_{cell}), porosity (P) and hop length of the samples ($Ni_{0.75}Zn_{0.25}La_xFe_{2-x}O_4$ (x=0.00, 0.02, 0.06, 0.1), were calculated from the XRD data. The results are depicted in Table 4.1. All these parameters are estimated from the intense peak (311) of the XRD diffraction pattern.

The average crystallite sizes of the synthesized nanoparticle were calculated using the intense peak (311) by using the Debye-Scherer equation (4.1) (Shahid *et al*., 2020).

$$D = \frac{\kappa\lambda}{\beta\cos\theta} \quad (4.1)$$

Where D= the average crystalline diameter, λ is the wavelength of x-rays (1.5406 Å), β is the full width at half maximum (FWHM), θ is the Bragg's angle corresponding to the plane (311), and κ= 0.94 represents crystalline shape factor (Dasan *et al*., 2017).

As per calculation, the obtained average crystallite sizes were estimated from 43.9 nm to 23.41 nm and presented in Table 4.1, which confirms the synthesis of nanosized crystalline powders. The result shows that decreasing crystallite size increases the content of La^{3+} ions in NZF spinel ferrite. This is attributed to many issues. The most crucial reasons are electronic configurations, valences, and ionic radii discrepancies between La^{3+} and Fe^{3+} ions. Moreover, since the bond energy of RE^{3+}–O^{2-} is greater compared to that of Fe^{3+}–O^{2-}, an extra amount of energy is required to incorporate RE^{3+} ions into spine ferrite lattice to form RE^{3+}–O^{2-} (Ateia *et al*., 2020). This required extra energy hinders the crystallization process and the growth of grains in RE^{3+}-doped samples. Therefore, a reduction in crystalline nature with smaller crystallite size is detected (Ateia *et al*., 2020; Dasan *et al*., 2017). Mansour et al.(year?) reported similar behavior for decreasing lattice parameter of $Co_{0.5}Cu_{0.5}La_xFe_{2-x}O_4$ ferrite nanoparticles and explicated its behavior using the same reason (Mansour *et al*., 2021).

The lattice constant, α, of the synthesized powder was also calculated using cell software by using equation 4.2 and found to be in the range of 8.328 Å and 8.56 Å.

$$a = d_{hkl}\sqrt{h^2+k^2+l^2} \quad (4.2)$$

Where 'α' is the lattice constant, d is the interplanar distance, and (h, k, l) are the Miller indices (Mansour *et al*., 2021).

The ionic radii of elements impact the lattice constantly (Shahid *et al*., 2020). As depicted in Table 4.1, the lattice constant, α, of $Ni_{0.75}Zn_{0.25}La_xFe_{2-x}O_4$ increases after the addition of a small amount of La^{3+} ions (x=0.00, 0.02, and 0.06) at first, and then decreased when the doping amount of La^{3+} ions increased to x = 0.1. The initial increase in the lattice constant of the as-prepared ferrite

samples can be explained based on the ionic radius of metal ions in the samples. As is known, the radius of La^{3+} ion (1.060 Å) is larger than that of Fe^{3+} ion (0.645 Å). Therefore, the exchange of larger ionic radii of La^{3+} ions in the arrangement of the smaller Fe^{3+} ions on the octahedral B-site would cause asymmetry in the structure, which leads to the expansion of the unit cell and results in larger lattice constants (Wu *et al.*, 2015). However, a further increase of La^{3+} ions concentration to 0.1 leads to a decrease in lattice constant because all La^{3+}ions may not occupy the lattice sites and may deposit onto grain boundaries to form a secondary phase, $LaFeO_3$, thereby causing the lattice contraction (Dasan *et al.*, 2017; Jacob *et al.*, 2018; Wu *et al.*, 2015).

Using the cell constant value, the unit cell volumes of $Ni_{0.75}Zn_{0.25}La_xFe_{2-x}O_4$ were calculated using equation 4.3 and found to be between 577.72 $Å^3$ and 583.8702 $Å^3$.

$$V_{cell=a^3} \tag{4.3}$$

where V_{cell} = unit cell volume and a^3 = lattice constant

The X-ray density (ρ_x) value of $Ni_{0.75}Zn_{0.25}La_xFe_{2-x}O_4$ nanocrystallites were determined based on equation 4.4. The calculated values depicted in Table 4.1 for ρ_x show that as the concentration of La^{3+} increased, theoretical x-ray density increased because it mainly depends on the higher molecular weight La^{3+} than Fe^{3+} (Ateia *et al.*, 2020).

$$\rho_x = \frac{8M_w}{N_A V_{cell}} \tag{4.4}$$

where M = molar mass, V = cell volume, and N_A = the Avogadro number (6.022×10^{23} mol^{-1}).

The specific surface area (SSA) is given by equation 4.5

$$SSA = \frac{6000}{\rho_x D} \tag{4.5}$$

where D = the average crystalline diameter, ρ_x = theoretical x-ray density and SSA=specific surface area.

The small size of the particles causes them to produce a large surface area that interacts with photons of solar light, which in return increases the photocatalytic performance and electrochemical conductivity of synthesized material.

It is worthwhile to mention the influence of large ionic radii on hopping lengths of spinel lattice. Utilizing the value of the lattice constant (a), the distance between magnetic ions available in the tetrahedral (A-site) and octahedral (B-site), i.e., hopping lengths (L_A and L_B), respectively, was calculated by using the following equations 4.6 and 4.7 (Dubey *et al*. 2021):

$$L_A = \frac{a\sqrt{3}}{4} \tag{4.6}$$

$$L_B = \frac{a\sqrt{2}}{4} \tag{4.7}$$

where a = lattice constant

Table 4.1 depicts the calculated values of hopping lengths. L_A and L_B are directly proportional to lattice parameters; they increase with the concentration of La^{3+} ions.

Table 4.1: Lattice parameters for $Ni_{0.75}Zn_{0.25}La_xFe_{2-x}O_4$ (x=0.00, 0.02 0.06, and 0.10)

Samples	**2θ (degree)**	**FWHM (β) (degree)**	**d (Å)**	**D (Å)**	**α (Å)**	**V_{cell} ($Å^3$)**	**ρ_x ($g/Å^3$)**	**SSA (m^2/g)**	**L_A (Å)**	**L_B (Å)**
NZF	35.5945	0.19400	2.5087	449.4	8.328	577.7	524	0.025	3.60	2.94
NZL_2F	35.6319	0.25440	2.5176	342.7	8.350	582.2	525	0.033	3.61	2.95
NZL_6F	35.5966	0.29340	2.5200	237.1	8.358	583.9	531	0.047	3.62	2.96
$NZL_{10}F$	35.6778	0.36930	2.5145	231.1	8.339	580.0	542	0.046	3.61	2.95

The detailed analysis of XRD results showed that the composition of La^{3+} at x=0.06 had a relatively lower crystal size, large lattice constant, and high active surface area, which may lead to a lower catalytic activity than the other compositions.

The XRD patterns for rGO, $Ni_{0.75}Zn_{0.25}La_{0.06}Fe_{1.94}O_4$, and $Ni_{0.75}Zn_{0.25}La_{0.06}Fe_{1.94}O_4$@rGO NCs are illustrated in Figure 4.6c. The XRD patterns for $Ni_{0.75}Zn_{0.25}La_{0.06}Fe_{1.94}O_4$ observed at 2θ values of 30.3º, 35.5º, 37.17º, 43.3º, 53.8º, 57.4º, and 63º were predominantly observed in the XRD patterns of $Ni_{0.75}Zn_{0.25}La_{0.06}Fe_{1.94}O_4$@rGO NCs samples. This confirms that the crystal structures of the face-centered cubic spinel ferrite remain stable (Ahmed *et al.*, 2020). Meanwhile, the rGO (002) peak at 2θ value of 22.5 ° *is* suppressed (Ahmed *et al.*, 2021). This may be attributed to the poor ordering of nanosheets and the uniform distribution of NZL_6F nanoparticles over the surface of rGO, as it has a higher surface area (Jun *et al*., 2020).

4.2.4 UV-Vis DRS analysis

UV-visible diffusion reflectance spectra can directly reflect the absorption characteristics of semiconductor materials. Figure 4.7a illustrates the UV-visible diffusion reflectance spectra of $Ni_{0.75}Zn_{0.25}La_xFe_{2-x}O_4$ (x=0.00, 0.02, 0.06, and 0.1) NPs using percent diffuse reflectance (% DR). The % DR spectra of all the synthesized samples were measured from 200 to 800 nm. Both UV and visible absorption bands were observed. The introduction of La^{3+} ions cause an increase in the localized donor concentrations near the CB, leading to a higher number of free charges that absorb photons from a lower O 2p energy level to a higher Fe 3d energy level (Lemziouka *et al*., 2020). It is evident from Figure 4.7a that increasing the concentration of La^{3+} ions lead to a simultaneous increase in the percentage absorbance in the UV and visible irradiation ranges. Additionally, a 6 mol% doping of La^{3+} ions demonstrate a better enhancement in absorption potential in the visible light region.

The band gap energy (E_g) is the equivalent photon energy required to create an electron-hole pair, and it is given by ($h\nu/\lambda_{max}$) against maximum absorbance (Sedky, *et al*., 2019). E_g is an important parameter to characterize the semiconductor materials for investigating their photoactive response under solar light irradiation (Farooq *et al.,* 2019). To determine the optical band gap energy of powder samples, the Kubelka-Munk (K-M) theory, and the DRS data were used, as shown in equation 4.7b. This equation shows a direct relationship between Kubelka–Munk function F(R) and absorption coefficient (α) (Almessiere *et al*., 2019).

$$F(R_\infty) = \frac{(1-R_\infty)^2}{2R} = \frac{K}{S} = \frac{2.303\epsilon C}{S} = \alpha \tag{4.8}$$

where R = reflectance and depends on the Kubelka–Munk function, $F(R_\infty)$ = ratio between absorption coefficient (K), and S = scattering coefficient, ∞ = thickness of the layer created by nanocrystals in the sample holder of the spectrometer.

The energy band gap (E_g) estimated by applying Cody model which based on a constant dipole matrix approximation and a different expression for the absorption coefficient (equation 4.9) was used to identified the effect of doped lanthanum ion (Raciti *et al*., 2017). The obtained band gap energy (E_g) provides another relation between α and E_g (Nguyen *et al.*, 2019).

$$\alpha(h\nu)h\nu)^{\frac{1}{n}} = B(h\nu - Eg) \tag{4.9}$$

where: A = a proportionality constant (A = 4πk/λ); k = the absorption index or absorbance), α = the absorption coefficient, and hν = the photon energy.

The power n specifies the transition of electrons. Hence, depending upon the type of electronic transition, the value of n could be 1/2, 2, and 3 for direct allowed, indirect allowed, and indirect forbidden, respectively (Patil *et al*., 2017; Rashmi *et al*., 2017; Tatarchuk *et al*., 2017). In this work, the best linear fit was observed for n = 1/2, which was assigned for direct allowed transition (Figure 4.7b).

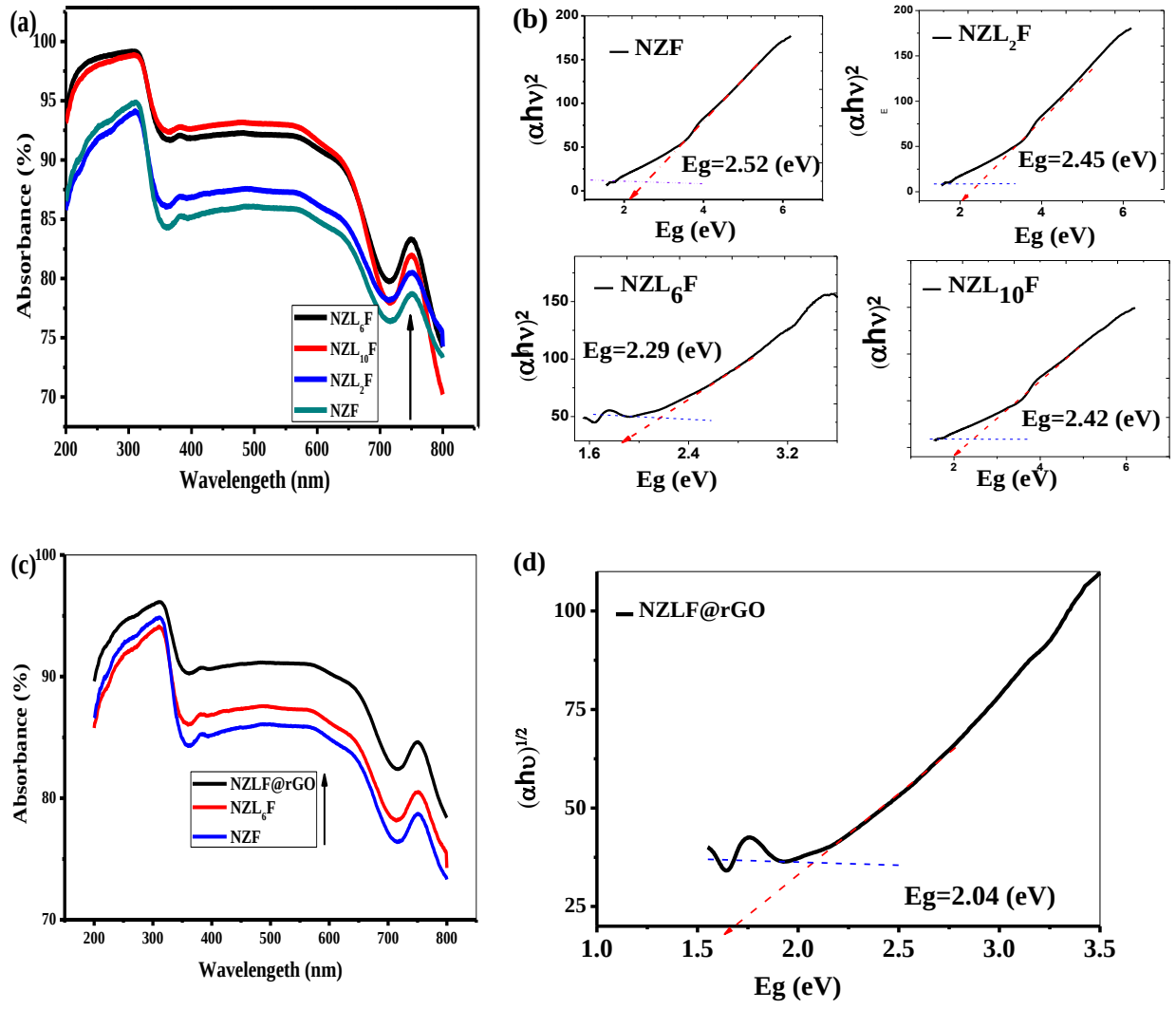

Figure 4.7: Absorbance spectra (a) and their respective optical band gap (b) for $Ni_{0.75}Zn_{0.25}La_xFe_{2-x}O_4$ (x=0.00, 0.02, 0.06 & 0.1); the percentage absorbance spectra (c) and their respective Cody plot (d) for NZL_6F@rGO NCs).

As a result, the direct E_g value for $Ni_{0.75}Zn_{0.25}La_xFe_{2-x}O_4$ (x=0.00, 0.02, 0.06, and 0.1) were extracted through the intersection between the base line and the linear fit of $(\alpha/h\nu)^2$ determined by extrapolating a straight line segment of Cody plot to $(\alpha h\nu)^2 = 0$ (Almessiere *et al*., 2019). The respective plots are illustrated in Figure 4.7b. This procedure is commonly used to characterize the semiconductors (Tatarchuk *et al*., 2017). The Cody plot obtained the band gap energy values of NZF, NZL_2F, NZL_6F, and $NZL_{10}F$ were obtained. The band gap can be tuned based on several factors: crystallite, size, structural parameters, and impurities (Mansour *et al*., 2021). The calculated E_g values of NZLF nano ferrites are illustrated in Figure 4.7b. The entire band gap values lie in the visible region (i.e., < 3.0 eV) and enable the absorption of photons of light in the visible spectrum and closely agree with the previously reported studies (Lemziouka *et al.*, 2020).

The energy gap possesses a peculiar behavior: a red shift from 2.06 eV to 1.84 eV (for $0.0 \leq x \leq 0.06$) and a blue shift $x \geq 0.1$). Two scenarios can explain this behavior. First, La content generates many donor levels in the forbidden band, producing E_g decrement (Aslam *et al*., 2021). Second, the increment of E_g can be understood by considering the Burstein-Moss effect, linked to the increase of charge carriers concentration, which blocks the lowest conduction band states (Burstein-Moss effect), and then transitions can occur only toward higher energy states (Aslam *et al.*, 2021)Also, the conductivity increment of NZF nano ferrites with further La^{3+} doping confirms the E_g behavior in that range.

Figure 4.7c shows the UV-visible absorption spectra of NZF, NZL_6F NPs, and NZLF@rGO explored by the percent of absorbance measurements and Tucks plot for the composite samples. All the synthesized samples have a characteristic percentage of absorption bands around 200 to 650 nm. As compared to the pristine NZF ferrites and NZL_6F spin ferrites, NZLF@rGO NCs have higher absorption potential in the visible range of light with a noticeable red shift in the absorption edge to the near-infrared range (Irfan *et al.* 2017).

As illustrated in Figure 4.7d, the band gap energy for NZF, NZL_6F, and NZLF@rGO was calculated by extrapolating a straight line segment of the Cody plot ($\alpha h\nu = 0$) (Lemziouka, *et al.*, 2020; Naik *et al.*, 2018). The figure illustrates that NZLF@rGO NCs have smaller band gaps with a broad light absorption range. Such band narrowing and enhancement in absorption in the visible region attributed to the integration of two-dimensional graphene sheets in NZLF@rGO NCs (Javed *et al*., 2019). Although the leading role of rGO is to inhibit the recombination of the photogenerated

electron-hole pairs, it also causes the narrowing of the band gap and increases the visible range of absorption bands (Javed *et al*., 2019).

4.2.5 Photoluminescence (PL) analysis

The PL analysis was carried out to investigate the photogenerated electron-hole (e^--h^+) pair entrapment, migration, and recombination rates at the surface of the semiconductor photocatalyst. Figure 4.8a illustrates that the PL spectra of $Ni_{0.75}Zn_{0.25}La_xFe_{2-x}O_4$ (x=0.00, 0.02, 0.06, and 0.1) were analyzed at the excitation wavelength of 370 nm. Subsequent electronic emissions were noticed between 400 and 600 nm at room temperature. All the synthesized samples have three peaks at 426, 480, and 512 nm assigned to the transition from the $3d^5$ state to the $3d^4\,4s^1$ state of Fe^{3+}, zinc defect, and oxygen defect, respectively (Debnath *et al*., 2020).

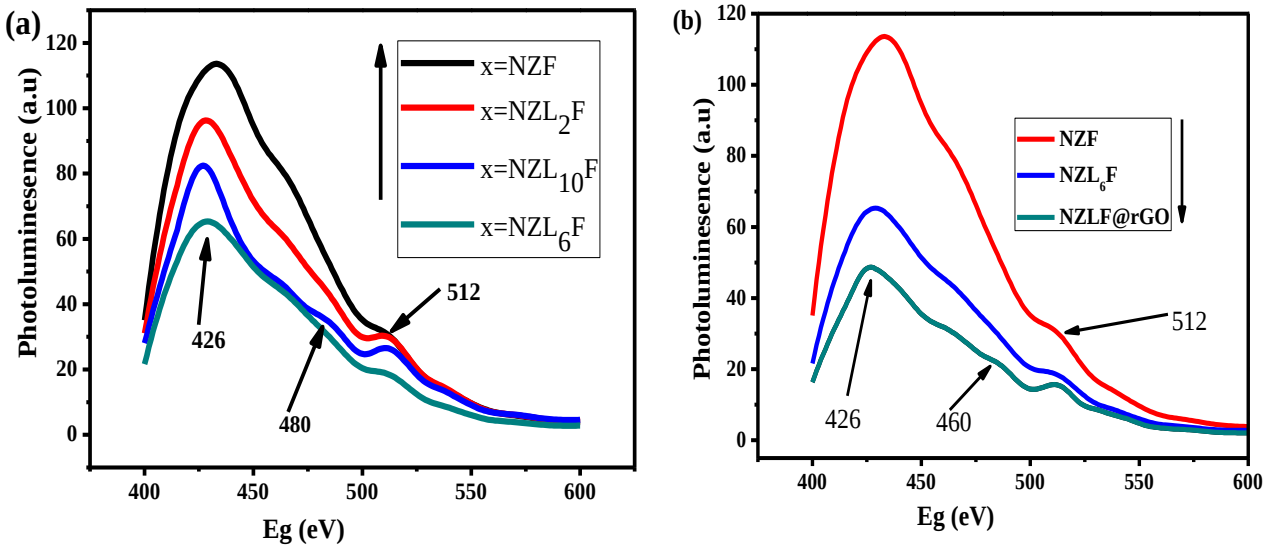

Figure 4.8: Photoluminescence spectra of $Ni_{0.75}Zn_{0.25}La_xFe_{2-x}O_4$ (a) and NZLF@rGO. (b) at the excitation wavelength of 370 nm

It is well-known that the peak intensity of PL emission spectra is directly related to the recombination rate of photo-generated electron-hole pair (Ahmed *et al*., 2021). The weaker PL emission intensity manifested a slow rate of electron-hole recombination (Chen, *et al*, 2017; Alam, 2018; Khan *et al*., 2019). This suppression of the recombination of photogenerated electrons and holes is one of the underlying causes of the materials' outstanding photocatalytic performance toward the mineralization of pollutants. The pristine nickel-zinc spinel ferrite NPs exhibited prominent emission intensity at 426 nm, which indicates the rapid recombination rate of the

photogenerated charge carriers. While the doping of La^{3+} ions, the intensity of emission peaks tends to be reduced, attributed to the formation of additional band edges, which leads to a delay in the recombination rate of the photo-generated electron-hole pairs. Among the doped ferrite samples, the La^{3+} ions at the concentration of 6% have low emission intensity, indicating a slow recombination rate.

Figure 4.8b illustrates that the PL spectra of NZF, NZLF, and NZLF@rGO NCs, analyzed at the excitation wavelength of 370 nm, subsequent electronic emissions were observed between 400 and 600 nm at room temperature. Since the peak intensity of PL emission spectra is directly related to the recombination rate (Ahmed *et al*., 2021), the weaker PL emission intensity manifested a slow electron-hole recombination rate for stronger emission vise-versa is true (Chen *et al.*, 2017; Alam, 2018; Khan *et al.*, 2019). As seen in Figure 4.8b, the intensity of the emission peaks becomes reduced when doped with La^{3+} ions. Also, a significant reduction in the intensity of PL was observed with the introduction of rGO, which is due to the suppression of the recombination rate of photogenerated charge carriers (Ahmed *et al*., 2021). This is evident as rGO plays a crucial role in increasing the life span of excited electrons, which enhances the photocatalytic performance of La^{3+} ion-doped NZF NPs (Khan *et al.*, 2019).

4.2.6 SEM-EDX analysis

The surface morphology and compositional analysis of NZF, NZL_6F, and NZLF@rGO samples were analyzed from SEM micrographs and EDX, as illustrated in Figure 4.9. The SEM micrographs of NZF and NZL_6F samples [Figure 4.9(a, b)] show an agglomerated porous-like structure characteristic of the sol-gel combustion method. During the sol-gel combustion synthesis, large volumes of gases are released, which cause pores and voids in the samples and affirm the formation of porous structured materials (Dubey, *et al.* 2018). Furthermore, with the doping of La^{3+} ions, the NZL_6F samples show the formation of spherical grain-like morphology with less agglomeration. Their high surface energy, strong intrinsic magnetic interactions (Li *et al*., 2019 ; Raje *et al.*, 2021), the existence of a secondary phase ($LaFeO_3$) is responsible for the formation of agglomeration. (Rashmi *et al*., 2017; Mansour *et al*., 2021)

Figure 4.9c illustrates that NZL_6F nanoparticles have a good dispersion of spherical-shaped nanoparticles on a graphene sheet with slight agglomeration (Javed *et al*., 2019). The formation of Fe-O-C bonds between $Ni_{0.75}Zn_{0.25}La_{0.06}Fe_{1.94}O_4$ nanoparticles and graphene is responsible for

forming this slight agglomeration (Rahman *et al.*, 2020). In general, the SEM micrographs of $Ni_{0.75}Zn_{0.25}La_{0.06}Fe_{1.94}O_4$@rGO NCs confirmed the successful formation of a La^{3+} ion-doped NZF nanocomposite of ferrite with rGO.

The EDX spectra of NZF, NZL_6F NPs, and NZLF@rGO NCs recorded in the 0-10 keV binding energy range are illustrated in Figure 4.9(d-f). As seen in the figure, the emission peaks for Ni, Zn, Fe, La, O, and C are prominent (Ateia *et al.*, 2020). These results indicate the successful incorporation of La^{3+} ions into NZF ferrite and the formation of the desired nanocomposite. The EDX results also reveal the formation of the pure sample without any impurities during synthesis (Raje *et al.*, 2021). The intensity of the EDX peaks at different energies is related to their percentage composition.

The insets of Figure 4.9(d-f) provide information on the weight and atomic percentage of the elemental composition in the synthesized nanomaterials. With doping of La^{3+} ions, the intensity of Fe^{3+} peaks becomes reduced (Ateia *et al.*, 2020). This indicates that La^{3+} ions are successfully incorporated into the structure of NZF spinel ferrite. With the formation of the composite, the intensity of the O peak was found to increase, which also confirmed the presence of the principal element of the composite, O, in the desired proportion of the chemical composition (Rahman *et al.*, 2020; Raje *et al.*, 2021). The estimated weight percentage agrees with the starting stoichiometric ratio of the investigated samples.

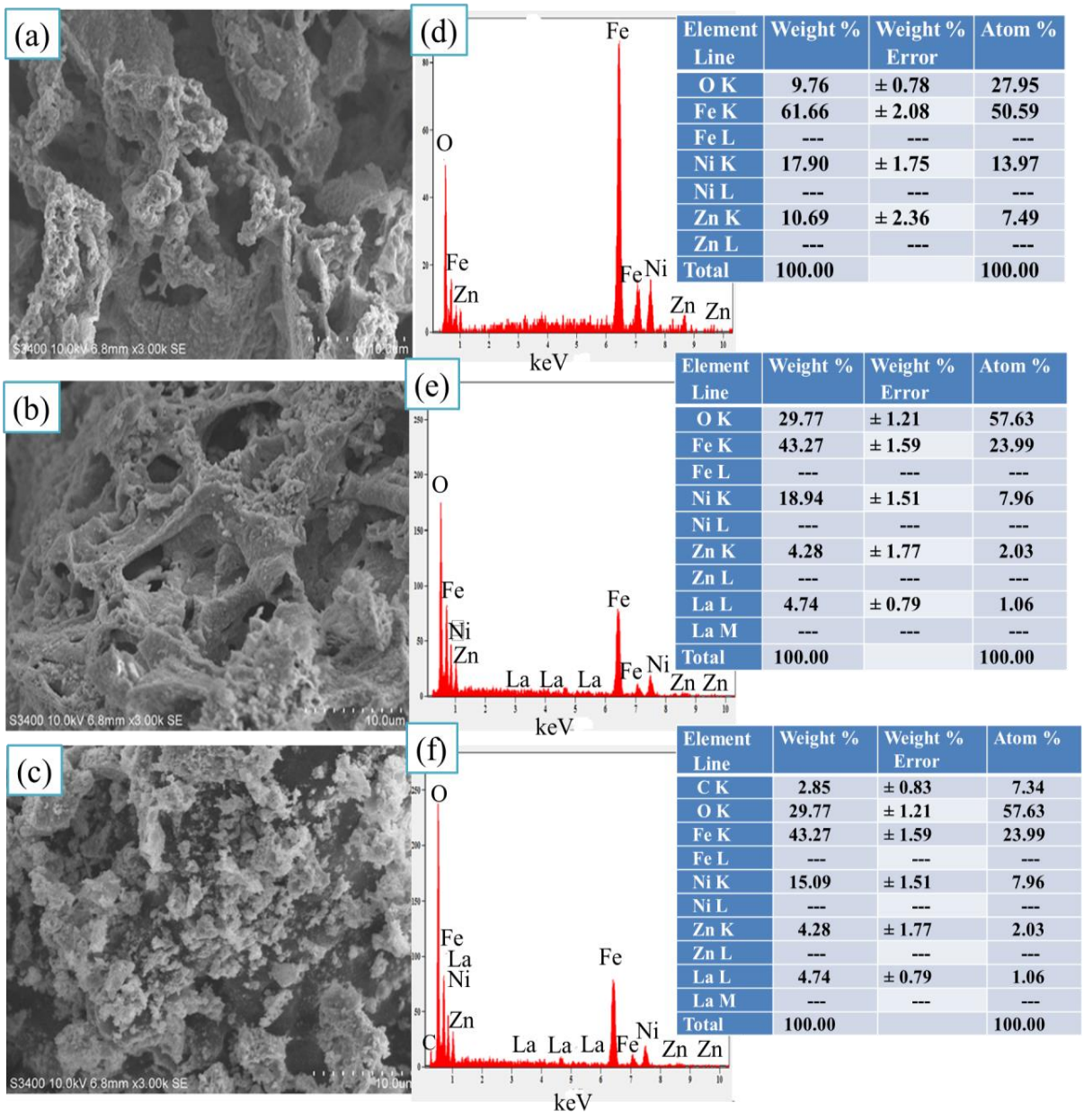

Element Line	Weight %	Weight % Error	Atom %
O K	9.76	± 0.78	27.95
Fe K	61.66	± 2.08	50.59
Fe L	---	---	---
Ni K	17.90	± 1.75	13.97
Ni L	---	---	---
Zn K	10.69	± 2.36	7.49
Zn L	---	---	---
Total	100.00		100.00

Element Line	Weight %	Weight % Error	Atom %
O K	29.77	± 1.21	57.63
Fe K	43.27	± 1.59	23.99
Fe L	---	---	---
Ni K	18.94	± 1.51	7.96
Ni L	---	---	---
Zn K	4.28	± 1.77	2.03
Zn L	---	---	---
La L	4.74	± 0.79	1.06
La M	---	---	---
Total	100.00		100.00

Element Line	Weight %	Weight % Error	Atom %
C K	2.85	± 0.83	7.34
O K	29.77	± 1.21	57.63
Fe K	43.27	± 1.59	23.99
Fe L	---	---	---
Ni K	15.09	± 1.51	7.96
Ni L	---	---	---
Zn K	4.28	± 1.77	2.03
Zn L	---	---	---
La L	4.74	± 0.79	1.06
La M	---	---	---
Total	100.00		100.00

Figure 4.9: SEM images of (a) $Ni_{0.75}Zn_{0.25}Fe_2O_4$; (b) $Ni_{0.75}Zn_{0.25}La_{0.06}Fe_{1.94}O_4$ and (c) $Ni_{0.75}Zn_{0.25}La_{0.06}Fe_{1.94}O_4$@rGO NCs at magnification of 5000X: (d-f) respective EDX spectra

4.2.7 TEM, HRTEM and SAED analysis

Figure 4.10 illustrates the images of TEM, HRTEM, and SAED for $Ni_{0.75}Zn_{0.25}La_{0.06}Fe_{1.94}O_4$ NPs and $Ni_{0.75}Zn_{0.25}La_{0.06}Fe_{1.94}O_4$@rGO NCs. The TEM images of the samples revealed the spherical and crystalline morphology of the nanoparticles (Raje *et al.*, 2021). The assembled spheres showed that the produced particles had a strong connection, dispensability, and homogeneity, with

some aggregation (Dasan *et al*., 2017). The average particle size of the as-prepared sample determined using image J software was 36 nm, which agrees with the XRD analysis (Raje *et al*., 2021).

The HR-TEM image illustrated in Figure 4.10b displays the polycrystalline structure of NZL_6F NPs and the lattice fringes with interplanar spacing of 0.44 nm corresponding to (111) atomic plane of cubic spinel crystal structure of the NZLF NPs (Dasan *et al.,* 2017; Li *et al.*, 2019). The presence of this lattice also confirmed the successful formation of spinel crystals. The inset of Figure 4.10b illustrates the inverse fast Fourier transmission (IFFT) pattern of NZLF, which confirms the polycrystalline nature of synthesized nanoparticles (NZLF) (Raje *et al*., 2021).

The selected area of electron diffraction patterns (SAED) of La^{3+} ion doped nickel-zinc spinel ferrite illustrated in Figure 4.10c exhibited the formation of isolated diffraction rings. The diffraction rings of the plane; (111), (220), (311), (222), (511), and (440) are permitted planes of face-centered cubic structured spinel ferrite (Dasan *et al.,* 2017; Pawar *et al*., 2020). Similarly, the pattern shows a bright, intense ring of (311) plane consistent with the intense peaks depicted in the XRD pattern, as illustrated in Figure 4.7, confirming the creation of a spinel ferrite sample (Pawar *et al.*, 2020). The white circular spots in the center of the SAED pattern also confirm the polycrystallinity of the sample (Dasan *et al.*, 2017). Moreover, the spots that are visible outside of the ring correspond to small amounts of $LaFe_2O_3$ (Raje *et al*., 2021).

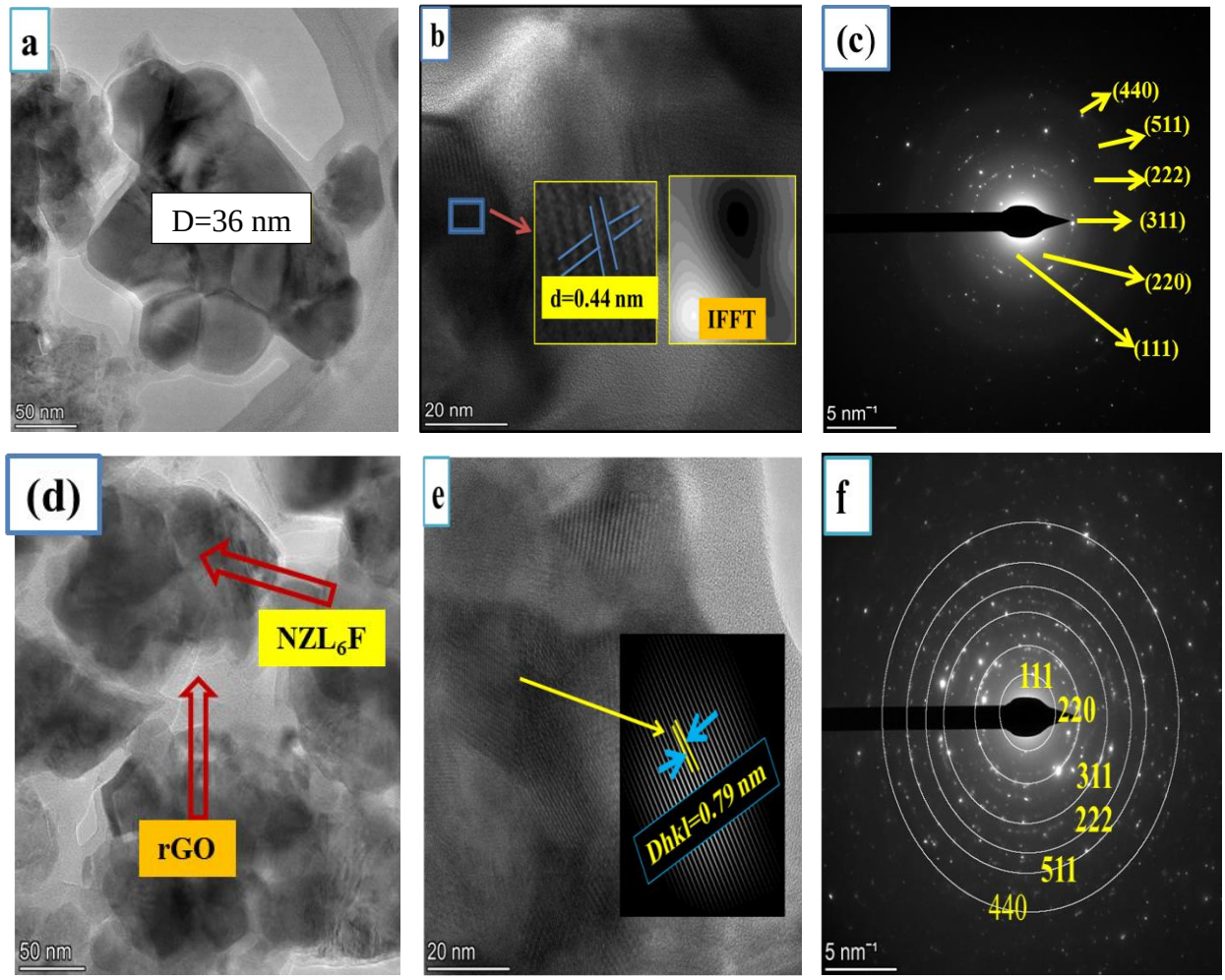

Figure 4.10: (a) TEM images; (b) HR-TEM image of calcined NZL_6F; (c) selected-area electron diffraction; (b) inset is the magnified lattice fringes with d-spacing of 0.44 nm and IFFT pattern, and (d, f) TEM image, HR-TEM image and SAED of NZL_6F@rGO respectively. The inset in (e) shows the magnified lattice fringes with a d-spacing of 0.79 nm.

Figure 4.10d illustrates the TEM image of lanthanum-doped NZF spinel ferrite and its composite with rGO (NZLF@rGO). As seen in the figure, the crumpled and translucent sheet-like structure of rGO is widely disseminated as free sheets due to deformation during exfoliation (Li *et al.*, 2019). NZL_6F NPs were found to have a spherical structure that overlaid the erratic black La^{3+} particles heterogeneously distributed with aggregation on the rGO sheets (Shahid *et al.*, 2020). In the HRTEM image of the synthesized nanocomposite (Figure 4.10e), the interplanar distance was found to be 0.79 nm, calculated from the profile of inverse fast Fourier transmission (IFFT) pattern using Image J software (inset of Figure 4.10e*).* Moreover, the HRTEM image and SAED pattern

of NZLF@rGO NCs in Figure 4.10(e, f) show the polycrystallinity of the composite and the existence of NZL_6F ferrite NPs and rGO in the composite (Shahid *et al.*, 2020).

4.2.8 X-ray Photoelectron Spectroscopy (XPS) analysis

The surface composition and corresponding valance states of the elements present on $Ni_{0.75}Zn_{0.25}La_{0.06}Fe_{1.94}O_4$@rGO nanocomposite were characterized by XPS spectroscopy, as illustrated in Figure 4.11. As revealed in the XPS survey spectrum in Figure 4.11a, the NZLF@rGO nanocomposite is composed of Ni, Zn, La, Fe, O, and C elements (Ganie *et al*., 2021). The XPS profile of La 3d in the range of 830 to 870 eV is separated into two central pairs of peaks, revealing the binding energy of La $3d_{3/2}$ and La $3d_{5/2,}$ which indicates the presence of La^{3+} ions in the nanocomposite (Jun *et al.*, 2020), (Figure 4.11b). The deconvoluted Ni 2p spectrum (Figure 4.11c) comprising two major peaks at 854 eV and 872 eV, assigned to Ni 2p3/2 and Ni 2p1/2, respectively, while the $Ni^{2+\cdot}$ satellite peaks at 861.3 eV and 878 eV are for Ni^{2+} $2p_{3/2}$ and Ni^{2+} $2p_{1/2,}$ respectively (Ganie *et al*., 2021).

Figure 4.11d illustrates the spectrum of Zn 2p with two peaks with binding energies of 1021.48 eV and 1044.29 eV, assigned to Zn 2p3/2 and 2p1/2 respectively, deciding the existence of Zn^{2+} ions in the composite (Ganie. Similarly, the Fe 2p deconvoluted spectrum (Figure 4.11e) showed two prominent peaks with binding energies of 710.7 eV and 724.3 eV, ascribed to Fe 2p3/2 and Fe 2p1/2, respectively. This indicates the presence of Fe^{3+} ions in the nanocomposite (Rather *et al.*, 2021). Besides that, the Fe $2p_{3/2}$ spectrum of nanocomposite has two peaks with binding energies of 710.3 eV and 712.5 eV assigned to Fe^{3+} (B-site) and Fe^{3+} (A-site). The peak at 718.2 eV corresponds to the satellite peak of Fe 2p1/2 (Ganie *et al*., 2021)Figure 4.11f illustrates the spectrum of C 1s in wide, with three peaks at binding energies of 284.7 eV, 285.7 eV, and 289 eV corresponding to the graphitic C-C, C=O, and C-C=O conforming that carboxylic groups were still present in the rGO (Ganie, Bano, et al., 2021) and responsible as the host material received the guest ferrite nanoparticles. The XPS spectrum of O 1s (Figure 4.11g) reveals two peaks, the first at 530 eV, which corresponds to the presence of metal-oxide lattice in the composite (Ganie et al., 2021), and the second at 531.5 eV may be related to the surface adsorbed oxygen (Rather *et al.*, 2021). Overall, the XPS analysis confirmed the existence of all the respective elements and their ionic states, which agrees with the EDS analysis.

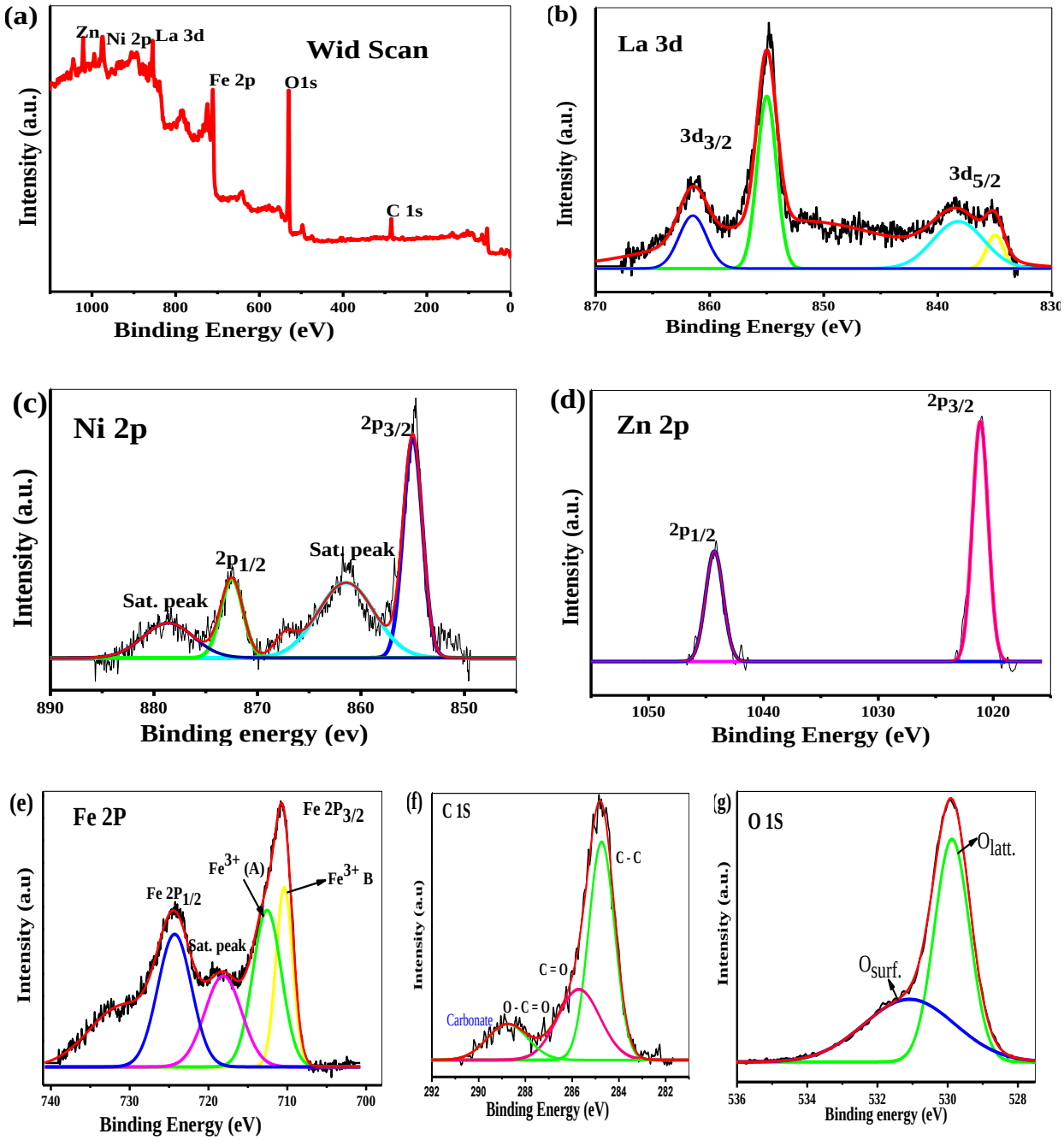

Figure 4.11: (a) Survey scan and high-resolution XPS profiles of: (b) La 3d; (c) Ni 2p; (d) ZN 2p; (e) Fe 2p; (f) C 1s; (g) O 1s of $Ni_{0.75}Zn_{0.25}La_{0.06}Fe_{1.94}O_4$@rGO nanocomposite.

4.2.9 BET analysis

The information related to the specific surface area, meso/macroscopic appearance, and nature of the nano-scale pores is vital in determining the surface properties of the nanoscale materials (Somvanshi *et al*., 2020). For this purpose, the 'Brunauer-Emmett-Teller' technique, abbreviated

BET, is useful. Thus, in the present study, the BET isotherms were obtained for NZF, NZL_6F, and NZLF@rGO samples by physisorption of N_2. The different surface parameters, such as BET surface area, volume of the pores, average pore radius, etc., were estimated using this physisorption. As illustrated in Figure 4.12, the BET spectra of all the samples displayed a type IV isotherm, which is believed to be a typical trait of mesoporous structures (Fouad et al., 2014). This indicated the involvement of four different nitrogen adsorption-desorption stages, including a regular upsurge of N_2 adsorption at lower relative pressure (P/P_o), a pace at transitional P/P_o corresponds to capillary condensation process within the mesopores, a plateau with a slight inclination at high P/P_o, due to multilayer adsorption on the surface of the nanocomposite and a sudden upsurge in N_2 adsorption at saturation value ($P/P_o = 1.0$) which corresponds to the filling of all existing pores (Rather *et al*., 2021).

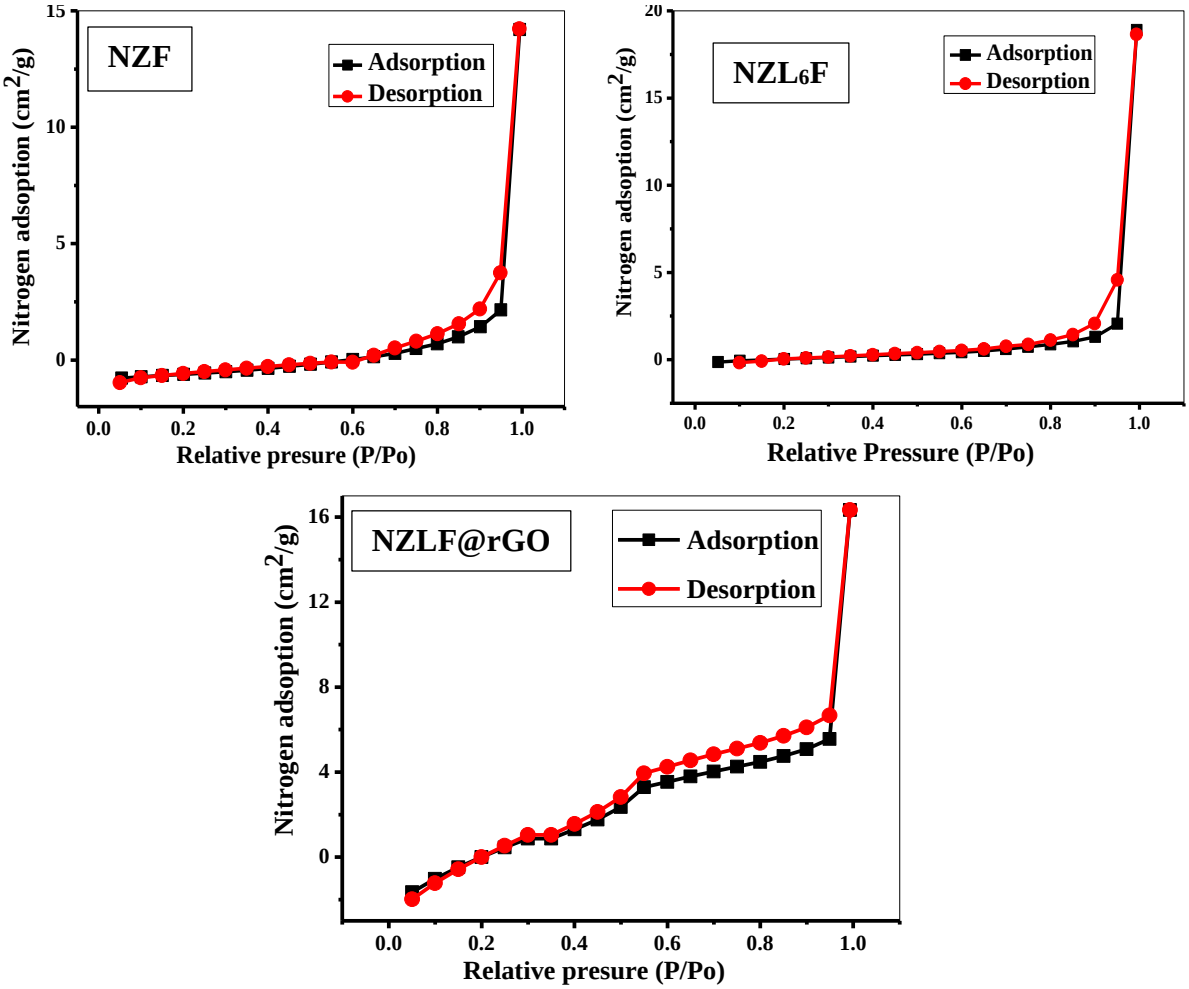

Figure 4.12: N_2 adsorption/desorption isotherm at 77K for $Ni_{0.75}Zn_{0.25}Fe_2O_4$, $Ni_{0.75}Zn_{0.25}La_{0.06}Fe_{1.94}O_4$ nanoparticles and $Ni_{0.75}Zn_{0.25}La_{0.06}Fe_{1.94}O_4$@rGO nanocomposites.

The parameters such as surface area, pore size, and pore volumes were calculated from the obtained BET data and depicted in Table 4.2. wherein it is seen that the NZLF@rGO nanocomposite has a larger surface area and smaller pore size distribution with higher pore volume than the bare NZF and La^{3+} doped NZF. Since the surface area is directly related to the degree of adsorption of organic pollutants on the surface of the catalyst and interfacial energy, the increase of BET leads to an enhancement in the nucleation rate (Fouad e*t al*., 2014). This revealed that the composite has more adsorption and reactive sites on its surface. It is evident that the composite has a more significant performance in conductivity and photocatalytic degradation of contaminants (Ahmed *et al.*, 2021)Moreover, it was found that the average pore volume value increases from 0.024 cc/g to 0.035 cc/g with the doping of La^{3+} ions in NZF ferrites and the formation of a composite with rGO. This increase in average pore volume is apparent as the average pore radius increased with La^{3+} ion doping and the introduction of rGO.

Table 4.2: BET surface area, pore size, and pore volume of $Ni_{0.75}Zn_{0.25}La_{0.06}Fe_{1.94}O_4$ nanoparticles and $Ni_{0.75}Zn_{0.25}La_{0.06}Fe_{1.94}O_4$@rGO nanocomposite.

Sample	**BET surface area (m^2/g)**	**Pore size (nm)**	**Pore volume (cc/g)**
$Ni_{0.75}Zn_{0.25}Fe_2O_4$	2.410	1.7078	0.024
$Ni_{0.75}Zn_{0.25}La_{0.06}Fe_{1.94}O_4$	2.620	1.5278	0.029
$Ni_{0.75}Zn_{0.25}La_{0.06}Fe_{1.94}O_4$@rGO	5.449	1.5272	0.035

4.3. Characterization of Eu^{3+} Ion Doped NZF Spinel Ferrite NPs and $Ni_{0.75}Zn_{0.25}Eu_{0.06}Fe_{1.94}O_4$@rGO NCs

4.3.1. FTIR analysis

The spinel phase formation of Eu^{3+} ions doped $Ni_{0.75}Zn_{0.25}Fe_2O_4$ NPs were characterized by FTIR techniques. The FTIR spectra of $Ni_{0.75}Zn_{0.25}Eu_xFe_{2-x}O_4$ (x=0.00, 0.02, 0.06, and 0.1) samples were analyzed in the frequency range of 400-4000 cm^{-1} (Figure 4.13). The FTIR spectra of synthesized samples contained two characteristic absorption bands in the 400-600 cm-1 range corresponding to stretching vibrations of metal-oxygen bonds at tetrahedral and octahedral sites of their crystal lattice denoted by the tetrahedral site (ν_1) and octahedral site (ν_2), respectively (Aslam *et al.*, 2021; Baig *et al.*, 2020). These are typical of a spinel structure and confirm the formation of cubic spinel

ferrite (Baig *et al*., 2020.). Since the Fe^{3+} ions enter the A-site, it leads to the variation in the bond length of Fe^{3+}-O^{2-} and the expansion of A and B sites (Patil *et al.*, 2017; Jacob *et al.*, 2018). Moreover, the shift in position and intensity of both bands is attributed to the formation of a new bond (Eu^{3+}-O^{2}) in the octahedral site (B-site), migration of ions, and variation of M-O bond length (Patil *et al*., 2017). The results found in FTIR analysis were strongly supports the XRD analysis.

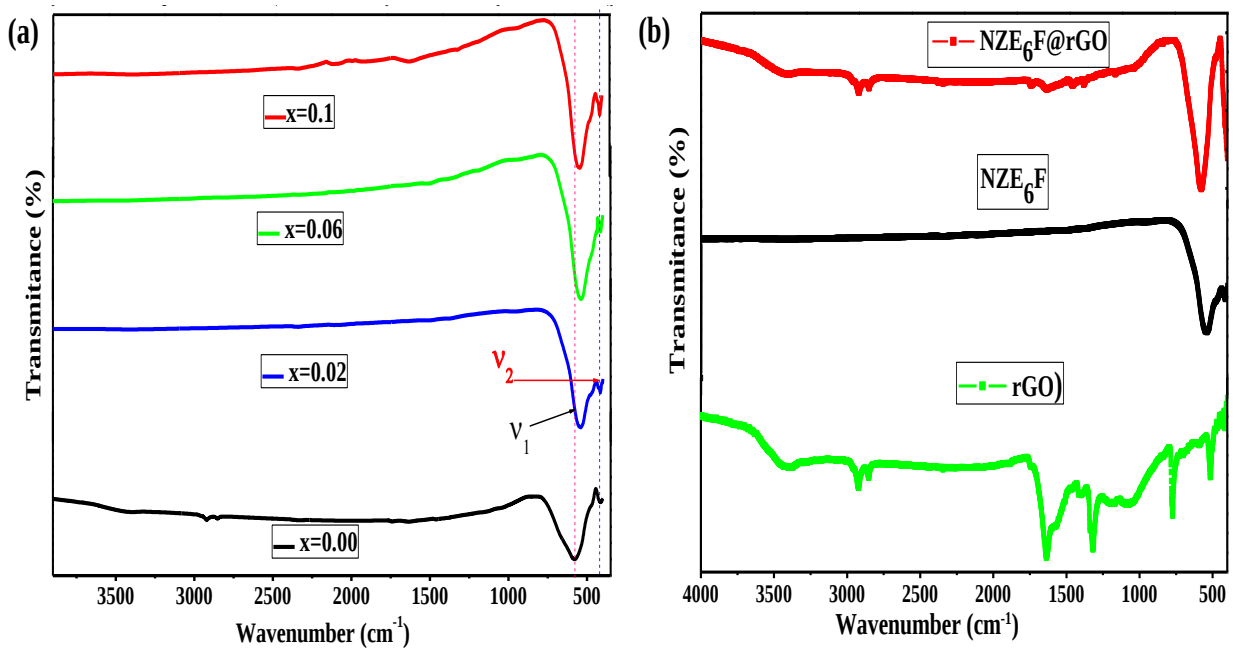

Figure 4.13: FTIR spectra of (a) $Ni_{0.75}Zn_{0.25}Eu_xFe_{2-x}O_4$ nanoparticles; and (b) rGO, $Ni_{0.75}Zn_{0.25}Eu_{0.06}Fe_{2-x}O_4$ and $Ni_{0.75}Zn_{0.25}Eu_{0.06}Fe_{2-x}O_4$@rGO.

Figure 4.13b illustrates the FTIR spectra of rGO, NZE_6F, and NZEF@rGO NC. The bands between 410 and 580 cm^{-1} correspond to the M–O bond in the ferrite structure of NZEF@rGO NCs. The bands at 1620 cm^{-1}, 2930 cm^{-1}, and 3432 cm^{-1} correspond to the functional groups C=C, CH_2, and O-H, respectively, in the spectrum of rGO. These bands are also present in the spectrum of the NZEF@rGO nanocomposite.

4.3.2 XRD analysis

Figure 4.14 illustrates the X-ray diffraction (XRD) patterns of $Ni_{0.75}Zn_{0.25}Eu_xFe_{2-x}O_4$ (x=0.00, 0.02, 0.06, and 0.1) obtained at a calcination temperature of 800 ℃ for 3 hours. At x = 0, all the reflection peaks are indexed as (111), (220), (311), (222), (400), (422), and (511) without any impurities (Hossain *et al*., 2018). This is the cubic phase of the spinel structure of NZF with the

Fd-3m space group (Patil *et al*., 2017). However, with the introduction of Eu^{3+} ions, the formation of a secondary phase (♠) and the change in the cubic structure from crystalline into an orthotropic structure were observed. This is caused by only a limited amount of Eu^{3+} ions (0.947 Å), which replace Fe^{3+} ions (0.67 Å) in the spinel lattice (Shahid *et al*., 2020). Therefore, after the solubility limits were reached, some of the Eu^{3+} ions accumulated on the grain boundaries and formed a secondary phase (♠) designated as Europium orthoferrite, ($EuFeO_3$) (Šoka *et al*., 2018; Phor *et al*., 2020). Furthermore, the change in position and broadening of the diffraction peaks with increasing concentration of Eu^{3+} ions induce lattice strain and lower the crystalline nature of the material (Shahid *et al*., 2020).

Various crystallographic structural parameters of Eu^{3+} ion doped NZF spinel ferrite are depicted in Table 4.3. The most intense peak (311) was used to calculate all the lattice parameters.

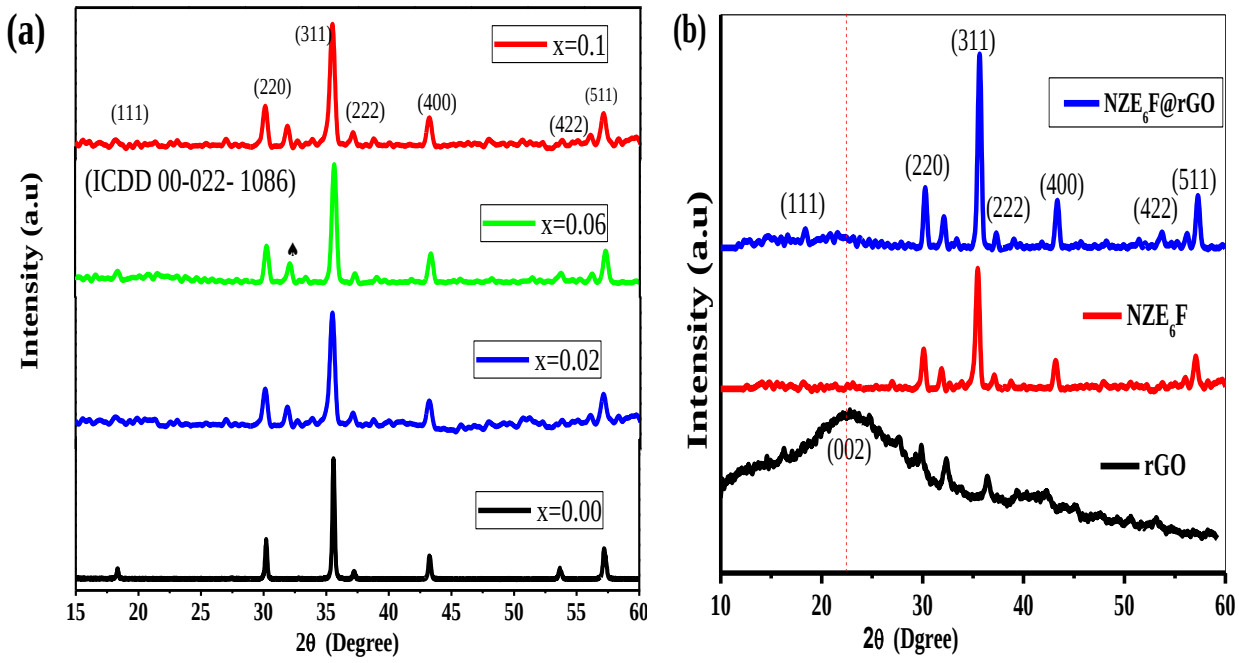

Figure 4.14: XRD patterns of (a) Eu^{3+} ion doped NZF spinel ferrite and; (b) rGO, $Ni_{0.75}Zn_{0.25}Eu_{0.06}Fe_{2-x}O_4$ and $Ni_{0.75}Zn_{0.25}Eu_{0.06}Fe_{2-x}O_4$@rGO nanocomposites.

The samples' average crystallite sizes were estimated using Scherrer's equation in Table 4.3. The table shows that the crystallite size varies with the doping of larger ionic radii of Eu^{3+} ions. This can be attributed to the strain in the lattice and the compression caused by the formation of a secondary phase ($EuFeO_3$), which affects the growth of grains (Šoka *et al*., 2018). Due to this

reason, the crystal sizes of $Ni_{0.75}Zn_{0.25}Eu_xFe_{2-x}O_4$ decrease with increasing content of Eu^{3+} ions (Mullai *et al*., 2012; Anwar *et al*., 2018).

The nanocomposite's lattice constant, ɑ, was also calculated using cell software using equation (4.2). As can be seen from Table 4.3, the lattice constant, *a,* increases with the doping of Eu^{3+} ions. This is attributed to the difference in ionic radii of Eu^{3+} ions and Fe^{3+}. The exchange of smaller Fe^{3+} ions (0.67 Å) in octahedral B-site by larger ionic radii of Eu^{3+} (0.947 Å) leads to the expansion of the unit cell and results in larger lattice constants (Wu *et al*., 2015; Dubey, *et al*., 2018; Lemziouka *et al*., 2020). But the further increase of Eu^{3+} ions concentration (x= 0.1) leads to a decrease in lattice constant because all Eu^{3+}ions may not occupy the lattice sites and may deposit onto grain boundaries to form a secondary phase, $EuFeO_3$, thereby causing lattice contraction (Wu *et al*., 2015; Dasan *et al*., 2017; Jacob *et al*., 2018).

Additional crystallographic parameters, including X-ray density (dx), unit cell volume (V_{cell}), surface area (S), and hopping length (L_A and L_B) of $Ni_{0.75}Zn_{0.25}Eu_xFe_{2-x}O_4$ (x=0.00, 0.02, 0.06, 0.1) were calculated using the equations 4.3-4.7. Table 4.3 shows a linear dependence of X-ray density on Eu^{3+} ion concentration. This variation in density is a direct consequence of the higher molecular weight of Eu than Fe^{3+} ion. It is worthwhile to mention the influence of large ionic radii on the hopping lengths of the spinel lattice.

Table 4.3: Crystallographic parameter for $Ni_{0.75}Zn_{0.25}Eu_xFe_{2-x}O_4$ (x=0.00, 0.02 0.06, and 0.10).

Samples	**2θ (Degree)**	**d (Å)**	**D (nm)**	**ɑ (Å)**	**ρ_x (g/Å^3)**	**SSA**	**L_A (Å)**	**L_B (Å)**
NZF	35.5945	2.5187	44.94	8.328	434	0.026	3.21	2.60
NZE_2F	35.6319	2.4276	38.27	7.450	435	0.034	3.22	2.63
NZE_6F	35.5966	2.4400	27.71	7.458	441	0.040	3.23	2.64
$NZE_{10}F$	35.6778	2.4245	21.41	7.439	452	0.050	3.22	2.62

As can be seen from the XRD pattern of $Ni_{0.75}Zn_{0.25}Eu_{0.06}Fe_{1.94}O_4$@rGO NCs in Figure 4.14b, all the diffraction peaks corresponding to the face-centered cubic structure of Ni0.75Zn0.25Fe2O4 nano ferrite appear stable in the composite. This revealed the presence of $Ni_{0.75}Zn_{0.25}Eu_{0.06}Fe_{1.94}O_4$ NPs without losing their crystal structure. The characteristic peaks of rGO (002) at a 2θ value of

22.5° were suppressed, indicating the destruction of the regular stacking of the rGO sheets due to the dispersion of nanoparticles over the surface of the graphene nanosheets (Rahman *et al*., 2020).

4.3.3 UV-Vis DRS analysis

Figure 4.15a illustrates the absorption spectra and Cody's plots for pristine NZF and NZF NPs doped with various concentrations of Eu^{3+} ions. The obtained absorbance spectra showed that the entire sample exhibited a broad absorption band in the visible range of light. Meanwhile, the absorption edge redshifts to a higher wavelength with the increased concentration of Eu^{3+} ions. This is because the doping of Eu^{3+} ions increases the concentration of free charges close to the conduction band, which leads to the absorption of more photons from the lower O 2p energy level to the higher Fe 3d energy level (Lemziouka *et al.*, 2020). These are the primary reasons for the increasing absorption edge with the concentration of Eu^{3+} ions. However, when the concentration of Eu^{3+} ions reaches ten mol%, the absorption band decreases and blue shifts to a lower wavelength.

The band gap energies of $Ni_{0.75}Zn_{0.25}Eu_xFe_{2-x}O_4$ were calculated from DRS data using the Cody's model and estimating the values by extrapolating the Cody plot to $(\alpha h\nu)^2=0$. As observed in Figure 4.15b, the band gap values lie in the visible region, i.e., < 3.0 eV, which enables absorption of the visible light photons in the spectrum. However, compared to the bare NZF nanoparticles, the band gap energies of NZEF decrease. This is because the electronic band structure of NZF ferrite is formed by overlapping of the orbitals between O-2p and Fe-3d energy levels (Patil *et al*., 2017). While in the case of Eu^{3+} ion doped NZF ferrite, the 4f doping energy levels of Eu are formed just below the conduction band of NZF (Patil *et al*., 2017), which causes a decrease in the band gap. Since the 4f doping energy levels of Eu^{3+} ions interact strongly with the valance O-2p orbitals, the electrons are transferred from Eu energy level to the conduction band of NZF (Fe-3d orbit) (Aslam *et al*., 2021; Patil *et al*., 2017; Rashmi *et al*., 2017). After reaching the maximum limits of Eu^{3+} ion doping, at x=0.1, excess charge carriers formed, which leads to blocking the lowest conduction band states of ferrite and causes the transitions only toward higher energy states (Aslam *et al*., 2021)From the above results, it can be predicted that the narrow band gap ferrite ($Ni_{0.75}Zn_{0.25}Eu_{0.06}Fe_{1.94}O_4$ = 2.30 eV) exhibits excellent electrochemical conductivities and photocatalytic applications under visible light irradiation.

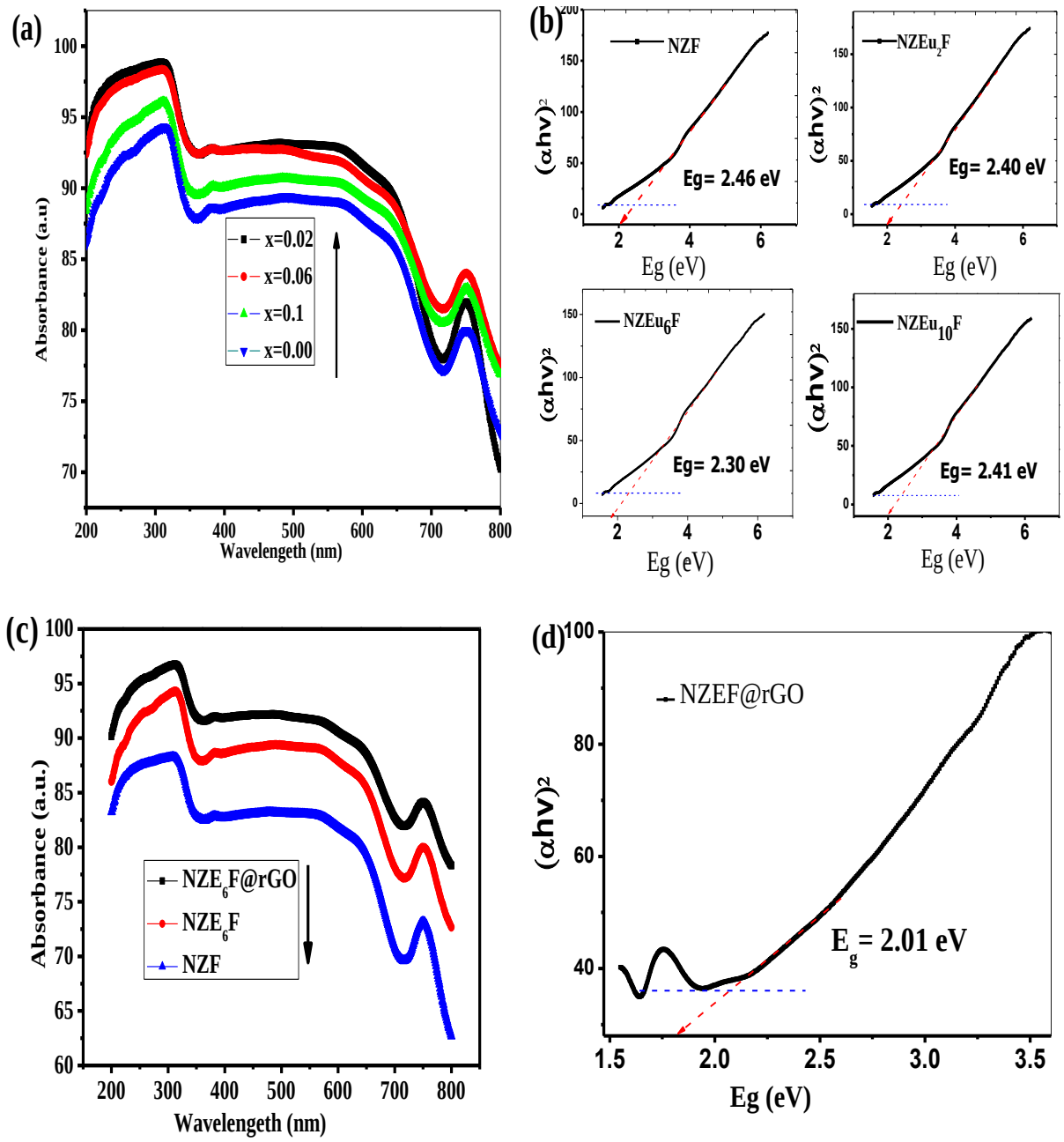

Figure 4.15: Absorbance spectra (a) and their respective optical band gap (b) for $Ni_{0.75}Zn_{0.25}Eu_xFe_{2-x}O_4$ (where: x=0.00, 0.02, 0.06 & 0.1); the percentage absorbance spectra (c) and their respective Cody plot (d) for NZE_6F@rGO NCs).

Figure 4.15c shows the diffusion reflectance spectra of $Ni_{0.75}Zn_{0.25}Fe_2O_4$, $Ni_{0.75}Zn_{0.25}Eu_{0.06}Fe_{1.94}O_{.4}$ nanoparticles, and $Ni_{0.75}Zn_{0.25}Eu_{0.06}Fe_{1.94}O_4$@rGO NCs. As shown in the Figure, the light absorption ranges of pristine $Ni_{0.75}Zn_{0.25}Eu_{0.06}Fe_{1.94}O_4$ were changed by doping Eu^{3+} ions. Meanwhile, introducing rGO enhanced relatively intense absorption, especially in the

visible region. This enhancement of light absorption is caused due to the background of rGO, which reduces the reflection of visible light (Liang *et al.*, 2018; Acharya, *et al*., 2023). Therefore, better utilization of visible light by the NZEF@rGO nanocomposite was expected, and it could exhibit outstanding photocatalytic applications under visible light irradiation.

The prepared sample's optical (direct) band gap energy value was obtained by plotting the linear part of the Cody's plot (Figure 4.15d). The results show that the band gap energy of Eu^{3+} ions doped NZF ferrite nanoparticles decreases by adding rGO. This decrease of band gap energy with the addition of rGO is caused by increasing the surface area of nanoparticles, the conduction rate of electrons, and the formation of a strong interaction between the Eu^{3+} ions doped nanoparticles and rGO (Mishra *et al.*, 2023). This also shows the ability of rGO to modify spinel ferrite for harvesting available visible light photons, which enhances the efficiency of visible-light-driven photocatalytic applications.

4.3.4 Photoluminescence (PL) analysis

The PL intensity is directly related to the recombination rate of the electron-hole pairs, i.e., weaker PL response leads to slow recombination of photogenerated charge carries (Alam, 2018). Figure 4.16a illustrates the PL spectra of the synthesized pristine and Eu^{3+} ion-doped NZF nano ferrite at an excitation wavelength of 370 nm. As illustrated in Figure 4.16, the PL spectra of the NZF sample had intense and broad emission intensity at 431 nm, which denotes the fast and direct recombination of the photon-exited charge carriers. Before doping of Eu^{3+} ions, there are three prominent peaks were observed at 409, 431, and 462 nm corresponding to near band edge (NBE), transitions from $3d^5$ stat to $3d^4$ $4s^1$ state of Fe^{3+} and interstitial zinc defect, respectively (Debnath, 2020). After the doping of Eu^{3+} ions, two additional emission peaks were observed at 486 nm and 523 nm, which are also related to the transition of the $3d^5$ state of Fe^{3+} ions to the 4f state of Eu^{3+} ions and O defect, respectively (Irfan *et al*., 2017).

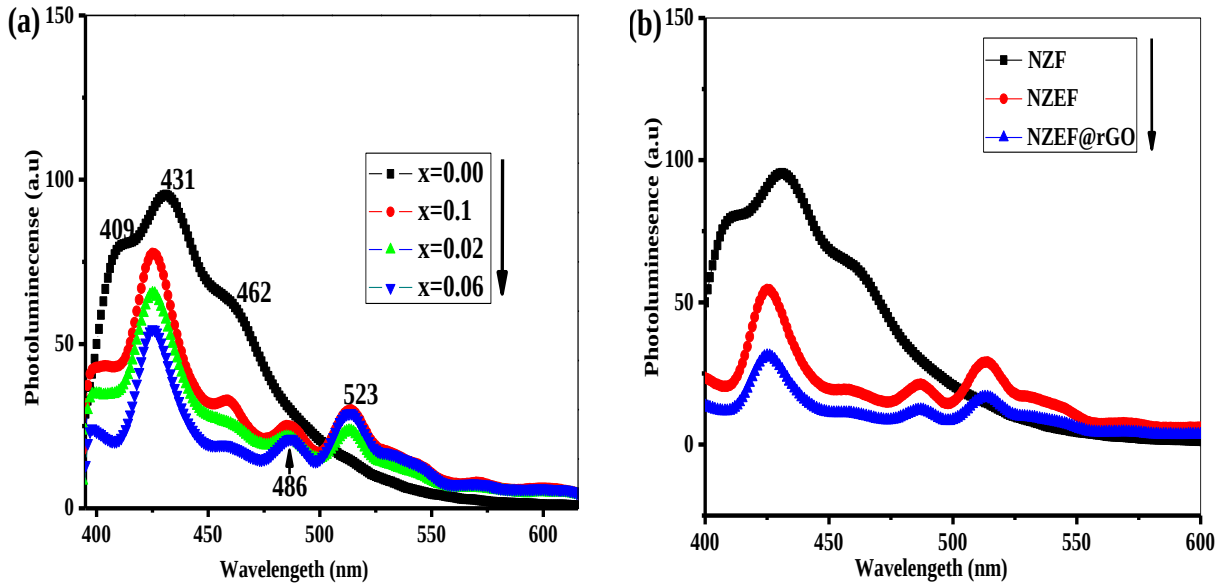

Figure 4.16: Photoluminescence spectra of (a) $Ni_{0.75}Zn_{0.25}Eu_xFe_{2-x}O_4$ and (b) the nanocomposite samples at an excitation wavelength of 370 nm.

The low emission intensity of Eu-doped NZF nanoparticles, especially at x=0.06, indicates that the doping of Eu^{3+} ions can capture the photo-induced charge carriers and slow the recombination rate of electrons-hole pairs (Khan, et al. 2019). Therefore, by doping Eu^{3+} ions at 6 mol%, $Ni_{0.75}Zn_{0.25}Eu_{0.06}Fe_{1.94}O_4$, the nanoparticles can perform better separation efficiency, which is directly related to the well-performing photocatalytic activity.

As illustrated in Figure 16b, the Eu^{3+} ion doped NZF ferrite (NZE_6F) and the nanocomposite sample (NZEF@rGO) showed emission peaks at similar wavelengths with decreasing intensity. However, in comparison with NZE_6F, the PL intensity of NZEF@rGO was more reduced. This reduction of PL intensity with the presence of rGO denotes the effective separation of the photo-induced electron-hole pairs. This is because rGO is a good electron accepter, which leads to diminishing the recombination rates of photo-induced charge carriers (Chen *et al*., 2017). Most often, the weak photoluminescence intensity is related to low charge carrier recombination, which exhibits high photocatalytic activity (Damian *et al*., 2013). As a result, the nanocomposite of Eu-doped NZF ferrite with rGO (NZEF@rGO) may be an excellent candidate for photocatalytic application under visible light irradiations.

4.3.5 SEM-EDX analysis

The surface morphology of NZF, NZE_6F, and NZEF@rGO samples was analyzed by scanning their surface, and NZEF@rGO samples were analyzed using SEM/EDX. Figure 4.17(a-c) illustrates the SEM micrographs of the samples. The morphology of the bare NZF spinel ferrite sample exhibits a porous-like spherical shape. However, the Eu^{3+} ion doped NZF spinel ferrite shows a stacked structure of grains with slight agglomeration (Debnath *et al.*, 2020). The strong intrinsic magnetic attraction and surface energy are responsible for the observed agglomeration of the nanoparticles (Li *et al.*, 2019a). The average size of these nanoparticles, $Ni_{0.75}Zn_{0.25}Eu_{0.06}Fe_{1.94}O_4$, as calculated using Image J software, ranged from 50 to 58 nm, which is slightly greater than the XRD results due to the formation of grain growth crystal structure.

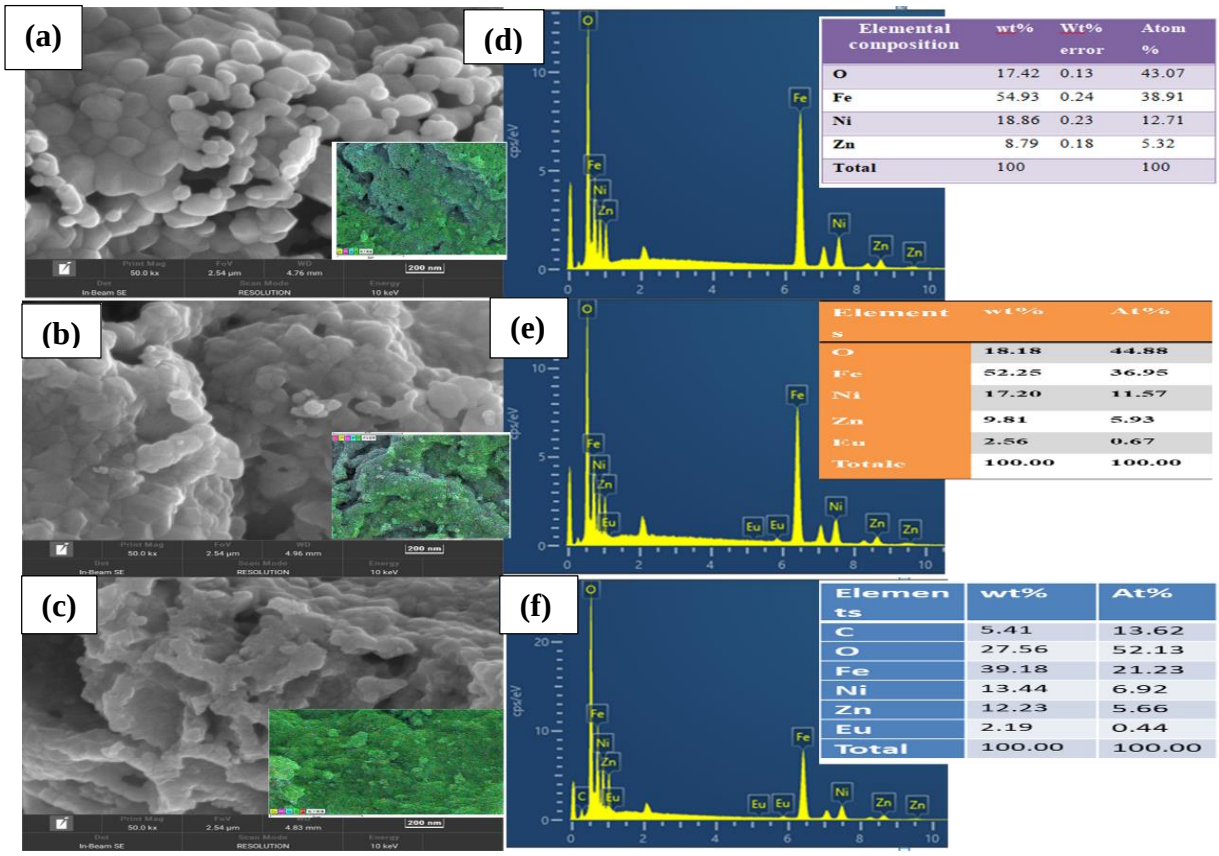

Figure 4.17: SEM images of (a) $Ni_{0.75}Zn_{0.25}Fe_2O_4$; (b) $Ni_{0.75}Zn_{0.25}Eu_{0.06}Fe_{1.94}O_4$ and (c) $Ni_{0.75}Zn_{0.25}Eu_{0.06}Fe_{1.94}O_4$@rGO nanocomposite at magnification of 5000X with insets showing the respective elemental mapping at magnification of 5000X: (d-f) depicts the EDX spectra and elemental composition of the samples.

As can be seen in the SEM image of NZEF@rGO nanocomposite (Figure 4.17c), $Ni_{0.75}Zn_{0.25}Eu_{0.06}Fe_{1.94}O_4$ nanoparticles act as a spacer that resists restacking of rGO and fully embedded into the wrinkled graphene nanosheet. This indicates the successful formation of a nanocomposite with decreasing agglomeration (Rashmi *et al.*, 2017). Figure 4.17(a-c) 's insets depict the elemental mapping of NZF, NZE_6F, and NZEF@rGO, respectively. The mapping of the samples showed a homogeneous distribution of Ni, Zn, Eu, Fe, C, and O elements (Mahdikhah *et al.*, 2020). Moreover, the elemental composition and purity of the nanocomposite samples analyzed by EDX, illustrated in Figure 4.17(d-f), showed the presence of only Ni, Zn, Eu, Fe, C, and O without any impurity. The results are consistent with the XRD and XPS results. The weight percentage of the elements is consistent with the stoichiometric atomic proportion and formation of the expected ferrite compositions (Debnath, 2020).

4.3.6 TEM, HR-TEM and SAED analysis

The morphology, particle size, and crystalline structure of $NZEu_6F$ and NZEuF@rGO using TEM, HR-TEM, and SAED are illustrated in Figure 4.18. The TEM image depicted in Figure 4.18a confirms the formation of spherical-shaped $NZEu_6F$ nanoparticles, which overlap with the irregular black particles of Eu (Tsvetkov *et al*., 2016). Using Image J software, an average particle size of 26 nm was obtained, consistent with the XRD results (Toksha *et al.*, 2011). Furthermore, the HRTEM image of $NZEu_6F$ illustrated in Figure 4.18b displays the formation of the ferrite's highly ordered polycrystalline lattice structure. The lattice fringes of $NZEu_6F$ with the d-spacing value of 0.26 nm are consistent with the lattice spacing value of basal (112) planes of the cubic spinel crystal obtained by XRD (Das *et al*., 2020).

As observed from Figure 4.18c, the selected area electron diffraction (SAED) pattern of $NZEu_6F$ contains a highly ordered sharp concentric ring with a bright spot arising from Bragg's reflection of an individual crystal over the ring. This indicates the polycrystalline nature of the synthesized nanoparticles (Debnath, 2020). The SAED pattern displayed a bright diffraction ring of the (311) plane, corresponding to the intense diffraction peak elucidated in the XRD pattern, indicating the formation of a spinel ferrite (Pawar *et al.*, 2020).

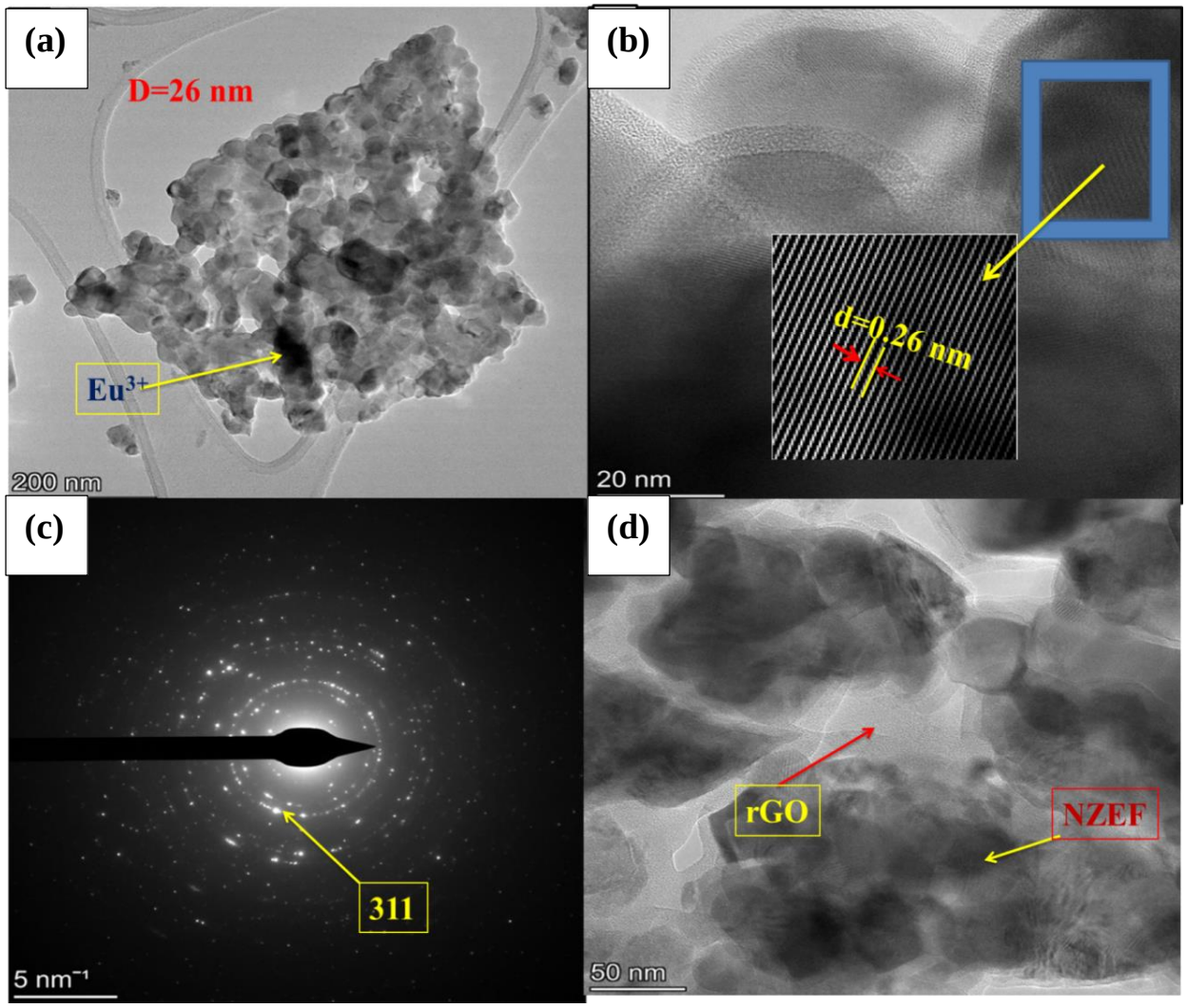

Figure 4.18: NZE_6F (a) TEM image; (b) HR-TEM image of sample calcined at 800 ℃ with inset the magnified lattice fringes having d-spacing of 0.44 nm and IFFT pattern; (c) SAED and (d) TEM image of NZEF@rGO.

The TEM image of NZEF@rGO nanocomposite [Figure 4.18(d)] illustrates that the spherical-shaped NZE_6F nanoparticles are evenly distributed with little agglomeration over the surface of wrinkled rGO nanosheets. The figure illustrates the high distribution of crumpled and transparent amorphous sheet-like structures of rGO formed due to exfoliation (Li *et al*., 2019). The dispersion of NZE_6F nanoparticles over the crumpled nanosheets of rGO prevented the restacking of rGO, while the strong interaction between nanoparticles and rGO also prevented the agglomeration of NZE_6F ferrite nanoparticles (Shahid *et al*., 2020). The results indicate that the high porosity

formation of the desired nanocomposite is effective for forming efficient photocatalytic and electroactive electrodes (Li *et al.*, 2019).

4.3.7 BET analysis

Surface area and porosity are the most essential characteristics of a semiconductor, which affect the conductivity, properties, and efficiency of the photocatalyst in the degradation of pollutants (Nasirian, 2006). Brunauer, Emmet Teller (BET) analysis is a preferred technique to determine the area of a solid. Figure 4.20a-c illustrates the N_2 adsorption-desorption isotherms of NZF, NZE_6F, and NZEF@rGO nanocomposites and their S_{BET}. The S_{BET} values for NZF, NZE_6F, and NZEF@rGO nanocomposites were 2.41, 2.51, and 4.47 m^2g^{-1}, respectively. The S_{BET} of NZF ferrite further increased with the doping of Eu^{3+} ions. The increasing trend in SBET with doping of Eu^{3+} ions is in good agreement with the decrement in average crystallite size determined by XRD, as it is well known that the smaller the crystallite size, the more the surface area (Somvanshi *et al.*, 2020). The SBET increased with the introduction of rGO in the nanocomposites. The increasing SBET of NZEF ferrite nanoparticles with the addition of rGO is related to the reduction of the degree of their agglomeration (Ahmed *et al.*, 2021). It is evident that a photocatalyst with a high SBET has a higher performance in the eradication of contaminants (Nasirian, 2006)As a result, the NZEF@rGO nanocomposite is anticipated to have better photocatalytic performance than pristine and Eu-doped NZF ferrite nanoparticles.

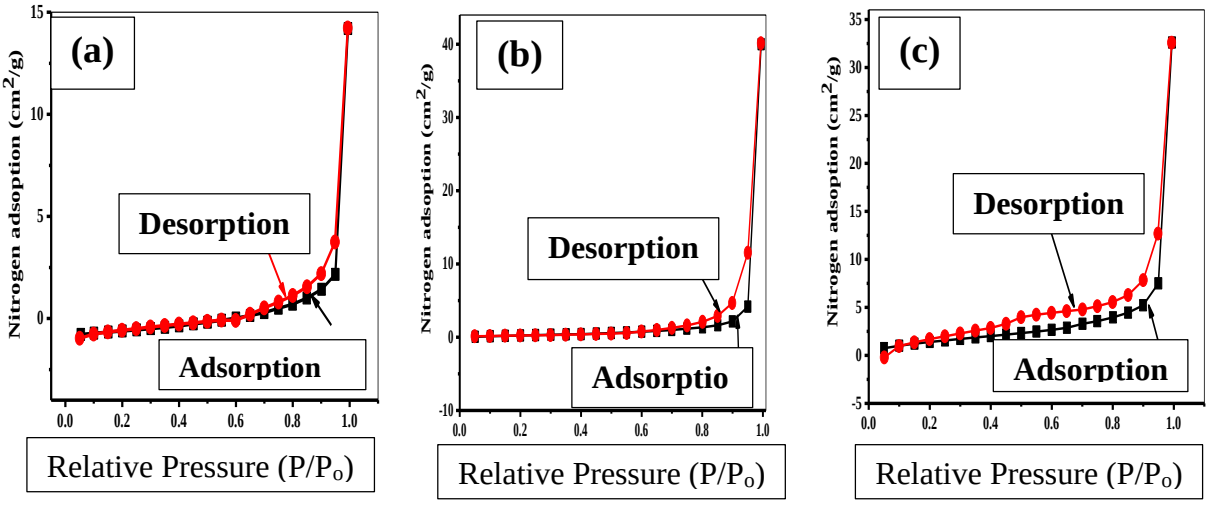

Figure 4.19: N_2 adsorption/desorption isotherm at 77K for $Ni_{0.75}Zn_{0.25}Eu_{0.06}Fe_{1.94}O_4$ (a), $Ni_{0.75}Zn_{0.25}Eu_{0.06}Fe_{1.94}O_4$ NPs (b), nanoparticles and $Ni_{0.75}Zn_{0.25}Eu_{0.06}Fe_{1.94}O_4$@rGO NCs (c).

4.3.8 XPS analysis

The elemental analysis of $Ni_{0.75}Zn_{0.25}Eu_{0.06}Fe_{1.94}O_4$@rGO nanocomposite is illustrated in Figure 4.19. Figure 4.20a illustrates that the XPS survey spectrum in wide scan shows the core photoionization peaks for C1s, O1s, Fe 2p, Ni 2p, Zn 2p, and Eu-3d at their corresponding binding energies (Ganie *et al.*, 2021) confirming the successful formation of the NZEF@rGO nanocomposite without the presence of any impurities. The deconvoluted spectrum of Eu-3d (Figure 4.20b) shows two prominent binding energy peaks at 1164.58 eV and 1134.73 eV, ascribed to Eu $3d_{3/2}$ and Eu $3d_{5/2}$ respectively, indicating Eu^{3+} ions in the composite (Jun et al., 2020).

The deconvoluted Ni 2p spectrum (Figure 4.20c) shows two significant peaks at 854 eV and 872 eV assigned to Ni $2p_{3/2}$ and Ni $2p_{1/2}$, respectively (Ganie *et al.*, 2021). Figure 4.20d illustrates the XPS spectrum of Zn 2p at 1,021.48 eV and 1,044.29 eV, which are the binding energies of Zn 2p3/2 and 2p1/2, respectively. Similarly, the Fe 2p deconvoluted spectrum (Figure 4.20e) illustrates two prominent binding energy peaks at 710.7 eV and 724.3 eV, ascribed to Fe $2p_{3/2}$ and Fe $2p_{1/2,}$ respectively, indicating Fe^{3+} ions in the composite (Mahdikhah *et al.,* 2020; Rather *et al.,* 2021). The C1s peak (Figure 4.20f) is characterized by a dominant C-C peak at 284.6 eV, signifying the restoration of sp2 carbon states in the graphene structure, and the C=O and O-C=O peaks at 286.3 eV and (give eV value), respectively (Ganie *et al*., 2021; Mahdikhah *et al*., 2020). The XPS spectra of O1s (Figure 4.20g) peak at 530 eV is deconvoluted into two main components of the binding energy 529.86 eV and 531.01 eV, which are attributed to the M-O-M and C-O bonds, respectively (Mahdikhah *et al.*, 2020). The results confirm that the NZEF@rGO NCs sample contains all the respective elements with their ionic states without impurities, supporting the XRD and EDX elemental mapping analysis results.

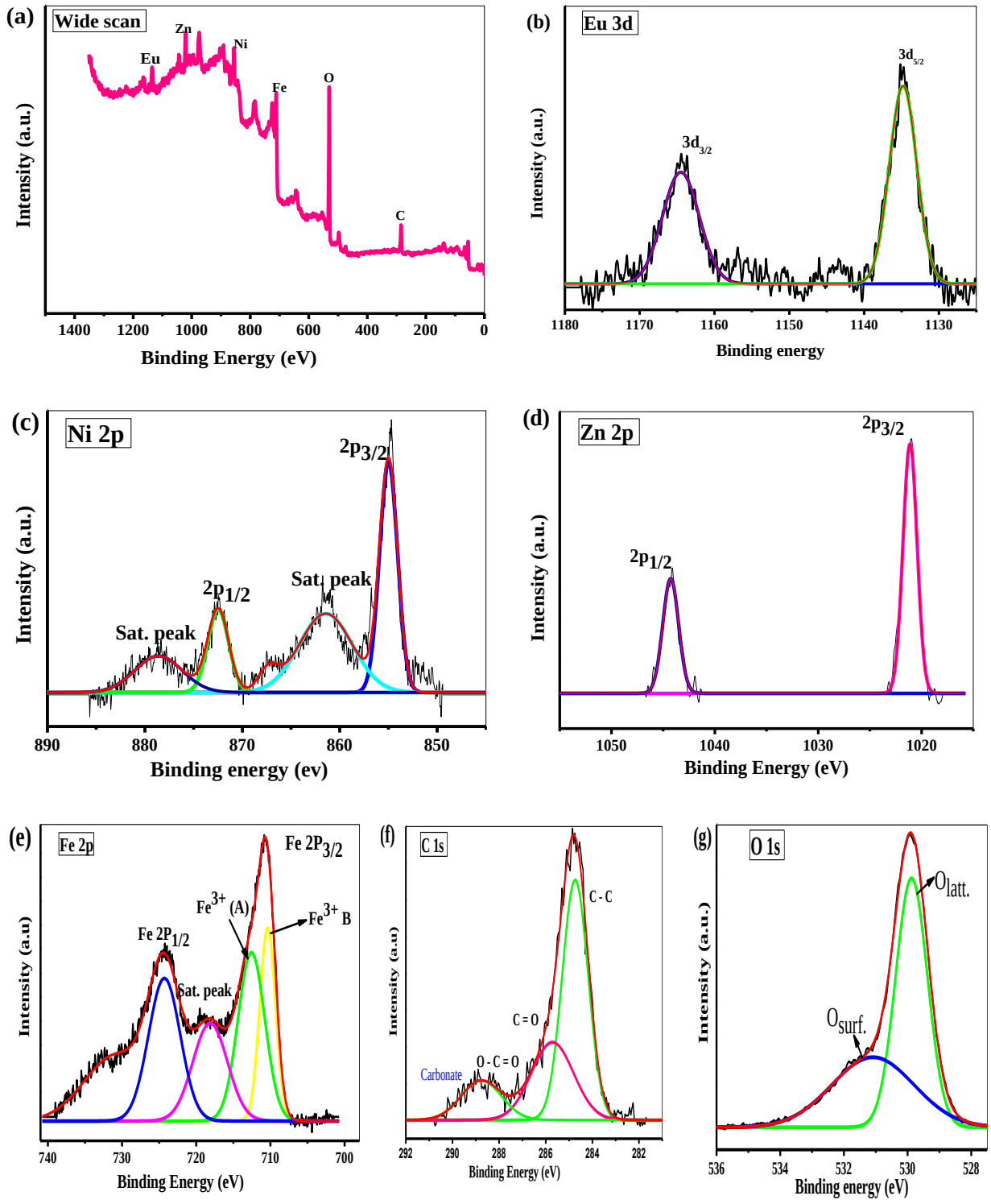

Figure 4.20: XPS spectra of $Ni_{0.75}Zn_{0.25}Eu_{0.06}Fe_{1.94}O_4$@rGO nanocomposite.

4.4 Characterization of NZL-EF Spinel Ferrite NPs and NZL-EF@rGO NCs

4.4.1 XRD analysis

Figure 4.21 illustrates the XRD patterns of rGO, co-doped NZLEF, and NZL-EF@rGO nanocomposites. The planes corresponding to 2θ values of 30.3º, 35.6º, 37.17º, 43.3º, 53.8º, 57.4º, and 63 ℃ are consistent with the XRD patterns of La and Eu doped NZF spinel ferrite discussed in sections 4.2.2 and 4.3.3 respectively. These diffraction planes confirm the formation of face-centered cubic structured spinel ferrite with the presence of a secondary phase (♥) corresponding to the formation of orthoferrite [La-$EuFeO_3$] (Ahmed, *et al.*, 2020; Shahid *et al.*, 2020). The XRD pattern of NZLEF (Figure 4.21b) shows that the peak intensities of orthoferrite (♥) increase on co-doping of La^{3+} and Eu^{3+} ions into the pristine NZF. In the XRD pattern of NZLEF@rGO (Figure 4.21(c)], all the diffraction peaks corresponding to NZLEF spinel ferrite are present in the composite, confirming the co-doped nanoparticles. Even though the crystal structure of NZLEF nanoparticles remained stable after the formation of NZL-EF@rGO, the characteristic peak (002) for rGO at a 2θ of 26.6° was suppressed, evidencing the distortion of the regular stack of rGO sheets and the formation of a strong interaction of the nanoparticles with rGo (Rahman *et al.*, 2020).

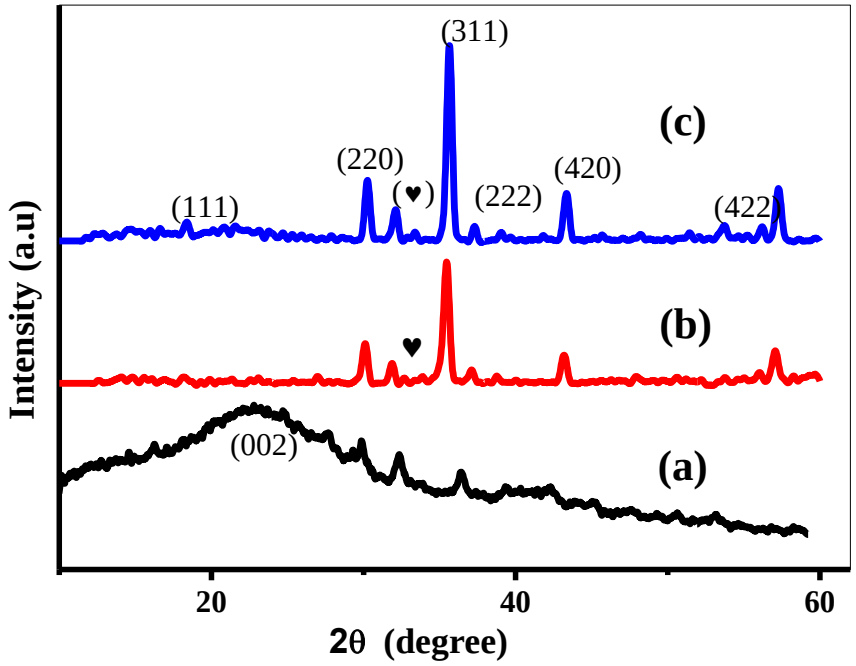

Figure 4.21: XRD patterns of (a) rGO; (b) NZLEF; and (c) NZL-EF@rGO

4.4.2 SEM -EDX analysis

The morphology, elemental mapping, and elemental composition of NZLEF@rGO nanocomposite are illustrated in Figure 4.22. The SEM image of NZL-EF@rGO nanocomposite in Figure 4.22(a) shows that La^{+3}-Eu^{+3} ion doped NZF nanoparticles were successfully embedded in graphene sheets, indicating the formation of the nanocomposite (Shahid *et al.*, 2020) EDX and elemental mapping (Figure 22(b, c) do not show any preferential segregation of heavy elements, indicating a homogeneous chemical composition. The elemental mapping shows the presence of different elements, including Ni, Zn, Fe, La, Eu, O, and C (Almessiere *et al.*, 2019) indicating the formation of the nanocomposite without any impurities. The inset in Figure 4.22 (c) shows the atomic percentage of each element in the synthesized nanomaterials, which agrees with the stoichiometric ratio of the precursor used during their synthesis.

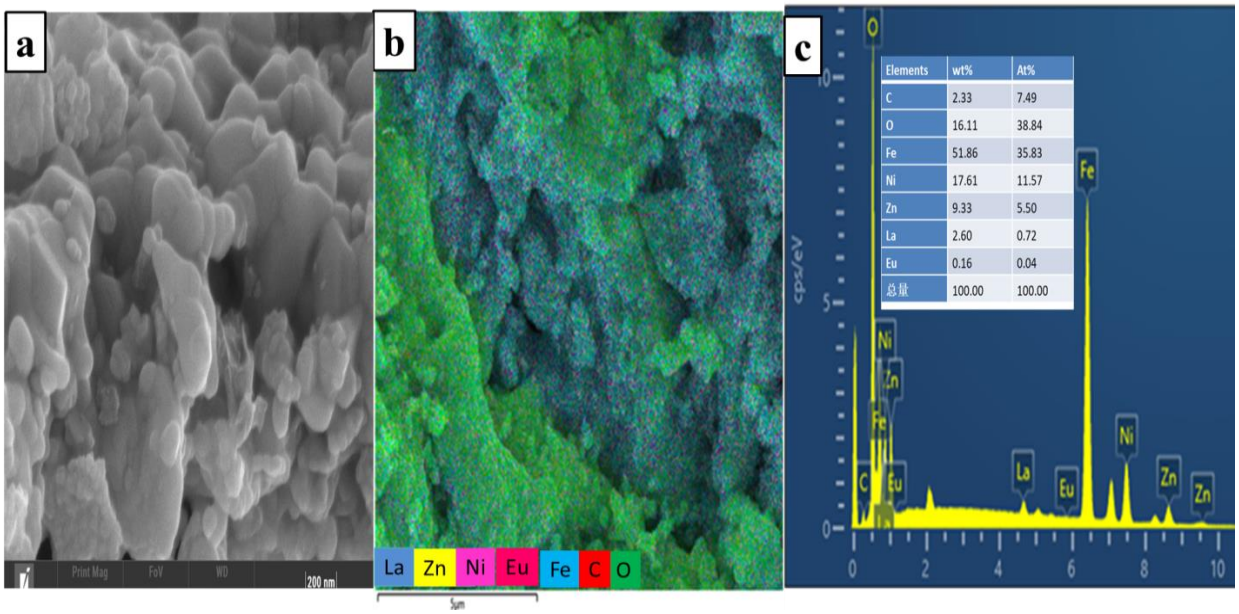

Figure 4.22: (a) SEM image; (b) elemental mapping; and (c) EDX spectrum of NZL-EF@rGO nanocomposite.

4.4.3 XPS analysis

The surface composition with corresponding valance states of the elements present in the surface of $Ni_{0.75}Zn_{0.25}$La-$EuFO_4$@rGO nanocomposite is illustrated in Figure 4.23. of the spectrum in wide shows the core photoionization peaks for C 1s, O1s, Fe 2p, Ni 2p, Zn 2p La-3d, and Eu-3d (Jun *et*

al., 2020; Li *et al.*, 2019). These peaks confirm the conformation of co-doped (NZLEF@rGO) nanocomposite without any impurities (Rather *et al.*, 2021).

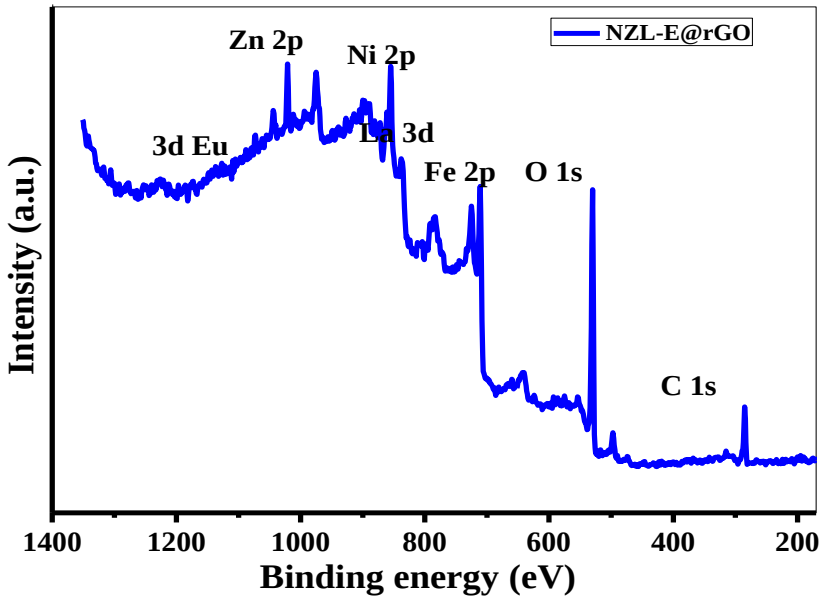

Figure 4.23: XPS spectrum of $Ni_{0.75}Zn_{0.25}La\text{-}EuFe_{1.94}O_4$@rGO nanocomposite.

4.4.4 BET analysis

The photocatalytic process is related to the adsorption–degradation-releasing mechanism, and the adsorbed organic pollutants on the surface of photocatalysts are essential for the photo-induced reaction (Irfan *et al.*, 2017). In Figure 4.24, the BET analysis illustrated that S_{BET} for NZLEF@rGO (6.04 m^2/g). As compared to NZE_6F, NZL_6F, NZL-EF samples, NZL-EF@rGO NCs has a significantly larger surface area (Irfan *et al.*, 2017). The photocatalytic performance is strongly influenced by the surface area due to the introduction of rGO (Ahmed *et al.*, 2021). Based on this, it can be predicted that the composite of co-doped NZF ferrite provides more adsorption and reactive sites on the surface, improving the nanocomposite's properties and application performance.

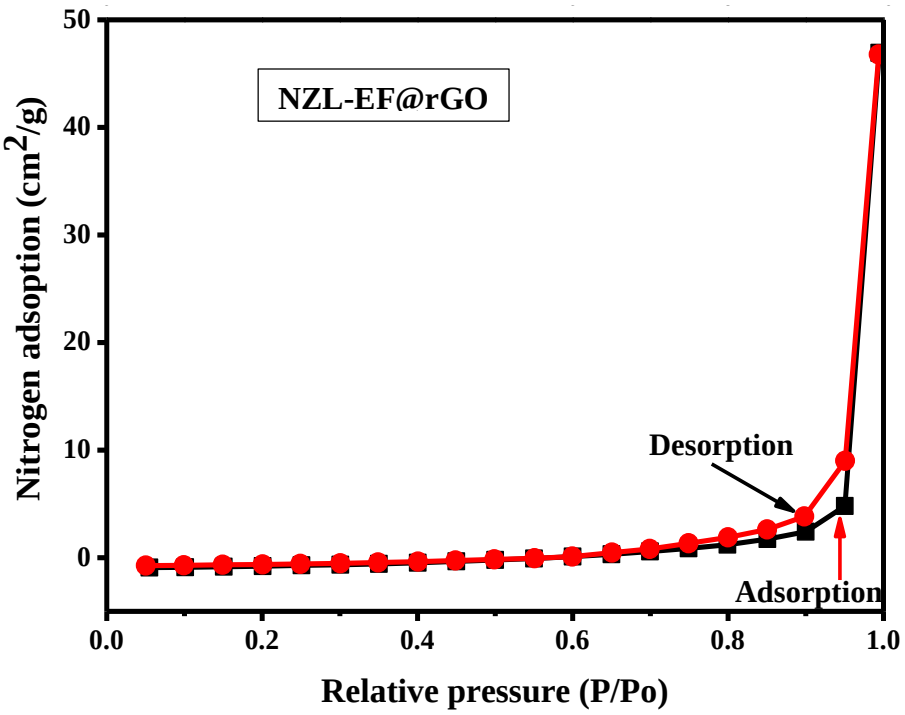

Figure 4.24: Nitrogen adsorption/desorption isotherm of $Ni_{0.75}Zn_{0.25}La$-$EuFe_{1.94}O_4$@rGO nanocomposite.

4.4.5 DRS analysis

Figure 4.25a illustrates the absorbance spectra and Cody's plots for NZLF, NZLEF, and NZLEF@rGO nanocomposites. The co-doped of NZLEF and NZLEF@rGO nanocomposites co-doped with La^{3+} and Eu^{3+} ions result in a high absorption edge over a wide range of visible light and smaller band gap energy than NZF ferrite. Accordingly, co-doping of La^{3+} and Eu^{3+} ions and the introduction of rGO significantly influence the direct E_g magnitude in comparison with ZNLF and NZEF (Figure 4.25b), due to factors such as creating an energy level, interface defects in the structure, crystallite size, and presence of trace impurities by substitution ions (Belaiche *et al.*, 2020). These band gap decrements and increases in the absorption band may be caused by the synergistic influence of the nano-ferrite with La^{3+} and Eu^{3+} ions. This leads to a decrease in the electron-hole recombination and a decrease in the E_g value. This motivates the prediction of the applicability of the co-doped nanocomposite for visible-light-driven photocatalytic activity and electrochemical conductivity applications.

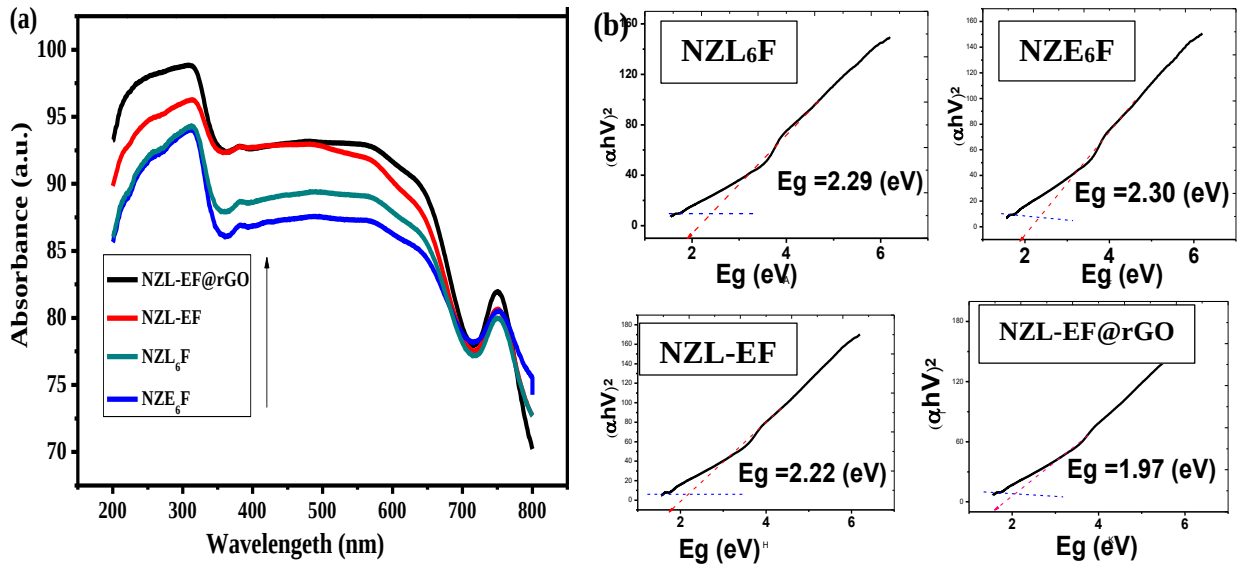

Figure 4.25: percentage absorbance spectra(a) and DRS of NZEF, NZLF, NZEF, and NZLEF@rGO nanocomposites and (b).

4.5 Applications of $Ni_{0.75}Zn_{0.25}La_xFe_{2-x}O_4$ and $Ni_{0.75}Zn_{0.25}La_xFe_{2-x}O_4$@rGO NCs

4.5.1 Photocatalytic applications

Various studies have verified the role of spinel ferrite and its nanocomposites in purifying contaminated water. Thus, these nano ferrites are simple to regenerate and may be reutilized several times before losing their quality, resulting in lower treatment costs. These spinel ferrites are also helpful for photocatalytic activity due to their narrow bandgap (≤ 3 eV). When photons with higher energy are irradiated by sunlight, photoexcitation occurs at the surface of the photocatalyst nanoparticles due to the equal number of holes and electrons created throughout the conduction and valence bands, producing photo generated electron-hole pairs. This happens when the synthesized spinel ferrites have a bandgap energy value less than the energy of photons (Ahmad *et al*., 2023).

These photoexitons form strong oxidizing ($OH^{\bullet}$) and reducing ($O_2^{\bullet}$) species by reacting with the surrounding environment (H_2O and O_2), converting harmful organic pollutants into decomposition products.

The photocatalytic efficiency of undoped, La^{3+} ion-doped NZF ferrite and NZLF@rGO nanocomposite under visible light irradiation against MO and MB selected as representative of

organic pollutants was tested. These experiments were conducted by mixing 100 mL of mixed dye solutions (10 mg/L) with 50 mg of the photocatalysts for 30 minutes under stirring in the dark to achieve adsorption-desorption equilibrium between the dyes and the photocatalysts. To test the degradation of mixed dyes, 5 mL of the suspension was taken at intervals of 5 minutes and analyzed using a UV-Vis spectrophotometer.

Figure 4.26(a, b) illustrates the effect of La^{3+} ion content on the photocatalytic performance of $Ni_{0.75}Zn_{0.25}La_xFe_{2-x}O_4$ nanoparticles toward the degradation of mixed MB and MO dyes under visible light irradiation. From the figure, it is observed that with the substitution of La^{3+} ions, the degradation of mixed dyes increases. This increase in dye degradation is due to the narrow bandgap of rare-earth ions doped in NZF spinel ferrite compared to the undoped ferrite. According to the literature, the photocatalytic activity increases with decreasing energy band gap (Ahmad *et al.*, 2023). In addition, a second possible reason for the increasing degradation yield is that doping of rare earth ions in photocatalysts creates surface oxygen vacancies and defect states that enhance photocatalytic degradation (Peymani-Motlagh *et al.*, 2019).

The photocatalytic activity of $Ni_{0.75}Zn_{0.25}La_xFe_{2-x}O_4$ nanoparticles increases with increasing content of La^{3+} ions until it reaches 6 mol%, while it decreases with further increasing of La^{3+} ion content. This is because the excess of La^{3+} content causes more agglomerations of lanthanum $LaFe_2O_3$ on the surface of the NZF structure, which hinders the light absorption capability of NZF and blocks the active sites of NZF and promotes the recombination rate of photo-generated electron-hole pairs (Aslam *et al.*, 2021). The results are consistent with the band gap energy values obtained by DRS, which are related to the surface area, crystal size, and emission intensity analyzed by BET, XRD, and PL of the $Ni_{0.75}Zn_{0.25}La_xFe_{2-x}O_4$ nanocomposite.

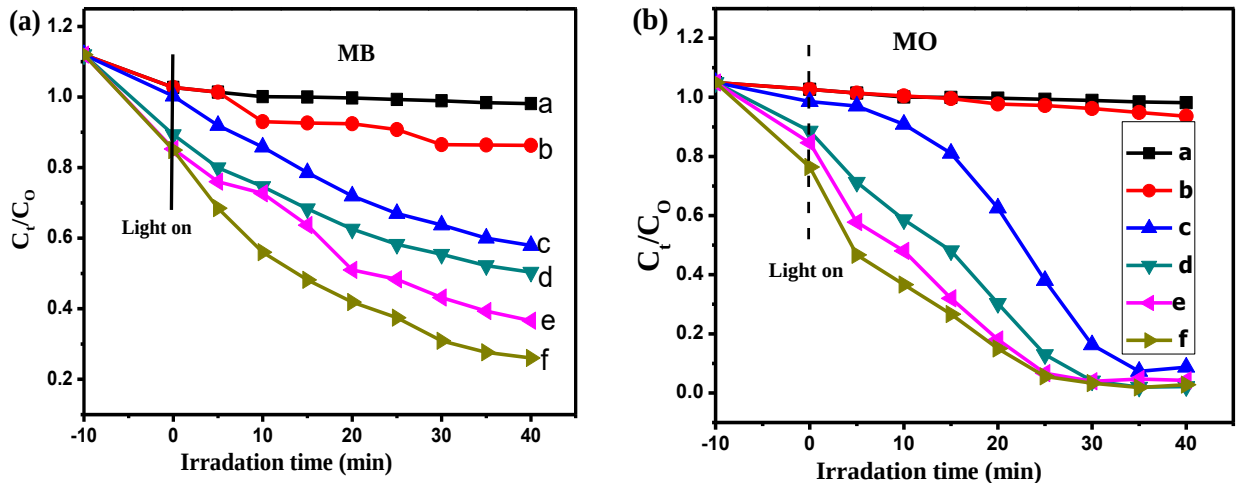

Figure 4.26: Degradation of the mixed dyes MB and MO by different mol% of La^{3+} ions; (a) in the dark, (b) blank, (c) NZF, (d) NZL_2F, (e) $NZL_{10}F$, and (f) NZL_6F.

Figure 4.27(a, b) illustrates the degradation of mixed dyes (MB and MO) under different experimental conditions, including in the dark, blank, by H_2O_2, NZF, NZL_6F, $NZL_6F + H_2O_2$, NZLF@rGO, and NZLF@rGO + H_2O_2 under visible light irradiation. The figure shows that an insignificant amount of degradation occurred when the mixed dyes were kept in the dark and irradiated with visible light without any photocatalyst. Only less than 4% degradation of the dyes was obtained with H_2O_2 under visible light irradiation after 40 minutes. As discussed in the preceding paragraph, doping of La^{3+} slightly enhanced the degradation efficiency of NZF ferrite NPs, and the introduction of rGO significantly improved it. Adding H_2O_2 as an oxidizing agent to NZLF@rGO further increases the degradation efficiency of mixed dyes due to forming more hydroxyl radicals (OH•), illustrated in Figure 4.27.

These results were attributed to the dual function of the $Ni_{0.75}Zn_{0.25}La_xFe_{2-x}O_4$@rGO nanocomposite, which serves to effectively separate photogenerated charge carriers in the $Ni_{0.75}Zn_{0.25}La_xFe_{2-x}O_4$ and rGO coupling system (Rahman *et al.*, 2020) and the formation of more hydroxyl radicals (•OH) via photoelectrochemical decomposition of H_2O_2 under visible light irradiation. Based on their outstanding performance for photocatalytic degradation of mixed organic pollutants, as illustrated in Figure 4.27, NZF ferrite doped with 6 mol% La^{3+} ions, and its nanocomposite with rGO in the presence of H_2O_2 was considered an efficient catalyst.

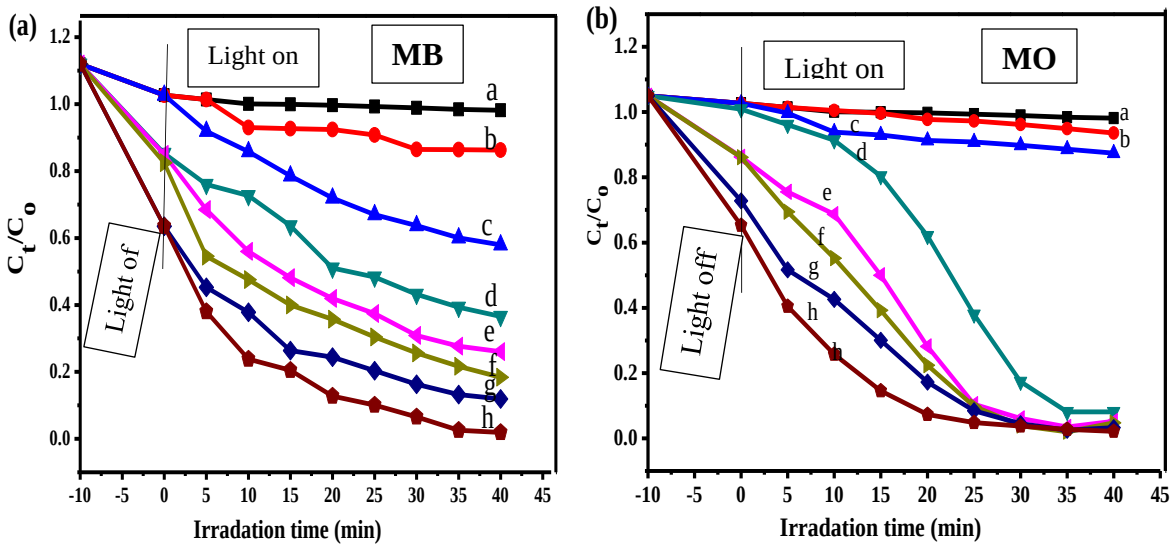

Figure 4.27: Degradation of mixed dyes MB and MO under different experimental conditions: (a) in the dark, (b) blank, (c) visible light + H_2O_2, (d) NZF, (e) NZL_6F, (F) NZL_6F + H_2O_2, (g) NZLF@rGO, (h) NZLF@rGO + H_2O_2.

The image in Figure 4.28 illustrates the decreasing green coloration of the mixed dye suspension with increasing irradiation time to an almost colorless solution. This indicates the breakdown of the structure of chromophores and the complete decomposition of mixed dyes in the solution after 40 minutes of visible light irradiation. (Alzahrani, 2017a).

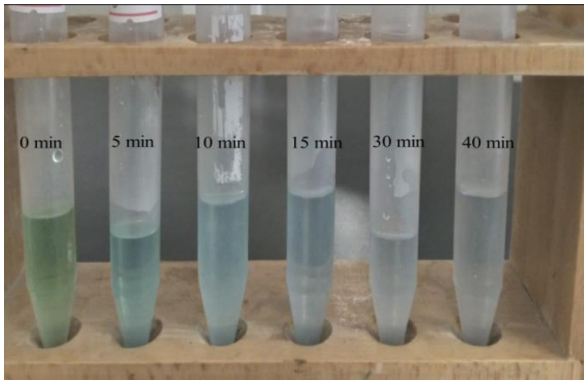

Figure 4.28: Image showing the change in color of mixed dyes with increasing exposure time (0-40 min) visible light irradiation using a 150 W lamp.

Figure 4.29 illustrates the photocatalytic degradation of mixed dyes (MB and MO) using different experimental conditions, including H_2O_2 without catalyst [Figure 4.29(a)], NZL_6F NPs with H_2O_2 [Figure 4. 29(b)], and NZLF@rGO nanocomposite with H_2O_2 [Figure 4. 29(c)] under visible light

irradiation. The results showed that, in all cases, the λ_{max} values for MO and MB are located at 465 and 665 nm, respectively, and do not change their position. However, their peak intensities decrease with increasing irradiation time (Alzahrani, 2017).

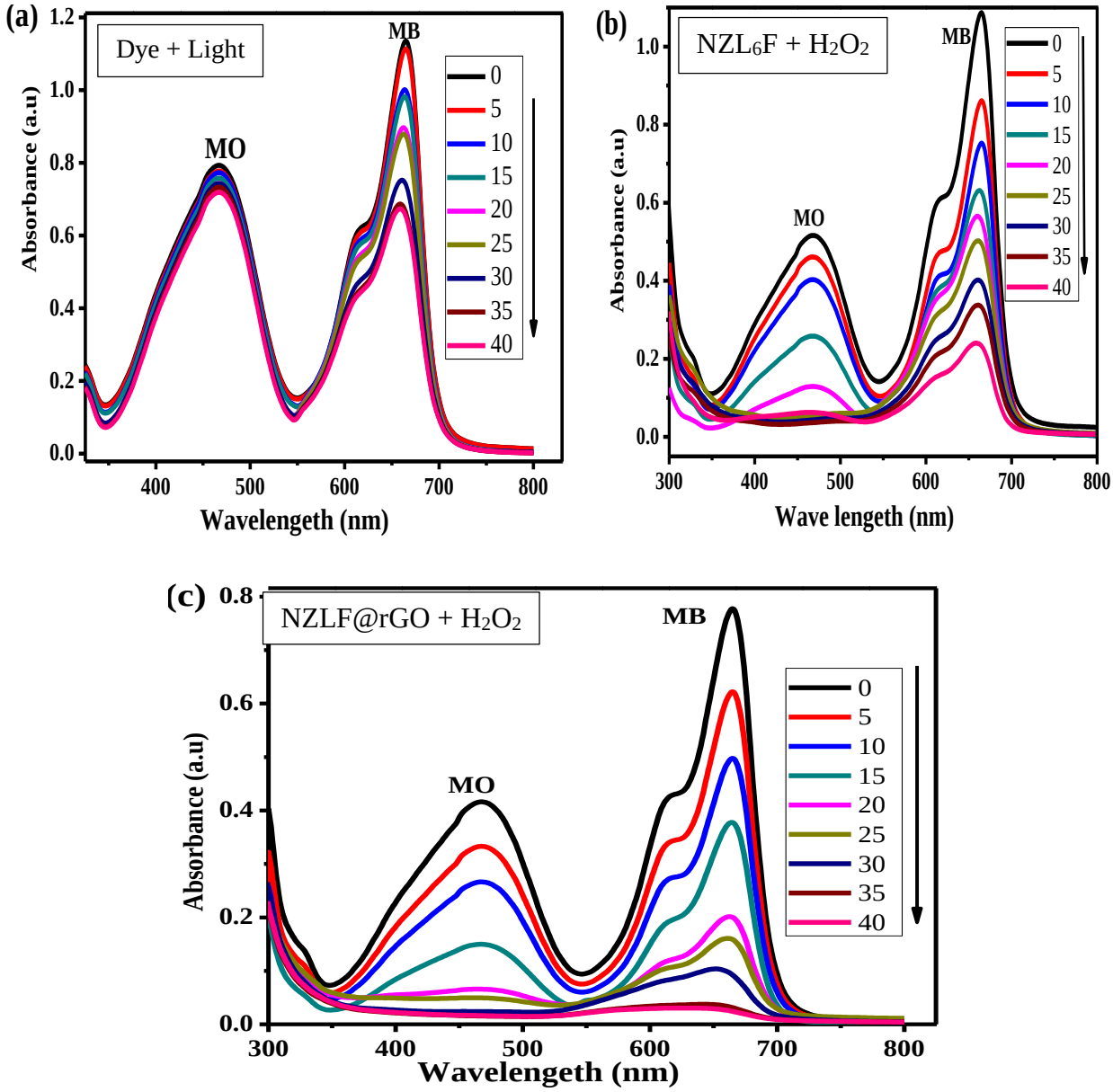

Figure 4.29: Absorption spectra of mixed dyes (MB and MO) in aqueous solutions taken at every 5 min interval with the conditions of (a) without photocatalyst; (b) with $Ni_{0.75}Zn_{0.25}La_{0.06}Fe_{1.94}O_4$ nanoparticles and (c) with $Ni_{0.75}Zn_{0.25}La_{0.06}Fe_{1.94}O_4$@rGO nanocomposites in the presence of H_2O_2 under optimized experimental conditions of pH nine, initial concentration of dyes at five mg/L and catalyst dosage of 50 mg at room temperature.

As illustrated in Figure 4.29(a), MO was slightly stable in blank conditions (without any catalyst), while MB underwent slight decomposition. This indicates the stability of the dyes under visible light irradiation in the absence of a photocatalyst (Rahman *et al*., 2020). While 78 % MB and 85 % MO photocatalytic degradation was obtained in the case of NZL_6F NPs with H2O2, it was improved up to ≥95 % MB and ≈98 % MO with the introduction of rGO (NZLF@rGO) using the same experimental conditions, i.e., under visible light irradiation for 40 min. This exceptional increase is because of the adsorption of more dye molecules by the large surface area of graphene, lowering of electron-hole pair recombination due to the fast transition of exited electronic and easy transition of electrons from the metal valence band to conduction band because of the lowering of E_g (Yousaf *et al*., 2020). As can be seen from Figure 4.29c, there was no absorption peak observed after 35 min of irradiation, which indicated the destruction of structures responsible for the color (chromophores) of the mixed dyes in solution (Alzahrani, 2017; Patil *et al*., 2019).

Table 4.4: Comparison of graphene-based nanocomposite for photocatalytic degradation of methylene blue (MB) and methyl orange (MO).

Dyes used	rGO based nanocomposite	Time/ min	Irradiation source	Degradation (%)	Reference
MB	$Ni_{0.65}Zn_{0.35}Fe_2O_4$	56	Visible	55	(Javed *et al*., 2019)
	$Ni_{0.5}Co_{0.5}Dy_{0.03}Fe_{1.97}O_4$	120		72.6	(Shahid *et al*., 2020)
	$Ni_{0.4}Co_{0.6}Er_{0.045}Fe_{1.95}O_4$	35		43.1	(Iftikhar *et al*., 2019)
	$NiCe_yFe_{2-y}O_4$/rGO	70		94.67	(Rahman *et al*., 2020)
	$Ni_{0.75}Zn_{0.25}La_{0.06}Fe_{1.94}O_4$@rGO	**40**		**95**	**Current work**
MO	$Bi_2Fe_4O_9$	330	Visible	90.22	(Zhao *et al*., 2022)
	$Co_{1-x}Zn_xFe_{2-y}R_yO_4$	90		71	(Mosleh, 2016)
	$CoFe_2O_4$	180		64	(Mahdikhah *et al*., 2020)
	$Ni_{0.75}Zn_{0.25}La_{0.06}Fe_{1.94}O_4$@rGO	***40***		***98***	***Current work***

Table 4.4 compares the percentage degradation of MB and MO using different graphene-based nanocomposites reported by previously published results with the current work. The table depicts that NZLF@rGO has the highest photocatalytic efficiency for the degradation of both MO and MB dyes in their mixture within a short period of visible light irradiation. The literature has reported mainly on degrading a single selected dye at a time. In contrast, the currently developed catalyst degraded both selected dyes simultaneously with a high percentage of degradation efficiency. Therefore, the magnetic NZLF@rGO NCs are predicted to be an efficient photocatalyst for the simultaneous degradation of mixed organic pollutants under visible light irradiation.

4.5.1.1 Optimization parameters

4.5.1.1.1 Effect of pH on the photocatalytic activity

The pH of the degradation medium is one of the critical parameters that influence the degradation of dyes as it affects the adsorption performance of the catalyst and natural dyes (Patil *et al*., 2019)Therefore, choosing an optimal pH to degrade the mixed organic dyes (MB and MO) using the NZLF@rGO nanocomposite was necessary. The impact of pH on the photocatalytic degradation of the binary dyes was investigated in the pH range of five to 11, as illustrated in Figure 4.30. A 0.1 M HCl and 0.1 M NaOH were used to adjust the pH of the solutions.

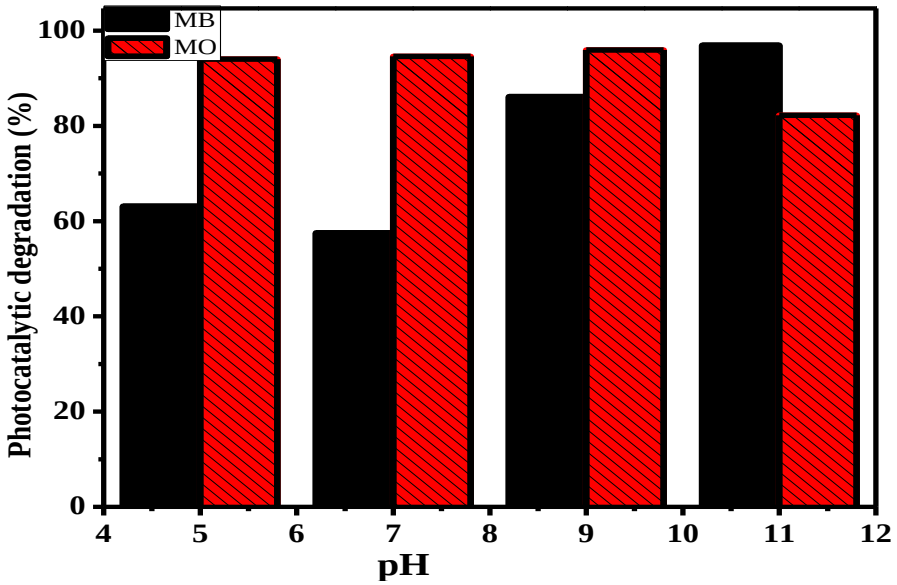

Figure 4.30: Effect of pH on the degradation efficiency of binary dyes.

Charges on the surface can describe the catalyst's ability to degrade organic pollutants at different pHs (Rahman *et al*., 2020). As per the reports of Rahman *et al*. (2020) and Ahmed *et al.* (2020), the rGO composite of spinel ferrites has a positive surface charge in acidic media and a negative surface charge in alkaline media. As a result, in acidic media, strong electrostatic interaction exists between the positively charged catalyst surface and anionic dyes (MO), resulting in high degradation efficiency. In an alkaline environment, there is also strong electrostatic interaction between the negatively charged surface of the catalyst and cationic dyes (MB), which also results in high degradation efficiency (Ahmed *et al*., 2021). Consequently, the interaction between the dye molecules and the catalyst's surface is the basic factor affecting the degradation efficiency. The decolorization of the anionic became much faster in acidic conditions, while in alkaline conditions, the cationic dye MB degraded more efficiently. Accordingly, both dyes were efficiently degraded at pH between 8 and 11, which are mildly basic media. The degradation efficiency for the chosen mixed dyes was better at pH nine for the dye MO and pH 11 for the dye MB. Since pH 9 is closer to neutral, it was chosen as a moderate pH value for further experiments.

4.5.1.1.2 Effect of catalyst dosage on the photocatalytic activity

The catalyst dosage is another crucial factor affecting the photocatalytic degradation of dyes. Figure 4.31 illustrates the effect of NZLF@rGO catalyst dosage on the percentage degradation of the binary organic dyes. It was assessed by changing the catalyst dosage from 25 to 100 mg/100 mL using a mixed dye concentration of 10 mg/100 mL and pH nine at 25 ^{o}C. The figure shows that the percentage degradation of the mixed dyes (MB and MO) is enhanced by increasing the catalyst dosage from 25 to 50 mg/100 mL but decreasing the above 50 mg catalyst dosage. The increase in degradation efficiency is attributed to (1) the availability of a large surface area and active sites for the adsorption of more dye molecules with an increase in the catalyst dose and (2) an increase in the mass-to-volume ratio of the photocatalyst. The decrease in photodegradation efficiency of the dyes at higher dosages (>50 mg) may be due to the formation of turbidity and agglomeration of catalyst particles that hinder the penetration of visible light onto the surface of the catalyst (Rahman *et al*., 2020). Therefore, the catalyst dose of 50 mg was used as the optimal dosage for the experiments

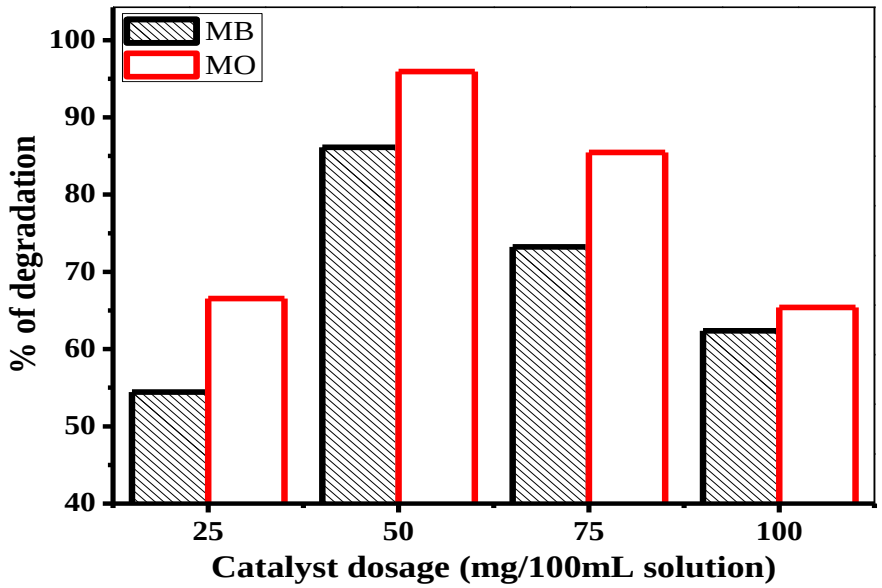

Figure 4.31: Catalyst dosage efficiency on the photodegradation of the binary dyes under visible light irradiation.

4.5.1.1.3 Effect of dye concentration on the photocatalytic activity

The dye concentration is also an essential parameter when assessing the efficiency of photocatalysts in the photodegradation process (Patil *et al*., 2019). Figure 4.32 illustrates the effect of the initial concentration of the dyes on the degradation efficiency of catalysts. As observed in the Figure, by increasing the initial concentration of the mixed dyes above 5 mg/100mL, the degradation efficiency of NZLF@rGO decreased. This is because the dye molecules are absorbed on the active surface of photocatalysts. As the mixed dye concentration increases, the active sites of the photocatalyst become more obscure, which reduces the amount of visible light that enters their surface and lowers the production of oxidative active species (Kour *et al*., 2023). Besides that, the dye molecules adsorbed on the catalyst's active surface also absorb a substantial amount of visible light, which also causes a decrease in the effectiveness of the degrading process (Patil *et al*., 2019). This clarifies that an optimized initial dye concentration is necessary at the desired photocatalyst dosage to display high degradation efficiency. Based on this fact, a 5 mg/L concentration of the mixed dye was selected as the initial dye concentration.

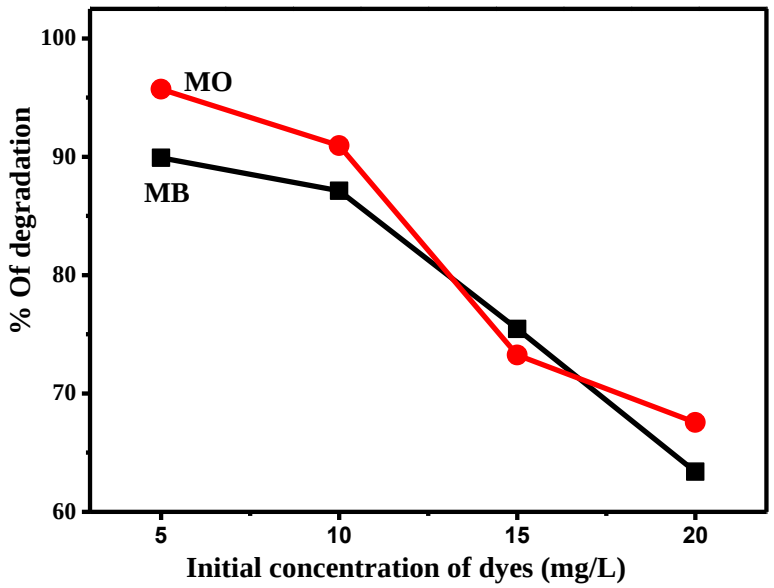

Figure 4.32: Effect of mixed dyes (MB and MO) concentration on photocatalytic activity of $Ni_{0.75}Zn_{0.25}La_{0.06}Fe_{1.94}O_4$@rGO nanocomposite.

4.5.1.1.4 Determination of active species

To determine the main reactive species involved in the photocatalytic degradation of mixed dyes, investigations on radical scavenging were conducted to examine the photodegradation mechanism. As illustrated in Figure 4.33, in the photocatalytic reaction system at 25 °C, potassium iodide (KI) and ascorbic acid (AA) were used as efficient radical scavengers for the hydroxyl (•OH) and superoxide ($O_2^{\bullet}$) radicals, respectively. Additionally, ethylenediaminetetraacetate (EDTA) and potassium dichromate ($K_2Cr_2O_4$) were introduced as the photogenerated electron (e^-) and hole (h^+) scavengers, respectively (Ahmed *et al.*, 2021; Kour *et al.*, 2023). Compared to other scavengers, adding KI significantly reduced the percentage degradation of mixed dyes, demonstrating that the hydroxyl radical (•OH) played a crucial role in the degradation process. Even though the role played by hydroxyl radical (•OH) is significant, the addition of scavengers AA, EDTA, and $K_2Cr_2O_4$ also reduces the degradation efficiency to a small extent, which shows the partial involvement of e^-, h^+, and $O_2^{\bullet-}$ in the degradation process, in the order of e-<h+< $O_2^{\bullet-}$< •OH.

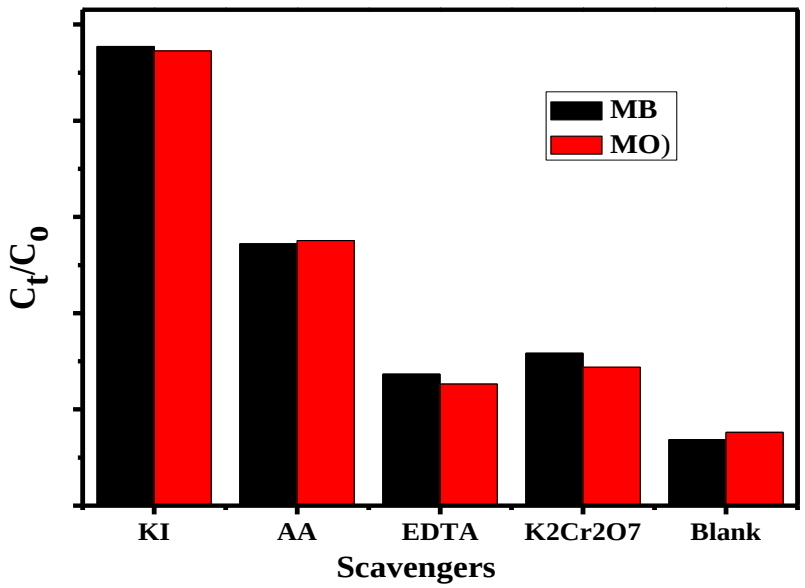

Figure 4.33: Effect of radical scavengers on the photocatalytic activity of $Ni_{0.75}Zn_{0.25}La_{0.06}Fe_{1.94}O_4$@rGO nanocomposite.

4.5.1.2 Photocatalytic mechanism of $Ni_{0.75}Zn_{0.25}La_xFe_{2-x}O_4$@rGO NCs

Creating electron-hole pairs in semiconductor materials in the presence of light is the basis for the photodegradation of organic contaminants. A possible photocatalytic mechanism of $Ni_{0.75}Zn_{0.25}La_{0.06}Fe_{1.94}O_4$@rGO nanocomposite is proposed (reactions 1 to 9) and illustrated in Figure 4.34 (Lu, *et al.* 2013; Iftikhar *et al.*, 2019; Shahid *et al.*, 2020). Upon irradiation by visible light, $Ni_{0.75}Zn_{0.25}La_{0.06}Fe_{1.94}O_4$ nanoparticles undergo charge separation, an electron excited from the VB to CB, causing the generation of holes in the VB and electron in CB simultaneously (Javed *et al.*, 2019) (reaction 1). Because graphene sheets are suitable electron acceptors (Lu *et al.*, 2013), the photogenerated electrons quickly migrate to the surface of the rGO sheet via the percolation mechanism, which suppresses the recombination of photogenerated charge carriers (reaction 2). This effect increases the efficiency of the photocatalytic process. Then, the rGO sheets activate the decomposition of H_2O_2 to produce $^{\bullet}OH$ radicals and OH^- ions (reaction 3). Additionally, the oxygen and electrons from graphene sheets combine to generate $O_2^{\bullet-}$ radicals (Ahmed, *et al.*, 2020) (reaction 4).

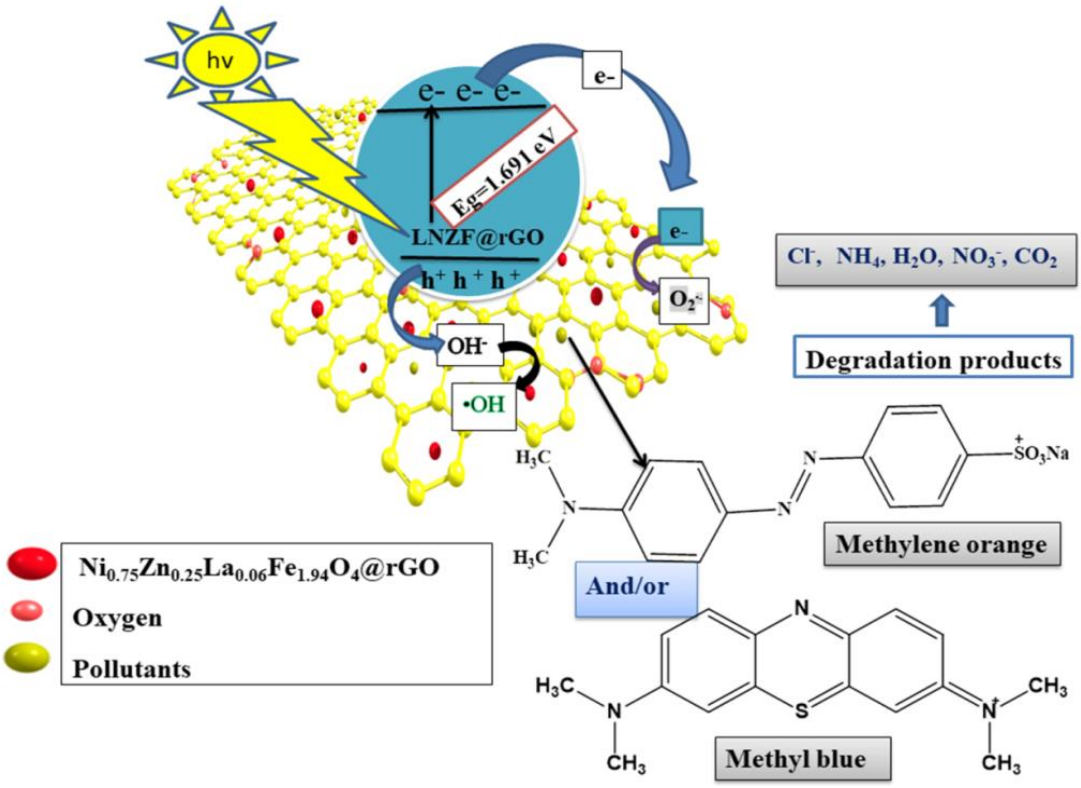

Figure 4.34: Graphical illustration of the photocatalytic degradation process.

The hydroxyl ion (OH^-) and the holes in the valance band combine to generate the radical (OH•) (reaction 5). Finally, the synthetic dyes (organic pollutants) are broken down into simpler molecules by the OH• and $O_2^{\bullet-}$ radicals (reaction 6). Thus, the $O_2^{\bullet-}$ and •OH radicals generated from the reactions are responsible for the decolorization of the dyes (Ahmed, *et al.*, 2020).

$$Ni_{0.75}Zn_{0.25}La_{0.06}Fe_{1.94}O_4 + hv \rightarrow Ni_{0.75}Zn_{0.25}La_{0.06}Fe_{1.94}O_4\,(h^+ + e\text{-}) \quad (1)$$

$$Ni_{0.75}Zn_{0.25}La_{0.06}Fe_{1.94}O_4\,(e\text{-}) + rGO \rightarrow Ni_{0.75}Zn_{0.25}La_{0.06}Fe_{1.94}O_4 + rGO(e\text{-}) \quad (2)$$

$$rGO(e\text{-}) + H_2O_2 \rightarrow \bullet OH + OH^- + rGO \quad (3)$$

$$rGO(e\text{-}) + O_2{}^{-2} \rightarrow rGO + {}^{\bullet}O_2{}^{-2} \quad (4)$$

$$Ni_{0.75}Zn_{0.25}La_{0.06}Fe_{1.94}O_4\,(h^+) + OH^- \rightarrow Ni_{0.75}Zn_{0.25}La_{0.06}Fe_{1.94}O_4 + \bullet OH \quad (5)$$

$$Ni_{0.75}Zn_{0.25}La_{0.06}Fe_{1.94}O_4\,(h^+_{(VB)}) + {}^{\bullet}OH + {}^{\bullet}O_2{}^{-2} + MB + MO \rightarrow \text{decolorization products} \quad (6)$$

4.5.1.3 Recyclability test of $Ni_{0.75}Zn_{0.25}La_xFe_{2-x}O_4$@rGO NCs

Investigating the recyclability and photostability of the developed photocatalytic materials is crucial to scale up the process and make it more cost-effective for commercial applications. To

confirm the recyclability of the $Ni_{0.75}Zn_{0.25}La_{0.06}Fe_{1.94}O_4$@rGO catalyst, photodegradation experiments conducted using predetermined optimized conditions were repeated five times using the catalyst separated from the preceding experiment. The results are illustrated in Figure 4.35(a, b). After each experiment, the $Ni_{0.75}Zn_{0.25}La_{0.06}Fe_{1.94}O_4$@rGO nanocomposite was magnetically separated from the reaction solution and reused in the following experiment [inset of Figure 4.35(b)].

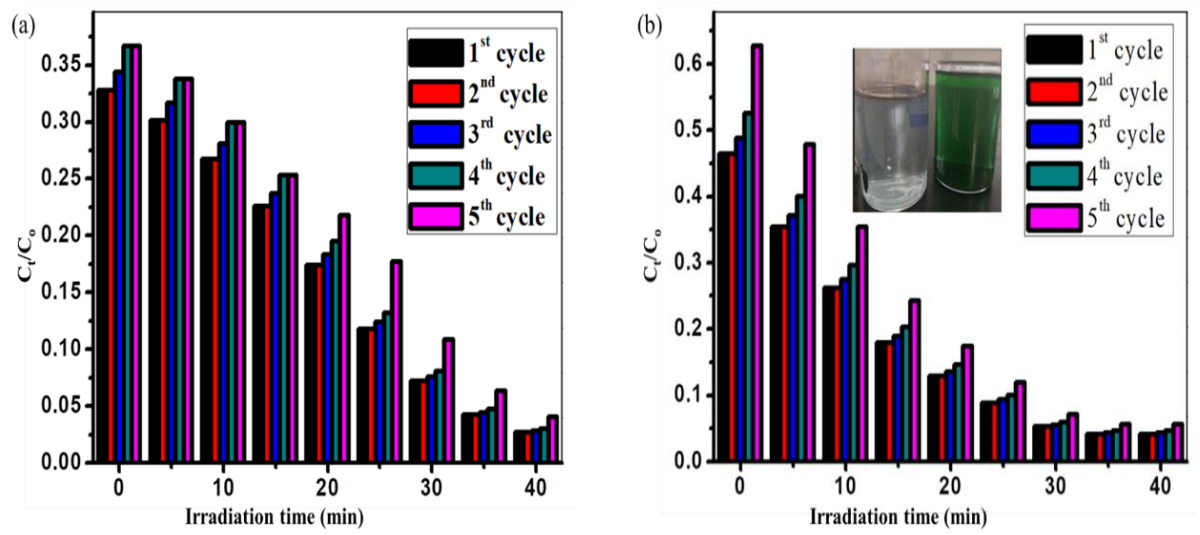

Figure 4.35: Recyclability of $Ni_{0.75}Zn_{0.25}La_{0.06}Fe_{1.94}O_4$@rGO nanocomposite on the photo-decolorization of (a) MB dye and (b) MO dye under visible light irradiation.

Magnetic separation does not depend on the working environment's pH, temperature, or ionic strength. The magnetic nanocomposite can be cleaned multiple times with double distilled water and ethanol before being dried at room temperature. From the results obtained, the decline in photocatalytic degradation efficiency of the nanocomposite after five cycles was 6.37 %, indicating the photostability of the catalyst. This decline in catalyst performance may be caused by several factors, including photocatalyst aggregation, the adsorption of intermediate products on catalyst-active sites, and the destruction of catalyst-active sites owing to photo corrosion (Ahmed *et al.*, 2021). The other reason is experimental errors since 100% of the photocatalyst cannot be recovered during magnetic separation. Nevertheless, results obtained from the experiments confirm that the nanocomposite has excellent stability and can be reused several times, holding promise for the photocatalytic degradation of organic pollutants under visible light irradiation.

4.5.2 Electrochemical sensor application

4.5.2.1 Electrochemical characterization of electrode modification

To clarify the differences among the electrochemical performance of the CPE, NZLF modified CPE and NZLF@rGO/CPE, electrochemical impedance spectroscopy (EIS) and cyclic voltammetry (CVs) were carried out using 5 mM $[Fe(CN)_6]^{-3/-4}$ and 0.1 M KCl at a scan rate of 50 mV s^{-1} between -0.8 V and 0.9 V. As such, the Nyquist plots showed a difference in response for the electrode (Figure 4.36). The diameter of the Nyquist plot semicircle directly corresponds to the charge transfer resistance, i.e., a semicircle with a small diameter is attributed to the low charge transfer resistance (R_{ct}) (i.e., highly conductive) (Darabi *et al.*, 2021).

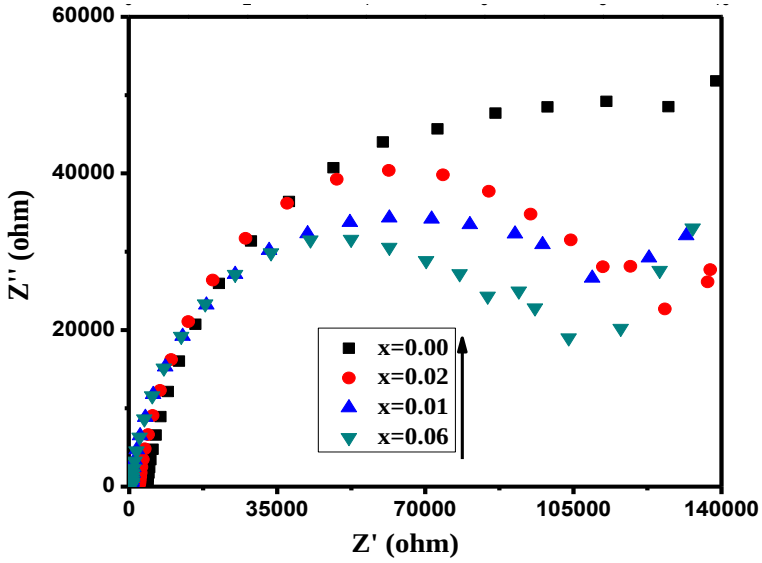

Figure 4.36: Electrochemical characterization of $Ni_{0.75}Zn_{0.25}La_xFe_{2-x}O_4$ using EIS at frequency range 10mHz-100 KHz, the potential range of −2.5 to 2.5 V (vs. Ag/AgCl electrode) and scanning rate 10 mV/s, and AC amplitude of 20 mV, under working conditions of 5 mM of $[Fe(CN)_6]^{-3/-4}$ redox probe in 0.1M KCl solution as a supporting electrolyte.

As can be seen from the Nyquist plot, a large diameter was observed at the CPE electrode. However, the diameter of the semicircles decreased when the concentration of La^{3+} ions increased in $Ni_{0.75}Zn_{0.25}La_xFe_{2-x}O_4$, exhibiting a decrease in the charge transfer resistance, which is related to the conducting nature of lanthanum (Zhang *et al.*, 2022). When the content of La^{3+} ions is more than 6 mol%, charge transfer resistance increases (i.e., decrease in conductivity), attributed to the aggregation of lanthanum orthoferrite, which blocks the electron transfer (Muthuselvi *et al.*, 2021).

Consistent results were obtained from CV characterization at a scan rate of 50 mV s^{-1} (Figure 4.37). The current response is directly related to the redox probe signal (Afkhami *et al.*, 2020), and the results obtained from EIS and CV characterization showed that CPE modified with 6 mol% of La^{3+} ions doped NZF has a greater current repose and electrochemical conductivity. Consequently, 6 mol% of La^{3+} ions were selected as the optimum concentration for fabricating the electrode in the subsequent experiments.

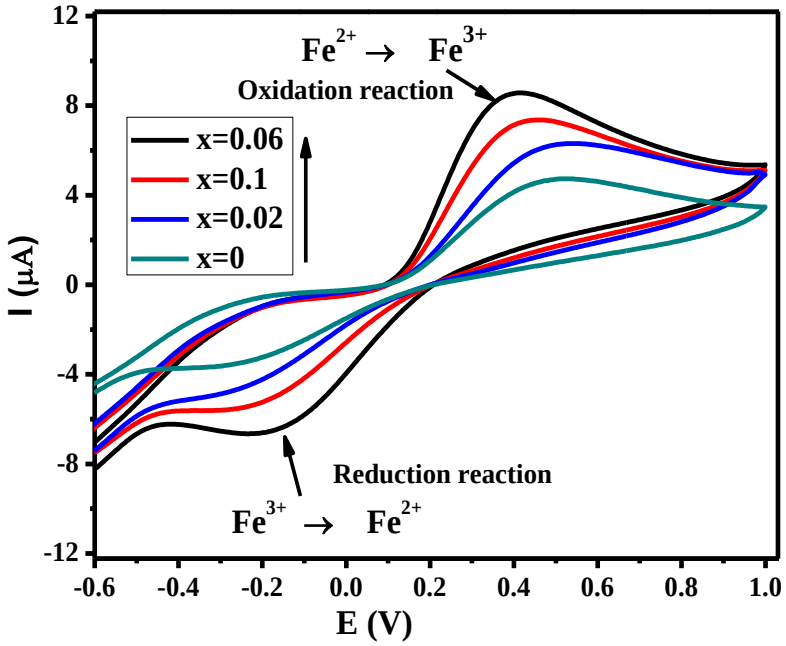

Figure 4.37: Electrochemical characterization of $Ni_{0.75}Zn_{0.25}La_xFe_{2-x}O_4$ using CV at a scan rate of 50 mV/S under working conditions of 5 mM of $[Fe(CN)_6]^{-3/-4}$ redox probe in 0.1M KCl solution as a supporting electrolyte.

Figure 4.38 illustrates the electrochemical analysis of the bare CPE, NZF/CPE, NZL6F/CPE, and NZLF@rGO/CPE using EIS and CV. The Nyquist plots in Figure 4.38a show that the R_{ct} of bare CPE, NZF, La^{3+}/NZF, and NZLF@rGO were 4812, 3614, 2444, and 1466 Ω, respectively. It is observed that NZLF@rGO/CPE showed the smallest charge transfer resistance and significant lowering of the semicircle. At the same time, NZLF@rGO/CPE shows the highest peak current response in four modified electrodes, as illustrated in Figure 4.38b. This is mainly because the introduction of rGO offers a large surface area, accelerating the transfer of electrons and creating conditions for better contact with the electrode material (Muthuselvi *et al.*, 2021). The slight reduction of ΔE can be attributed to the dispersion of NZLF in rGO and the high conductivity of

reduced graphene oxide (Zhang *et al.*, 2022). The above results informally prove that NZLF@rGO/CPE is preferably electrochemically active.

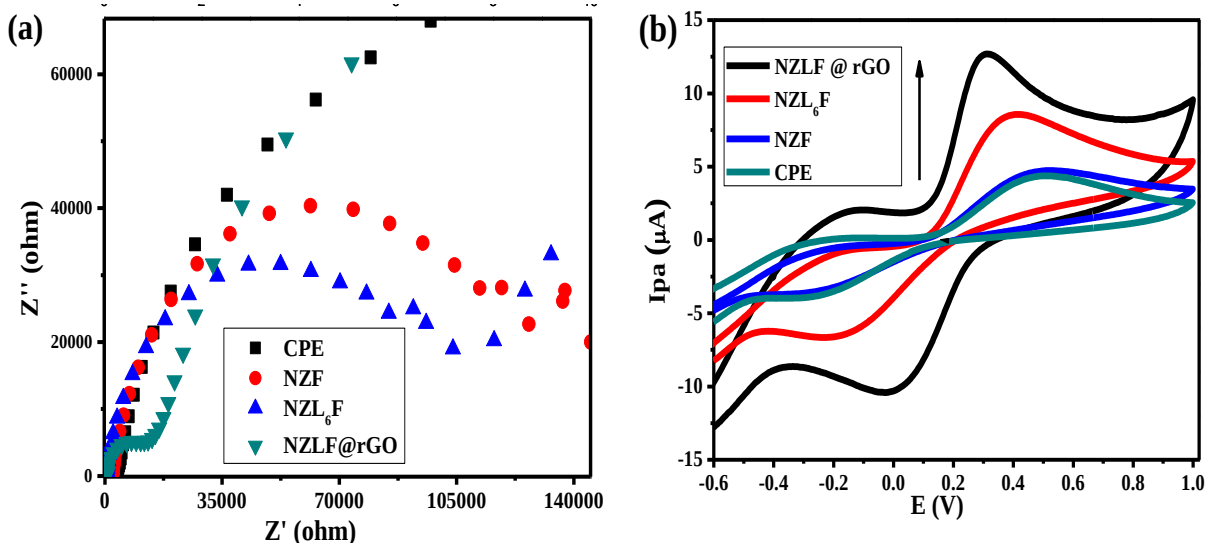

Figure 4.38: (a) Nyquist plots from impedance measurements in the presence of 5 mM of $[Fe(CN)_6]^{3-/4-}$ and 0.1 M KCl solutions as supporting electrolytes. Conditions: potential range of −2.5 to 2.5 V (vs. Ag/AgCl electrode), AC amplitude of 20 mV, and (b) CV plots of the modified electrode at a scan rate of 50 mV/s.

The electrode's surface area influences the reaction rate in an electrolytic cell. The electroactive surface area of bare CPE, NZF/CPE, NZLF/CPE, and NZLF@rGO/CPE were evaluated using the CV plots of 5 mM $K_3[Fe(CN)_6]$ and 5 mM $K_4[Fe(CN)_6]$ in 0.1M KCl using the Randles- Sevcik formula given in equation 4.11 (Tran *et al.*, 2019).

$$I_{pa} = 2.686x10^5 n^{3/2} A D^{1/2} v^{1/2} C \quad (4.11)$$

I_p = peak current (A); n = number of electrons transfer occurred in the redox reaction $[Fe(CN)_6]^{3-} \rightleftharpoons [Fe(CN)_6]^{4-} + e^-$; C= stand for the concentration of $[Fe(CN)_6]^{3-/4-}$ (5 mM); A = electrode active area (cm^2); D = diffusion coefficient of $[Fe(CN)_6]^{3-/4-}$ in solution (7.6 x 10^{-6} cm^2/s) and ν = potential scan rate (V/s).

The active surface area of the bare CPE, NZF/CPE, NZLF/CPE, and NZLF@rGO/CPE were estimated to be 0.16, 0.96, 0.98, and 1.02 cm^2, respectively. The increase in surface area of the electrode is directly related to an enhancement of the rate of reaction in electrolytic cells and the rate of current flow through the electrodes. Therefore, the sensitivity and rate of electron transfer

ability of the electrodes are directly proportional to the electro-active surface area (Zhang *et al.*, 2022). This also inferred that NZLF@rGO was an efficiently modified CPE electrode for fabricating electrochemically sensitive electrodes (NZLF@rGO/CPE).

Based on the results, NZLF@rGO nanocomposite was selected as the best candidate for modifying the surface of CPE (NZLF@rGO/CPE) to fabricate an efficient electrochemical sensor for detecting food colorants.

4.4.1.1. Electrochemical detection of Sunset Yellow (SY) and Taritrazine (TZ)

The electrochemical response of SY and TZ was examined separately and simultaneously on the surface of bare CPE, NZF/CPE, NZL6F/CPE, and NZLF@rGO/CPE with a scan rate of 50 mV/s in 0.1 M PBS as an electrolyte (Figure 4.39)**.**

The CVs of SY and TZ, analyzed individually, illustrated in Figure 4.39(a & b), exhibit peaks at potentials of 0.8 and 1.02 V, respectively, corresponding to their oxidation peaks (Ghoreishi *et al.*, 2012). Figure 4.39c illustrates two distinct oxidation peaks at the same potentials of SY and TZ, confirming the possibility of simultaneous detection of SY and TZ in their mixture without interfering with one another. Amongst, a significant oxidation response for both SY and TZ was obtained at NZLF@rGO/CPE, with a slight shifting of potential. This indicates that the CPE electrode modified with NZLF@rGO has the highest electrocatalytic activity for simultaneous detection of mixed dyes due to the reason discussed for EIS and CV analyses. The absence of a reduction signal on the reverse scan confirmed that permanent oxidation of SY and TZ on the surface of all the desired electrodes (Ghoreishi *et al.,* 2012). Consistent results were also obtained using differential pulse voltammetry (SWV) [Figure 4.39d], wherein the two distinct oxidation peaks correspond to SY and TZ at potentials of +0.769 and +1.027 V, respectively. These results are consistent with previously reported research (Karim-Nezhad *et al*., 2017; Penagos-Llanos *et al.*, 2020; Moarefdoust *et al*., 2021)

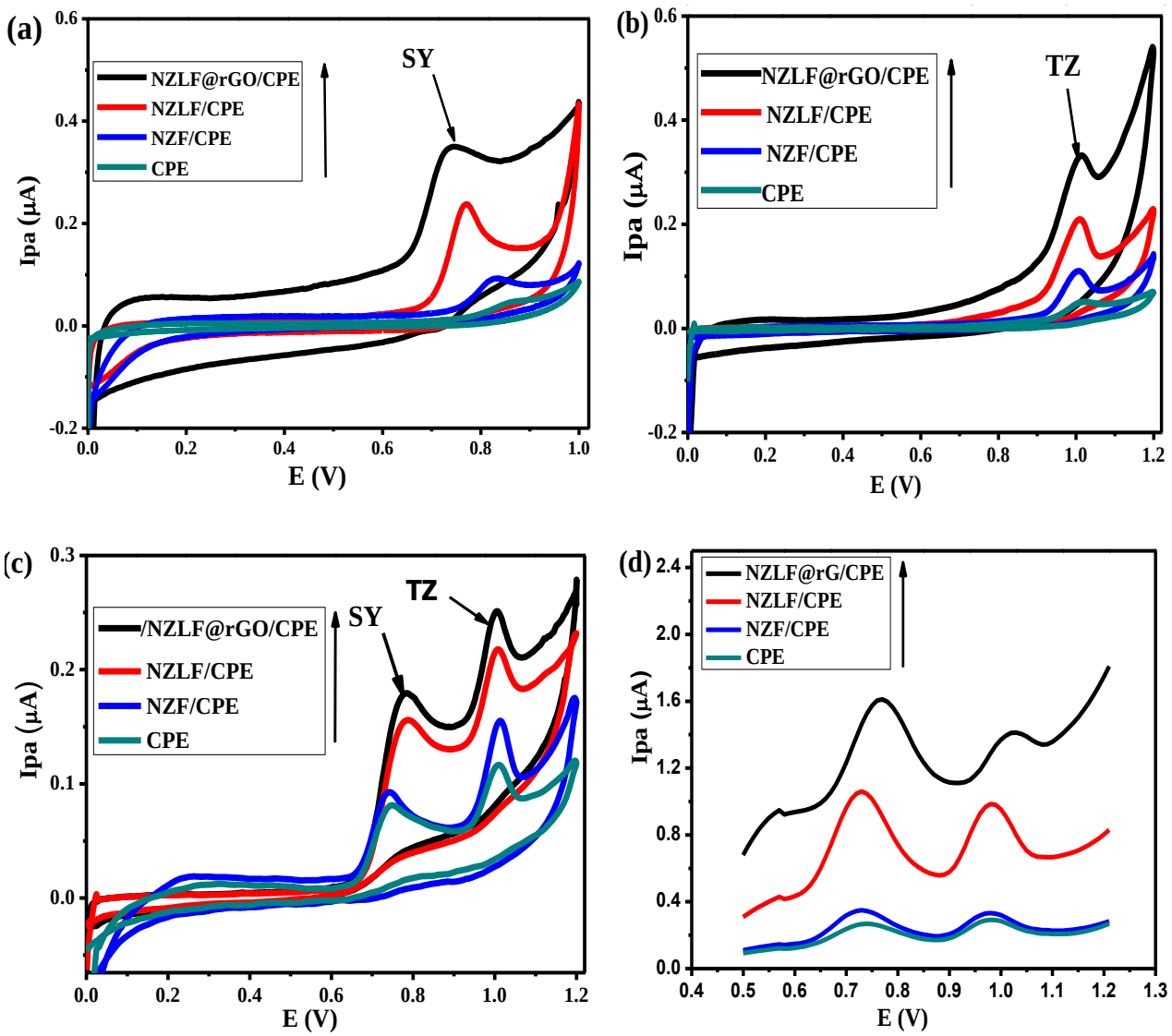

Figure 4.39: CV plots of (a) 0.1 mM of SY; (b) 0.1 mM of TZ; (c) 0.1 mM of SY and TZ; and (d) SWV plots of 0.1 mM of SY and TZ at the bare and modified electrodes.

In general, according to the findings of CV and SWV results, relative to bare CPE, NZF, and NZL_6F, the highest anodic peak current for SY and TZ are found in the NZLF@rGO/CPE with the sharpness of the peak. The synergetic effect of $Ni_{0.75}Zn_{0.25}Fe_2O_4$, La^{3+} ions, and rGO effectively improves the electrochemical response of the CPE by increasing the active surface area of the electrode, transfer of electrons, and electrode conductivity. From this, it can be predicted that the fabricated electrode (NZLF@rGO/CPE) is efficient enough to determine SY and TZ colorants in their mixtures.

The proposed mechanism of the electrochemical oxidation process for SY and TZ colorants is illustrated in Figure 4.40 (Jin *et al.*, 2016 ; Bessegato *et al.*, 2019 ; Taei, 2020).

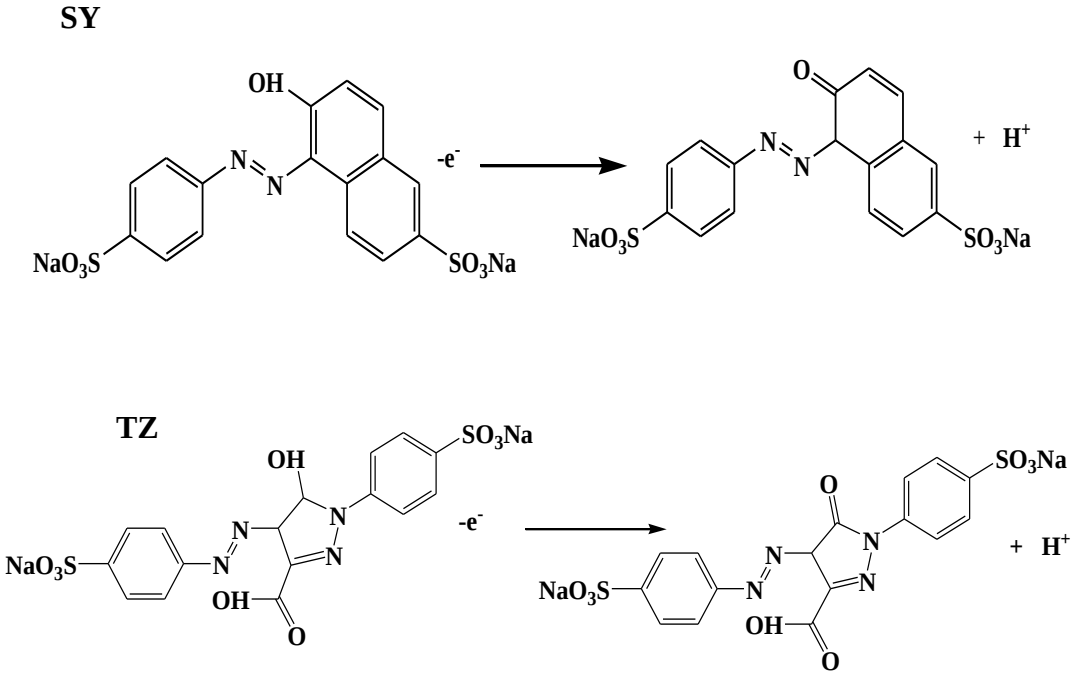

Figure 4.40: Electrochemical oxidation mechanism of SY and TZ

4.5.1.1 Conditions Optimization

The experimental parameters, including pH value and scan rate, were optimized to obtain an efficient current response during the electrochemical detection of SY and TZ.

4.5.1.1.1 Effect of pH

The pH of the electrolyte solution has a remarkable influence on the SY and TZ electrooxidation on the NZLF@rGO/CPE. Figure 4.41 illustrates the influence of pH on the peak current of SY and TZ in the pH range of 2-8 to establish the ideal acidity and alkalinity of the medium for measuring azo dyes on the proposed sensor. As illustrated in Figure 4.4a, the I_p of SY and TZ tend to increase with pH and reach a maximum at pH 6, above which it decreases. This may result from the adsorption behavior of SY and TZ on the NZLF@rGO/CPE (Hoan *et al.*, 2020). SY and TZ are protic aromatic molecules (Figure 4.41) and can become deprotonated to form negatively charged species (anions) at higher pH (Arancibia *et al.*, 2014). Simultaneously, the surface of NZLF@rGO/CPE also becomes negatively charged at high pH (Ahmed *et al.*, 2021; Rahman *et*

al., 2020). As a result, less intensive adsorption of the analytes on the electrode might occur, reducing the I_p (Masoumeh *et al*., 2020). The maximum current for the mixed SY-TZ colorants was observed at pH six and was used as an optimum pH value for detecting both dyes using the NZLF@rGO/CPE electrode.

The pH effects on peak potentials (E_p) of SY and TZ oxidation on the NZLF@rGO/CPE were also studied. Figure 4.41b illustrates that the oxidation peak potentials of SY and TZ shifted to low positive values with increasing pH, indicating that the protons participated in the redox reaction (Jin *et al*., 2016). Figure 4.41b shows the linear relationship between the pH and the peak potentials of SY and TZ with the slope values of 0.051 and 0.053 V for TZ and SY, respectively. These values are also close to the electrochemical process's theoretical value of 0.059 V/pH, suggesting that oxidation of SY and TZ involves an equal number of protons and electrons (Hoan *et al*., 2020).

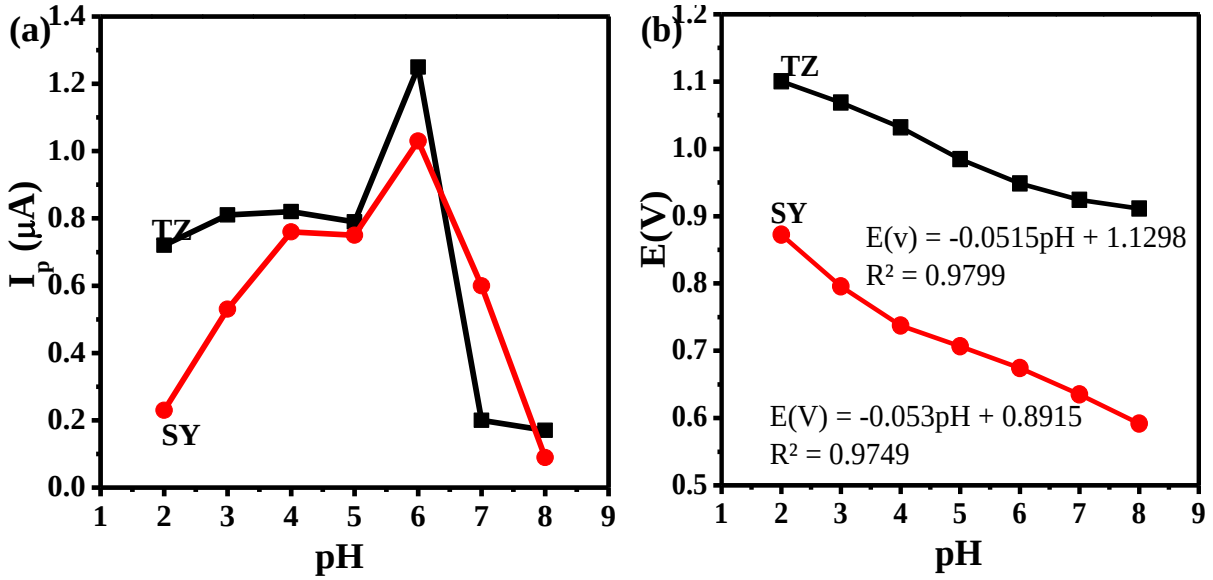

Figure 4.41: Effect of pH for 0.1 mM of SY and TZ at NZLF@rGO/CPE in phosphate buffer solution at a scan rate of 50 mV/s (a) change in the catalytic current; (b) linear relationship of pH value and the anodic peak potential.

4.5.1.1.2 Influence of potential scan rate (v)

The effect of the scan rate on the electrochemical signals of SY and TZ was assessed by changing the scan rate from 10 to 100 mV s^{-1} (Figure. 4.42). Figure 4.42a illustrates the effects of scan rate on the electrochemical response of SY and TZ by CV on NZLF@rGO/CPE in 0.1 M PBS at pH

6. It is seen that the oxidation peak currents of SY and TZ linearly increase with the increase in scan rates. Their corresponding oxidation peak potentials also shift to more positive potentials, confirming the involvement of a single proton in the reaction (Ghoreishi *et al*., 2012; Hoan *et al*., 2020).

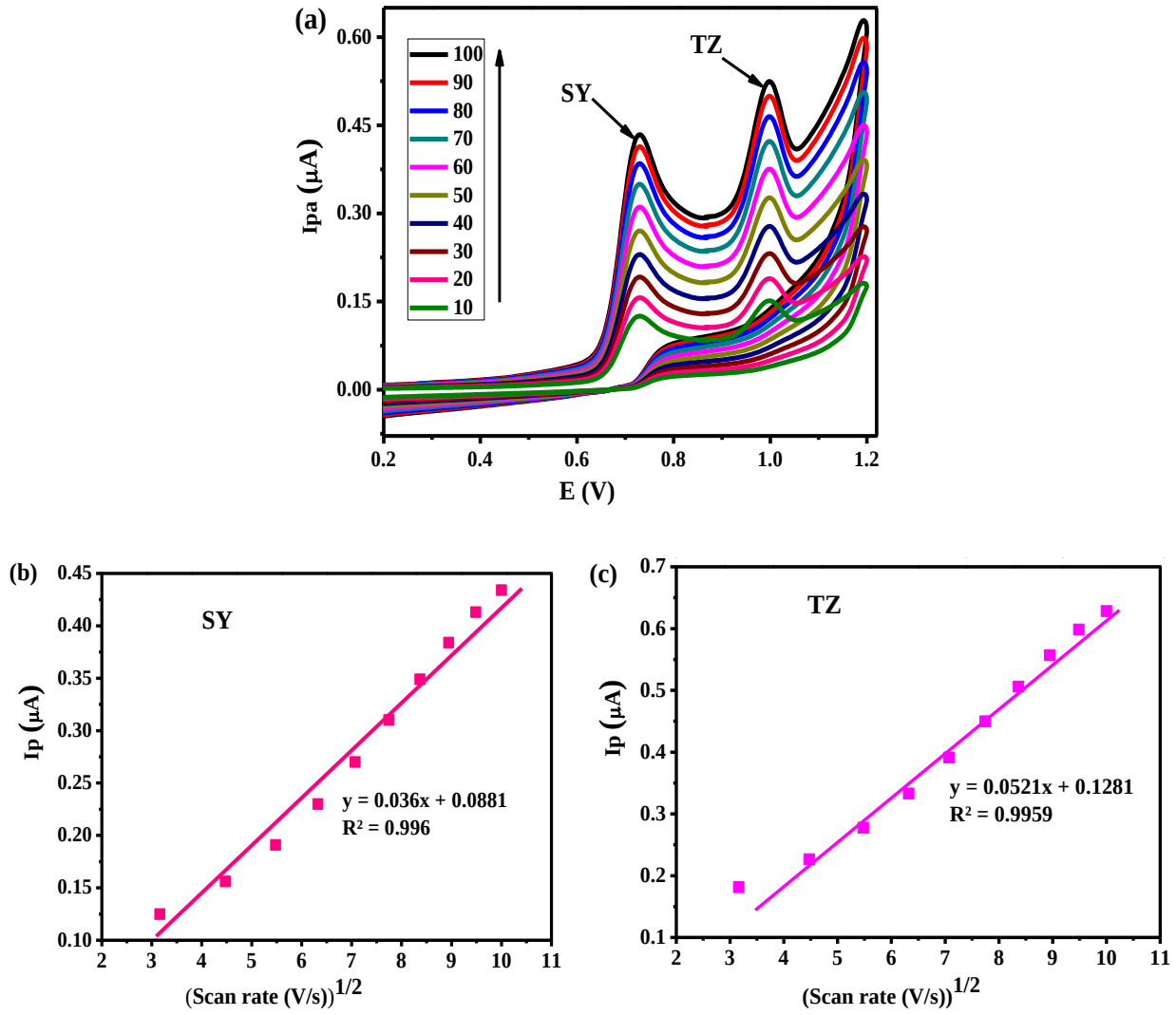

Figure 4.42: CVs of 0.1 mM SY and TZ in 0.1 M phosphate buffer solution at pH six at the NZLF@rGO/CPE surface (v) (a) influence of potential scan rate; and (b, c) plot of the linear variation of peak current (I_p) vs. the square root of scan rate ($v^{1/2}$) for SY and TZ, respectively.

In Figure 4.42(b, c), it is observed that the anodic peak currents of both SY and TZ increase linearly with the increase in scan rate; using the calibration equations,

$$I_p\ (SY) = 0.036x + 0.0881\ (R^2 = 0.996) \qquad (4.12)$$

I_p (TZ) = 0.0521x + 1281 (R^2 =0.9959) (4.13)

This linear variation of peak current (Ip) vs. the square root of scan rate ($\nu^{1/2}$) for SY and TZ corresponds to the electrode oxidation reaction controlled by diffusion coefficient and the involvement of a single proton in the reaction (Ghoreishi *et al*., 2012; Oliveira *et al*., 2015; Karim-Nezhad *et al*., 2017; Perdomo *et al*., 2017).

4.5.1.1.3 Electrochemical Detection of SY and TZ on the Modified Electrode

Differential pulse voltammetry (DPV) was employed to study the sensitivity and accuracy of NZLF@rGO/CPE for detecting and quantifying SY and TZ. Parameters for DPV included pulse height of 50 mV, pulse width of 5 ms, step height of five mV, and stipe time of 100 ms (Ghoreishi *et al*., 2012).

The limit of detection (LOD) for the analyses was calculated using equation 4.14 (Wang *et al*., 2016).

$$LOD = \frac{3S_b}{m} \quad (4.14)$$

m = slope of the calibration line, S_b = the standard deviation of the blank.

Figure 43a illustrates the DPV response of SY in the concentration range of 0 µM to 105 µM on NZLF@rGO/CPE under the fixed amount of ten µM of TZ using optimized experimental conditions. To this end, the intensity of anodic current for SY linearly increases with concentration while TZ was kept constant (Darabi *et al*., 2021). A LOD of 0.0021 µM was calculated from the calibration curve.

Figure 4.43b illustrates the DPV response of TZ in the concentration range of 0 to 120 µM with a fixed amount of ten µM of SY. To this end, the intensity of anodic current for TZ linearly increased with concentration while the SY was kept constant. The respective calibration curve was found to contain two linear regions:

first from 0-30 µM with the regression equation

I_p (µA) = 0.0947x + 0.489 (R^2 = 0.988) (4.15)

the second linear region from 40-120 µM with the regression equation

I_p (µA) =0.2422x + 0.7506 (R^2 = 0.993) (4.16)

A LOD of 0.0034 µM was determined based on the first range (Jin *et al.*, 2016).

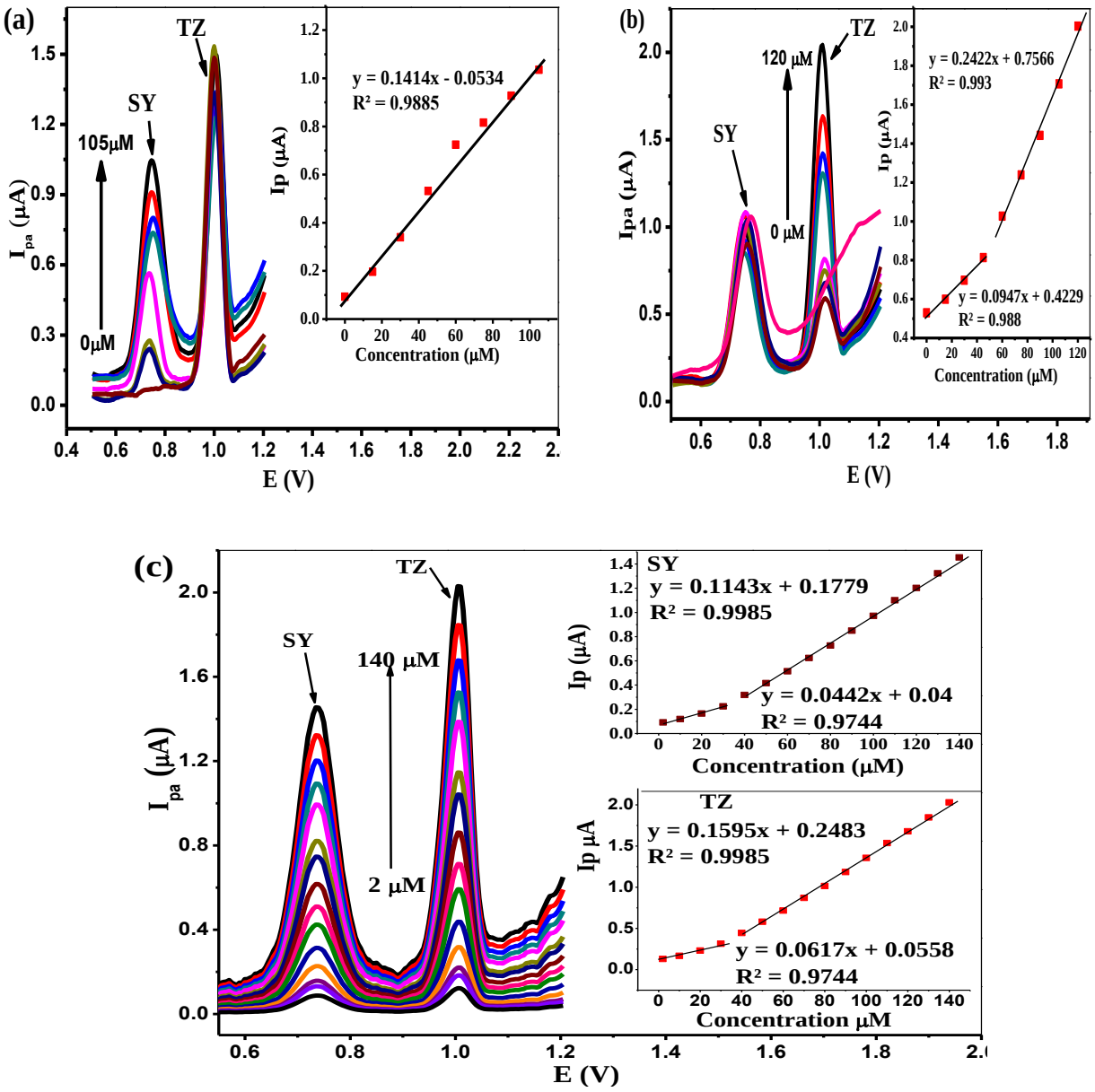

Figure 4.43: Calibration curves for the corresponding DPV voltammograms (inset) for determination of (a) SY (0 to 105 µM) in the presence of ten µM of TZ; (b) TZ (0 to 120 µM) in the presence of ten µM SY; (c) simultaneous determination of SY and TZ (1 to 140 µM) ten µM in a 0.1 M PBS on the surface of the working electrode, NZLF@rGO/CPE. Condition: pulse height 50 mV, pulse width (P_W) of five ms, step height five mV, step time 100 ms, potential range - two to +two V, scan rate 50 mV/s, current range ten mA.

For simultaneous detection (Figure 4.43c), it was found that the peak current for both SY and TZ increased linearly over the concentration range of two to 140 μM. As shown in the inset of Figure 4.43c, the oxidation peak current of SY and TZ versus their concentration on NZLF@rGO/CPE has a good linearity in the range of 2 μM to 140 μM with two linear functions. That can be described by the influence of diffusion for lower ranges and then by the phenomena of adsorption at higher range (Stankovic *et al.*, 2018). This analysis calculated 0.0041 and 0.0032 μM LOD values for SY and TZ, respectively, from the lower range of the calibration curves. The results show that the slope value for SY is lower than that for TZ, but the detection limit is lower for TZ. The presence of TZ may affect the absorption of SY on the surface of the electrode because NZLF@rGO/CPE has high activity towards TZ in the presence of SY (Penagos-Llanos *et al.*, 2020)The results confirmed the development of a well-performing electrode for detecting SY and TZ individually or in combination simultaneously. As depicted in Table 4.5, the electrode's sensing capabilities were compared with literature reports to assess SY and TZ.

4.5.1.2 Reproducibility, Repeatability, Stability and Selectivity of the Method

A solution containing 5.0 μM of SY and TZ was applied to analyze the reproducibility, repeatability, and stability of NZLF@rGO/CPE by DPV. The reproducibility analysis was studied by fabricating five NZLF@rGO/CPE modified electrodes using the same method and applied to determine SY and TZ (Figure 44a). The relative standard deviation (% RSD) of 3.57 and 3.75 % for SY and TZ were obtained, respectively, which suggested excellent reproducibility of NZLF@rGO/CPE. Six repetitive experiments were conducted using a single electrode to analyze repeatability (Figure 44b). The NZLF@rGO/CPE electrode surface was renewed by removing a small plug of the old electrode surface with a glass rod and flattening the resulting new surface on paper. The RSD for the six replicate measurements for SY and TZ was 2.1 and 3.7%, respectively. Moreover, the stability of NZLF@rGO/CPE was evaluated over two weeks by regular detection of SY and TZ at three-day intervals using the same electrode under optimized experimental conditions (Figure 44c. After two weeks, a 96.04% initial response of the electrode remained, which confirmed that the NZLF@rGO/CPE exhibited good storage stability under optimal conditions. In the presence of food additives, including sugar and salts, the interference selectivity of NZLF@rGO/CPE was examined (Figure 44d). According to the experimental findings, no effects were observed in the detection of 5.0 μM SY and TZ following the addition of 1.0 mM of

Zn^{2+}, Cu^{2+}, Fe^{3+}, Mg^{2+}, Ca^{2+}, CO_3^{-}, SO_3^{2-}, NO_3^{-} ions, Cl^{-}, glycine, vitamin C, glucose, sucrose, and benzoic acid. Due to its operational stability and enhanced selectivity, this sensor exhibited promising quality for usage in real samples with little sample preparation.

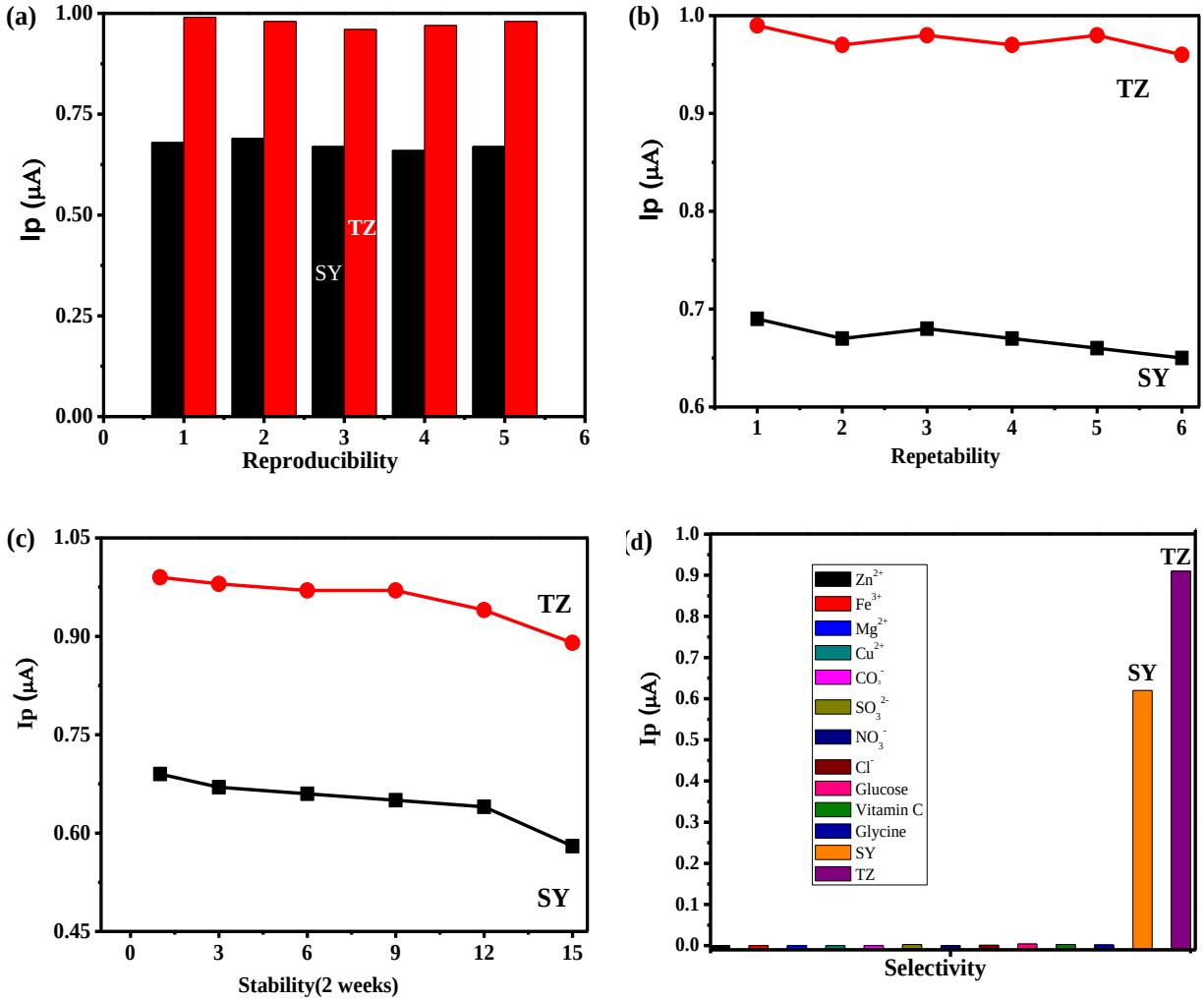

Figure 4.44: Reproducibility, repeatability, stability, and selectivity test of the NZLF@rGO/CPE; (a) peak current response of 5 µM of SY and TZ at five electrodes, (b) repetitive measurement of 5 µM of SY and TZ at one electrode, (c), stripping response of 5 µM of SY and TZ dyes storage up to two weeks, (d) effect of interferences.

4.5.1.3 Application of Real Samples

The practical applicability of the developed sensor, NZLF@rGO/CPE, real samples analysis was employed to determine SY and TZ in (orange powder, mango juice, and pineapple powder by spiking under optimum conditions using DPV. The results are depicted in Table 4.5. No special

preparation was required to analyze liquid samples, whereas powder samples took 5 g and dissolved in ten mL of DD water. 2 mL of samples were diluted ten times with 0.1 M of PBS (pH 6) to reduce the interference. The concentrations of SY and TZ in the selected samples were obtained based on the calibration graph measured using the DPV signals. The recovery experiments were also conducted by spiking different known concentrations of selected samples of food products. As depicted in Table 4.5, the NZLF@rGO/CPE obtained a reasonable recovery of 92-97% for SY and 91-95% for TZ. These results are within the acceptable limits (90-100%). This suggested that the developed electrode sensor is highly accurate, sensitive, and selective for detecting SY and TZ in actual samples (Karim-Nezhad *et al*., 2017; Masoumeh *et al*., 2020).

Table 4.5: Analysis of real samples: pineapple powder, orange powder, and mango juice for detecting SY and TZ. The concentrations are expressed in μM. n = 4.

Sample	**Spike**	**Concentration unknown**		**Concentration spiked**		**Recovery (%)**	
		SY	**TZ**	**SY**	**TZ**	**SY**	**TZ**
Pineapple powder	-	0	0	-	-	-	-
	10	15.6	40.8	24.8	49.9	92	91
		12.3	43.2	21.9	52.7	95.7	95
Orange powder	-	0	0	-	-	-	-
	10	25.3	44.5	34.9	53.9	96	94
		30.2	49.3	39.9	58.7	97	94
Mango juice	-	0	0	-	-	-	-
	10	20.1	36.3	29.8	45.6	97	93
		24.2	38.9	33.9	48.3	97	94

4.5.1.4 Comparison of Current Method with the Reported Methods

The new method's versatility was compared with previous reports using electrodes modified with other metal ion oxides. The many properties that are summarized in Table 4.6 (Raril *et al*., 2018; Chebotarev *et al.*, 2019; Ghoreishi *et al*., 2012; Manjunatha, 2018; Tran *et al.*, 2019; Masoumeh *et al.*, 2020; Akkapinyo *et al.*, 2021; Moarefdoust *et al.*, 2021). It clearly shows that the proposed electrode has the lowest detection limits for simultaneous detection of SY and TZ, which is better

than many of the previous sensors and has a, more extensive linear range than the sensors with the lowest detection limit. In addition, they are electrodes with more complex modifications, while the suggested electrode used economical equipment in a relatively short time. This strategy may have been predicted as a promising technique for applying as a practical application. It also offers maximum repeatability, reproducibility, and selectivity.

Table 4.6: Comparison between variously reported literature and the present work for simultaneous detection of SY and TZ.

Electrodes	**Concentration range (μM)**		**LOD (μM)**		**References**
	SY	**TZ**	**SY**	**TZ**	
In^{3+}/NiO RLHNSs/GCE	1–70	1–70	0.0027	0.0031	Moarefdoust *et al*., 2021
rGO-methionine/SPCE	1-50	1-85	0.048	0.041	Akkapinyo *et al*., 2021
TX-100/CPE	-	6 - 1×100	-	1.114	Raril *et al*., 2018
SG/CPCl/CPE	0.02–1	0.04–1	0.005	0.008	Chebotarev *et al*., 2019
ERGO/GCE	0.05–1	-	0.0192	-	Tran *et al*., 2019
nAu/CPE	0.1–2	0.05–1.6	0.03	0.002	Ghoreishi *et al*., 2012
PGMCPE	-	1-100		150	Manjunatha, 2018
$ZnCrFeO_4$/CPE	0.07-47.5	0.05-19	0.002	0.01	Masoumeh *et al*., 2020
NZLF@rGO/CPE	***2-140***	***2-140***	***0.0067***	***0.0048***	***Current work***

4.6 Applications of $Ni_{0.75}Zn_{0.25}Eu_xFe_{2-x}O_4$ and $Ni_{0.75}Zn_{0.25}Eu_xFe_{2-x}O_4$@rGO NCs

4.6.1 Photocatalytic applications

The comparison of the photocatalytic activities of the synthesized samples, $Ni_{0.75}Zn_{0.25}Eu_xFe_{2-x}O_4$ (x = 0.00, 0.02, 0.06, and 0.1) nanocomposites, for simultaneous degradation of mixed dyes MO and MB under visible light irradiation, is illustrated in Figure 4.45. As compared to the pure NZF spinel ferrite nanoparticles, Eu^{3+} ion doped NZF ferrite nanoparticles showed enhanced photocatalytic activity in the degradation of the mixed dyes MO and MB, which is due to the synergistic effect of the doping Eu^{3+} ions (Tsvetkov *et al*., 2019). As seen in Figure 4.45(A & B), amongst the different concentrations of Eu^{3+} ion doped NZF spinel ferrite nanoparticles, the 6 mol% (x=0.06) of Eu^{3+} ion doped NZF spinel ferrite had the highest degradation efficiency of the

mixed MB and MO dyes. This result is consistent with the characterization results, including crystal size, bandgap energy, and intensity of emission peaks obtained under the respective analysis of XRD, UV-Vis-DRS, and PL. From this, it is possible to affirm that the band gap energy, crystal size, and surface area of the catalysts are the main factors for the efficiency of photodegradation of organic pollutants.

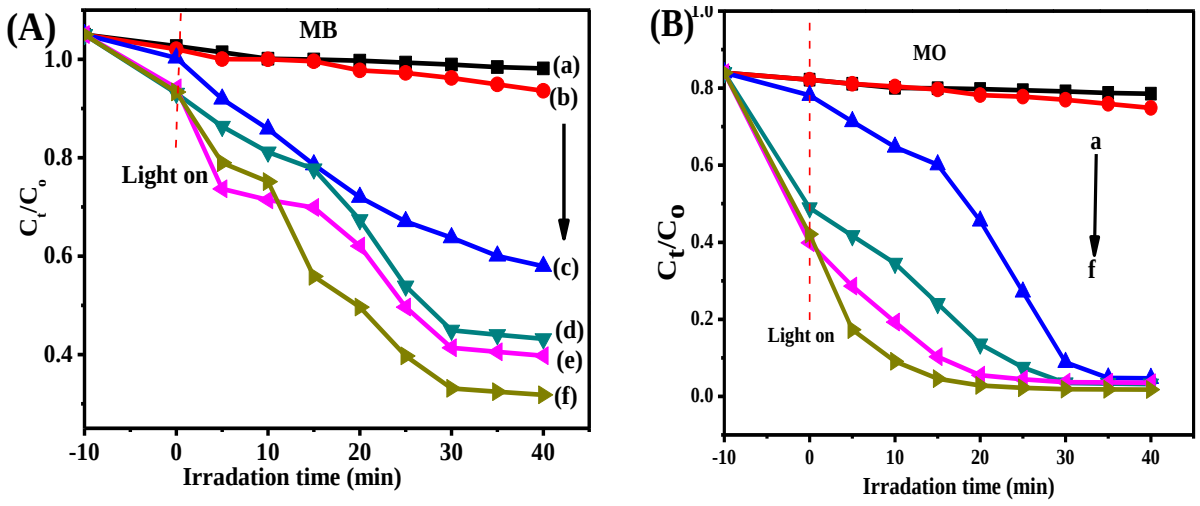

Figure 4.45: Degradation curves (C_t/C_0 dependence on the irradiation time) for the mixed dyes MB and MO under different experimental conditions, (a) dark, (b) blank, (c) NZF; (d) NZE_2F, and (e) $NZE_{10}F$; (f), NZE_6F.

Thus, 6 mol% of Eu^{3+} ion doped NZF spinel ferrite ($Ni_{0.75}Zn_{0.25}Eu_{0.06}Fe_{1.94}O_4$) was selected for the synthesis of the nanocomposite with reduced graphene oxide ($Ni_{0.75}Zn_{0.25}Eu_{0.06}Fe_{1.94}O_4$@rGO) and used for the subsequent photocatalytic activity experiments.

Figure 4.46 illustrates the degradation curves for MB and MO under different experimental conditions. From the degradation profiles of the dyes [Figure 4.46(A & B)], it is observed that there is no degradation of the dyes in the dark and blank (under visible light irradiation without catalyst) (Tsvetkov *et al.*, 2019). In the presence of H_2O_2 and visible light irradiation without a catalyst, only < 5% degradation occurred for both dyes. Using the nano ferrite catalysts (NZF, $NZEu_6F$), more than 85% of both dyes (MB and MO) degraded (Patil *et al.*, 2017).

The adsorption of pollutants on the surface of the photocatalyst is a prerequisite for degradation efficiency (Tsvetkov *et al.*, 2019). The introduction of rGO in the photocatalyst leads to an increase

in the adsorption sites, which leads to an improvement in the degradation performance of the photocatalyst (Liang *et al*., 2018). Therefore, a higher percentage of both dye molecules were degraded using NZEF@rGO nanocomposite. The presence of peroxide as an oxidizing agent also promotes the degradation of mixed dyes MB and MO within a short period (Patil et al., 2017). This is explained based on the fact that the addition of H_2O_2 increases the concentration of •OH radicals, thereby improving the rate of photocatalytic oxidation (Alam, 2018; Patil et al., 2017).

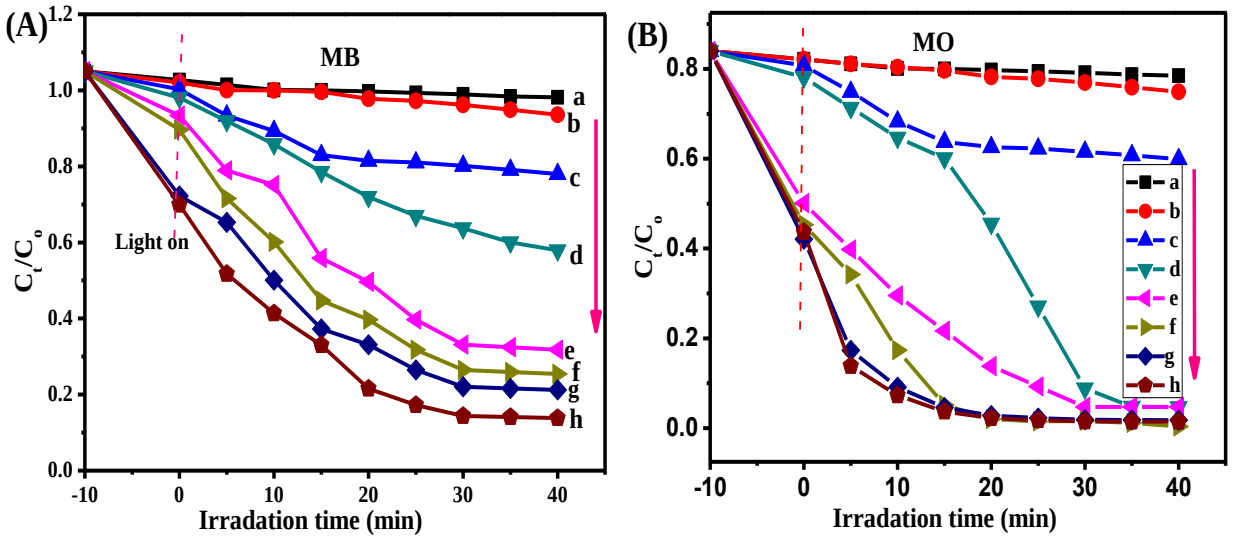

Figure 4.46: Photocatalytic degradation of mixed dyes MB and MO under conditions of (a), dark; (b) blank; (c) MB/MO + light + H_2O_2; (d) NZF; (e) NZE_6F; (f) NZE_6F + H_2O_2; (g) NZEF @rGO; and (h) NZEF@rGO nanocomposite + H_2O_2.

Figure 4.47(a-c) illustrates the UV-visible spectra for photocatalytic degradation of the mixed dyes MB and MO simultaneously under the conditions including the absence of photocatalyst, with NZE_6F nanoparticles and NZEF@rGO nanocomposite respectively, under visible light irradiation for 40 minutes. The presence of MO and MB in their mixture is indicated by the peaks at 464 nm for MO and two absorption peaks at 609 and 664 nm for MB (Nguyen *et al*., 2019).

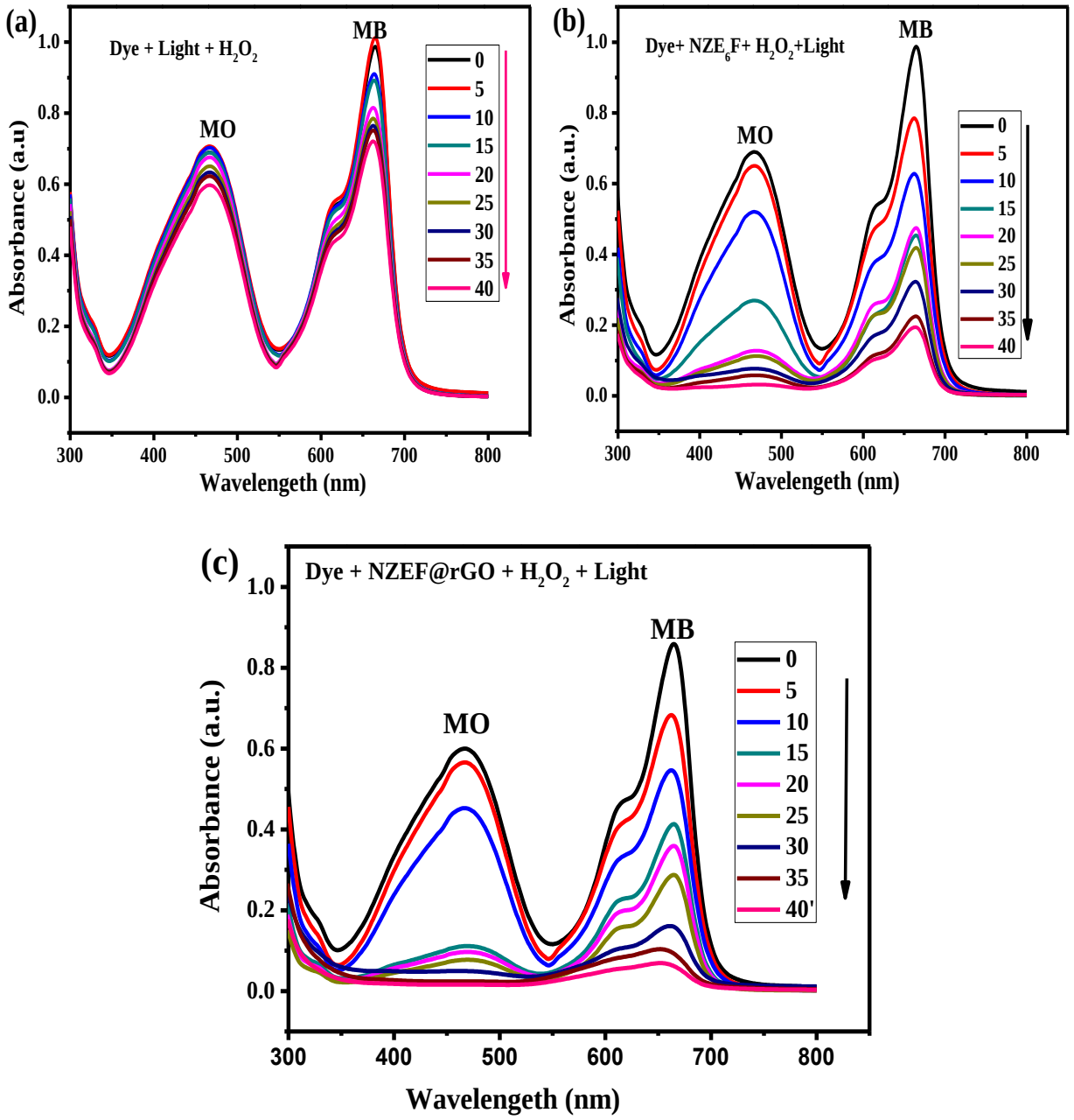

Figure 4.47: Absorption spectra of mixture dyes (MB and MO) in aqueous solutions taken at predefined times (a) without photocatalyst; (b) with NZE_6F SPFNPs; and (c) with NZEF@rGO nanocomposite in the presence of H_2O_2 under optimized experimental conditions of pH 9, initial concentration of dyes 10 mg/L and catalyst dosage of 50 mg at room temperature.

In Figure 4.47a, it is seen that < 5 % of the mixed dyes MB and MO degraded in the presence of only H_2O_2 under visible light irradiation in 40 minutes, suggesting that both dyes are stable under visible light irradiation of light in the absence of catalyst. In the presence of

$Ni_{0.75}Zn_{0.25}Eu_{0.06}Fe_{1.94}O_4$ photocatalyst (Figure 4.46b), a degradation efficiency of MO (82%) and MB (75%) is obtained, which indicated the positive influence of NZE_6F photocatalyst on the degradation of the mixed dyes (O *et al*., 2019). Figure 4.46c illustrates the effect of rGO on the photocatalytic activity of NZE_6F nanoparticles for the degradation of mixed dyes. It is observed that compared to the NZE_6F catalyst, the NZEF@rGO nanocomposite is more efficient for the degradation of the mixed dyes (i.e., 97% for MO and 92% for MB) under the same optimized conditions. This is due to the rGO nanosheets, which serve as an electron sinker by accepting the photo-induced electrons rapidly from NZE_6F nanoparticles and impeding their recombination with the photo-induced holes (Patil *et al.*, 2017). This causes the production of highly reactive radical species, which significantly enhance catalytic degradation of the mixed dyes MO and MB under visible light irradiation (Ali, *et al.*, 2020).

4.6.1.1 Optimization of Parameters

4.6.1.1.1 Effect of pH

Since the pH dictates the surface charge properties of the catalysts and the adsorption behavior of pollutants on the surface of catalysts, it plays a significant role in the reaction mixture of heterogeneous photocatalysis (O *et al*., 2019). Figure 4.48 illustrates the effect of pH on the degradation efficiency of the mixed dyes MO and MB in the presence of NZEF@rGO nanocomposite. The degradation of MO was nearly consistently high until pH nine, whereafter it decreased, whereafter it decreased with further increases in pH. Conversely, the degradation of MB increased with the increase in pH *(*Rahman *et al.*, 2020*).* This variation of degradation efficiency with pH is directly related to the surface charge of the NZEF@rGO nanocomposite at different pH. Hence, the cationic dye MB may dissolve under acidic conditions, while the anionic dye MO has a strong electrostatic interaction with the catalyst's surface, facilitating its degradation rate. Meanwhile, the cationic dye MO dissolves at a higher pH (alkaline media). In contrast, the anionic dye MB interacts with the surface of the NZEF@rGO nanocomposite, which facilitates its degradation rate (Ahmed *et al*., 2021). Accordingly, the expected degradation efficiency for both dyes was obtained at pH nine. Hence, the subsequent experiments employed it as an optimum pH value.

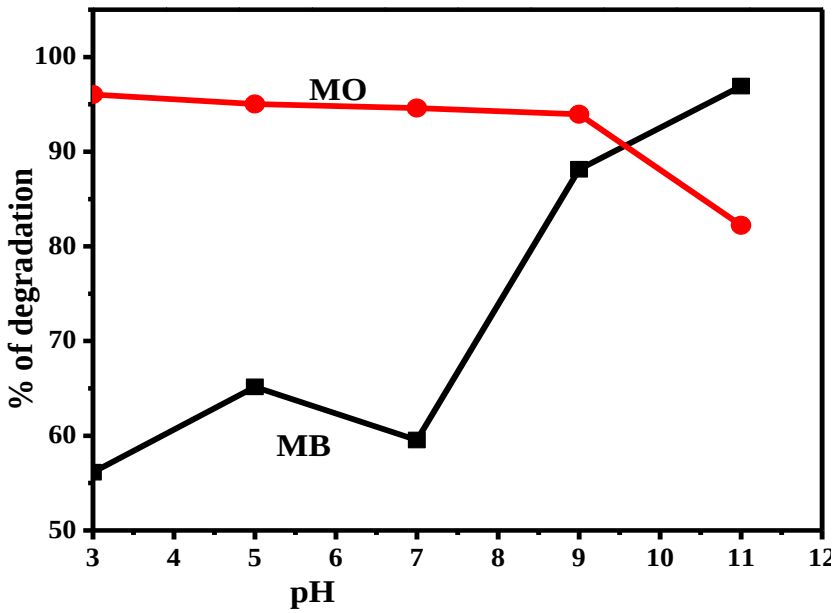

Figure 4.48: Effect of pH on the mixed dyes MO and MB degradation efficiency.

4.6.1.1.2 Effect of Catalyst Dosage

The amount of photocatalyst is a crucial factor that significantly influences the photo-removal rate of organic dyes (Rahman *et al.*, 2020). Thus, to evaluate the effect of catalyst dosage on the photodegradation of binary dyes (MB and MO), experiments were performed by changing the catalyst dosage from 25 to 100 mg. At the same time, all other experimental conditions were maintained the same way for photocatalytic activity. As illustrated in Figure 4.49, the degradation efficiency for both dyes increased with increasing catalyst dosage from 25 to 50 mg/L and then decreased. The increase in photodegradation efficiency with an increase in catalyst dosage is attributed to the availability of more active sites that allow light penetration, improving the photocatalytic activity. The decreasing degradation efficiency after reaching the optimal dosage of 50 mg/L is attributed to the increasing turbidity of the solution and aggregation of the catalyst, which causes inhibition of light penetration, leading to a decrease in the degradation efficiency (Patil *et al.*, 2019). Thus, 50 mg/L was the optimum MO and MB degradation catalyst dosage.

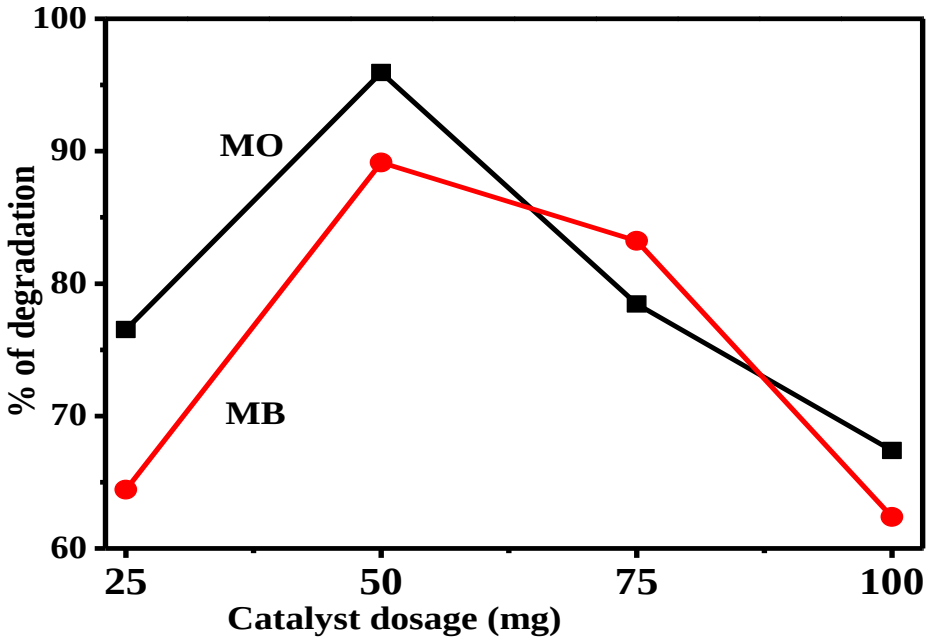

Figure 4.49: Effect of catalyst dosage on the degradation efficiency of combined MB and MO dyes under visible light irradiation.

4.6.1.1.3 Effect of Initial Dye Concentration

The initial concentration of dyes is one of the essential parameters taken into consideration for assessing the photocatalytic activity (Rahman *et al*., 2020). Hence, the effect of the initial concentration of MB and MO was studied by varying their concentration from 5 to 20 mg/L in the presence of the NZEF@rGO nanocomposite with a catalyst dosage of 50 mg at pH nine under irradiation of visible light, as illustrated in Figure 4.50. The results showed that the percent degradation of both dyes (MB and MO) decreased with an increase in the initial concentration of dyes from five mg/L to 20 mg/L. The reason for the slow degradation of substrates at high concentrations is due to the adsorbed dye molecules which obscure the active site of the catalyst, and the intense color of the substrate suppers the falling of light on the catalyst surface to generate charge carriers (Patil *et al.*, 2019). Thus, the number of active species the catalyst forms becomes limited at high substrate concentrations. The limited reactive species against the increased dye concentration decreases the catalysts' degradation efficiency. Thus, 10 mg/L of dye was taken as a moderate initial dye concentration.

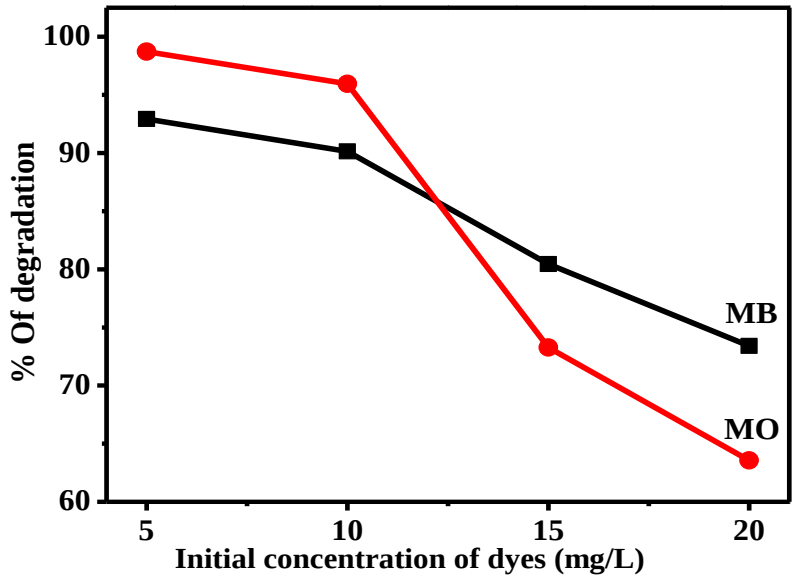

Figure 4.50: Effect of MB and MO dye concentration on their degradation using $Ni_{0.75}Zn_{0.25}Eu_{0.06}Fe_{1.94}O_4$@rGO nanocomposite at pH 9.

4.6.1.1.4 Reactive Species Trapping Study

Scavenger experiments were conducted to ascertain the main reactive species involved in degrading the mixed dyes MB and MO using NZEF@rGO nanocomposite, as illustrated in Figure 4.51. For this experiment, scavengers including disodium ethylenediaminetetraacetate (EDTA-2Na), $K_2Cr_2O_4$, KI, and AA, respectively, were used for trapping h^+, e^-, •OH and $O_2^{\bullet-}$ radicals formed during the photo-oxidation process (Alam *et al*., 2018 ; Ahmed *et al*., 2021). As illustrated in Figure 4.51, the photocatalytic system without a scavenger resulted in a higher decomposition rate than a scavenger-assisted system. Amongst the scavengers, adding KI significantly reduced the percentage degradation of the mixed dyes by quenching the •OH radicals formed in the reaction mixture, indicating that these radicals were actively involved in the degradation process. Furthermore, the degradation efficiency of the mixed dyes was slightly reduced with the addition of EDTA, $K_2Cr_2O_4$, and AA, indicating that in addition to •OH radicals, e^-, h^+, and $O_2^{\bullet}$ radicals were also involved in the degradation process in decreasing order of $e^- < h^+ < O_2^{\bullet-} <$ •OH.

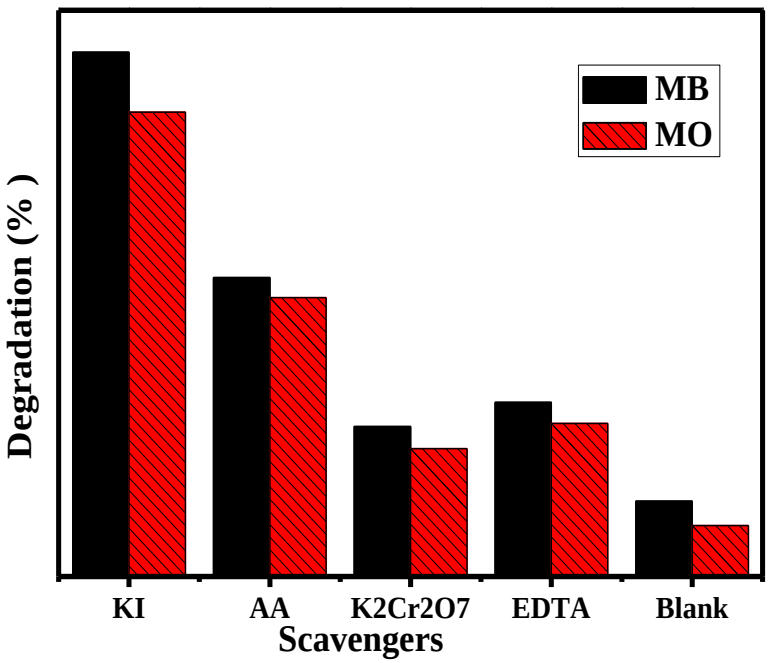

Figure 4.51: Effect of scavenger on the mixed dyes MB and MO degradation using $Ni_{0.75}Zn_{0.25}Eu_{0.06}Fe_{1.94}O_4$@rGO nanocomposites at pH 9.

4.6.1.1.5 Reusability of the Catalyst

The long-term usability of the catalyst is also an important factor in mitigating organic pollutants from wastewater (Alam, 2018). The recyclability was tested by reusing the photocatalyst NZEF@rGO for five consecutive cycles for degradation of the mixed MB and MO dyes at predetermined optimized conditions illustrated in Figure 4.52(a &b). After the first degradation cycle, the catalyst was isolated by applying an external magnetic field, washed with double distilled water followed by ethanol to remove the impurities, and dried at room temperature after each subsequent cycle. After five cycles, the loss in degradation efficiency is 8.23 % for MB and 4.56 % for MO. This signified the photostability of the NZEF@rGO nanocomposite photocatalyst. This loss of catalytic performance is attributed to a combination of factors, including the aggregation of the photocatalyst nanoparticles, the adsorption of intermediate products on the catalyst active sites, and the destruction of catalytic sites owing to photo corrosion and experimental error. The results suggest that the magnetic NZEF@rGO nanocomposite photocatalyst has excellent stability for reusing several times and is promising for degrading organic pollutants under invisible light irradiation.

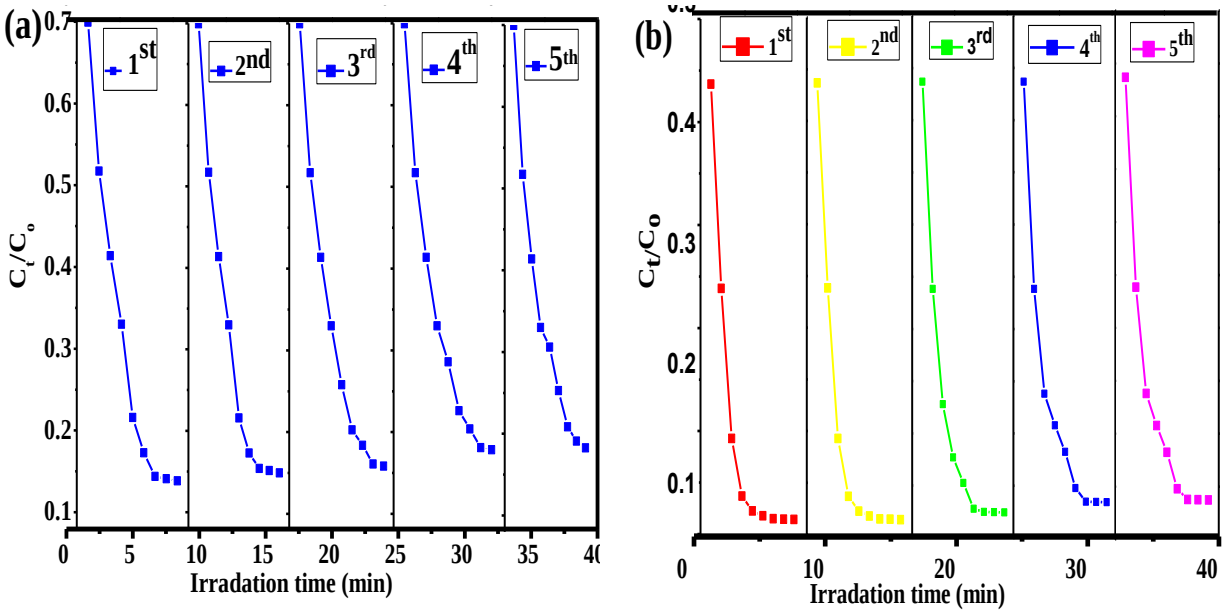

Figure 4.52: Recyclability of NZEF@rGO nanocomposite photocatalyst for the degradation of mixed dyes (a) MB and (b) MO under visible light irradiation.

4.6.2 Electrochemical sensor application

4.6.2.1 Electrochemical characterization of the modified electrode

Electrochemical impedance spectroscopy (EIS) and cyclic voltammetry (CV) were used to determine the electrochemical activity of the fabricated electrodes. 5 mM of ferricyanide ($K_3[Fe(CN)_6]$) was used as the redox probe in 0.1 M KCl electrolyte solution. Figure 4.53(a, b) illustrates the cyclic voltammogram and the Nyquist plot, respectively, for bare CPE and $Ni_{0.75}Zn_{0.25}Eu_xFe_{2-x}O_4$ (x = 0.00, 0.02, 0.06, and 0.1) modified CPEs. The current response is the signal of the redox probe (Akkapinyo *et al.*, 2021). As illustrated by the cyclic voltammograms in Figure 4.53a, the catalytic current response of CPE increased with increasing the content of Eu^{3+} ions, obtaining the highest current response at 6 mol% Eu^{3+} ions. This increase is attributed to the conductive nature of Eu^{3+} ions (Hossain *et al.* 2018).

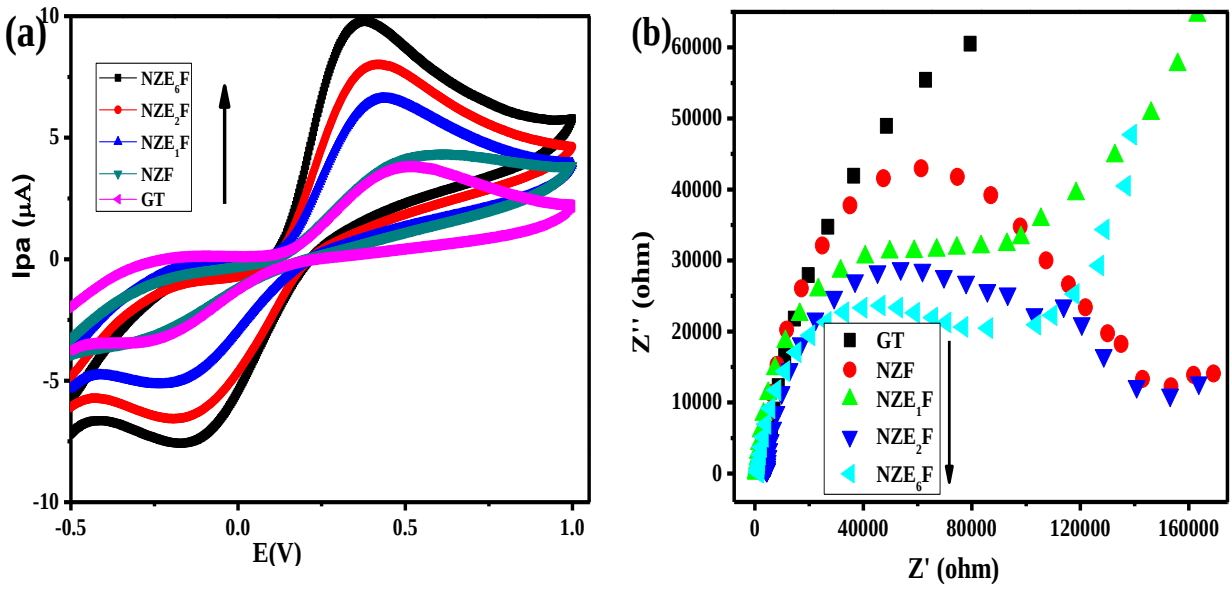

Figure 4.53: Bare CPE and modified CPEs (a) CV voltammograms showing the current response at a scan rate of 50 mV/s and (b) EIS in the frequency range of 10 mHz -100 KHz under working conditions of 5 mM of $[Fe(CN)_6^{3-/4-}]$ in 0.1M KCl solution as a supporting electrolyte.

A consistent result was obtained by EIS, as illustrated in Figure 4.53(b). Compared to the bar CPE electrode, the semi-circle diameters of the modified CPE dramatically decreased, with increasing content of Eu^{3+} ions. This indicates decreasing charge transfer resistance and/or increase in conductivity (Darabi *et al.*, 2021). Amongst the nanocomposites, the nanocomposite with 6 mol%

Eu^{3+} ions ($Ni_{0.75}Zn_{0.25}Eu_{0.06}Fe_{1.94}O_4$) performed better for the modification of CPE and was thus employed for the subsequent studies

Figure 4.54a illustrates the Nyquist plots of bare CPE and CPE modified with NZF, NZE6F, and NZEF@rGO in the frequency range of 10 mHz to 100 KHz. NZEF@rGO/CPE showed a significant change in the diameters of the semicircles, indicating that the introduction of rGO significantly enhanced the rate of electron transfer and the conductivity of the CPE electrode.

The cyclic voltammograms illustrated in Figure 4.54b also showed that the most significant current response occurs in NZEF@rGO/CPE attributed to the high surface area and fast electron transfer rate of rGO (Akkapinyo *et al.*, 2021).

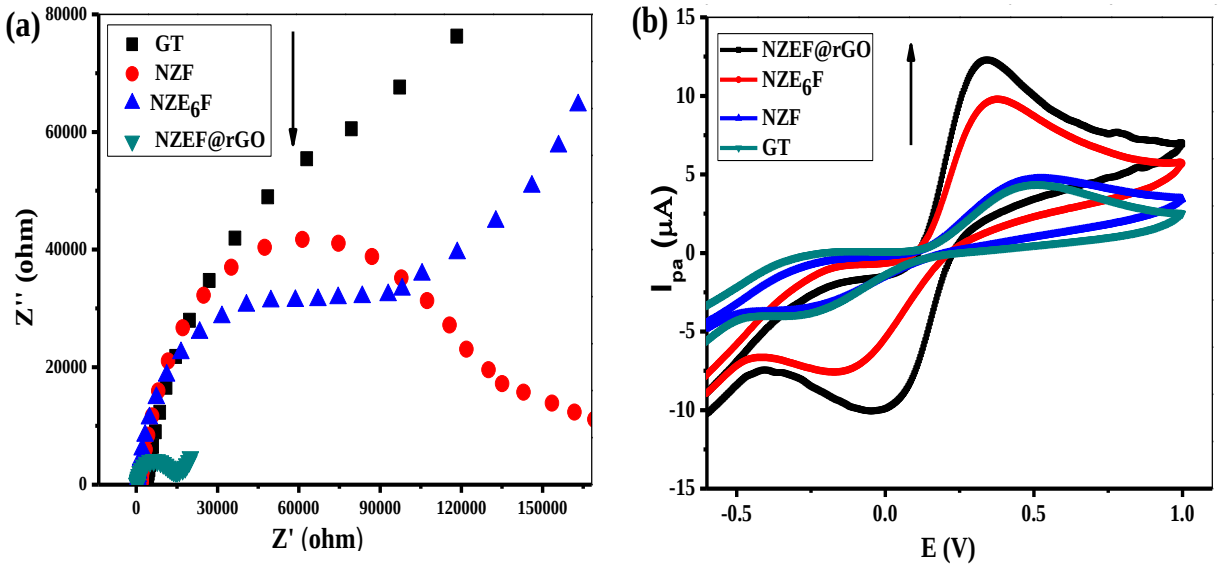

Figure 4.54: (a) Nyquist plots in the frequency range of ten mHz -100 KHz, and (b) the CV plots of the electrodes at a scan rate of 50 mV/s, under the working conditions of 5 mM of $[Fe(CN)_6]^{3-/4-}$ in 0.1 M KCl solution as supporting electrolyte.

To assess the effective surface area of the CPE and the CPE electrodes modified with NZF/CPE, NZE_6F/CPE, and NZEF@rGO/CPE cyclic voltammograms were recorded using 5 mM $[Fe(CN)_6]^{3-/4-}$ in 0.1 M KCl at different potential scan rates. Figure 4.55 illustrates the dependence of I_{pa} Vs $\upsilon^{1/2}$ for CPE and the modified CPEs.

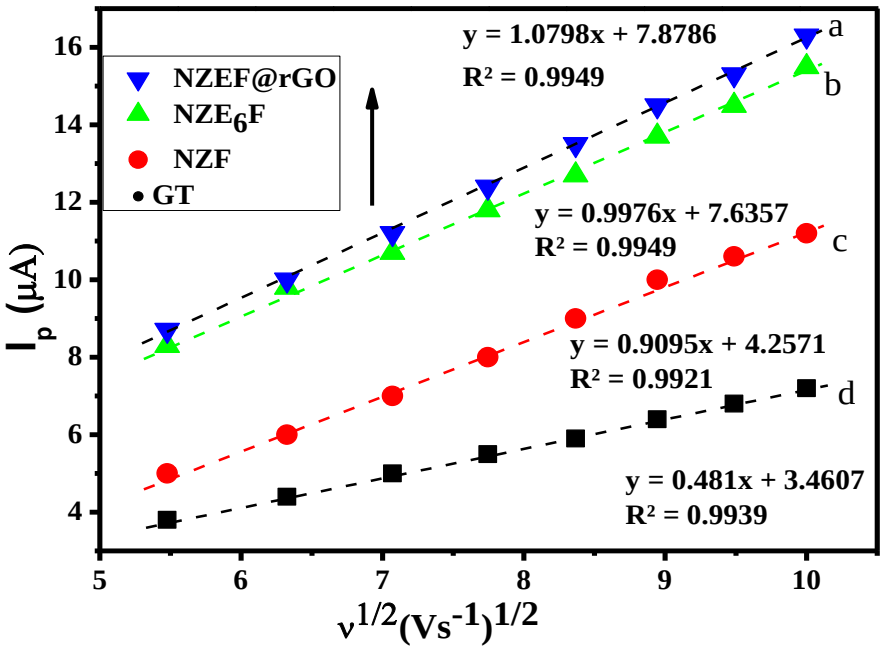

Figure 4.55: I_{pa} vs.. $\upsilon^{1/2}$ vs. I (mA) plots of the bare CPE and the CPE electrodes modified with NZF/CPE, NZE_6F/CPE, and NZE_6F@rGO/CPE using 5 mM $[Fe(CN)_6]^{3-/4-}$ in 0.1M KCl at different potential scan rate.

The effective surface area of the electrodes was calculated using the Randles-Sevcik formula (equation 4.17), and the slope of voltammograms of I_{ap} vs. $\upsilon^{1/2}$ was used as an effective surface area of electrodes (Tran et al., 2019).

$$I_{pa} = 2.686x10^5 n^{3/2} A D^{1/2} v^{1/2} C \quad (4.17)$$

I_p = peak current (A); n = number of electrons transfer occurred in the redox reaction (n=1); C = stand for the concentration of $[Fe(CN)_6]^{3-/4-}$ (5 mM); A = electrode active area (cm^2), D = diffusion coefficient of $[Fe(CN)_6]^{3-/4-}$ in solution (7.6 x 10^{-6} cm^2/s) and ν = potential scan rate (V s^{-1}).

The calculated electro-active surface area was 0.48, 0.90, 0.99, and 1.08 for CPE, NZF/CPE, NZE_6F/CPE, and NZEF@rGO/CPE, respectively. The effective surface area of the electrode is directly related to the rate of reaction, the electron transfer ability of the electrode, the rate of current flow through the electrode, and the sensitivity of the electrode (Zhang et al., 2022)The NZEF@rGO/CPE has a large active surface area, which allows for greater sensitivity, the highest current flow ability, and a fast electron transfer rate.

4.6.2.2 Electrochemical response of SY and TZ on modified CPE electrodes

Figure 4.56 illustrates the CV voltammograms of SY and TZ using the bare CPE electrode and CPE electrodes modified with Eu^{3+} ion doped NZF spinel ferrite and rGO. The voltammograms of SY and TZ in Figure 4.56(a, b) exhibited the individual detection of SY and TZ oxidized at peak potentials of 0.8 and 1.02 V, respectively (Raril *et al.*, 2018 ; Darabi *et al*., 2021). Figure 4.56c illustrates two distinct oxidation peaks attributed to the colorants with their respective peak potentials, exhibiting simultaneous analysis of SY and TZ in their mixture (Stozhko *et al*., 2022). These anodic peaks of SY and TZ appeared with all electrodes (Ghoreishi *et al*., 2012). However, the current responses varied with increasing CPE < NZF/CPE < NZE_6F/CPE < NZEF@rGO/CPE.

The current response is directly related to the redox activity of dyes (Akkapinyo *et al.*, 2021). The bare CPE depicted a small electrochemical current response, indicating weak catalytic activity of the dyes in the bare electrode. In contrast, some improvement of electrochemical response was observed on NZF and NZEF-modified CPE electrodes. With the introduction of rGO, a significant improvement in catalytic activities and rate of electron transfer on the NZEF@rGO/CPE electrode was observed, attributed to the high surface area and conductivity nature of rGO sheets. This phenomenon affects the improvement in electrochemical sensitivity (Akkapinyo *et al.*, 2021). As a result, the NZEF@rGO/CPE electrode significantly enhanced the electrochemical response with a slight shifting of potential for both SY and TZ dyes, either separately or simultaneously, in their mixture.

The absence of a reduction signal in the reverse scan indicates that SY and TZ are permanently oxidized at the surface of all the electrodes, in agreement with the literature (Ghoreishi *et al.*, 2012; Karim-Nezhad *et al*., 2017; Moarefdoust *et al*., 2021). Moreover, consistent results were obtained using the SWV method, as illustrated in Figure 4.56(d). The two distinct oxidation peaks for SY and TZ were observed on the surface of each of the electrodes with their corresponding potentials of +0.728 and +0.98 V, respectively (Moarefdoust *et al*., 2021).

These findings confirm that the synergetic effect of $Ni_{0.75}Zn_{0.25}Fe_2O_4$, $Eu^{3+,}$ and rGO effectively improved the electrochemical behavior of SY and TZ and the effectiveness of the fabricated electrodes for simultaneous determination of mixed colorants without any interference effects (Masoumeh *et al*., 2020).

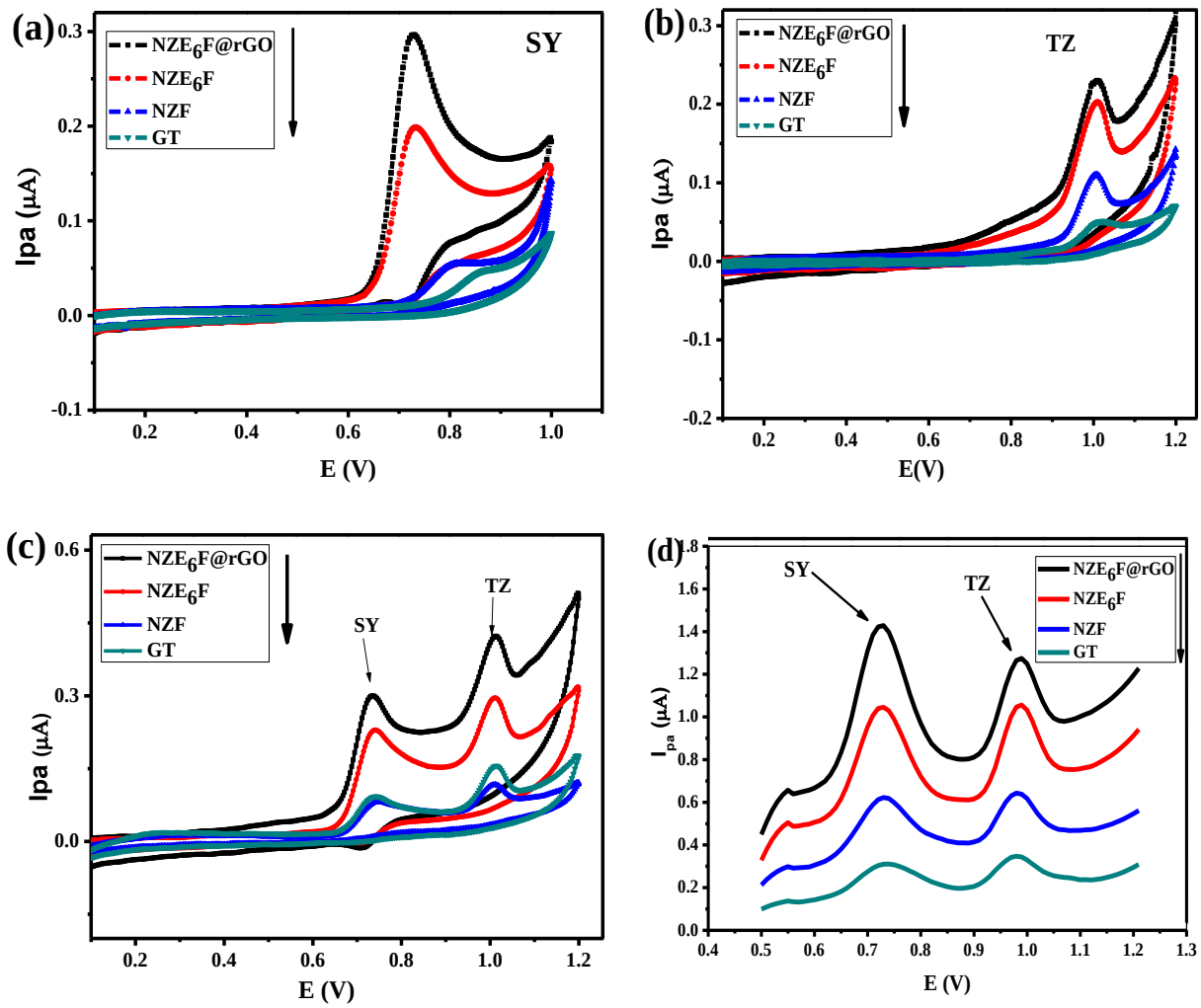

Figure 4.56: CV plots of (a) 0.1mM of SY, (b) 0.1 mM of TZ, (c) 0.1 mM of SY and TZ, and (d) square wave plots of 0.1 mM of SY and TZ at the bare and the modified electrodes.

4.6.2.3 Optimization of parameters

4.6.2.3.1 Effect of pH

The pH of the supporting electrolyte is a critical parameter required to obtain the best catalytic current response of SY and TZ (Rovina *et al*., 2021). The effect of pH on the electrochemical oxidation response of SY and TZ was studied on the NZEF@rGO/CPE by CV with 0.1 M PBS as a supporting electrolyte in the pH range two ≤ to ≤ eight, as illustrated in Figure 4.57(a, b) respectively. The results showed that the electrochemical oxidation response of both SY and TZ at the surface of NZEF@rGO/CPE increased slightly in acidic conditions and got maximum oxidation response at the pH of 6 while further increasing of the pH led to a decrease in the catalytic

response of the electrode. The decreasing electrochemical response with increasing pH is attributed to the change of the analytes (SY and TZ) into anionic form, which leads to ionic repulsion with the surface of the electrode (Ghoreishi *et al.*, 2012). Therefore, pH six was chosen as the optimum pH value for further electrochemical oxidation studies of SY and TZ dyes at the NZEF@rGO/CPE surface.

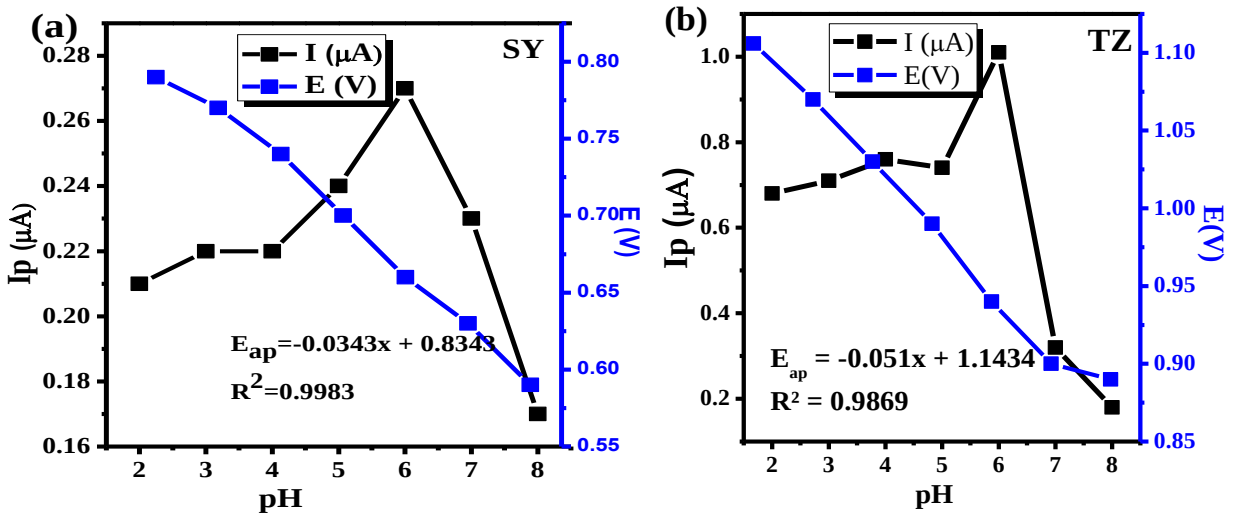

Figure 4.57: pH effect on the anodic current and potential of 0.1 mM of SY, and (b) TZ in 0.1 M phosphate buffer solution at a scan rate of 50 mV/s on NZEF@rGO/CPE between pH 2 - 8.

Additionally, in both cases, there is a linear relationship between the anodic peak potential (Eap) of SY and TZ and the pH of the buffer solution. On the other hand, the E_{ap} of SY and TZ shifted in the negative direction with an increase in the solution's pH [Figure 4.57(a, b)], confirming protons' involvement in the electrochemical process. The linear regression using equations 4.18 and 4.19 are as follows.

$$E_{ap} = -0.048pH + 0.8343;\ R^2 = 0.9983\ \ (SY) \tag{4.18}$$

$$E_{ap} = -0.051pH + \ 1.1434;\ R^2 = 0.9869\ \ (TZ) \tag{4.19}$$

The slope value of E_{ap} = 0.048 V/pH for SY and 0.051 V/pH for TZ was in approximation to the theoretical Nernst value (0.059V/pH) and indicated the involvement of an equal number of protons and electrons in the oxidation process (Stozhko *et al.*, 2022). The results evidence that the electrochemical detection of both SY and TZ dyes was pH dependent. An electrolyte solution at

pH 6 was the optimum for detecting SY and TZ in their mixture at the surface of NZEF@rGO/CPE with a high electrochemical response. The possible oxidation mechanism of SY and TZ is summarized by equation 4.20 as follows.

$$\text{Dye} \rightarrow \text{Dye (oxidation} + e^- + H^+) \quad (4.20)$$

Where: dye = sunset yellow and tartrazine.

4.6.2.3.2 Effect of the scan rate

Figure 4.58 illustrates the effect of the scan rate on the oxidation peak current of SY and TZ in the range of 10 -100 mV/s. Figure 4.58a illustrates that SY and TZ's oxidation peak current responses increase linearly with the scan rate. The linear plot of the peak current vs. the square root of the scan rate estimates whether the electrooxidation reaction is controlled by diffusion or adsorption (Ghoreishi *et al*., 2012) (Penagos-Llanos *et al*., 2020). If the plot of Ip vs. $v^{1/2}$ passes the origin, this process is controlled by diffusion; otherwise, it is controlled by adsorption (Hoan *et al*., 2020). The corresponding linear equations were $I_{pa} = 0.041(\text{mV s}^{-1}) + 0.0083$, $R^2 = 0.9886$ for SY (Figure 4.58b) and $I_{pa} = 0.0499\ (\text{mV s}^{-1}) + 0.0077$, $R^2 = 0.9915$ for TZ (Figure 4.58c). The results indicated that besides the linear proportionality between the catalytic current response and the square root of scan rates passing through the origin indicates that the electrochemical reactions of SY and TZ on NZEF@rGO/CPE electrode were a diffusion control process with the involvement of an equal number of electrons and protons (Oliveira *et al*., 2015; Karim-Nezhad *et al*., 2017; Perdomo *et al*., 2017; Darabi *et al*., 2021).

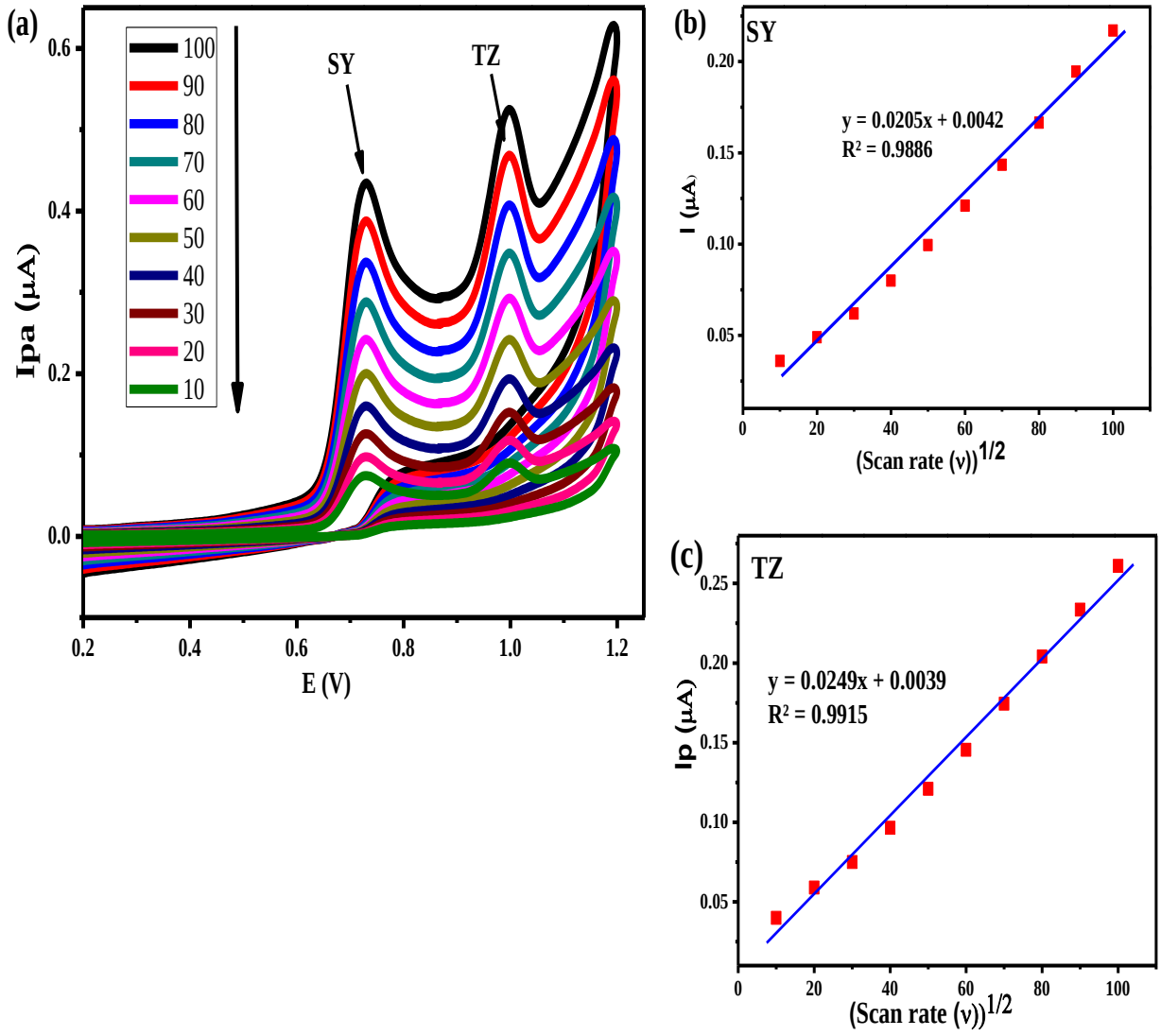

Figure 4.58: CV of (a) 0.1 mM SY and TZ in a 0.1 M phosphate buffer solution of pH 6 at the NZEF@rGO/CPE surface with varying scan rates from 10 to 100 mV/s, and (b and c) the corresponding plots of the linear variation of peak current (I_p) vs. the scan rate (mV/s) for SY (b) and TZ.

4.6.2.4 Simultaneous determination of SY and TZ

Current responses illustrated in Figure 4.59 were obtained at the optimized DPV parameters of pulse height of 50 mV, pulse width of 5 mS, step height of 5 mV, and step time of 100 mS for the separated and simultaneous determination of SY and TZ at the surface of the NZEF@rGO/CPE electrode. In Figure 4.59a, the DPV response was obtained by changing the SY concentration from 0 to 80 µM, while the concentration of TZ was kept constant (10 µM). The anodic current response

of SY increased linearly with an increase in the concentration of SY, while the current response of TZ remained constant. On the other hand, in the presence of a constant concentration of SY (10 µM), the anodic current response of TZ increased linearly with concentration. In contrast, the anodic current intensity of SY remained constant (Figure 4.59b). The results indicate that the DPV technique allows determining SY and TZ simultaneously without interference with the voltammetric response of each other (Penagos-Llanos *et al*., 2020).

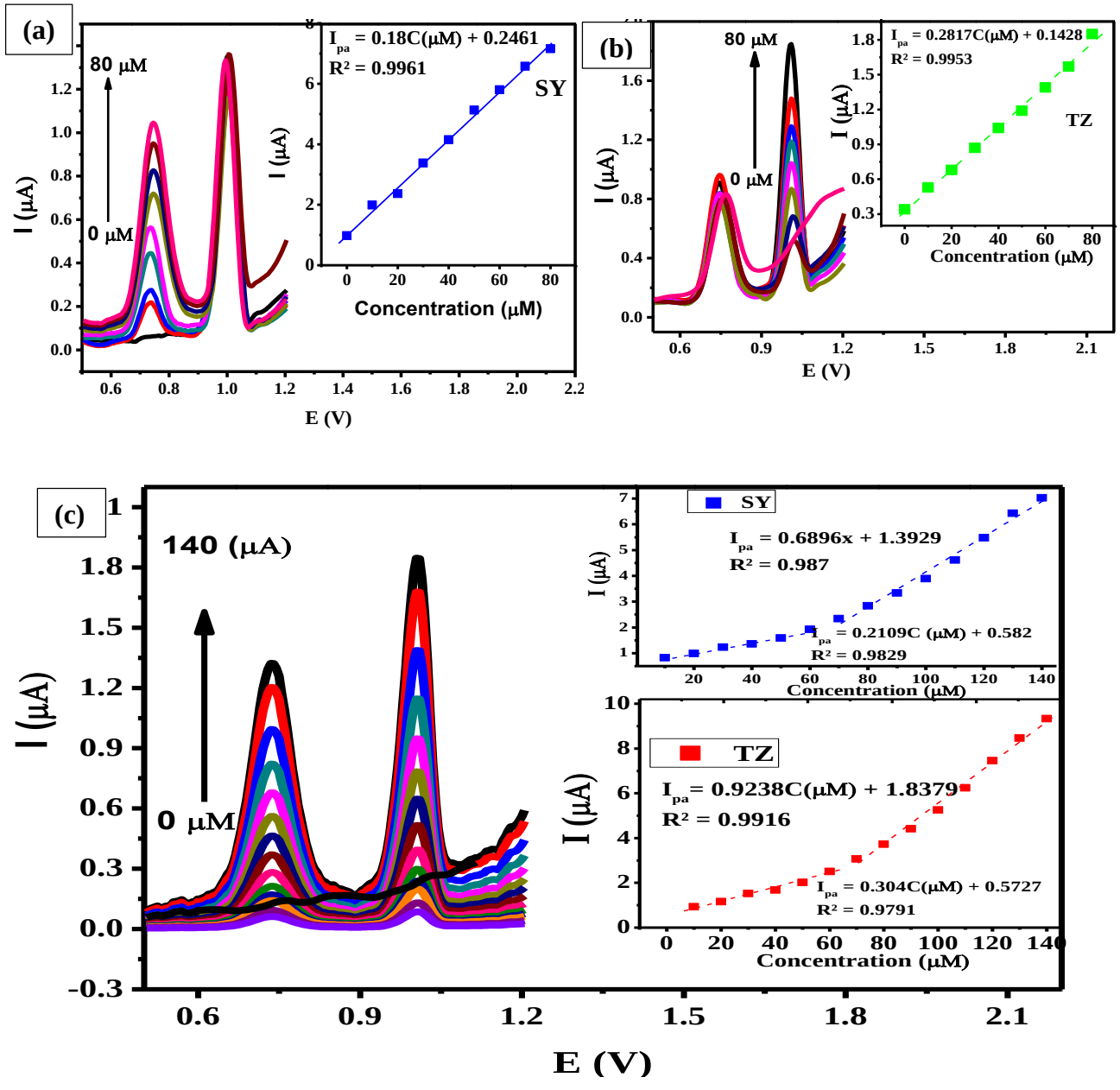

Figure 4.59: DPV voltammograms with calibration curves (inset) for the determination of (a) SY (0 to 80 µM within the range of 10 µM) in the presence of 10 µM of TZ; (b) TZ (0 to 80 mM within

the range of 10 μM) in the presence of 10 μM SY; (c) simultaneous determination of SY and TZ (0 to 140 μM within the range of ten μM) in a 0.1 M phosphate buffer solution as supporting electrolyte (pH 6), on the surface of the NZEF@rGO/CPE working electrode.

Figure 4.59c illustrates two well-distinguishable anodic peaks at the potentials of 0.73 and 1.00 corresponding to the oxidation of SY and TZ, respectively, which indicates the simultaneous detections of SY and TZ on the NZEF@rGO/CPE electrode. The current response of SY and TZ linearly increased with increasing concentrations of both colorants simultaneously in the range of 0 to 140 μM. The inset of Figure 4.59c illustrates the calibration curves for SY and TZ. The respective calibration curves for the colorants contain two linear regions that can be described by the influence of diffusion for lower ranges and then by the phenomena of adsorption (Stankovic et al., 2018). The LODs determined based on the first linear range were obtained using equation 4.21 (Moarefdoust et al., 2021).

$$\mathrm{LOD} = \frac{3s}{m} \tag{4.21}$$

s = the standard deviation of blank and m = the slope of calibration curve.

The LOD for SY and TZ were 0.0046 μM and 0.0034 μM, respectively.

In addition to that, based on equation 4.22, the sensitivity of the modified electrode towards the oxidation of SY and TZ was calculated as 0.21 μA μmol L^{-1} and 0.30 μA μmol $L^{-1,}$ respectively (Zhang *et al*., 2022).

$$Sensitivity = \frac{m}{A} = slope \tag{4.22}$$

A = the area of the active site of the electrode, and m = the slope of calibration curve.

The modified electrode's sensitivity towards SY in the absence of TZ was 0.18 μA μmol L^{-1}, while its sensitivity towards TZ in the absence of SY was 0.28 μA μmol L^{-1}, which is higher than for SV. Despite this, the results suggest that the colorants can be determined simultaneously without interference.

4.6.2.5 Reproducibility, Repeatability and Stability of the method

The storage stability, repeatability, and reproducibility of NZEF@rGO/CPE were studied in a solution containing 10 µM of SY and TZ using the DPV. Six NZEF@rGO/CPE electrodes fabricated by the identical procedure were used to determine 10 µM SY and TZ. The reproducibility, expressed as a percent of the relative standard deviations (RSD %) for SY and TZ, was calculated using the relation (RSD % = (standard deviation/mean) *100). The reproducibility of 4.75 and 4.34 %, respectively, suggest the excellent reproducibility of NZEF@rGO/CPE. Six successive measurements of ten µm SY and TZ were carried out using the same modified electrode to analyze repeatability. The RSD % for SY and TZ were 2.8 and 4.1%, respectively, indicating suitable method repeatability. Moreover, after three weeks of dry storage at room temperature with periodical measuring of the peak current of SY and TZ, 95 % of the initial current signal was retained, indicating the fabricated electrode had acceptable long-term stability. The excellent long-term stability, reproducibility, and repeatability of the NZEF@rGO/CPE make them attractive in the field of analytical application for the analysis of real samples.

4.6.2.6 Real sample analysis

To test its practical applicability, the developed sensor, NZEF@rGO/CPE, was used to determine the concentration of SY and TZ in different synthetic food products by spiking them under optimized experimental conditions. Synthetic food products, including mango juice, orange powder, and pineapple powders, were purchased from the local market. 2 mL of samples were diluted ten times with 0.1 M of PBS (pH 6) to reduce the interference effect. The concentrations of SY and TZ in the actual food samples were obtained based on the calibration curves using the DPV signal. After that, a standard addition method was used to conduct the recovery experiments (Table 4.8). The recovery for both analytes was more than 93%, which indicates the potential accuracy and feasibility of the sensor NZEF@rGO/CPE for selective detection of SY and TZ in real samples. Each measurement underwent four replicate measurements in which the calculated value of RDS was below five percent, confirming the accuracy of the developed sensor (Karim et al., 2017; Taei, 2020).

Table 4.7: Detection of SY and TZ in real samples (mango juices, the powder of orange and pineapple) using the electrode NZEF@rGO/CPE.

Sample	Spike (μM)	Concentration unknown		Concentration spiked		Recovery %		RDS %	
		SY	TZ	SY	TZ	SY	TZ	SY	TZ
Pineapple powder	-	0	0	-	-	-	-	-	-
	10	12.2	40.8	21.6	40.8	94	99	3.5	4.7
		14.8	45.3	24.1	54.9	96	98	5	4.4
Orange powder	-	0	0	-	-	-	-	-	-
		24.2	41.7	34.0	50.8	98	98	4	3.9
	10	27.4	38.3	36.9	47.7	98.3	94	4.4	4.5
Mango juice	-	0	0	-	-	-	-	-	-
	10	18.6	32.6	27.9	42.0	93	98	4.9	4.8
		23.7	35.1	33.2	44.8	99.3	97	3.6	4

4.6.2.7 Comparison of the present method with reported methods in the literature

Table 4.8 compares the performance of the NZEF@rGO/CPE electrode and electrodes reported in the literature for the detection of SY and TZ. As seen in Table 4.8, the performance of the NZEF@rGO/CPE electrode is comparable to or better than the reported modified electrodes (Ghoreishi *et al*., 2012; Sierra-rosales *et al*., 2017; Chebotarev *et al.*, 2019; Masoumeh et al., 2020; Akkapinyo *et al*., 2021; Moaref *et al.*, 2021; Stozhko *et al*., 2022). The estimated LOD was 0.0043 μM and 0.0034 for SY and TZ, respectively. In addition, the present method has improved by simplifying the preparation of the electrode through a simple modification process, saving time. Furthermore, the method can be performed relatively quickly using inexpensive equipment with LOD.

Table 4. 8: Comparison of the developed electrode for simultaneous detection of SY and TZ with electrodes reported in the literature.

Electrode	SY		TZ		Method	References
	Concentration range (µM)	LOD (µM)	LR (µM)	LOD (µM)		
$ZnCrFeO_4$/CPE	0.07-47.5	0.02	0.05-19	0.01	DPV	Masoumeh *e al*., 2020
GrP/CPE	0.005–1.0	0.072	0.02-7.5	0.082	DPV	Stozhko *et al*., 2022
In^{3+}/NiO RLHNSs/GCE	10–700	0.002	10–700	0.0031	DPV	Moarefdoust *et al*., 2021
nAu-CPE	0.1–2	0.03	0.055–1.6	0.02	DPV	Ghoreishi *et al*., 2012
SG/CPCl/CPE	0.02–1	0.005	0.04–1	0.008	DPV	Chebotarev *et al*., 2019)
MWCTs-GCE	1–7	0.22	1–7	0.12	DPV	Sierra-rosales *et al*., 2017
rGO-methionine/SPCE	10–50	0.048	10-85	0.041	DPV	Akkapinyo *et al*., 2021
NZEF@rGO/CPE	***0-140***	***0.0046***	***0-140***	***0.0034***	***DPV***	***This work***

4.7 Applications of NZL-EF@rGO Nanocomposites

4.7.1 Photocatalytic application

Figure 4.60 illustrates the photocatalytic degradation of MB and MO dyes in their mixture under various experimental conditions, including in the dark + H_2O_2, NZE_6F + H_2O_2, NZL_6F + H_2O_2, NZLEF + H_2O_2, and NZL-EF@rGO + H_2O_2 under visible light with irradiation.

Compared to mono-doped NZF ferrite, co-doped NZF ferrite displays more efficient and rapid degradation of MB and MO under the same experimental conditions [Figure 4.60A & B)]. Furthermore, the degradation efficiencies obtained using NZL-EF@rGO nanocomposite were 99% for MO and 96% for MB; this shows that NZL-EF@rGO is more efficient than the NZ_6LF and NZE_6F catalysts. In addition to the effect of the rGO nanosheets, the synergetic effect of La and Eu in their co-doping also significantly enhances the degradation of mixed dyes MO and MB under visible light irradiation.

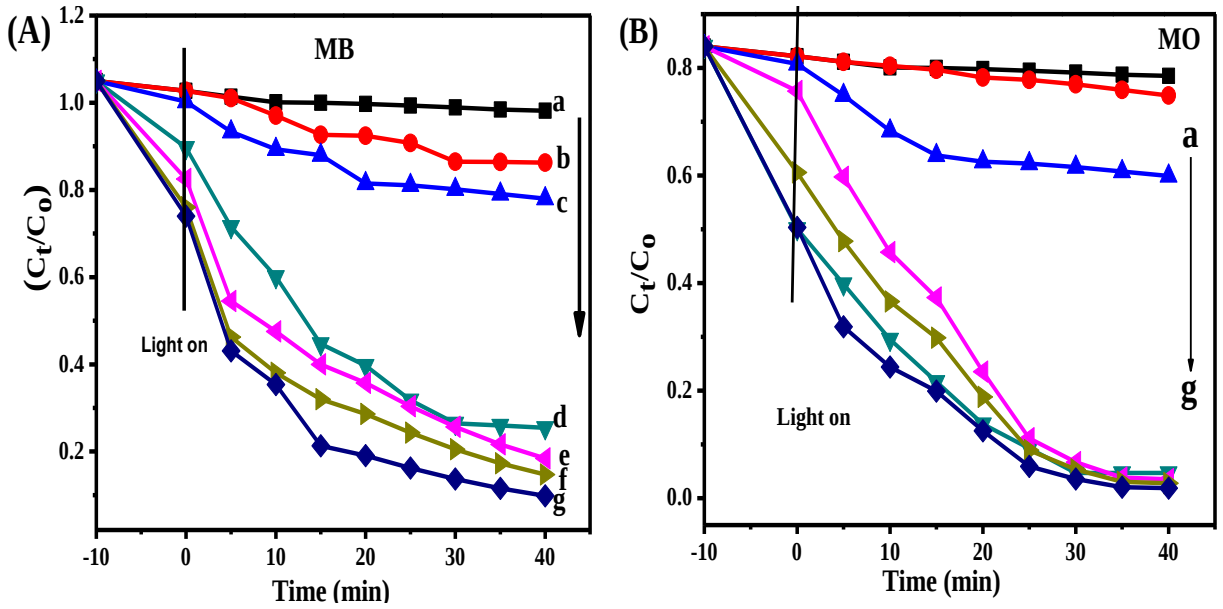

Figure 4.60: Degradation of mixed dyes MB and MO using different experimental conditions: (a) dark; (b) blank; (c) + visible light + H_2O_2O; (d) NZE_6F; (e) NZL_6F; (F) NZL-EF + H_2O_2, (g) NZLEF@rGO nanocomposite + H_2O_2 under optimized experimental conditions of pH 9, initial concentration of dyes 10 mg/L and catalyst dosage of 50 mg at room temperature.

4.7.2 Electrochemical sensor application

The electrochemical analysis of the co-doped NZF ferrite and its composite with rGO was carried out using CV and EIS under the same experimental conditions as for La^{3+} and Eu^{3+} ions substituted NZF, discussed in the previous sections. The corresponding results are illustrated in Figure 4.61(a, b). The co-doped NZF spine ferrite has a higher current response in CV while a smaller semicircle radius in the Nyquist plot of EIS than the mono-doping of La^{3+} and Eu^{3+} ions. This indicates that the co-doping of La and Eu together has a better electrochemical response with higher conductivity than their single-ion doping. Furthermore, after the introduction of rGO, the current response and

the conductivity of co-doped NZF ferrite significantly improved, indicating that the synergetic effect of La, Eu, rGO, and NZF efficiently improved the sensitivity and conductivity of the surface of the modified electrode for the detection of food colorants.

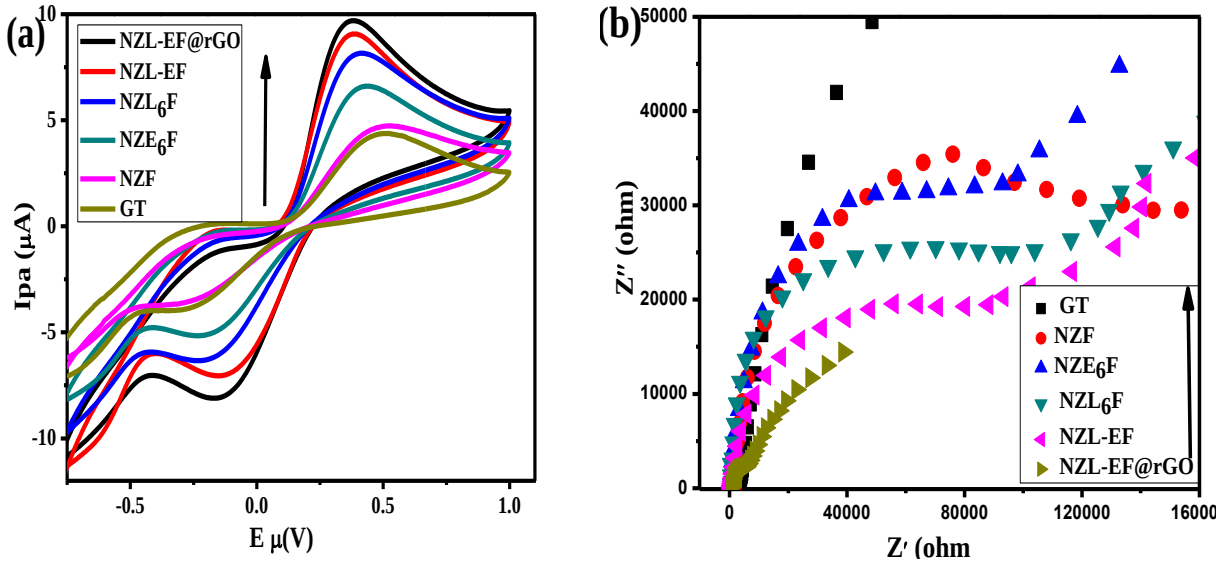

Figure 4.61: (a) CV plots of the modified electrode at a scan rate of 50 mV/S; (b) Nyquist plots at the frequency range of 10 mHz -100 KHz under working conditions of 5 mM of $[Fe(CN)_6]^{3-/4-}$ in 0.1 M KCl solution as a supporting electrolyte.

4.7.2.1 Electrochemical response of SY and TZ

Figure 4.62 illustrates t the cyclic voltammograms and square wave voltammograms for different electrodes in the potential range 0-1.200 V versus Ag/AgCl in the presence of SY and TZ at pH 6. As illustrated in Figure 4.62a, the cyclic voltammograms show an irreversible oxidation peak at all electrodes. At the same time, a quasi-reversibility of SY was observed at NZLEF@rGO/CPE, indicating the co-doped composite's sensitivity. From the comparison of curves A and B in mono-doped ferrite, NZL_6F shows more sensitivity, while the peak current of both SY and TZ were further increased at co-doped ferrite (curve C), attributed to the synergistic effects of La and Eu and their coupling effect in electronic properties (Irfan *et al*., 2017). On the other hand, a significant enhancement of the oxidation peak currents of SY and TZ was achieved at the NZLEF@rGO/CPE (curve D). The results are ascribed to the synergistic effects of all components of the modified electrode and unique properties of rGO, such as large surface area, strong absorptivity ability, and inherent conductivity (Rovina *et al*., 2021).

As can be seen from the SWV in Figure 4.62b, comparing the other electrodes, the electrodes modified with the rGO composite of the co-doped NZF ferrites had a significant oxidation current response for both colorants SY and TZ.

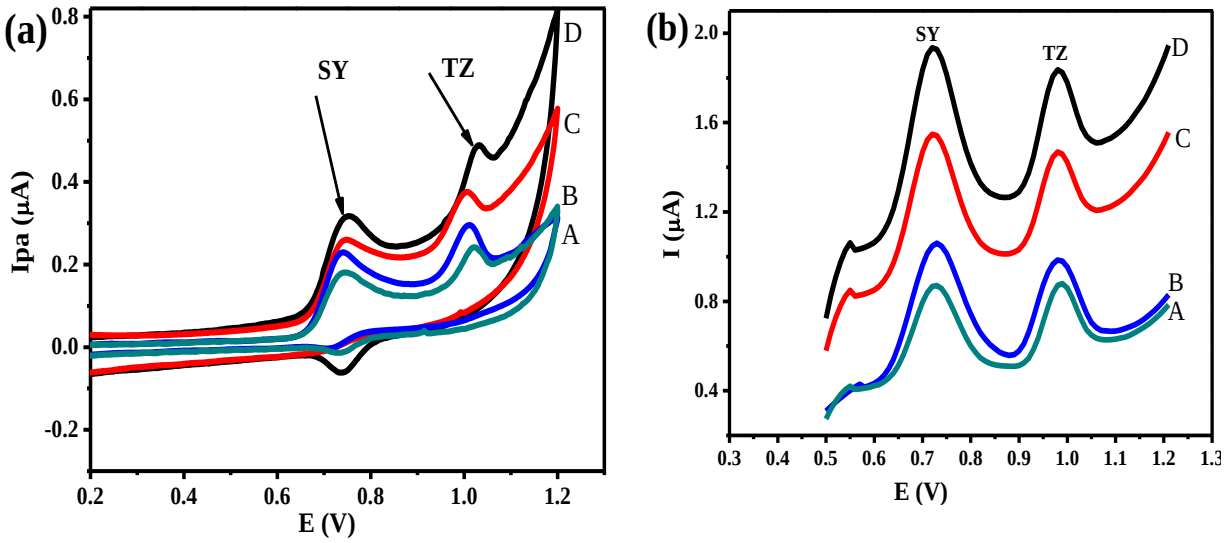

Figure 4.62: Cyclic voltammogram (a) and Square wave voltammograms (b); of SY and TZ on the curve (A) NZE_6F; (B) NZL_6F/CPE; (C) NZL-EF/CPE and (D) NZL-EF@rGO modified carbon paste electrode at pH 6.0.

CHAPTER FIVE

5 CONCLUSIONS AND RECOMMENDATIONS

Nickel-zinc ferrite nanoparticles doped with rare earth ions ($Ni_{0.75}Zn_{0.25}RE_xFe_{2-x}O_4$; x= 0.00, 0.02, 0.06, and 0.1) and their composites with rGO were successfully synthesized using a simple and low-cost sol-gel auto-combustion method. The synthesis involved a calcination temperature of 800 °C and a sonication step. The rGO was synthesized using Tours' method. The samples were characterized using XRD, FTIR, SEM/EDX, TEM, HR-TEM/SAD, XPS, BET, PL, and UV-Vis. The characterization results confirmed the formation of spherical-shaped FCC polycrystalline structures of spinel ferrite nanoparticles with high purity. The optical and electrochemical analyses confirmed that the samples can be used for photocatalytic activity and electrochemical sensors.

The photocatalytic efficiency of both $Ni_{0.75}Zn_{0.25}RE_{0.06}Fe_{1.94}O$ NPs and $Ni_{0.75}Zn_{0.25}RE_{0.06}Fe_{1.94}O$ @rGO nanocomposites were tested on simultaneously degradation of MB and MO under their mixture. The $Ni_{0.75}Zn_{0.25}RE_{0.06}Fe_{1.94}O$ @rGO nanocomposites was degraded the mixed dyes more efficiently (92-96% for MB and 97-99% for MO) and quickly. This suggesting that under the optimized conditions $Ni_{0.75}Zn_{0.25}RE_{0.06}Fe_{1.94}O$@rGO composite can efficiently decontaminate wastewater through Photo-Fenton activity. An optimal catalyst dosage of 50 mg at pH 6 was found for degrading a 10 mg/L concentration of mixed dyes MB and MO. In conclusion, the $Ni_{0.75}Zn_{0.25}RE_{0.06}Fe_{1.94}O$ @rGO composite has a potent visible light active photocatalyst for simultaneously degrading mixed organic pollutants from polluted water.

In the electrochemical study, a CPE was effectively modified with a $Ni_{0.75}Zn_{0.25}RE_{0.06}Fe_{1.94}O$ @rGO nanocomposite and used for the quantitative and selective detection of mixed food colorants SY and TZ. The results showed that the $Ni_{0.75}Zn_{0.25}RE_{0.06}Fe_{1.94}O$ @rGO/CPE provided an increased effective surface area. The method demonstrated practicality by accurately identifying coloring compounds in soft drinks without the need for sample preparation to analyze actual samples.

Further research on the detection and determination of multiple colorants is recommended. The proposed method was relatively simple, fast, and economical for detecting the target coloring agents in food samples.

The NPs and the nanocomposite are nontoxic, simple to fabricate with high yield in preparation, and effectively applicable for environmental remediation for the purification of polluted water and the detection of synthetic food colorants in food products. Therefore, further studies are recommended to scale up their production and practical application. Additionally, as indicated in the results of the preliminary test analysis, co-doped NZF ferrites exhibit significant performance in both the photocatalytic degradation process and electrochemical detection of food colorants compared to the mono-doped samples. Hence, future studies are recommended to examine the co-doping of RE in more detail.

REFERENCES

Adam, M. S. S., Hafez, A. M., & Khalaf, M. M. (2020). Rare earth Ce- and Nd-doped spinel nickel ferrites as effective heterogeneous catalysts in the (ep)oxidation of alkenes. *Journal of the Iranian Chemical Society*, *17*(12), 3237-3250.

Afkhami, A., Aghajani, S., Mohseni, M., & Madrakian, T. (2015). Effectiveness of Ni0.5Zn0.5Fe2O4 for the removal and preconcentration of Cr(VI), Mo(VI), V(V) and W(VI) oxyanions from water and wastewater samples. *Journal of the Iranian Chemical Society*, *12*(11), 2007-2013.

Afkhami, A., Moradi, M., Bahiraei, A., & Madrakian, T. (2016). A Sensitive Method for Electrochemical Determination of, *1*(2), 249-257.

Agboola, P. O., Haider, S., & Shakir, I. (2022). The impact of rare earth Nd^{3+} cations on structural, spectral, magnetic and dielectric parameters of $NiFe_2O_4$ nanoparticles. *Journal of Taibah University for Science*, *16*(1), 392-400.

Ahmad, I., Safdar, M., Yasmin, N., Iftikhar, A., Kalsoom, A., Khalid, S., … Mirza, M. (2023). Rare earth ions (La^{3+},Nd^{3+}) substituted cobalt–strontium spinel ferrites for photocatalytic degradation of textile dyes. *Water Practice and Technology*, *18*(8), 1742-1755. https://doi.org/10.2166/wpt.2023.119

Ahmed, A., Usman, M., Wang, S., Yu, B., & Shen, Y. (2021). Facile synthesis of Zr 4 + substituted Mn 0 . 2 Co 0 . 8 Fe 2 − x O 4 nanoparticles and their composites with reduced graphene oxide for enhanced photocatalytic performance under visible light irradiation. *Synthetic Metals*, *277*(April), 116766.

Ahmed, M. A., Ateia, E., Salah, L. M., & El-Gamal, A. A. (2005). Structural and electrical studies on La3+ substituted Ni-Zn ferrites. *Materials Chemistry and Physics*, *92*(2-3), 310-321.

Ain, N., Shaheen, W., Bashir, B., Abdelsalam, N. M., Farooq, M., Azhar, M., & Shahid, M. (2016). Electrical , magnetic and photoelectrochemical activity of rGO / MgFe 2 O 4 nanocomposites under visible light irradiation. *Ceramics International*, *42*(10), 12401-12408.

Akkapinyo, C., Subannajui, K., Poo-Arporn, Y., & Poo-Arporn, R. P. (2021). Disposable electrochemical sensor for food colorants detection by reduced graphene oxide and methionine film modified screen printed carbon electrode. *Molecules*, *26*(8).

Alam, U. (2018). derived rare earth metal (La , Nd , Sm and Dy) -doped, 17582-17594.

MA Ali, MM Uddin, MNI Khan, FUZ Chowdhury, SM Hoque and SI Liba (2017). Magnetic

properties of Sn-substituted Ni–Zn ferrites synthesized from nano-sized powders of NiO, ZnO, Fe_2O_3, and SnO_2. *Chinese Physical Societyociety*, *26*(7), 077501.

Almessiere, M. A., Slimani, Y., Korkmaz, A. D., Baykal, A., & G, H. (2019). Structural, magnetic, and microwave absorption properties of $SrCe_xFe_{12-x}O_{19}$/PVP composites, 30671-30684.

Almessiere, M. A., Slimani, Y., Korkmaz, A. D., Baykal, A., Güngüneş, H., Sözeri, H., … Manikandan, A. (2019). Impact of La^{3+} and Y^{3+} ion substitutions on structural, magnetic and microwave properties of $Ni_{0.3}Cu_{0.3}Zn_{0.4}Fe_2O_4$ nanospinel ferrites synthesized: Via sonochemical route. *RSC Advances*, *9*(53), 30671-30684.

Alzahrani, E. (2017a). Photodegradation of Binary Azo Dyes Using, 95-115.

Alzahrani, E. (2017b). Photodegradation of Binary Azo Dyes Using Core-Shell /TiO; Nanospheres. *American Journal of Analytical Chemistry*, *08*(01), 95-115.

Anandan, S., Ikuma, Y., & Murugesan, V. (2012). Highly active rare-earth-metal La-doped photocatalysts: Fabrication, characterization, and their photocatalytic activity. *International Journal of Photoenergy*, *2012*.

Anwar, A., Yousuf, M. A., Tahir, B., Shahid, M., Imran, M., Khan, M. A., … Warsi, M. F. (2018). New Er^{3+}-substituted $NiFe_2O_4$ Nanoparticles and their Nano-heterostructures with Graphene for Visible Light-Driven Photo-catalysis and other Potential Applications. *Current Nanoscience*, *15*(3), 267-278.

Anwar, A., Zulfiqar, S., Yousuf, M. A., Ragab, S. A., Khan, M. A., Shakir, I., & Warsi, M. F. (2020). Impact of rare earth Dy+3 cations on the various parameters of nanocrystalline nickel spinel ferrite. *Journal of Materials Research and Technology*, *9*(3), 5313-5325.

Arancibia, M. G., Rojas-romo, C., & Edgar, N. (2014). Adsorptive Stripping Voltammetric Determination of Tartrazine and Sunset Yellow in Gelatins and Soft Drink Powder in the presence of Cetylpyridinium Bromide, 11 (17), 1-10.

Aslam, A., Morley, N. A., Amin, N., Arshad, M. I., Ajaz un Nabi, M., Ali, A., … Jamil, Y. (2021). Study of structural, optical and electrical properties of La^{3+}doped $Mg_{0.25}Ni_{0.15}Cu_{0.25}Co_{0.35}Fe_{2-x}La_xO_4$ spinel ferrites. Physica B: Condensed Matter, (602), 412565.

Ateia, E. E., Abdelmaksoud, M. K., Arman, M. M., & Shafaay, A. S. (2020). Comparative study on the physical properties of rare-earth-substituted nano-sized $CoFe_2O_4$. *Applied Physics A: Materials Science and Processing*, *126*(2), 1-10.

Baig, M. M., Zulfiqar, S., Yousuf, M. A., Touqeer, M., Ullah, S., Agboola, P. O., … Shakir, I.

(2020). Structural and photocatalytic properties of new rare earth La^{3+} substituted $MnFe_2O_4$ ferrite nanoparticles. *Ceramics International*, *46*(14), 23208-23217.

Belaiche, Y., Minaoui, K., Ouadou, M., Elansary, M., & Unit, N. (2021). New Nanosized (Gd^{3+}, Sm^{3+}) Co-doped Zinc Ferrite for TelecommunicationTelecommunication Applications . Magnetic and Structural. *Physica B: Condensed Matter, 619*, 413262.

Benvidi, A., Nafar, M. T., Jahanbani, S., Tezerjani, M. D., Rezaeinasab, M., & Dalirnasab, S. (2017). Developing an electrochemical sensor based on a carbon paste electrode modi fi ed with nano-composite of reduced graphene oxide and $CuFe_2O_4$ nanoparticles for determination of hydrogen peroxide. *Materials Science & Engineering C*, *75*, 1435-1447.

Bessegato, G. G., Brugnera, M. F., & Zanoni, M. V. B. (2019). Electroanalytical sensing of dyes and colorants. *Current Opinion in Electrochemistry, 16*, 134-142.

Bharamagoudar, R. C., Patil, A. S., Mathad, S. N., Kumbar, V. M., & Kankanawadi, L. B. (2019). Magnetic and Antibacterial Studies of Nanoferrites Prepared by Self Propagating High-Temperature Synthesis Route. *Acta Chemica Iasi*, *26*(2), 249-262.

Burda, C., Chen, X., Narayanan, R., & El-sayed, M. A. (2005). Synthesis and Characterization of Ag_2O Nanoparticles for Photocatalytic Applications, *Review, Chem. Rev. 105, 1025.*

Chebotarev, A., Koicheva, A., Bevziuk, K., Pliuta, K., & Snigur, D. (2019). Simultaneous determination of Sunset Yellow and Tartrazine in soft drinks on carbon-paste electrode modified by silica impregnated with cetylpyridinium chloride. *Journal of Food Measurement and Characterization*, 13, 1964–1972.

Chen, H., Liu, W., & Qin, Z. (2017). $ZnO/ZnFe_2O_4$ nanocomposite as a broad-spectrum photo-Fenton-like photocatalyst with near-infrared activity. *Catal. Sci. Technol. 7(11)*, 2236-2244.

Chufa, B. M., Gonfa, B. A., Anshebo, T. Y., & Workneh, G. A. (2021). A Novel and Simplest Green Synthesis Method of Reduced Graphene Oxide Using Methanol Extracted Vernonia Amygdalina. *Large-Scale Production*, (*2021)*, 1-9.

Ciocarlan, R., Seftel, E. M., Mertens, M., Pui, A., Mazaj, M., Novak, N., & Cool, P. (2018). Materials Science & Engineering B Novel magnetic nanocomposites containing quaternary ferrites systems photocatalysts for wastewater remediation under solar light irradiation. *Materials Science & Engineering B*, *230*(2017), 1-7.

Communication, I. C., & Taei, M. (2020). Simultaneous determination of sunset yellow and tartrazine in soft drinks samples using nanocrystallites of spinel ferrite- modified electrode,

8, 67-79.

Compton, O. C., & Nguyen, S. T. (2010). Graphene oxide, highly reduced graphene oxide, and graphene: Versatile building blocks for carbon-based materials. *Small*, *6*(6), 711-723.

Cortinez, D., Palma, P., Castro, R., & Palza, H. (2020). A multifunctional bi-phasic graphene oxide/chitosan paper for water treatment. *Separation and Purification Technology*, *235*(2018), 116181.

D. L. Chaudhari, D. S. Choudhary | K. G. Rewatkar. (2020). Spinel Ferrite Nanoparticles Synthesis, Characterization and Applications. *International Journal of Trend in Scientific Research and Development*, *4*(3), 973-978.

Damian Wojcieszak, Danuta Kaczmarek, Jaroslaw Domaradzki, and M. M. (2013). Correlation of photocatalysis and photoluminescence effect in relation to the surface properties of TiO_2:Tb thin films. *International Journal of Photoenergy*, *11(17)*, 50-372.

Darabi, R., & Shabani-Nooshabadi, M. (2021). $NiFe_2O_4$-rGO/ionic liquid modified carbon paste electrode: An amplified electrochemical sensitive sensor for determination of Sunset Yellow in the presence of Tartrazine and Allura Red. *Food Chemistry*, *339*(2020), 127841.

Dasan, Y. K., Guan, B. H., Zahari, M. H., & Chuan, L. K. (2017). Influence of La^{3+} substitution on structure, morphology and magnetic properties of nanocrystalline Ni-Zn ferrite. *PLoS ONE*, *12*(1), 1-14.

Debnath, S., & Das, R. (2020). Study of the optical properties of Zn doped Mn spinel ferrite nanocrystals shows multiple emission peaks in the visible range e a promising soft ferrite nanomaterial for deep blue LED. *Journal of Molecular Structure*, *1199*, 127044.

Demir Korkmaz, A. (2020). Influence of Rare Earth Substitution on the Magnetic Properties of Spinel Ferrites. *Mühendislik Bilimleri ve Tasarım Dergisi*, *8*(2), 625-634.

Dhiman, M., Chudasama, B., Kumar, V., Tikoo, K. B., & Singhal, S. (2019). Augmenting the photocatalytic performance of cobalt ferrite via change in structural and optical properties with the introduction of different rare earth metal ions. *Ceramics International*, *45*(3), 3698-3709.

Dimiev, A. M., & Tour, J. M. (2014). Mechanism of graphene oxide formation. *ACS Nano*, *8*(3), 3060-3068.

Division, F. T., DTIC. Hossain, M. A., Khan, M. N. I., Sikder, S. S. (2018). Complex Permeability and Dielectric Behaviors of Eu^{3+} Doped Ni-Zn Ferrites. *Journal of Asian Scientific Research, 8(1),* 21-29.

Dubey, H. K. (2018). Influence of trivalent rare earth (Dy^{3+}) ions substitution on the structural, magnetic and dielectric properties of nanosized $Ni_{0.6}Cd_{0.4}Dy_xFe_{2-x}O_4$ ferrites. 24, 270-320.

Dubey, H., Verma, C., Rai, U., Kumar, A., & Lahiri, P. (2019). Synthesis, characterization and properties of nickel based zinc ferrite nanoparticles. *Indian Journal of Chemistry -Section A IJC-A, 58*(04), 454-458.

Dubey, H, Martin Š., Mariana U., Rastislav D., (2018). Effect of lanthanum substitution on structural and magnetic properties of nickel zinc ferrites. *047802*.

Elayakumar, K., Dinesh, A., Manikandan, A., Palanivelu, M., Kavitha, G., Prakash, S., Baykal, A. (2019). Structural , morphological , enhanced magnetic properties and antibacterial bio-medical activity of rare earth element (REE) cerium (Ce^{3+}) doped $CoFe_2O_4$ nanoparticles. *Journal of Magnetism and Magnetic Materials, 476*(2018), 157-165.

Elements, R. (1966). How Do We Use the Quarterly *Gifted Child Quarterly, 10*(3), 154-154.

Farooq, M. H., Aslam, I., Shuaib, A., Anam, H. S., Rizwan, M., & Kanwal, Q. (2019). Band gap engineering for improved photocatalytic performance of CuS/TiO_2 composites under solar light irradiation. *Bulletin of the Chemical Society of Ethiopia, 33*(3), 561-571.

Fouad, S., Sabri, N., Jamal, Z. A. Z., Poopalan, P., Homola, J., Joshi, M., … López, A. (2014). Síntesis Y Caracterización De Nanopartículas De Plata Por La Ruta Sol-Gel A Partir De Nitrato De Plata. *Sensors, 1*(1), 177-184.

Ganie, A. S., Bano, S., Sultana, S., Sabir, S., & Khan, M. Z. (2021). Ferrite Nanocomposite Based Electrochemical Sensor: Characterization, Voltammetric and Amperometric Studies for Electrocatalytic Detection of Formaldehyde in Aqueous Media. *Electroanalysis, 33*(1), 233-248.

Ghanbari, M. H., Sharafi, P., Nayebossadr, S., & Norouzi, Z. (2020). Utilizing a nanocomposite consisting of zinc ferrite, copper oxide, and gold nanoparticles in the fabrication of a metformin electrochemical sensor supported on a glassy carbon electrode. *Microchimica Acta, 187*(10), 30-65.

Ghoreishi, S. M., Behpour, M., & Golestaneh, M. (2012). Simultaneous determination of Sunset yellow and Tartrazine in soft drinks using gold nanoparticles carbon paste electrode. *Food*

Chemistry, *132*(1), 637-641.

Gonçalves, P. A. D., & Peres, N. M. R. (2016). Simultaneous determination of Sunset yellow and Tartrazine in soft drinks using gold nanoparticles carbon paste electrode. *Food Chemistry*, *132*(1), 637-641.

Gupta, N. K., Gha, Y., Kim, S., Bae, J., & Kim, K. S. (2020). Photocatalytic Degradation of Organic Pollutants over MFe_2O_4 (M = Co , Ni , Cu , Zn) Nanoparticles at Neutral pH, *4*, 1-11.

Habte, A. T., Ayele, D. W., & Hu, M. (2019). Synthesis and Characterization of Reduced Graphene Oxide (rGO) Started from Graphene Oxide (GO) Using the Tour Method with Different Parameters. *Advances in Materials Science and Engineering, 2019(1)*, 1-9.

Hamdi, N., Bessais, L., & Belam, W. (2020). Sol-gel Autocombustion Elaboration and Physiochemical Characterizations of Cu^{2+} Substituted Cobalt Ferrite Nanoparticles Abstract :, *4*, 44-54.

Hanafi, R., Mayasari, R. D., Masmui, Agustanhakri, Raharjo, J., & Nuryadi, R. (2019). Electrochemical sensor for environmental monitoring system: A review. Dans *AIP Conference Proceedings*, 2169, 030007.

Harish, K. N., Naik, H. S. B., Viswanath, R., Bhojya Naik, H. S., Prashanth Kumar, P. N., & Viswanath, R. (2013). Optical and photocatalytic properties of solar light active Nd-substituted Ni ferrite catalysts: For environmental protection. *ACS Sustainable Chemistry and Engineering*, *1*(9), 1143-1153.

Hashim, N., Muda, Z., Hussein, M. Z., Isa, I. M., Mohamed, A., Kamari, A., … Jaafar, A. M. (2016). A brief review on recent graphene oxide-based material nanocomposites: Synthesis and applications. *Journal of Materials and Environmental Science*, *7*(9), 3225-3243.

Hoan, N. T. V., Minh, N. N., Trang, N. T. H., Thuy, L. T. T., Van Hoang, C., Mau, T. X., … Khieu, D. Q. (2020). Simultaneous Voltammetric Determination of Uric Acid, Xanthine, and Hypoxanthine Using $CoFe_2O_4$/Reduced Graphene Oxide-Modified Electrode. *Journal of Nanomaterials*, *2020*.

Hossain, M. A., Khan, M. N. I., & Sikder, S. S. (2018). Complex Permeability and Dielectric Behaviors of Eu^{3+} Doped Ni-Zn Ferrites. *Journal of Asian Scientific Research*, *8*(1), 21-29.

Ibhadon, A., & Fitzpatrick, P. (2013). Heterogeneous Photocatalysis: Recent Advances and Applications. *Catalysts*, *3*(1), 189-218.

Iftikhar, A., Yousaf, S., Ahmed Ali, F. A., Haider, S., Ud-Din Khan, S., Shakir, I., … Warsi, M. F. (2020). Erbium-substituted $Ni_{0.4}Co_{0.6}Fe_2O_4$ ferrite nanoparticles and their hybrids with reduced graphene oxide as magnetically separable powder photocatalyst. *Ceramics International*, *46*(1), 1203-1210.

Iftikhar, A., Yousaf, S., Ahmed, F. A., Haider, S., Khan, S. U., Shakir, I., … Farooq, M. (2019). with reduced graphene oxide as magnetically separable powder photocatalyst. *Ceramics International*, , 2, 0-1.

Iftikhar, A., Yousaf, S., Ahmed, F. A., Haider, S., Khan, S. U., Shakir, I., … Farooq, M. (2020). with reduced graphene oxide as magnetically separable powder photocatalyst. *Ceramics International*, *46*(1), 1203-1210.

Irfan, S., Li, L., Saleemi, A. S., & Nan, C. (2017). Enhanced photocatalytic activity of La^{3+} and Se^{4+} co-doped bismuth ferrite nanostructures. *Journal of Materials Chemistry A: Materials for energy and sustainability*, *5*, 11143-11151.

Jacob, J., Ikram, S., Jacob, J., Arshad, M. I., Mahmood, K., Ali, A., … Hussain, S. (2018). Tailoring the Structural , Magnetic and Dielectric properties of Ni-Zn- $CdFe_2O_4$ spinel ferrites by the substitution of Lanthanum ions Tailoring the structural , magnetic and dielectric properties of Ni-Zn- $CdFe_2O_4$ spinel ferrites by the substitution of. *Ceramics International*, *45*(3), 3563-3569.

Jadhav, S. A., Somvanshi, S. B., Khedkar, M. V, & Patade, S. R. (2020). Magneto - structural and photocatalytic behavior of mixed Ni – Zn nano - spinel ferrites : visible light - enabled active photodegradation of rhodamine B. *Journal of Materials Science: Materials in Electronics*, *4*(0123456789).

Jagiełło, J., Chlanda, A., Baran, M., Gwiazda, M., & Lipińska, L. (2020). Synthesis and characterization of graphene oxide and reduced graphene oxide composites with inorganic nanoparticles for biomedical applications. *Nanomaterials*, *10*(9), 1-19.

Javed, H., Rehman, A., Mussadiq, S., Shahid, M., Khan, M. A., Shakir, I., Warsi, M. F. (2019). Reduced graphene oxide-spinel ferrite nano-hybrids as magnetically separable and recyclable visible light driven photocatalyst. *Synthetic Metals*, *254*, 1-9.

Jha, A. R. (2014). *Rare Earth Materials*. Book chapter. 33487-2742.

Jiang, W., Wang, X., Wu, Z., Yue, X., Yuan, S., Lu, H., & Liang, B. (2015). Silver oxide as superb and stable photocatalyst under visible and near-infrared light irradiation and its photocatalytic

mechanism. *Industrial and Engineering Chemistry Research*, *54*(3), 832-841.

Joseph, S. L., John, A. O., Mugwang, F. K., & Katana, G. G. (2019). Tuning the Band Gap Energy of Reduced Graphene Oxide Using Biopolymer Chitosan for High Power and Frequency Device Applications. *American Journal of Polymer Science & Engineering*, *7*(1), 8-19.

Jun, B., Elanchezhiyan, S. S. D., Yoon, Y., Wang, D., Kim, S., Prabhu, S. M., & Park, C. M. (2020). Accelerated photocatalytic degradation of rhodamine B over carbonate-rich lanthanum-substituted zinc spinel ferrite assembled reduced graphene oxide by ultraviolet (UV)-activated persulfate. *Chemical Engineering Journal*, 124733.

Kaiser, M. (2017). Effect of rare earth elements on the structural, magnetic and electrical behavior of Ni-Zn-Cr nanoferrites. *Journal of Alloys and Compounds*, *719*, 446-454.

Karim-Nezhad, G., Khorablou, Z., Zamani, M., Seyed Dorraji, P., & Alamgholiloo, M. (2017). Voltammetric sensor for tartrazine determination in soft drinks using poly (p-aminobenzenesulfonic acid)/zinc oxide nanoparticles in carbon paste electrode. *Journal of Food and Drug Analysis*, *25*(2), 293-301.

Katsnelson, M. I. (2007). Graphene : carbon in Carbon is one of the most intriguing elements in the Periodic Table ., *10*(1), 20-27.

Kaur, M., & Kaur, N. (2016). Ferrites : Synthesis and Applications for Environmental Remediation. Book chapter 4, *1238* 113-136.

Keerthana, S. P., Yuvakkumar, R., Kumar, P. S., Ravi, G., & Velauthapillai, D. (2021). Rare earth metal (Sm) doped zinc ferrite ($ZnFe_2O_4$) for improved photocatalytic elimination of toxic dye from aquatic system. *Environmental Research*, 197, 111047.

Kefeni, K. K., & Mamba, B. B. (2020). Photocatalytic application of spinel ferrite nanoparticles and nanocomposites in wastewater treatment: Review. *Sustainable Materials and Technologies*, *23*, e00140.

Kesavamoorthi, R., & Raja, C. R. (2017). Substitution Effects on Rare-Earth Ions-Doped Nickel-Zinc Ferrite Nanoparticles. *Journal of Superconductivity and Novel Magnetism*, *30*(5), 1207-1212.

Khan, S. B., Irfan, S., & Lee, S.-L. (2019). Influence of Zn^{+2} Doping on Ni-Based Nanoferrites ; *Nanomaterials*, *9*, 2-17.

Kosowska, K., Domalik-pyzik, P., Krok-borkowicz, M., & Chłopek, J. (2019). Synthesis and Characterization of Chitosan / Reduced Graphene Oxide Hybrid Composites. *12(13)*: 2077.

Kour, S., Jasrotia, R., Puri, P., Verma, A., Sharma, B., Singh, V. P., … Kalia, S. (2023). Improving photocatalytic efficiency of $MnFe_2O_4$ ferrites via doping with Zn^{2+}/La^{3+} ions: photocatalytic dye degradation for water remediation. *Environmental Science and Pollution Research*, *30*(28), 71527-71542.

Labchir, N., Amaterz, E., Hannour, A., Ait hssi, A., Vincent, D., Ihlal, A., & Sajieddine, M. (2020). Highly efficient nanostructured $CoFe_2O_4$ thin film electrodes for electrochemical degradation of rhodamine B. *Water Environment Research*, *92*(5), 759-765.

Lacombe, S., & Keller, N. (2012). Photocatalysis: Fundamentals and applications in JEP 2011. *Environmental Science and Pollution Research*. *100,* 1-15.

Lakshmi, K. N., & Santhanalakshmi, J. (2020). Synthesis , Size Characterization and Photocatalytic Activities of Zinc Ferrites and Cobalt Ferrites Nanoparticles Using Oxidative Degradations of Methylene Blue , Crystal Violet and Alizarin Red Dyes in Aqueous Medium at 25 ° C. *23*, 121.

Lemziouka, H., BouLemziouka, H., Boutahar, A., Moubah, R., Omari, L. H., Bahhar, S., Lassri, H. (2020). Synthesis, structural, optical and dispersion parameters of La-doped spinel zinc ferrites $ZnFe_{2-x}La_xO_4$ (x = 0.00, 0.001, 0.005, 0.01 and 0.015). *Vacuum*, *182*, 109780.

Lemziouka, H., BouLemziouka, H., Boutahar, A., Moubah, R., Omari, L. H., Bahhar, S., … Lassri, H. (2020). Synthesis, structural, optical and dispersion parameters of La-doped spinel zinc ferrites $ZnFe_{2-x}La_xO_4$ (x = 0.00, 0.001, 0.005, 0.01 and 0.015). *Vacuum*, *182*, 109780.

Li, J., Zhou, D., Liu, W. F., Su, J. Z., & Fu, M. Sen. (2019a). Novel and facile reduced graphene oxide anchored Ni-Co-Zn-Nd-ferrites composites for microwave absorption. *Scripta Materialia*, *171*, 42-46.

Li, J., Zhou, D., Liu, W., Su, J., & Fu, M. (2019b). Scripta Materialia Novel and facile reduced graphene oxide anchored Ni-Co-Zn-Nd-ferrites composites for microwave absorption. *Scripta Materialia*, *171*, 42-46.

Liang, J., Wei, Y., Zhang, J., Yao, Y., He, G., Tang, B., & Chen, H. (2018). Scalable Green Method to Fabricate Magnetically Separable $NiFe_2O_4$-Reduced Graphene Oxide Nanocomposites with Enhanced Photocatalytic Performance Driven by Visible Light. *Industrial and Engineering Chemistry Research*, *57*(12), 4311-4319.

Lipskikh, O. I., Korotkova, E. I., Khristunova, Y. P., Barek, J., & Kratochvil, B. (2018). Sensors for voltammetric determination of food azo dyes - A critical review. *Electrochimica Acta*,

260, 974-985.

Liu, B., Kou, J., Li, F., Huo, D., Xu, J., Zhou, X., … Han, D. (2020). Lemon essential oil ameliorates age-associated cognitive dysfunction via modulating hippocampal synaptic density and inhibiting acetylcholinesterase. *Aging*, *12*(9), 8622-8639.

Lu, D., Zhang, Y., Lin, S., Wang, L., & Wang, C. (2013). Synthesis of magnetic $ZnFe_2O_4$/ graphene composite and its application in photocatalytic degradation of dyes. *Journal of alloys and compounds*, *579*, 336-342.

Lü, M. J., Li, J., Yang, X. Y., Zhang, C. A., Yang, J., Hu, H., & Wang, X. B. (2013). Applications of graphene-based materials in environmental protection and detection. *Chinese Science Bulletin*, *58*(22), 2698-2710.

Mahdikhah, V., Saadatkia, S., Sheibani, S., & Ataie, A. (2020). Outstanding photocatalytic activity of CoFe2O4 /rGO nanocomposite in degradation of organic dyes. *Optical Materials*, *108*, 110193.

Manjunatha, J. G. (2018). A novel voltammetric method for the enhanced detection of the food additive tartrazine using an electrochemical sensor. *Heliyon*, *4(11)*, e00986.

Mansour, S. F., Al-Hazmi, F., AlHammad, M. S., Sadeq, M. S., & Abdo, M. A. (2021). Enhancing the magnetization, dielectric loss and photocatalytic activity of Co–Cu ferrite nanoparticles via the substitution of rare earth ions. *Journal of Materials Research and Technology*, *15*, 2543-2556.

Mary, J., Devadathan, D., Baiju, V., Biju, R., & Raveendran, R. (2017). Photocatalytic Degradation of Azo Dye Congo Red Using Copper Oxide/Nickel Oxide Nanocomposite,*International J. of advanced materal*, *03(06)*, 284-287.

Masoumeh T., Hossein S., Masoud F., E. A. (2020). Simultaneous determination of sunset yellow and tartrazine in soft drinks samples using nanocrystallites of spinel ferrite- modified electrode, *8*, 67-79.

Mishra, S., & Acharya, R. (2020). Materials Today : Proceedings Photocatalytic applications of graphene based semiconductor composites : A review. *Materials Today: Proceedings*, (2020).

Mishra, S., & Acharya, R. (2020). Materials Today : Proceedings Photocatalytic applications of graphene based semiconductor composites : A review. *Materials Today: Proceedings*, 2, 164-169.

Moarefdoust, M. M., Jahani, S., Moradalizadeh, M., Motaghi, M. M., & Foroughi, M. M. (2021). An electrochemical sensor based on hierarchical nickel oxide nanostructures doped with indium ions for voltammetric simultaneous determination of sunset yellow and tartrazine colorants in soft drink powders. *Analytical Methods : Advancing Methods and Applications*, *13(21)*, 2396-2404.

Mohammed, H., Kumar, A., Bekyarova, E., Al-Hadeethi, Y., Zhang, X., Chen, M., … Rimondini, L. (2020). Antimicrobial Mechanisms and Effectiveness of Graphene and Graphene-Functionalized Biomaterials. A Scope Review. *Frontiers in Bioengineering and Biotechnology*, *8*, 465.

Mosleh, M. (2016). Synthesis, characterization and optical properties of neodymium doped nickel ferrite nanoparticles prepared by novel sol–gel method. *Journal of Materials Science: Materials in Electronics*, *27*(7), 6703-6707.

Mullai, R. U., Pradeep, P. P., & Chandrasekaran, G. (2012). Synthesis And Characterization Of Lanthanum Doped Mg-Zn Ferrite Nanoparticles Prepared by SOL-GEL Method, *5*(2), 78-85.

Muthuselvi, M., Jeyasubramanian, K., Hikku, G. S., Muthuselvan, M., Eswaran, M., Senthil Kumar, N., & Ponnusamy, V. K. (2021). Rare earth metal oxide-doped reduced graphene-oxide nanocomposite as binder-free hybrid electrode material for supercapacitor application. *International Journal of Energy Research*, *45*(6), 8255-8266.

Naik, R., Prashantha, S. C., Nagabhushana, H., & Girish, K. M. (2018). Electrochemical , photoluminescence and EPR studies of Fe^{3+} doped nano Forsterite : E ff ect of doping on tetra and octahedral sites. *Journal of Luminescence*, *197*(2017), 233-241.

Narang, S. B., & Pubby, K. (2021). Nickel Spinel Ferrites: A review. *Journal of Magnetism and Magnetic Materials*, *519*, 167163.

Nasirian, M. (2006). Development Of A Novel Photocatalyst For The Photocatalytic Treatment Of Industrial Wastewater. Thesis for fulfilment of the requirment of Doctor of Philosophy in Environmental Analytical Chemistry The National University of Malaysia 14647518/1

Nazim, M., Khan, A. A. P., Asiri, A. M., & Kim, J. H. (2021). Exploring Rapid Photocatalytic Degradation of Organic Pollutants with Porous CuO Nanosheets: Synthesis, Dye Removal, and Kinetic Studies at Room Temperature. *ACS Omega*, *6*(4), 2601-2612.

Nguyen, L. T. T., Nguyen, L. T. H., Manh, N. C., Quoc, D. N., Quang, H. N., Nguyen, H. T. T. Bach, L. G. (2019). A facile synthesis, characterization, and photocatalytic activity of

magnesium ferrite nanoparticles via the solution combustion method. *Journal of Chemistry*, *2019*, 8.

O, Z. Photocatalytic activity of $NiFe_2O_4$ and $Zn_{0.5}Ni_{0.5}Fe_2O_4$ modified by Eu (III) and Tb (III) for decomposition of Malachite Green, *3*, 1124-1132.

Of, S., Effect, T. H. E., Rare, O. F., Ions, E., & Structural, T. H. E. (2016). The structural , magnetic and electrical properties of cu-zn ferrites nanomaterials. *Journal of Magnetism and Magnetic*, *419*, 407-411.

Oliveira, R. De, Hudari, F., Franco, J., Valnice, M., & Zanoni, B. (2015). Carbon Nanotube-Based Electrochemical Sensor for the Determination of Anthraquinone Hair Dyes in Wastewaters, 22-35.

Patella, B., & Sunseri, C. (2018). Dottorato di ricerca in ' Scienza dei materiali e nanotecnologie Electrochemical sensors for environmental and clinical analyses Tutor : Carmelo Sunseri. *2*, 4-10.

Patil, S. B., Bhojya Naik, H. S., Nagaraju, G., Viswanath, R., & Rashmi, S. K. (2017). Synthesis of visible light active Gd^{3+}-substituted $ZnFe_2O_4$ nanoparticles for photocatalytic and antibacterial activities. *European Physical Journal Plus*, *132*(8), 328

Patil, S. B., Naik, H. S. B., Nagaraju, G., Viswanath, R., Rashmi, S. K., & Vijay, M. (2019). Sugarcane juice mediated eco-friendly synthesis of visible light active zinc ferrite nanoparticles : Application to degradation of mixed dyes and antibacterial activities Sugarcane juice mediated eco-friendly synthesis of visible light active zinc ferrite. *Materials Chemistry and Physics*, *212*, 351-362.

Pattanayak, U. (2017). Green Synthesis of Zinc Nanoparticle, (411), 1-70.

Pawar, D. B., Khirade, P. P., Vinayak, V., Ravangave, L. S., & Rathod, S. M. (2020). Sol–gel auto-ignition fabrication of Gd^{3+} incorporated $Ni_{0.5}Co_{0.5}Fe_2O_4$ multifunctional spinel ferrite nanocrystals and its impact on structural, optical and magnetic properties. *SN Applied Sciences*, *2*(10), 1713.

Penagos-Llanos, J., García-Beltrán, O., Nagles, E., & Hurtado, J. J. (2020). A New Electrochemical Method to Detect Sunset Yellow, Tartrazine and Thiomersal in a Pharmaceutical Dose Using a Carbon Paste Electrode Decorated with Molybdenum Oxide. *Electroanalysis*, *32*(10), 2174-2182.

Perdomo, Y., Arancibia, V., García-Beltrán, O., & Nagles, E. (2017). Adsorptive stripping

voltammetric determination of Amaranth and tartrazine in drinks and gelatins using a screen-printed carbon electrode. *Sensors (Switzerland)*, *17*(11), 1-10.

Peymani-Motlagh, S. M., Moeinian, N., Rostami, M., Fasihi-Ramandi, M., Sobhani-Nasab, A., Rahimi-Nasrabadi, M., … Ajami, N. (2019). Effect of Gd^{3+}-, Pr^{3+}- or Sm^{3+}-substituted cobalt–zinc ferrite on photodegradation of methyl orange and cytotoxicity tests. *Journal of Rare Earths*, *37*(12), 1288-1295.

Philosophy, D. O. F. (2018). Nd^{3+} Doped Mn-Zn Ferrite Nanoparticles : Effect Of Dopant Content Thesis submitted in fulfillment of the requirements for the Degree of, (November).

Phor, L., & Kumar, V. (2019). Structural, magnetic and dielectric properties of lanthanum substituted $Mn_{0.5}Zn_{0.5}Fe_2O_4$. *Ceramics International*, *45*(17), 22972-22980.

Phor, L., & Kumar, V. (2020). Structural , magnetic and dielectric properties of lanthanum substituted Structural , magnetic and dielectric properties of lanthanum substituted. *Ceramics International*, *45*(17), 22972-22980.

Power, A. C., & Morrin, A. (2013). Electroanalytical Sensor Technology. *Chapter 7, In book: Electrochemistry*, 38.

Raciti, R., Bahariqushchi, R., Summonte, C., Aydinli, A., Terrasi, A., & Mirabella, S. (2017). Optical bandgap of semiconductor nanostructures: Methods for experimental data analysis. *Journal of Applied Physics*, *121*(23).

Rahman, A., Warsi, M. F., Shakir, I., Shahid, M., & Zulfiqar, S. (2020). Fabrication of Ce^{3+} substituted nickel ferrite-reduced graphene oxide heterojunction with high photocatalytic activity under visible light irradiation. *Journal of Hazardous Materials*, *394*, 1-18.

Raje Shaikh, B. B., & Chishty, S. Q. (2021). Auto-ignition synthesis of rare-earth metal-doped Ni–Zn spinel ferrites for electronic applications. *Journal of Materials Science: Materials in Electronics*, *32*(19), 23999-24010.

Raril, C., Manjunatha, J. G., Tigari, G., & Hareesha, N. (2018). Fabrication of the Tartrazine Voltammetric Sensor based on Surfactant Modified Carbon Paste Electrode, *2*(4), 21-26.

Rashmi, S. K., Bhojya Naik, H. S., Jayadevappa, H., Viswanath, R., Patil, S. B., & Madhukara Naik, M. (2017). Solar light responsive Sm-Zn ferrite nanoparticle as efficient photocatalyst. *Materials Science and Engineering: B*, *225*, 86-97.

Rashmi, S. K., Naik, H. S. B., Jayadevappa, H., Viswanath, R., Patil, S. B., & Naik, M. M. (2017). Materials Science & Engineering B Solar light responsive Sm-Zn ferrite nanoparticle as e ffi

cient photocatalyst. *Materials Science & Engineering B*, *225*(May), 86-97.

Rather, S. U., Saeed, U., Al-Zahrani, A. A., Bamufleh, H. S., Alhumade, H. A., Taimoor, A. A., Alam, M. M. (2021). Doped Nanostructured Manganese Ferrites: Synthesis, Characterization, and Magnetic Properties. *Journal of Nanomaterials, 2021*.

Rahman, A., Warsi, M. F., Shakir, I., Shahid, M., & Zulfiqar, S. (2020). Fabrication of Ce^{3+} substituted nickel ferrite-reduced graphene oxide heterojunction with high photocatalytic activity under visible light irradiation. *Journal of Hazardous Materials*, 3, *394*, 1-18.

Rezlescu, N., & Rezlescu, E. (1997). Comparative study of the effects of rare earth ions in a high frequency Ni-Zn ferrite. *Journal De Physique. IV : JP*, *7*(1), C1-225-C1-226.

Riaz, A., Bibi, R., Jabeen, S., Zulfiqar, S., Agboola, P. O., Shakir, I., & Farooq, M. (2020). rGO sheets as green photocatalyst nano-heterostructured materials, *190*, 226-236.

Rimus, A., Herry, A., Jauhari, A., Kusumah, F., Lupitasari, A., Naufal, D., Wulan, R. (2023). Case Studies in Chemical and Environmental Engineering Recent trends of spinel ferrites (MFe_2O_4: Mn, Co, Ni, Cu, Zn) applications as an environmentally friendly catalyst in multicomponent reactions : A review. *Case Studies in Chemical and Environmental Engineering*, *7*, 100303.

Rovina, K., Siddiquee, S., & Md Shaarani, S. (2021). An electrochemical sensor for the determination of tartrazine based on CHIT/GO/MWCNTs/AuNPs composite film modified glassy carbon electrode. *Drug and Chemical Toxicology*, *44*(5), 447-457.

Samikannu, K. (2013). Sol-gel auto-combustion synthesis of cobalt ferrite and it's cytotoxicity properties. *Journal of Nanomaterials and Biostructures*, 4(8), 1601-1610.

Samoila, P, Sacarescu, L., Borhan, A. I., Timpu, D., & Grigoras, M. (2015). Journal of Magnetism and Magnetic Materials Magnetic properties of nanosized Gd doped Ni–Mn–Cr ferrites prepared using the sol–gel autocombustion technique, *378*, 92-97.

Samoila, Petrisor, Cojocaru, C., Cretescu, I., Stan, C. D., Nica, V., Sacarescu, L., & Harabagiu, V. (2015). Nanosized Spinel Ferrites Synthesized by Sol-Gel Autocombustion for Nanosized Spinel Ferrites Synthesized by Sol-Gel Autocombustion for Optimized Removal of Azo Dye from Aqueous Solution, 2015(5):1-13.

Samoila, Petrisor, Cojocaru, C., Sacarescu, L., Dorneanu, P. P., Domocos, A. A., & Rotaru, A. (2017). Remarkable catalytic properties of rare-earth doped nickel ferrites synthesized by sol-gel auto-combustion with maleic acid as fuel for CWPO of dyes. *Applied Catalysis B:*

Environmental, *202*, 21-32.

Sanida, A., Stavropoulos, S. G., Speliotis, T., & Psarras, G. C. (2019). Investigating the effect of zn ferrite nanoparticles on the thermomechanical, dielectric and magnetic properties of polymer nanocomposites. *Materials*, *12*(18), 3015.

Saravanan, M. (2022). Photocatalytic degradation of reactive black dye using ZnO – CeO_2 Nanocomposites, *2*, 1-24.

Sedky, A., Amin, S. A., & Mohamed, M. (2019). Electrical, photoluminescence and ferromagnetic characterization of pure and doped ZnO nanostructures. *Applied Physics A: Materials Science and Processing*, *125*(5).

Sevilla, P. (2013). Molecular characterization of drug´s nanocarriers based on plasmon-enhanced spectroscopy: Fluorescence (SEF) and Raman (SERS). *Optica Pura y Aplicada*, *46*(2), 111-119.

Shahid, M., Alsafari, I. A., Jamil, A., Ahmed Ali, F. A., Haider, S., Agboola, P., & Shakir, I. (2020). Dysprosium substituted nickel cobalt ferrite nanomaterials and their composites with reduced graphene oxide for photocatalysis. *Journal of Taibah University for Science*, *14*(1), 1308-1316.

Shaikh, B. B. R. (2021). Auto-ignition synthesis of rare-earth metal-doped Ni – Zn spinel ferrites for electronic applications. *Journal of Materials Science: Materials in Electronics, 32(19) 23999-24010*.

Shinde, S. S. (2016). Crystal Structure and Magnetic Interactions of Ferrites, *5*(11), 2015-2017.

Shume, W. M., Murthy, H. C. A., & Zereffa, E. A. (2020). A Review on Synthesis and Characterization of Ag_2O Nanoparticles for Photocatalytic Applications. *Journal of Chemistry*, *2020*. 15.

Sierra-rosales, P., Toledo-neira, C., & Squella, J. A. (2017). Sensors and Actuators B : Chemical Electrochemical determination of food colorants in soft drinks using MWCNT-modified GCEs. *Sensors & Actuators: B. Chemical*, *240*, 1257-1264.

Singh, R. K., Upadhyay, C., Layek, S., & Yadav, A. (2010a). Cation distribution of $Ni_{0.5}Zn_{0.5}Fe_2O_4$ nanoparticles. *MultiCraft International Journal of Engineering, Science and Technology*, *2*(8), 104-109.

Singh, R. K., Upadhyay, C., Layek, S., & Yadav, A. (2010b). Cation distribution of $Ni_{0.5}Zn_{0.5}Fe_2O_4$ nanoparticles. *International Journal of Engineering, Science and Technology*, *2*(8), 104-109.

Šoka, M., Ušáková, M., Dosoudil, R., Ušák, E., & Lokaj, J. (2018). Effect of lanthanum substitution on structural and magnetic properties of nickel zinc ferrites. *AIP Advances*, *8*(4), 047802.

Somvanshi, S. B., Jadhav, S. A., Khedkar, M. V., Kharat, P. B., More, S. D., & Jadhav, K. M. (2020). Structural, thermal, spectral, optical and surface analysis of rare earth metal ion (Gd^{3+}) doped mixed Zn–Mg nano-spinel ferrites. *Ceramics International*, *46*(9), 13170-13179.

Soufi, A., Hajjaoui, H., Elmoubarki, R., & Abdennouri, M. (2021). Applied Surface Science Advances Spinel ferrites nanoparticles : Synthesis methods and application in heterogeneous Fenton oxidation of organic pollutants – A review. *Applied Surface Science Advances*, *6*, 100145.

Spyrou, K., & Rudolf, P. (2014). An Introduction to Graphene, 1-20.

Srivastava, R., & Yadav, B. C. (2012). Ferrite Materials: Introduction, Synthesis Techniques, and Applications as Sensors. *International Journal of Green Nanotechnology*, *4*(2), 141-154.

Stankovic, D. M., Fabia, M., Vukadinovic, A., Dojc, B., & Antic, B. (2018). A Voltammetric Sensor Based on $MgFe_2O_4$ Decorated on Reduced Graphene Oxide-modified Electrode for Sensitive and Simultaneous Determination of Catechol and Hydroquinone, 1-9.

Stergiou, C., & Litsardakis, G. (2014). Structural and magnetic properties of yttrium and lanthanum-doped Ni-Co and Ni-Co-Zn spinel ferrites, *1627*(2015), 117-122.

Stozhko, N. Y., Khamzina, E. I., & Bukharinova, M. A. (2022). An Electrochemical Sensor Based on Carbon Paper Modified with Graphite Powder for Sensitive Determination of Sunset Yellow and Tartrazine in Drinks, 22(11), 4092..

Stradiotto, N. R., Yamanaka, H., & Zanoni, M. V. B. (2003). Electrochemical Sensors : A Powerful Tool in Analytical Chemistry. *Review Electrochemical Sensors : A Powerful Tool in Analytical Chemistry*, *2015*, 14801-970.

Tanwar, R., & Mandal, U. K. (2019). Photocatalytic activity of $Ni_{0.5}Zn_{0.5}Fe_2O_4$@polyaniline decorated BiOCl for azo dye degradation under visible light-integrated role and degradation kinetics interpretation. *RSC Advances*, *9*(16), 8977-8993.

Tartrazine, S. determination of sunset yellow and. (2020). Simultaneous determination of sunset yellow and tartrazine in soft drinks samples using nanocrystallites of spinel ferrite- modified electrode, *8*, 67-79.

Tatarchuk, T., Bououdina, M., Macyk, W., Shyichuk, O., Paliychuk, N., Yaremiy, I., … Pacia, M.

(2017). Structural, Optical, and Magnetic Properties of Zn-Doped $CoFe_2O_4$ Nanoparticles. *Nanoscale Research Letters*, *12*(1), 141.

Tavakkoli, N., Soltani, N., Shahdost-fard, F., Ramezani, M., Salavati, H., & Jalali, M. R. (2018). Simultaneous voltammetric sensing of acetaminophen, epinephrine and melatonin using a carbon paste electrode modified with zinc ferrite nanoparticles. *Microchimica Acta*, *185*(10), 1-11.

Toksha, B. G., Shirsath, S. E., Mane, M. L., Patange, S. M., Jadhav, S. S., & Jadhav, K. M. (2011). Autocombustion High-Temperature Synthesis , Structural , and Magnetic Properties of $CoCr_xFe_2À_xO_4$ ($0 \leq x \leq 1$. 0). *Journal of Physical Chemistry C*, *115*, 20905-20912.

Tran, Q. T., Phung, T. T., Nguyen, Q. T., Le, T. G., & Lagrost, C. (2019). Highly sensitive and rapid determination of sunset yellow in drinks using a low-cost carbon material-based electrochemical sensor Highly sensitive and rapid determination of sunset yellow in drinks using a low cost carbon material-based electrochemical. *Anal Bioanal Chem*, 411, 7539–7549.

Tsvetkov, M., Milanova, M., Pereira, L. C. J., Waerenborgh, J. C., Cherkezova-Zheleva, Z., Zaharieva, J., & Mitov, I. (2016). Magnetic properties of binary and ternary mixed metal oxides $NiFe_2O_4$ and $Zn_{0.5}Ni_{0.5}Fe_2O_4$ doped with rare earths by sol-gel synthesis. *Chemical Papers*, *70*(12), 1600-1610.

Tsvetkov, M. P., Ivanova, I. R., Valcheva, E. P., Zaharieva, J. T., & Milanova, M. M. (2019). modified by Eu (III) and Tb (III) for decomposition of Malachite Green. *Open Chem.*, *17*, 1124-1132.

Vasambekar, P. N., Shinde, T. J., & Gadkari, A. B. (2013). Nd^{3+} Substituted Nanocrystalline Zinc Ferrite Sensors for Ethanol, LPG and Chlorine. *Applied Mechanics and Materials*, *310*, 150-153.

Vedrtnam, A., Kalauni, K., Dubey, S., & Kumar, A. (2020). A comprehensive study on structure, properties, synthesis and characterization of ferrites. *AIMS Materials Science*, *7*(6), 800-835.

Vinosha, P. A., Manikandan, A., Ragu, R., Dinesh, A., Paulraj, P., Slimani, Y., … Nirmala, G. F. (2021). Exploring the influence of varying pH on structural, electro-optical, magnetic and photo-Fenton properties of mesoporous $ZnFe_2O_4$ nanocrystals. *Environmental pollution, (1987)*, *272*, 115983.

Wang, Jin, Yang, B., Zhang, K., Bin, D., Shiraishi, Y., Yang, P., & Du, Y. (2016). Highly sensitive

electrochemical determination of Sunset Yellow based on the ultrafine Au-Pd and reduced graphene oxide nanocomposites. *Journal of Colloid and Interface Science*, *481*, 229-235.

Wang, Joseph. (2018). Electrochemical sensor for environmental monitoring system: A review, *AIP Conference Proceedings*, *2669*, 030007.

Wang, Y., Wu, X., Zhang, W., & Chen, W. (2016). Synthesis and electromagnetic properties of La-doped Ni-Zn ferrites. *Journal of Magnetism and Magnetic Materials*, *398*, 90-95.

Wu, T., Shen, G., Ding, F., Li, D., & Zhong, H. (2020). Effects of La^{3+} doping on the structure, properties and application of Mn–Zn ferrite. *Materials Chemistry and Physics*, *252*, 123328.

Wu, X., Wu, W., Qin, L., Wang, K., Ou, S., Zhou, K., & Fan, Y. (2015). Structure and magnetic properties evolution of nickel-zinc ferrite with lanthanum substitution. *Journal of Magnetism and Magnetic Materials*, *379*, 232-238.

Yan, L., & Chen, W. (2011). Preparation of chitosan/graphene oxide composite film with enhanced mechanical strength in the wet state, 2018, 653-658.

Yenier, Z., Seki, Y., Şen, I., Sever, K., Mermer, Ö., & Sarikanat, M. (2016). Manufacturing and mechanical, thermal and electrical characterization of graphene loaded chitosan composites. *Composites Part B: Engineering*, *98*, 281-287.

Zhang, Q., Cheng, W., Wu, D., Yang, Y., Feng, X., Gao, C., Tang, X. (2022). An electrochemical method for determination of amaranth in drinks using functionalized graphene oxide / chitosan / ionic liquid nanocomposite supported nanoporous gold, *367*(2021).

Zhao, Y., Xu, M., Ji, Y., Dong, Y., Xing, G., Xia, P., … Qiao, L. (2022). Enhanced Photocatalytic Activities for Degradation of Dyes and Drugs by Crystalline Bismuth Ferrite-Modified Graphene Hybrid Aerogel. *Crystals*, *12*(11), 1604.